Numerical simulation for milling processes of thin wall structures

Adetoro, Oluwamayokun B.

School of Engineering and Material Science
Queen Mary, University of London

Numerical Simulation for Milling Processes of Thin Wall Structures

Oluwa**mayo**kun B. Adetoro

A thesis submitted for the degree of Doctor of Philosophy
at the University of London

Queen Mary
University of London

2009

Statement of Originality

I certify that this thesis, and the research to which it refers, are the product of my own work and that any ideas or quotations from the work of other people, published or otherwise, are fully acknowledged in accordance with the standard referencing practices of the discipline.

Abstract

In the aerospace industry, the manufacturing of structures as one monolithic piece is very common. At the same time, thin walled sections are becoming more wide spread due to weight requirements, environmental concerns and the general demand for higher efficiency. These thin walled sections are easily found within the aircraft wings, fuselage and engines. The machining of these sections is one of the most complex manufacturing processes in the aerospace industry, due to its low stiffness and it is investigated in this thesis.

In this thesis, an approach to predicting both the average and instantaneous cutting force coefficients required in force models, using a Finite Element Method (FEM) based on an Arbitrary Lagrangian-Eulerian formulation (ALE) is presented. Due to the inherent flexibility of both the cutter and the workpiece, the milling process is naturally accompanied by both dynamic and static vibrations. In order to investigate the dynamic vibrations, the dynamic parameters of both the cutter and the workpiece are required. A novel numerical and experimental investigation has been carried out in this thesis for the prediction of thin walled structure's damping parameters. A newly discovered approach to predicting the structural damping parameters is proposed and its applications in thin-wall machining is presented. An FEM and Fourier transform (FT) approach is presented, to obtain the frequency response function (FRF) required for the prediction of chatter vibration free cutting conditions.

A more accurate stability model that considers the effects of higher harmonics from highly intermittent milling process, the nonlinearity of the cutting force coefficients and axial immersion angle along the axial depth of cut is developed. A numerical approach to obtaining a converged solution to the stability model is presented. A method that uses the FEM and the FT approach and the improved stability model, whilst considering the nonlinearities of the thin-wall dynamics in predicted stable region is also presented.

Table of Contents

Acknowledgements

I would like to start by acknowledging the immense support and guidance provided by God not as a cliché rather as a reality and it is to Him I dedicate this work.

It is impossible to get very far without communication with others and sincere help and guidance from others before us…

I would like to express my sincere appreciation to my supervisor Dr. Pihua Wen, who has been more than just a research supervisor to me for many years. I greatly appreciate his guidance, advice, support and last but not the least, his transfer of knowledge.

I would also like to thank Dr. Wei-Ming Sim for his guidance, encouragement, help, immense support and above all, his sacrifice in hours of experimental tests right through the course of the project. I truly do appreciate it. I also appreciate Mr. Alister Reynish for the very helpful advice through his immense experience and his assistance in experimental tests.

I thank Dr. Ranjan Vepa for his support and the very helpful hours spent in explaining the fundamentals in the topic. I also thank my colleagues Mr. Zaheer Ikram, Dr. Chetan Jagadeesh and Mr. Jerome Irianto amongst others for their assistance and for providing a pleasant working environment.

I thank Airbus for providing all the experimental resources required and also for making the whole research experience a very delightful one.

Finally, I am most thankful to my entire family and my dear sister (Abimbola), for their sacrifice, continuous support and understanding during the course of this study.

This research has been jointly funded by Airbus and the Engineering and Physical Sciences Research Council (EPSRC).

List of Figures

List of Tables

Nomenclature

Roman

a	axial depth of cut
$a_{\lim}$	limiting axial depth of cut for chatter stability
$a_{\lim}^{*}$	converged limiting axial depth of cut for chatter stability
a^{m}	predicted axial depth of cut for m^{th} increment
$a_{11}, a_{12}, a_{21}, a_{22}$	constants arising from the particular integral of the equation of motion in transformed co-ordinates
$b_{11}, b_{12}, b_{21}, b_{22}$	constants arising from the particular integral of the equation of motion in transformed co-ordinates
d	nodal displacement vector
db	chip width
dF_{tj}, dF_{rj}, dF_{aj}	differential tangential, radial and axial cutting forces on flute j
dS	cutting edge length
dz	differential height of the chip segment
$\mathbf{f}$	force vector in transformed co-ordinate
f_v	frequency of dynamic vibrations
h	uncut chip thickness
$i(z)$	helix angle at elevation z
$\mathbf{i, j, k}$	directional vectors
k	integer number of vibration waves within a tooth period
m_{accel}	accelerometer's mass
$\mathbf{q}$	displacement in transformed co-ordinate

q_p	p^{th} mode displacement in transformed co-ordinate
r_{doc}	radial depth of cut
$r(z)$	cutter radius at elevation
$\mathbf{r}(\phi_j, z)$	vector from cutter centre to cutting edge
$\{r(i\omega)\}$	displacement vector in frequency domain
s	complex Laplace plane
s_p^+, s_p^-	complex roots of the characteristic equation in the transfer function matrix
s_t	feed per tooth
t	time
$\{\Delta(t)\}$	displacement vector in time domain
u, v, w	displacements in the X, Y and Z directions
u	displacement
$\dot{u}$	velocity
$\ddot{u}$	acceleration
x, y, z	coordinates of a given point in the 3-D Cartesian system
$\Delta x, \Delta y, \Delta z$	total relative displacement between cutter and workpiece in the global co-ordinates
$\left.\begin{matrix} x_c, x_w, y_c, \\ y_w, z_c, z_w \end{matrix}\right\}$	cutter and workpiece dynamic displacements in the global co-ordinates for the current tooth period
$\left.\begin{matrix} x_c^0, x_w^0, y_c^0, \\ y_w^0, z_c^0, z_w^0 \end{matrix}\right\}$	cutter and workpiece dynamic displacements in the global co-ordinates for the previous tooth periods
y_{pi}	actual data used in curve fitting

y_{pi}	curve fitting predictions
z	cutter geometry
$[A(t)]$	directional dynamic milling coefficient matrix
$A(\omega)$	accelerance frequency response function
$A_{new}(\omega)$	accelerance frequency response function compensated for accelerometer's mass
$\left.\begin{matrix} A_1, A_2, A_3, \\ B_1, B_2, B_3 \end{matrix}\right\}$	cutter geometry constants
$[B]$	strain-displacement matrix for 3-D elastic body
$[C]$	damping matrix
C_p	p^{th} mode modal damping
C_1, C_2, C_3, C_4, C_5	immersion Constants
C_{t1}, C_{r1}, C_{a1}	1st-order polynomial curve fitting for exponential tangential, radial and axial cutting force coefficients
C_{t2}, C_{r2}, C_{a2}	2nd-order polynomial curve fitting for exponential tangential, radial and axial cutting force coefficients
C_{t3}, C_{r3}, C_{a3}	3rd-order polynomial curve fitting for exponential tangential, radial and axial cutting force coefficients
D	cutter diameter
$D_{i=1-9}$	immersion Constants for modified mechanistic model
$[D]$	elasticity matrix
E	Young's modulus of elasticity
$F(\omega)$	input force in frequency domain
$\{\tilde{F}(s)\}, \{\tilde{X}(s)\}$	Laplace transforms of force and displacement vectors
F_t, F_n	tangential and normal cutting forces in orthogonal cutting

F_{xj}, F_{yj}, F_{zj}	cutting forces in feed x, normal y, and axial directions z on flute j
$[G_c], [G_w]$	cutter and workpiece transfer function
$[J]$	Jacobian matrix of coordinate transformation
$[K]$	stiffness matrix of structure
K_p	p^{th} mode modal stiffness
K_{di}, K_{ci}	direct and cross inner modulation dynamic cutting force coefficients
K_{do}, K_{co}	direct and cross outer modulation dynamic cutting force coefficients
K_s	specific cutting force coefficient
K_t, K_r, K_a	exponential tangential, radial and axial cutting force coefficients (exponential force model)
K_{tc}, K_{rc}, K_{ac}	tangential, radial and axial cutting force coefficients (linear-edge force model)
K_{te}, K_{re}, K_{ae}	exponential tangential, radial and axial cutting force coefficients (linear-edge force model)
$K_{tc1}, K_{tc2}, K_{tc3}$	tangential cutting force coefficients (non-linear edge force model)
$K_{rc1}, K_{rc2}, K_{rc3}$	radial cutting force coefficients (non-linear edge force model)
$K_{ac1}, K_{ac2}, K_{ac3}$	axial cutting force coefficients (non-linear-edge force model)
$[M]$	mass matrix of structure
M_p	p^{th} mode modal mass
$M_r M_z$	cutter geometry
N	number of teeth or flutes on the cutter

N_i	shape functions for subscript i node
$N_r, N_z,$	cutter geometry
P	a cutting point on cutting edge
$\{P\}$	external force
R	cutter radius
$[R]_p$	p^{th} modal residue
R_c, R_r, R_z	cutter geometry
T	tooth period
V	volume
X	feed direction coordinate axis
$\ddot{X}(\omega)$	acceleration in frequency domain
Y	normal direction coordinate axis
Z	axial direction coordinate axis

Greek

α, β	cutter geometry
$\alpha_{rlp}, \beta_{rlp}$	constants reflecting the residue of mode p at row r and column l of the transfer function matrix
$[\alpha_C]$	directional dynamic milling coefficients curve fitted polynomial constants
α_{rake}	cutter's rake angle in orthogonal cutting
α_u	Rayleigh, Caughey and proposed damping model's real constants

$\left.\begin{matrix}\alpha_{xx},\alpha_{xy},\alpha_{xz},\\ \alpha_{yx},\alpha_{yy},\alpha_{yz},\\ \alpha_{zx},\alpha_{zy},\alpha_{zz},\end{matrix}\right\}$	directional dynamic milling coefficients
ε	phase between successive waves in chatter vibrations
$\{\varepsilon\}$	strain tensor
$\varepsilon_x,\varepsilon_y,\varepsilon_z$	direct strain
ϕ	rotation angle of the cutter
$\phi_j(z)$	immersion angle of flute j at level z on the XY plane
ϕ_p	cutter pitch angle
ϕ_{start},ϕ_{exit}	start and exit angles of cut in milling
φ	material variable/property
γ_{flank}	cutter's flank angle
γ_{effect}	cutter's effective flank angle during cutting
$\gamma_{xy},\gamma_{yz},\gamma_{zx}$	shear strains
$\bar{\gamma},\bar{\kappa}$	average axial immersion angle
η^m	limiting axial depth of cut error for m^{th} axial depth of cut increment
κ	axial immersion angle
λ	wavelength of dynamic vibrations
ν	Poisson's ratio
ρ	density
$\{\sigma\}$	stress tensor
$\sigma_x,\sigma_y,\sigma_z$	direct stresses
$\tau_{xy},\tau_{yz},\tau_{zx}$	shear stresses

υ	cutting speed / material velocity
$\hat{\upsilon}_i$	mesh velocity
$\upsilon_{jc}, \upsilon_{jw}$	cutter and workpiece dynamic vibrations in tooth's local co-ordinates for the current toot period
$\upsilon_{jc}^0, \upsilon_{jw}^0$	cutter and workpiece dynamic vibrations in tooth's local co-ordinates for the current toot period
ω	frequency
ω_c	chatter frequency
ω_d	damped natural frequency
ω_n	undamped natural frequency
ω_{np}	p^{th} mode natural frequency
ω_T	tooth passing frequency
ξ, η, ζ	isoparametric natural element coordinates
ψ	phase shift of the eigenvalues
$\psi(z)$	lag angle at elevation z
ζ_p	p^{th} mode damping ratio
$\overline{\zeta}_p, \overline{\zeta}_h, \overline{\omega}_p, \overline{\omega}_h$	newly defined parameters for the prediction of damping ratio
$[\Phi]$	oriented transfer function
Λ	eigenvalue of dynamic milling force eigenvalue problem
Ω, n	spindle speed in rev per min
$\{\Psi_p\}$	p^{th} mode eigenvector

To the One with a perfect knowledge of the sciences governing everything in our physical world

Chapter 1

Introduction

1.1. Background of the Research

In aerospace, the manufacturing process is progressively limiting the use of joints through the manufacturing of structures as one monolithic piece. Machining is a very common operation in manufacturing, due to its versatility and its high material removal rate in producing parts of desired dimensions. Aircraft wing sections, fuselage sections, turbine blades and jet engine compressors, are all typical parts with sections produced from machined aluminium or titanium blocks. With environmental concerns and the general demand for higher efficiency, weight requirements compel the design of much thinner sections. For this reason, thin sections with a height to thickness ratio of 35:1 or even thinner are common in manufactured workpiece sections. Whilst on the one hand manufacturing of aluminium alloys is relatively easier compared to titanium alloys due to their relatively low yield stress, on the other hand thin-wall sections can be problematic due to added reduced structural stiffness. In order to maintain the quality of the machined parts there is usually a dimensional tolerance, which the machined parts have to satisfy. To enforce this, it is a general practice for machined parts to undergo inspection before they are certified for use. While parts

that fail this inspection are either scrapped or subjected to many hours of manual labour to remove the bad surface finish.

Machining processes used in manufacturing industries for the purpose of material removal vary in their design and approach. They generally can be grouped into three main categories:

- Cutting processes (including milling, drilling or lathe).
- Abrasive processes (including grinding, lapping and polishing).
- Special processes (including the use of chemical compounds, laser, water jet to remove material).

In milling the workpiece is fed past a rotating tool with one or more teeth, which makes it possible to attain very high 'Material Removal Rate' (MRR). This can be a major advantage in mass production. The tooth/teeth remove the material from the workpiece in the form of small individual 'chips'. The milling process can generally be grouped into three categories namely: peripheral/slab milling, face milling and end milling (Kalpakjian and Schmid, 2003). The cutting occurs along the teeth on the periphery of the tool in peripheral milling and the axis of rotation is parallel to the machined surface. In face milling however, the cutting occurs both along the teeth on the periphery and also the face of the tool. End milling is the most flexible of the three groups and can be used to cut out any desired shape using 5-axis milling machines. Face milling is different from end milling in that its axis of rotation is perpendicular to the workpiece surface. Even though the researches into the milling process have flourished extensively for over sixty years, study into the process is continually motivated by the manufacturing's ever increasing demand for better performance.

The study into the numerical simulations of the machining of thin-walled sections is the focus of this thesis. Machining time for wing sections such as wing box rib, wing spar or fuselage frame can easily range from 10 hours to 20 hours and one of the main problems encountered has to do with cutting conditions when machining thin-wall sections. Even though the project originated and was supported by an aircraft wing manufacturing company, its applications however are valid in other milling processes.

In milling the cutting conditions used are very important and must be chosen with care as they directly influence the cutting forces. The different excitations during milling process can be grouped into two main categories as follows:

1. Primary excitation: These sources must not be ignored but kept within safe levels as they can lead to extremely high vibrations, which if not prevented could lead to tool break, possibly damage the spindle and certainly cause wavy and bad surface finish. Primary sources include:

- Excitations from cutting forces. The cutting forces are direct periodic external forces acting on the system, which deflects both the workpiece and the tool. The machine, cutter and the workpiece are collectively referred to at times as 'the system'.
- Undulations left on machined surface. Due to the vibrations during the cutting process, the machined surface is wavy. While at the next subsequent tooth pass, the wavy surface finish causes fluctuations in the chip load, which in turn causes unsteady cutting forces.
- Damaged tool or worn out spindle. This causes a deviation from the designed performance and unsteady cutting forces.
- Tool run out. This is an offset in the tool, collet and spindle set up, characterised by the cutter having a rotational axis differing from its geometric axis. It can have adverse effects on the chip load distribution between the flutes, which invariably causes varying cutting forces.

2. Secondary excitations: The excitations causes by these sources are very minimal and most of which either resisted due to the system's stiffness or dampened out by the system's dynamics. Secondary excitations include mechanical vibrations (due to the motor, the motion of the machine table and so on) as well as acoustic vibrations.

The cutting forces cause structural vibrations in the workpiece, tool and spindle. These vibrations can be classified as free vibrations (occur after an external energy source is removed), forced vibrations (occur during the presence of an external energy source) and self-excited vibrations (Huo and Cheng, 2009). The self excited vibration has its source from the inherent structural dynamics of

the machine tool-workpiece and feedback responses. The self excited vibration is an effect of the undulations explained earlier. The optimum cutting case is when the undulations left on the machined surface are in phase with the undulations from previous tooth pass. The worst case however is when the phase angle between the two undulations is out of phase by 90^{o}. This leads to the phenomena known as ‘‘regenerative chatter’’ or simply ‘‘chatter’’, which is discussed in more detail in Chapters 4, 5 and 6. Chatter is usually characterised by a very bad surface finish and a drastic increase in both cutting forces and vibrations. Chatter as stated by Taylor is one of the most obscure and delicate of all problems facing the machinist (Taylor, 1907). It undermines the machinist's efforts, reduces productivity and surface quality in manufacturing. In some cases the surface finish can subsequently be improved, either during the finishing cut or by polishing the surface, while in other cases the workpiece has to be scrapped. Chatter is also undesirable due to its adverse effects on the tool and spindle life. The relative stiffness between the tool and the workpiece would determine which flexibility is dominant. The cutting conditions determine the cutting forces which lead to forced vibrations, while the cutting conditions also determine the onset of regenerative or self-excited vibrations. The forced vibrations can also lead to the onset of chatter. Though the forced vibrations can be reduced they can never be eliminated, while the self-excited vibrations occur when certain cutting condition are used. These conditions are jointly known as unstable cutting conditions.

1.2. The Scope of the Research

Currently during the manufacturing process, limited or no knowledge of stable cutting conditions compels process planners on most occasions to resort to a trial and error approach; the reliance of which is heavily dependent on the individual's experience. Even with the most experienced individuals, these selected trial conditions may still result in the onset of chatter, possibly excessive cutting forces and damage to tool, workpiece or machine. This is the purpose for the continuous investigations including this work, to better improve the cutting process. These studies utilise different approaches ranging from analytical to numerical methods. This work successfully:

- Made improvements to known and available cutting force models.
- Identified the possibility of predicting structural damping.
- Minimized the need for experimental methods.
- Made major improvements into the prediction of stable cutting conditions.

Right through the study, experimental validations are used extensively as this is one of the most reliable methods of checking the soundness and practicality of proposed theoretical results. The models developed in this thesis for the simulation of thin-wall machining are quite comprehensive and are believed to contribute to the literature on metal cutting.

1.3. The Structure of the Dissertation

The chapters of the thesis are organized as follows:

In Chapter 2, the literature into metal cutting in general, milling geometry, cutting force modelling, dynamic modelling, chatter stability prediction and Finite Element Method (FEM) modelling of metal cutting is introduced. This chapter provides an in-depth review of the literature into metal cutting process, with a quick summary presented in subsequent chapters.

Chapter 3 covers cutting force modelling. The well developed mechanistic approach to cutting force modelling is presented and the approach to calibrating its coefficients is explained. Improvements to this model are presented in the form of a higher order mechanistic model. This improvement would better model the cutting forces when the cutting force coefficients are not a linear function of the axial depth of cut although it does come at the price of added coefficients. The chapter then goes on to introduce the application of Finite Element Method (FEM) to calibrating both the instantaneous and average cutting force coefficients using an Arbitrary Lagrangian-Eulerian (ALE) formulation. The FEM approach eliminates the need for experimental calibrations of the cutting force coefficients, with the added advantages that makes it more attractive compared to experimental methods. These advantages include the possibility of heat analysis and being able to extract more results at any location on the model and so on.

In Chapter 4, the dynamics of the tool and the workpiece are the main focus. The structural stiffness and mass are well known for different materials, while the structural damping still remains an empirical parameter. In this chapter, a novel approach to predicting the structural damping is presented. Due to the complexity of damping, this approach is a start as it identifies certain trends defining the dependence of the damping parameters on the structures' geometry. Investigating why these trends exist could help to better understand structural damping and its prediction, even if it requires experimental calibrations of parameters like in stiffness and mass for different materials. In the later part of the chapter, a finite element analysis (FEA) and Fourier transform approach to extracting the systems transfer function is presented. This eliminates the need for experimental impact testing approach currently adopted.

Chapter 5 focuses on dynamic tool deflections. In this chapter, improvements to the well developed stability model used to predict stable cutting conditions are presented. The cutting force is more accurately modelled by considering the nonlinearity of calibrated cutting force coefficients and axial immersion angle. These improvements give a more accurate prediction of stable cutting conditions that agree very well with experimental results.

In Chapter 6, the dynamic deflections of thin-walled workpiece sections are investigated. The nonlinear dynamics of the workpiece were included in the prediction of stable cutting conditions. Apart from the more accurate predictions from the presented approach, it also does not require anymore experimental results as it uses numerical FEM results. It is shown in this chapter that when machining thin-wall sections, the variations in the dynamics along the tool path must be considered when predicting stable cutting conditions.

The thesis is finally concluded in Chapter 7, where a summary of all the contributions in the work is presented. Suggestions for future work are also presented in this chapter.

Chapter 2

Literature Review

Metal cutting can be said to have a very rich collection of different studies and research dating back as early as the 19th century. Arguably one of the first attempts to explain the mechanics of chip formation was by Timme in 1870 who from his observation of the cutting process, idealised the shear zone into a single shear plane (Henkin, 1962). Tresca later (in 1878) argued that the cutting process is through compression of the metal ahead of the tool and therefore chip failure should occur along the path of tool motion (Henkin, 1962). Timme later provided evidence that the cutting process is through shearing and not compression (Henkin, 1962); while Tresca later described the cutting process and chip formation in detail (Tresca, 1878). Mallock in 1881 presented a paper (Mallock, 1881) in which he first describes the chip formation in a similar concept as Piispanen (1948) and Merchant (1945). Mallock concluded that the deformation occurs at defined shear planes, inclined at an angle to the cutting direction.

Taylor later summarized his extensive experimental work in his 1907 ASME presidential address: ‘‘On the Art of Cutting Metals’’ (Taylor, 1907). Shore (1924) and Herbert (1926) were among the first to study the cutting temperature using the tool – work thermocouple method. Ernst and Martellotti examined ‘built-up edge’ in their study. Piispanen (1948), Ernst and Merchant (1940) and Merchant (1945) derived an expression for the shear plane. The shear

plane was defined as the plane in which the shearing stresses reach a maximum. Lee and Schaffer (1951) used the slip line theory to analyse the stress and strain distribution in metal cutting. Other analyses of metal cutting prior to the development of the Finite Element Method (FEM) (such as Oxley, 1963; Fenton, 1969 and Hastings, 1980) were mainly based on these two models. These models were however focused on orthogonal and oblique machining/metal cutting.

In this chapter, a review of the literature is given for different topics, to set a good base for the relevant chapters that follow.

2.1. Milling Geometry

As explained in Chapter 1, in milling, the workpiece is fed past a rotating tool with one or more teeth; hence the machined surface consists of series of surface segments generated by each of the individual cutting edges on the tool as shown in Figure 2.1. There are two different types of milling orientations as shown in Figure 2.1, namely: upmilling or conventional milling and downmilling or climb milling. The first studies into milling were by (Airey, 1921; Parsons, 1923; Sawin, 1926) and their studies were on chip formation and spindle power. Martellotti (1941) carried out an in-depth study on the kinematics of milling and showed that the path of the tooth is described as trochoidal and not circular due to the linear motion of the tool. However, it can be approximated as circular if the radius of the cutter is much larger than the feed per tooth, which is generally the case when milling. Martellotti derived expressions for the amplitude of tooth marks left of the machined surface and for the undeformed chip thickness (which is used in cutting force models) as,

$$h = s_t \sin\phi,$$

where, h is the undeformed chip thickness (refer to Figure 2.2), s_t is the feed per tooth and ϕ is the immersion angle.

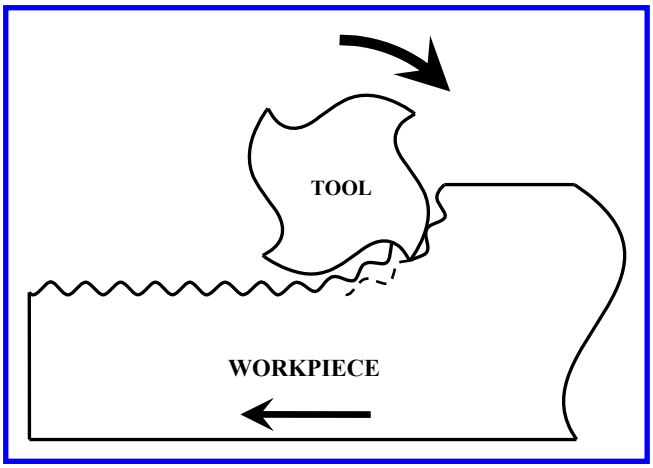

(a) Down/climb-milling

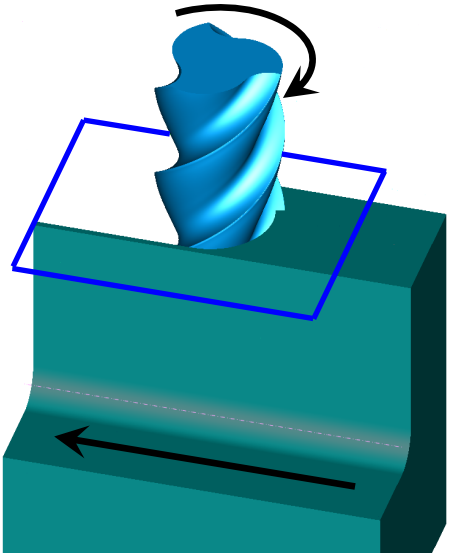

(b) Milling process geometry

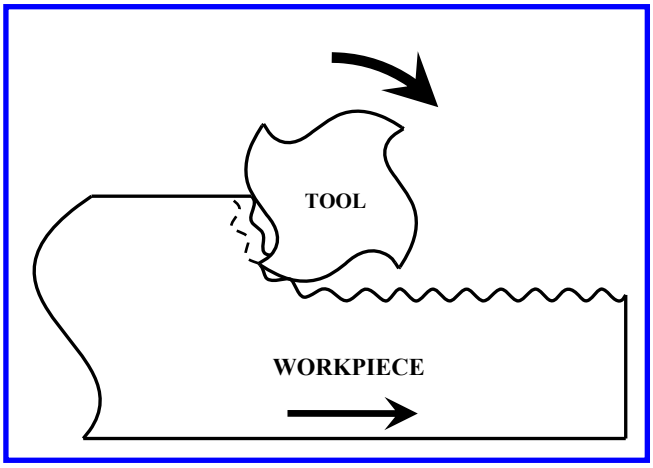

(c) Up/conventional-milling

Figure 2.1 - Milling geometry.

A generalised model for general end mills similar to the representation used by APT (Automatically Programmed Tools) and Computer-Aided Design/Manufacturing (CAD/CAM) systems have been reported by several studies (Engin 2001a&b; Gradisek, 2004). In these studies the geometry of the end milling tool was fully defined analytically, which often serves the beginning of recent studies into cutting force modelling. The model by Gradisek et al. (2004) is detailed in this thesis for the tool used through the course of this work.

2.2. Cutting Force Modelling

The prediction of the cutting forces usually serves as the beginning of many studies as most problems in metal cutting are linked to or originate from the cutting forces. There have been different attempts and models proposed to model the cutting forces in milling.

One of the very first studies of milling cutting forces was by Sawin (1926), where expressions for the milling forces were defined in terms of the cutting coefficient; though for the upmilling case he also gave an expression similar to Martellotti for the uncut chip thickness. The study gave different examples however with no experimental validation. Due to the large quantity of sampled data and its practicality, experimental methods to predict cutting force are less preferred compared to analytical or semi-analytical methods. One of the first comprehensive analytical studies into milling cutting force modelling and prediction for slab and face milling processes was by Sabberwal and Koenigsberger (Koenigsberger, 1961; Sabberwal, 1961). The cutting force coefficient, termed as the ‘specific cutting pressure’ was experimentally shown to be a function of the chip thickness using the instantaneous tangential force and uncut chip area. Cutting force models that utilise experimentally calibrated cutting force coefficients are generally known as ‘mechanistic’ models. A similar model was used by Tlusty and MacNeil (1975) in their study of cutting force prediction during: the entry of the tool into cut (transient state), full engagement (steady state) and also the time delay experienced between consecutive engagement. They also proposed defining the radial force as a function of the tangential force, which reduces the cutting force coefficients required to just one. Kline et al. (1982a,

1982b) later proposed a mechanistic approach to extracting the exponential coefficients and predicting the cutting force by discretising the tool into disk elements along the tool axis. Other studies using the exponential mechanistic force model are reported in (Devor, 1980; Sutherland, 1986; Altintas, 1991). In opposition to the mechanistic model is the mechanics force model, in which the cutting force coefficients are obtained using the oblique mechanics theory. This has also been adopted in numerous studies (Brown, 1964; Armarego, 1985; Armarego, 1989; Budak, 1996). Brown and Armarego (1964) showed that the force coefficients can be split into two types: cutting force coefficient and edge force coefficient. By splitting the coefficients they become constants and not a function of the uncut chip thickness.

When predicting the cutting forces in milling, better accuracy is acquired when tool deflections and runout are modelled. The modelling of tool deflections and runout, also allows for the prediction of surface accuracy for given cutting conditions. Perhaps the earliest studies to consider tool deflections, tool runout and surface accuracy were made at the National Twist Drill and Tool Co. (Kline, 1982b), during which the surface accuracy and tool deflections were measured experimentally. It was deduced that in up or conventional milling, the tool always deflected towards the workpiece thereby over-engaging the workpiece and vice versa for down or climb milling. Fujii (1979) later studied the effect of tool and workpiece deflections on surface errors by predicting the surface error profile using measured tool and workpiece deflection data. Following their developed mechanistic exponential force model in (Devor, 1980), Kline et al. further developed the model to include tool and workpiece deflections hence surface error predictions (Kline, 1982b). This was possibly one of the first studies to predict tool and workpiece deflections using Finite Element Method (FEM). Their study was presented with experimental comparisons. In the model, the cutting forces are first predicted assuming a rigid tool-workpiece system and then surface error predictions are conducted. Kline (1983) later developed a mathematical model for the cutter runout which again was based on the mechanistic exponential force model previously proposed in (Kline, 1982a, 1982b). The expressions defining the tool runout were presented and included in the mechanistic force model with experimental validations; although the cutting forces were still predicted assuming

a rigid tool-workpiece system. In a later study, attempts were made to incorporate the inherent flexibility of the system in the cutting forces and surface error predictions (Sutherland, 1986). In this study, Tlusty's dynamic chip thickness regeneration model (Tlusty, 1981) was used to obtain improved chip thickness prediction. The mechanics force model in which the coefficients are split into cutting and edge force coefficients was later adapted to include tool runout by Armarego in an ongoing study reported in (Armarego, 1989, 1991). Montgomery and Altintas (1991) later made an attempt to model the milling process, where the system's kinematics is used to define the cutter and workpiece motion. Apart from its complexity, the model's draw back is in its inability to accurately model the friction on the cutting edge and both the rake and flank faces of the cutter. Ismail et al. (1993) presented a mechanistic exponential force model to predict the surface finish whilst including the effects of flank wear and tool dynamics.

The studies have so far been on face and peripheral milling using flat end mills. Perhaps one of the first studies to present a force model for ball end mill was by Koch et al. (1990). They developed a Computer-Aided Engineering (CAE) Module to calculate the cutting forces in 3-axis milling using both a flat end mill and a ball-end mill; although without experimental validations. Yang and Park (1991) studied the prediction of the cutting forces for ball end mills using plane rake faces. The series of plane rake faces are modelled as oblique cutting edges. Feng et al. (1994) developed the mechanistic exponential force model, using the discretization approach by Kline (1982a) to model the cutting forces for a ball end mill. They also developed a simplified cutter runout model to include the effects of the cutter axis offset on the undeformed chip geometry. Lim et al. (1993, 1995) used this model to simulate the surface errors, where the cutter or tool holder deflections were modelled using cantilever beam theory. Sim and Yang also modelled the cutting force in ball-end milling using the mechanistic force model, whilst taking account of cutter deflections through the equilibrium equation (Sim, 1993). Ramaraj and Eleftheriou (1995) modelled the cutting forces for a tapered end mill using the kinematics and analysis of the shearing process. Tai and Fuh (1995) used the intersection of a spherical surface and a skew plane to define the cutting edge and used the oblique cutting theory to model the force system in ball end milling, whilst including the tool axis offset. The cutting force components on

the oblique edge were modelled using the energy method. Altintas and Lee (1996) used the oblique cutting edge theory to model the cutting force for a general helical end mill, including dynamic vibrations. The cutting force model used is similar to the mechanics force model by Armarego (1989). Yucesan and Altintas used a semi-mechanistic model similar to the model presented by Yucesan et al. (1994), where pressure and friction on the cutting edge were modelled using cutting force coefficients that were dependent on the cutter geometry and the feed-rate. The approach used to model the tool geometry and the definition for the cutting edge length proposed in this model (Yucesan, 1996) was later used by Engin and Altintas along with the CAD/CAM system of defining the envelope of the milling cutter (Engin, 1999a&b; Altintas, 2001). In these studies the modelling of the cutter was generalised for different end milling tools. Altintas (2000) later adapted this model to the cutting force model by Armarego (1989) for flat end mills. After this, Gradisek (2004) adapted the geometry model to Armarego's (1989) cutting force model for general end milling tools, where they presented how to extract the six (cutting and edge) force coefficients.

Yun and Cho (2000, 2001) later proposed an approach to extract exponential cutting force coefficients that are dependent only on the uncut chip thickness. This approach includes the runout parameter of the cutter. The advantage the exponential force model has over the linear edge force model is seen in this study. The main complication is obtaining the exponential cutting force coefficients as a function of only the uncut chip thickness. The size effects on the cutting force coefficient was obtained by re-scaling the uncut chip thickness using the minimum and maximum uncut chip thicknesses analytically predicted from the uncut chip model. The applications of the proposed approach were later presented (Ko, 2002; Yun, 2002a; Yun, 2002b) and applied to ball-end milling (Ko, 2004) with experimental validations presented. Liu et al. (2002a, 2004) have presented an improved cutting force model based on the oblique cutting theory for peripheral milling, which includes the size effects and the influence of the effective rake angle. The exponential tangential cutting force coefficient was modelled using the initial total cutting energy per unit volume in the oblique cutting theory. This improved cutting force model was later applied to ball-end milling (Liu, 2005a).

In an attempt for a much faster and efficient approach to calibrating the cutting force coefficients, Wan et al. presented an approach that includes the tool runout when calibrating exponential cutting force coefficients (Wan, 2006), Adetoro and Wen (2008, 2009a) presented an FEM approach to calibrating cutting force coefficients. In the study carried out by Wan et al. it was shown that the cutting forces can be separated into a nominal component with no runout influence and perturbation component influenced by the cutter runout. The FEM approach presented by Adetoro et al. (2009a) is discussed in the Chapter 3.

In this thesis, two different force models are proposed. The first is the FEM approach proposed by Adetoro and Wen (2009a). This approach aims to extract both the linear edge force and exponential cutting force coefficients solely through the use of FEM simulations. The second is an improvement on the already developed linear edge force model. This improvement aims to improve the accuracy of the model by taking into account the nonlinear relationship between the cutting force coefficients and the uncut chip thickness.

2.3. Dynamic Metal Cutting Modelling

In order to fully analyse and study different problems encountered in milling, the dynamic nature must be modelled. There have been numerous studies on dynamic modelling of milling with an ultimate aim to create a unified model that would fully incorporate all dynamic aspects both in the workpiece and the tool. These studies have however been met with some complications or the other that demand the use of various assumptions. Much like in dynamic orthogonal cutting in dynamic milling, each tooth is removing material from an undulated surface which was generated by the previous tooth due to both tool and workpiece vibrations as shown in Figure 2.2. These vibrations would always exist due to the intrinsic stiffness of both structures; however the aim is to keep the vibrations minimal and stable or constant. Therefore the tool's vibration at the previous pass had an amplitude of z_0 (outer modulation) while the current tool is vibrating with an amplitude of z (inner modulation). It is the analysis of this model that has been the topic of many of the early studies like the ones reported in (Albrecht, 1962; Klegg, 1965; Wallace, 1965, 1966; Das, 1967; Knight, 1970; Srinivasan, 1978a).

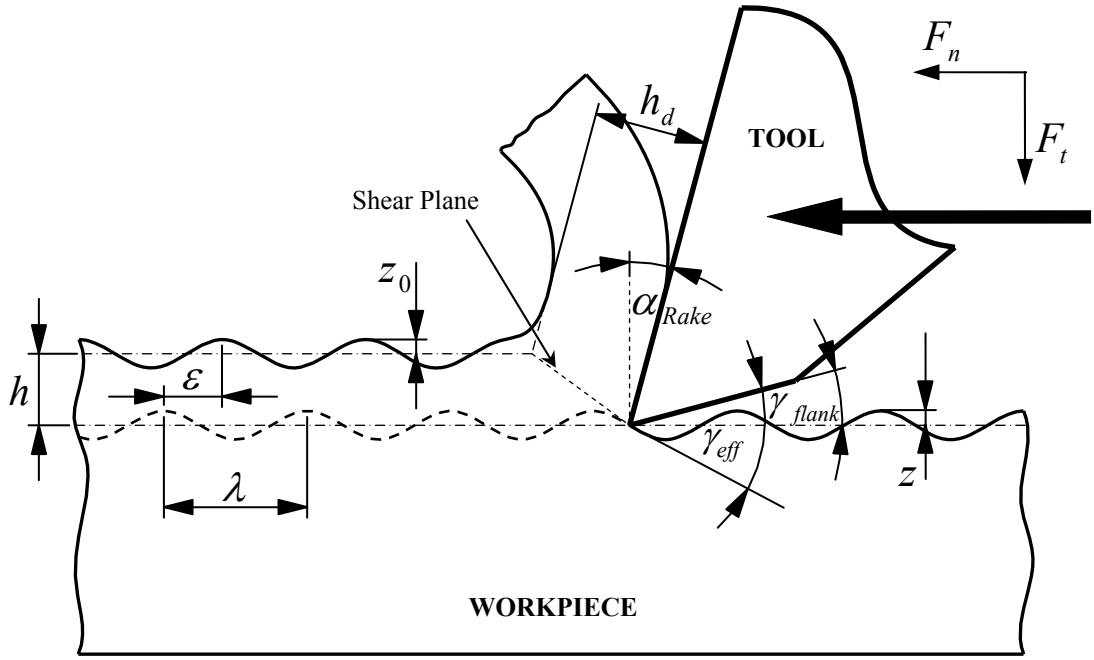

Figure 2.2 – Dynamic milling model.

Therefore the transfer function of the cutting process (in Figure 2.2) is defined by superposition of two processes that contribute to the cutting force; the first being wave generation (the creation of new undulations on the machined surface trailing behind the tool) and the second being wave removal (the machining of old undulations created by previous cut. An expression for the tangential and normal forces was proposed by Peters et al. (1971) and can be defined as,

$$F_n = a\left(K_{di} z + K_{do} z_0\right)$$

$$F_t = a\left(K_{ci} z + K_{co} z_0\right)$$

where F_n and F_t are the normal and tangential cutting forces, a is the width of the cut perpendicular to the 2-D plane in Figure 2.2., K_{di} and K_{ci} are called the direct and cross inner modulation ‘‘Dynamic Cutting Force Coefficients’’ (DCFC), while K_{do} and K_{co} are the direct and cross outer modulation DCFCs. The dynamic cutting force coefficients are simply the proportionality constant between the forces and the depth of cut z and their experimental extraction has been the topic of several studies reported in (Tobias, 1965; Klegg, 1965; Goel, 1967; Kals, 1971; Peters, 1971; Srinivasan, 1978b), while attempts to obtain them

analytically are reported in (Sisson, 1969 and Wu, 1989). The wavelength λ shown in Figure 2.2 is expressed by Tlusty (1978) as,

$$\lambda = \frac{v}{f_v}$$

where v is the cutting speed, and f_v is the vibration frequency.

At the early stages of research into the problem of chatter, there were some misconceptions as to what process was responsible for the onset of instability. One of the early studies that attempted to explain the source of chatter was by Arnold (1946), in which he considered the existence of negative damping to be the only source for chatter to occur. This comes from the variation of the rake angle due to the vibrating tool and changing cutting velocity directions (Tlusty, 1978). The oscillation of the shear angle observed by Knight (1970) was considered as the source of chatter by Sarnicola (1973) due to its effects on the cutting forces. The shear plane is shown in Figure 2.2 while the shear angle is the angle this plane makes with the direction of the tool. The oscillation of the shear angle is owing to the undulations left on the surface due to vibrations. Nigm and Sadek (1977) carried out experimental studies on the variations of the shear plane and the dynamic cutting coefficient with various cutting conditions. Their results show that the magnitude of the shear plane oscillation (defined as the change in shear angle divided by the change in the uncut chip thickness, h) decreased with the increase in feed, cutting speed and also the rake angle for both wave generation (inner modulation) and wave removal (outer modulation). The uncut chip thickness is shown in Figure 2.1, while the deformed chip thickness is identified as h_d. Although the relief angle γ_{flank} (or clearance angle) shown in Figure 2.2, plays no role in shear angle oscillation, it however plays an important role in another occurrence known as ‘‘process damping’’. The effect relief angle, γ_{eff} varies as the tool vibrates as seen in Figure 2.2 and if the tool is imagined to continue in the path traced out ahead of it, the effective relief angle will start to decrease after the tool reaches its maximum amplitude. As the relief angle decreases, the normal force acting on the tool increases and this effect is known as process damping (Tlusty, 1978). It reaches a minimum (hence maximum process

damping) at the middle of the downward slope and a maximum at the middle of the upward slope. This effect of this on the cutting process stability has been considered by Kegg, (1965) and Sisson and Kegg (1969), although the effects of the process damping diminishes as the cutting speed increases (Tlusty, 1978).

More recently, Liu et al. (2002b) proposed an improved dynamic cutting force model for peripheral milling. This model included the size effect of the undeformed chip thickness and the influence of the effective rake angle. Their study also showed how the cutting force coefficients can be extracted from experimental results, and case studies of the effect of the cutting conditions on the cutting forces with an aim to improve dimensional or surface form errors. In a study later carried out by Liu and Cheng (2005b), the improved cutting force model developed in (Liu, 2002a) was used along with system's identified transfer function to predict the dynamic cutting forces, vibrations and surface finish. The simulations were carried out using a developed Simulink program, which modelled the dynamic deflections of both the cutter and the workpiece; while Luo et al (2005) proposed a new modelling approach, which uses a developed Simulink program to model the dynamic cutting process.

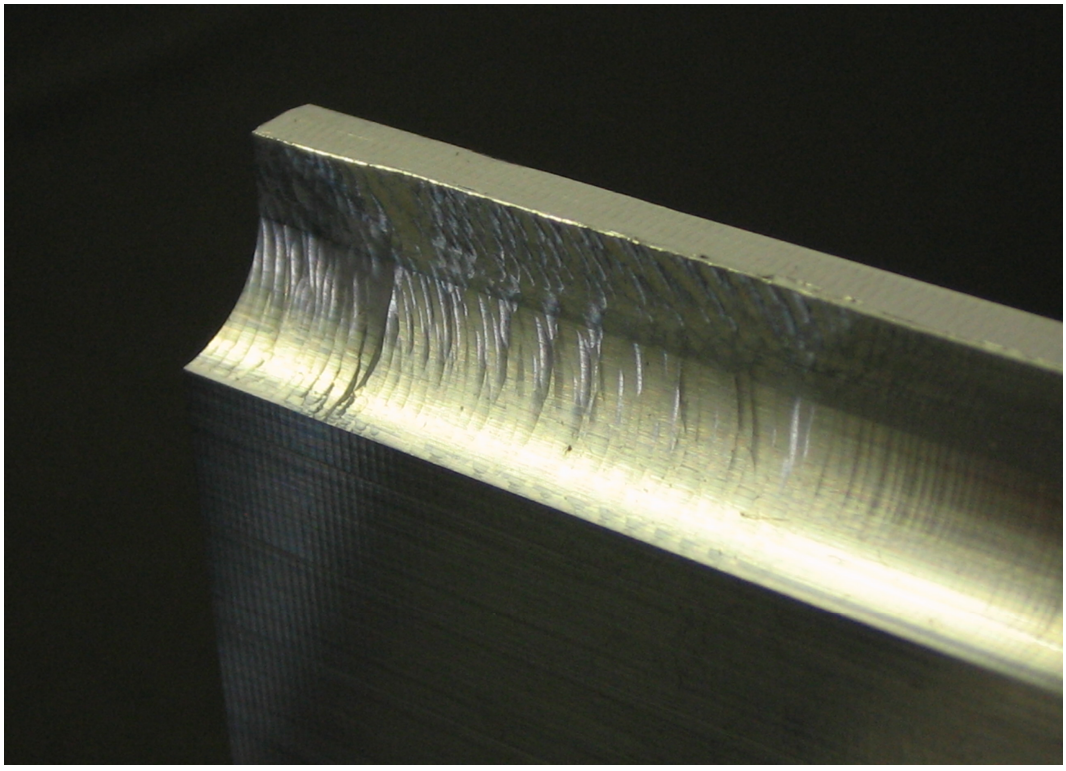

Figure 2.3 – Bad surface finish due to chatter marks.

2.4. Chatter Stability Modelling

The development of chatter during milling operations is so troublesome that it has been the main topic of studies over the past 5 decades. Chatter causes the machinist all kinds of trouble including bad surface finish from teeth or chatter marks (Figure 2.3), damages to the spindle-tool assembly, inefficiency through lost labour hours and wasted materials and so on. It was stated much earlier into the studies in metal cutting process by Taylor (1907) that chatter is the most obscure and delicate of all problems facing the machinist.

In the milling process, forces are induced at each of the cutter teeth in contact with the workpiece and these forces in turn excite the machine-tool and workpiece structure. Due to the inherent feedback that exists between the cutting forces and the structures deflection, there are conditions under which this system becomes unstable. This instability leads to a condition known as self-excited chatter. Once chatter develops the chip load that is cut by the tool becomes periodically greater than the intended chip load (by set cutting conditions), which inevitably leads to cutting force peaks increasing (some times twice as much) beyond their nominal peaks within a very short time. It is this sudden increase that could possibly lead to tool and machine damages. Although the studies cited in section 2.3 tried to explain the source of chatter, the main aim was to understand the dynamic cutting process and the effects the cutting conditions have on the process. Following the early assumption that the existence of negative damping was a necessary condition and only source for chatter, were the two simultaneous pioneering discoveries by Tobias (1958) and Tlusty (1963). They recognized that the most important sources of self-excitation, regeneration and mode coupling were associated with the structural dynamics of the machine tool-workpiece system and the feedback response between subsequent cuts. At this early stage, the stability lobes approach that is widely used by researches to predict the stable margin was also established by Tobias (1958); while Tlusty and Polacek obtained the classical definition of chatter free axial depth of cut,

$$a_{\lim} = \frac{1}{2K_s \operatorname{Re}[G]_{\min}}$$

where K_s is the specified cutting force coefficient, $\mathrm{Re}[G]_{\min}$ is the minimum value of the real part of the structure's transfer function in the direction normal to the machined surface. This was later improved by Tlusty (1967) to include the effect of the spindle speed on the chatter frequency ('lobbing effect'). Other studies on the stability of metal cutting were reported by Merritt (1965).

Though, a pioneering research, the stability models by Tobias and Tlusty are only applicable to orthogonal metal cutting (Figure 2.2) where the directional dynamic milling coefficients are constant and not periodic. This is quite the contrary in milling due to the rotating cuter with multiple teeth. In order to accommodate this directional dynamic milling coefficients, time domain simulation of the milling process was introduced by Tlusty (1981, 1983). Slavicek (1965) and Vanherck (1967) made the assumption that all the cutter teeth have a constant directional orientation in their study of the effect of irregular pitch on the stability. Sridhar et al. (1968a, 1968b) and Hohn (1968) later carried out an in-depth study in which they introduced time-varying directional coefficients in their chatter stability analysis. They used the system's state transition matrix in their stability model, which helps to eliminate the periodic and time delay terms. Optiz et al. (1968, 1970) used an average value of the periodic directional coefficients in the analysis. Tlusty (1970) made an attempt to apply the orthogonal model to the milling process by assuming the teeth of the tool had equal pitch, was simultaneously in cut and that the motion was rectilinear with constant depth of cut. The Nyquist criterion was used by Minis and Yanushevsky (1990, 1993) and Lee et al. (1991a, 1991b) to obtain the stability limits. Lee et al. used the mean value method to replace the time varying directional coefficients by a constant. Up until this point there existed no proposed analytical approach to predicting the stability margin for milling, whilst respecting the varying directional dynamic milling coefficients.

Following the in-depth work by Budak, (1994), Altintas and Budak (1995, 1995, 1998, 1999) later proposed an analytic approach in which the zeroth order term in the Fourier series expansion (single frequency solution or zeroth order approximation) of the time varying coefficients was adopted. A similar model was later used by Altintas et al. (1999), where they proposed an average scheme of the

immersion angle (refer to Chapter 5). The analytical model was later extended to include three directions by Altintas (2001), where the axial immersion angle was assumed to be constant. Except for flat end mills however, the axial immersion angle, is a function of the axial depth of cut. Campa et al. (2007) later proposed an averaging approach to calculating the axial immersion angle in order to solve the stability model analytically. However, the axial immersion angle was still assumed to be a constant.

Of recent, the focus of researchers is more on the possible presence of additional lobes around high spindle speed ranges as identified by Davies et al. (2000, 2002). This was following his study on the impact dynamics of thin-walled structures (1996), where they investigated the effects of impact dynamics in the milling of thin-walled component. The presence of additional lobes can be effective when milling thin webs, where the dynamics are dominant in one direction and/or when the radial depth of cut is very small, thereby causing a highly intermittent milling process and exhibiting a significant number of tooth passing frequency harmonics. These additional lobes are due to period doubling or flip bifurcation. While the mono-frequency solution only predicts quasi-periodic chatter due to Hopf bifurcation, the harmonics of the tooth passing frequencies would have to be considered in order to predict flip bifurcations as presented by Budak and Altintas (1998), Merdol and Altintas (2004) and other studies on flip bifurcation reported in (Insperger, 2000; Insperger, 2004; Stepan, 2005; Gradisek, 2005). Merdol and Altintas (2004) used the approach proposed by Minis and Yanushevsky (1993) to model the added lobes due to highly intermittent cutting process. Zatarain et al. (2006) studied the influence the helix angle has on chatter stability and the helix angle was shown to reduce the importance of higher order harmonics; while Insperger (2008) recently studied the effect the tool runout has on the chatter frequency.

There are always some levels of assumptions made in research to simplify models to a point where solutions can be obtained at a reasonable cost. This has obviously been employed in the studies reviewed. However researchers are reviewing these assumptions in an attempt to improve and eliminate discrepancies often observed in obtained results. Amongst these assumptions are,

- The system's transfer function: To analytically predict the stable region the dynamic parameters identified at the cutter-workpiece contact zone are used. The classic approach to obtaining the dynamic parameters is through impact tests. Unlike in tool chatter, the dynamic parameters are not constant along the workpiece and are constantly changing as material is removed and the geometry changes. Attempts were made by Thevenot (2006) to use this varying dynamics in thin wall machining to initiate the variation of the spindle speed along the workpiece in order to improve surface finish. The tendency in this approach however is for new marks to be left on the surface due to the change in cutting conditions as seen from their experimental results. Budak considered the variations of the dynamics of the cutter and the workpiece along the axial direction (Budak, 1995, 1998). Seguy et al. (2008) just recently carried out a study to include the varying dynamics along a thin wall and thin floor section, although the results showed certain discrepancies which could have arisen from the assumptions made. It is however clear in thin wall machining that it is insufficient to assume the dynamics of the workpiece are constant, which was the case in previous studies. An FEM approach presented by Adetoro (2009b, 2009g) was used to incorporate this changing dynamics in the stability margin prediction by Adetoro et al. (2009f). Their results were validated with very good agreement with experimental results as shown in Chapter 6.

- The cutting force coefficients: In all the previous studies, the cutting force coefficients used in modelling the cutting force were assumed to be constant along with the axial immersion angle for the prediction of stable conditions. However the cutting force coefficients are well known to be a function of the axial depth of cut as reported by (Lim, 1995; Gadalla, 1997; Engin, 1999a&b, 2001a&b; Altintas, 2000, 2001; Gradisek, 2004), where the calibrated coefficients are generally fitted quite accurately with a polynomial expression. Adetoro et al. (2009e) recently proposed some modifications to the stability lobe model by Altintas (2001). The modifications allow for the inclusion of the nonlinear nature of the cutting force coefficients and the axial immersion angle along the axial depth of cut

in the prediction of more accurate stable cutting conditions. The results were obtained using a numerical approach.

In this thesis, a novel approach to predicting structural damping parameters is presented. This novel approach was proposed by Adetoro (2009c, 2009d) and it identifies certain trends in the effect the geometry has on the damping parameters. The possibility to predict the structural damping would obviously eliminate the need for experimental methods. The FEM approach to predicting the structure's transfer function presented by (Adetoro, 2009b, 2009g) is discussed. To fully take advantage of the damping prediction approach especially in thin wall machining, this FEM approach is used. This shows how the stable margins for subsequent walls can be predicted without the need for experimental impact testing. The improvements to the analytical stability lobes model proposed by Adetoro et al. (2009e) are later presented. The improvement to the stability lobe model eliminates the assumption that the cutting force coefficients and axial immersion angles are constant. A quick numerical approach to obtaining a solution for the model was proposed and presented here. Later on in this thesis, the FEM approach to modelling nonlinear thin wall dynamics by Adetoro et al. (2009f) is discussed.

2.5. Finite Element Modelling

In contrast to the analytical approach is the FEM approach to simulate the milling process and with the development of the finite element method, orthogonal and oblique cutting processes have been extensively analysed using FEM based techniques. FEM simulations are generally based on three main formulations. The first of these is the Total or Updated Lagrangian Formulation, which was the basis of Klamecki's study (1973). He was the first to introduce FEM technique into machining, using a three-dimensional elastic-plastic finite element method. This study was however limited to just the initial stages of chip formation. Similarly, Shirakashi and Usui (1974) applied the elastic-plastic finite element method to orthogonal metal cutting process. In this, they modified the shape of the chip until it was consistent with the plastic flow generated. Iwata (1984) also used a rigid-plastic finite element method to consider the effect of friction between the tool rake and face. In their model the shape of the model was

predicted and modified repeatedly based on the distribution of flow stress. The first analysis to simulate the movement of the tool into the workpiece and continuous chip formation along a predefined ‘‘parting line’’ was by Strenkowski and Carroll (1985). They used a finite element program (‘NIKE2D’) adopting the ‘‘Updated-Lagrangian’’ formulation (ULF) and also proposed a separation criterion to simulate chip formation. This separation criterion was based on the effective plastic strain (critical limit of 0.5) at the tool tip region of the workpiece. Strenkowski and Carroll found that the separation criterion value used had a significant effect on the residual stress in the workpiece and little effect on the chip geometry and the cutting force. Lee and Wilkening (1982) were however the first to attempt chip formation by the use of an element death option in the model, but this model was not realistic as friction in the secondary shear zone was ignored.

Shih et al. (1990) carried out a study on the effects, elasticity, viscoplasticity, temperature, strain-rate and large strain have on the stress-strain relationship and the effects large friction have on the tool-chip interface. Their study was also based on the Updated-Lagrangian formulation. The separation criterion used was based on the distance between the node connecting the chip and workpiece (crack tip) and the tool tip. This type of criterion has been adopted in a number of studies to model orthogonal metal cutting, however with different values used (Shih, 1996; Mamalis, 2001; Baker, 2002; Carrino, 2003; Rosa, 2007). Shet et al. (2000) simulated orthogonal metal cutting using a separation criterion based on a critical stress. Lei, et al. (1999) used a crack length versus time separation criterion, based on the movement of the tool. Ceretti et al. (1996) used an Implicit Lagrangian FE code (‘DEFORM-2D’) to study continuous and segmented chip formation. In their model, a damage criterion similar to that of Lee and Wilkening (1982) was used, where the damaged element is removed from the domain. The downside of this approach is that the removal of elements corresponds to loss of mass. The only way to minimize this would be to have very small element sizes along the tool path, which would come at a higher computational cost. Zhang (1999) carried out a detailed study on the separation criteria used by different researchers in their studies. The study showed that none

of the existing criteria is universal and deduced that there is the need to develop a comprehensive criterion to ensure consistency in FEM models and results.

To avoid the use of separation criteria while using a Lagrangian formulation, the cutting action can be simulated as the continuous indentation and plastic flow of the material around the tool. The tool is fed into the workpiece and as soon as the elements become distorted, a re-mesh is carried out. The point of re-mesh is determined by a set of specified criteria. This method was used by Sekhon and Chenot (1993), Madhavan et al. (2000) and Bil et al. (2004). One of the main problems with this approach is its high computational cost. Frequent remeshing and a very high mesh gradation is required to minimize the errors (Baker, 2002). Bil et al. compared three different finite elements models of orthogonal metal cutting with experimental data. Two of these models used continuous remeshing and the third was based on a damage criterion. While it was noted that the friction parameter drastically affects the results, it was also noted that even though the re-meshing approach produced better results, there was still the need for a better separation criterion.

Opposite to the Lagrangian formulation, is the Eulerian formulation, which is more suitable for fluid flow problems involving a control volume where the mesh is spatially fixed. However, its first application to metal cutting was reported by Usui et al. (1978) and Lajczok (1980). In the study by Lajczok, the tool forces and geometry obtained experimentally were applied to the workpiece surface, thereby omitting the chip in the model. The residual stress and plastic deformation zone in the workpiece were validated experimentally. A similar approach was used by Natarajan and Jeelani (1983) in modelling the residual stresses in the workpiece. Strenkowski and Moon (1990) analysed a steady-state orthogonal cutting with the capability to predict chip geometry and chip-tool contact length. In their simulation, the mesh was not entirely spatially fixed as they employed a method proposed by Zienkiewicz et al. (1978) to obtain the shape of the chip. In this method, the free surface of the chip was calculated by adjusting its location (through an iterative process) to enforce a zero normal surface velocity component. Also based on an Eulerian formulation, Moriwaki et al. (1993) developed a rigid-plastic finite element model to examine the effects of the tool edge radius on the depth of cut in the micro cutting process. Other studies carried

out with the use of pure Eulerian formulation were reported by Strenkowski et al. (2002) and Athavale (1997).

What makes the Lagrangian formulation very attractive in modelling metal cutting is that the mesh covers and moves together with the material. Therefore, no a priori assumption of the chip is required because the chip develops as the tool progresses through the workpiece. Moreover, the analysis can model the indentation, incipient and the steady state stages in metal cutting. At the same time, this formulation also suffers some disadvantages, the most important of which is the need for a separation criterion. The use of separation criterion to model chip formation is not reliable, as there exists no universal and consistent criterion as explained by Zhang (1999). Not only are there different types/methods of applying the separation criteria, there is also no physical indication as to what criterion value is to be used. Another factor concerning the use of separation criterion is the use of a parting line. As the simulation progresses, the distortion of the nodes along the parting line can cause instabilities in the algorithm. This is because the separation criteria approach works best when the nodes are precisely in front of the approaching tool. A similar problem was experienced by Bil et al. when using damage models for chip separation (Bil, 2004). Furthermore, the parting line restricts the types of tools used in the model to sharp edged tools (Movahhedy, 2000). Another major disadvantage of using the Lagrangian formulation is that, as the material is highly sheared in reality on passing through the shear plane or primary shear zone, so are the model elements, thereby causing highly distorted elements. The Eulerian formulation on the other hand, does not suffer the same disadvantages as the Lagrangian formulation. In addition, because the material flows into the model, the domain can be designed to include only the area near the shear zone, thereby improving on computational cost. The only major disadvantage to this approach is that, knowledge of the volume of the domain (chip) and its precise boundary conditions are required a priori.

It is due to the above shortcomings that the third formulation called Arbitrary Lagrangian-Eulerian (ALE) formulation is an ideal formulation to adopt as it combines the advantages of pure Lagrangian and pure Eulerian formulations. Frank and Lazarus (1964) and Noh (1964) first proposed it, for two-dimensional hydrodynamic problems using finite difference schemes. It was called Coupled or

Mixed Eulerian-Lagrangian method or code at the time and was later introduced to finite element method by Donea et al. (1977). The ALE formulation has been used in several applications, mainly involving large deformations (e.g. metal forming, metal cutting and metal forging). Some studies using ALE to model metal cutting are reported by Ozel et al (2005, 2007). The ALE formulation combines the advantages of both the Lagrangian and Eulerian formulations, rendering it a more versatile formulation; as the main advantages of Lagrangian are also the main disadvantages of the Eulerian and vice versa.

So far the studies have been focused on analysing orthogonal metal cutting and turning. Ozel and Altan (2000) modelled flat end milling using a single insert flat end mill. They had to split the tool cutting edges into two regions (primary and secondary cutting edges). Pantale et al. (2004) presented a three-dimensional oblique model to simulate the milling process using damage criterion (Johnson–Cook's). A full three-dimensional simulation was briefly reported, however it was not validated and no results were presented, as more investigation was needed.

Recently, an FEM approach to predicting the cutting force coefficients discussed in section 2.2 was simultaneously proposed by Gonzalo et al. (2009) and Adetoro and Wen (2009a). The approach by Adetoro and Wen is discussed in depth in this thesis in Chapter 3. This novel simulation approach uses a general FE commercial package (Abaqus Explicit) to simulate flat-end milling process. Chapter 3 then follows on to propose an efficient method to extract the cutting force coefficient for both the linear edge and exponential force models discussed in section 2.2.

Chapter 3

Cutting Forces

3.1. Introduction

The accurate prediction of cutting forces in milling is essential when analysing and predicting machine-tool vibrations through workpiece and tool deflections, tool wear, workpiece surface quality, geometrical accuracy, onset and/or possible regeneration of chatter. The prediction of the cutting forces is equally important at the tool design stage as it aids the selection of optimum tool design concepts, modifications and materials. The prediction of cutting forces prediction is also essential for the jig and fixture strength requirements and for determining power requirements, hence the majority of studies have been focused on the accurate prediction of milling forces. In other studies, it would serve as the beginning as it is in this work.

In the study carried out by Sawin (1926), the milling forces were defined in terms of cutting coefficients. Martellotti carried out an in depth study of the kinematics of milling, the tooth path during milling and chip formation (Martellotti, 1941). Tlusty and MacNeil (1975) later showed that further to assuming the tangential force is proportional to the chip load as presented by Koenigsberger and Sabberwal (1961), the radial force can be defined as proportional to the tangential force. This model is termed the exponential cutting

force model as it uses a single cutting force coefficient that is a variable of the uncut chip thickness due to the influence of the size effects, while Sabberwal proposed the exponential expression for the exponential cutting force coefficient (Sabberwal, 1961). Due to the finite sharpness of the tool as the chip thickness is reduced to zero, there will always be some cutting force due to the rubbing of this finite edge. Therefore the cutting force does not reduce proportionally to zero, rather it converges to some value, which is consequently observed as an infinite increase in the force coefficients, hence the term exponential. The value the cutting force converges to is dependent on the cutting edge radius and is known as the edge force. Therefore, the larger the edge radius (i.e. the bluntness) of the cutter, the larger the edge force becomes and the greater the size effect. For a perfectly sharp tool however, the edge force is zero as explained by (Boothroyd and Knight, 1989). Kline later proposed the discretisation of the tool into disk elements along its axis and the differential forces on each element are combined to give the total cutting force on the tool (Kline, 1982).

Brown and Armarego later proposed the slitting of the cutting forces into edge/ploughing forces and cutting forces, characterised by edge and cutting force coefficients (Brown, 1964). This gives constant values for the coefficients that are independent of the uncut chip thickness. This force model was later termed the 'linear edge cutting force' model. The tool geometry modelling and approach and the definition for the cutting edge length proposed Yucesan (Yucesan, 1996) was improved and well defined for different types of end mill shapes by Altintas and Engin (2001a&b). Gradisek et al. (Gradisek, 2004) later proposed an approach to extracting the cutting force coefficients mechanistically for a general end mill based on the force model by Brown and Armarego (Brown, 1964). An approach to extracting instantaneous/exponential cutting force coefficients and the runout parameters for general end milling process was presented by Wan et al. (Wan, 2007). They separated the perturbation terms due to cutter runout in the cutting force model from the terms not influenced by the tool runout.

In contrast to the analytical approach is the 'Finite Element Method' (FEM) approach to simulate the milling process. Orthogonal and oblique cutting processes have been extensively analysed using FEM based techniques. Studies using a Lagrangian mesh formulation are reported in (Klamecki, 1973; Shet,

2001; Baker, 2002; Carrino, 2003). While studies using an Eulerian mesh formulation are reported in (Usui, 1978; Lajczok, 1980; Strenkowski, 1990; Moriwaki, 1993). Arbitrary Lagrangian-Eulerian (ALE) mesh formulation was introduced to FEM by Donea et al., (Donea, 1997) where it was used to model processes involving large deformations. The ALE formulation combines advantages of both the Lagrangian and Eulerian formulations, rendering it a more versatile formulation. As it is known, the main advantages of Lagrangian are the main disadvantages of the Eulerian and vice versa. As a solution to the disputed separation criteria used in simulations using a Lagrangian mesh formulation, studies have been conducted using an ALE mesh formulation (Ozel, 2005, 2007). Recently, Finite Element Method approaches to extracting the cutting force coefficients have been reported by Gonzalo et al. (2008) using a Lagrangian mesh formulation and Adetoro and Wen (2009a) using an ALE mesh formulation. The later approach is discussed in-depth in the fourth section of this chapter.

Thus this chapter is structured as follows; the geometry of a general end mill is described in the second section; the tool to be used during the course of this thesis is mechanistically calibrated in the third section and improvements to the linear edge force model are later presented; the FEM approach to extracting the coefficients for both the linear edge force and exponential force models is finally presented in the fourth section.

3.2. Geometry of a General End-Mill

The generalised model for general end mills similar to the representation used by APT and CAD/CAM systems have been reported by several studies (Engin 2001a; Gradisek, 2004). Though only two types of end mill tools are used in this chapter, the model is summarised here for completion. The cutter's envelope is defined by seven independent geometric parameters D, R_c, R_r, R_z, α, β and H as shown in Figure 3.1. Hence for a bull nose as used in this section, by following the convention $\{D, R_c, R_r, R_z, \alpha, \beta, H\}$ the tool can be is defined by $\{20,5,5,5,0,0,5\}$. In order to predict the cutting force at a given point P along the cutting edge (Figure 3.2), the chip load and cutting force components (tangential, radial and axial), along with above defined cutter geometry are required. The point P along the cutting edge is defined by its elevation z (along the tool axis), radial distance $r(z)$ (from the tool axis), axial immersion $\kappa(z)$, and radial lag angle $\psi(z)$ (Figure 3.2). Where the axial immersion is defined as the angle between the tool axis and the normal to the cutting edge at point P and the radial lag angle is angle between the tangential line at tool tip O and line from point P to the tool axis.

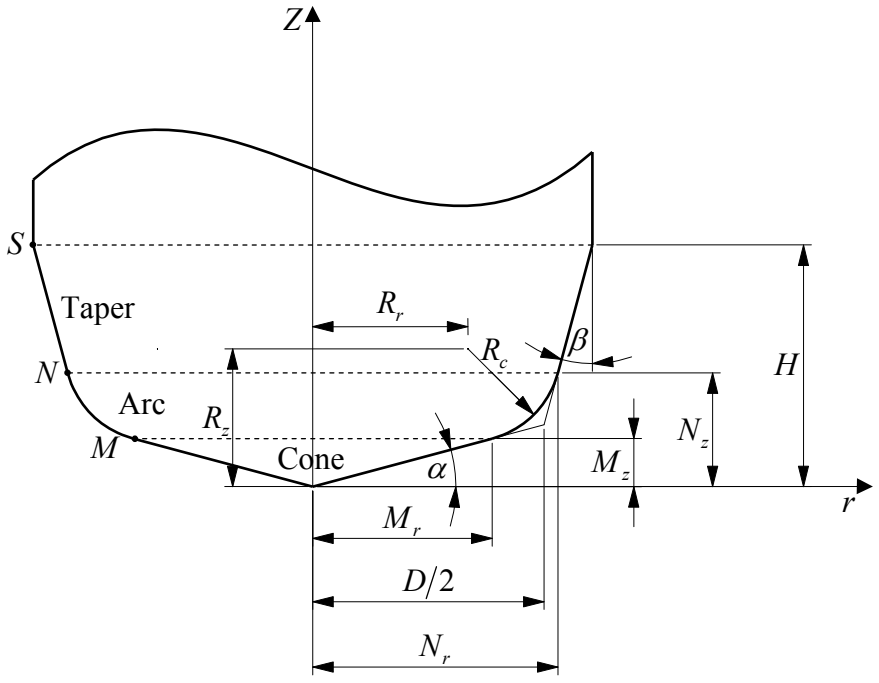

Figure 3.1. Geometry of a general end milling tool.

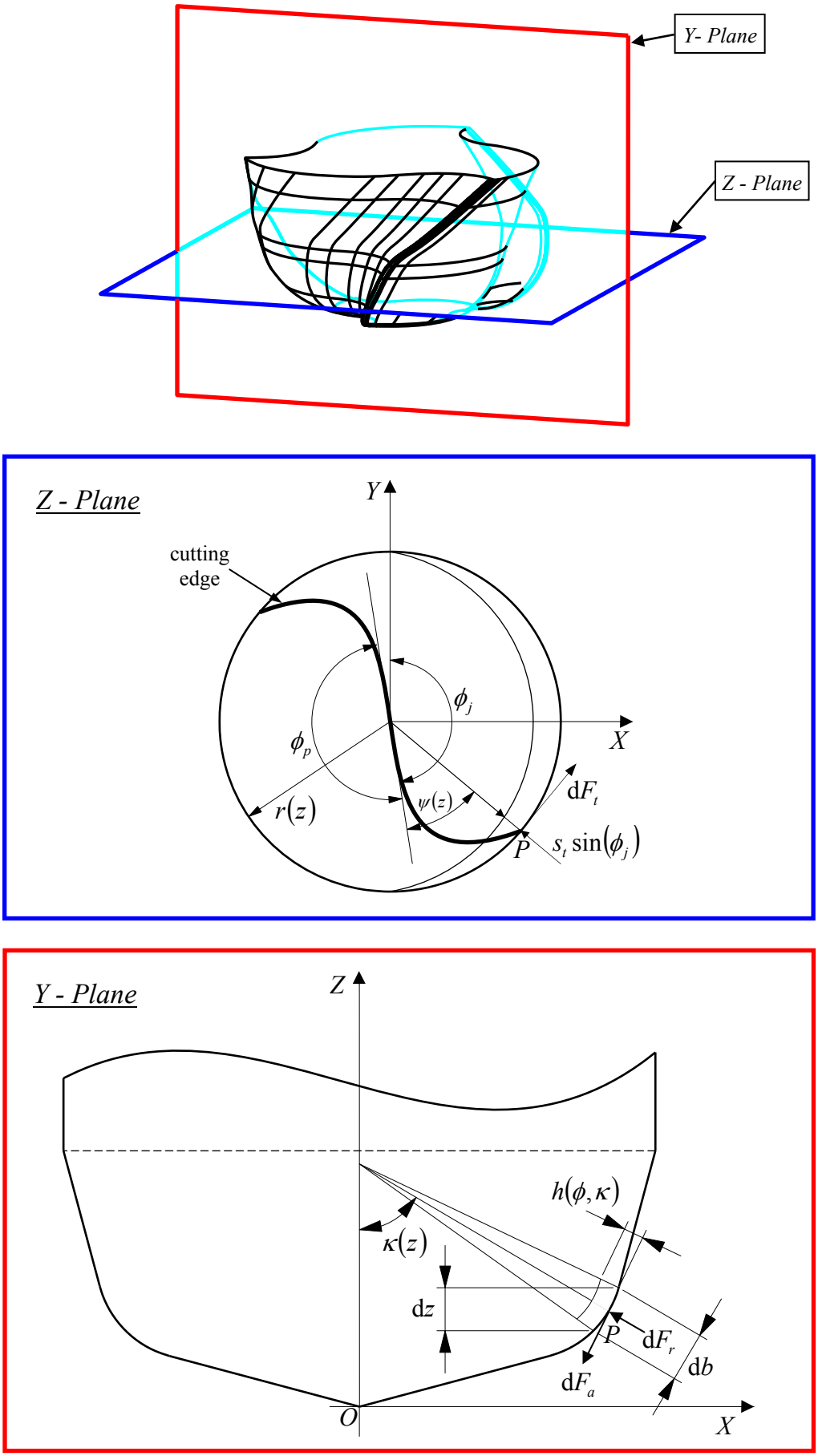

Figure 3.2. Tool dimensions and chip load.

A vector drawn from the cutter tip to point P on the j-th cutting edge in cylindrical coordinates is defined (Engin, 2001a) as,

$$\mathbf{r}(\phi_j, z) = \mathbf{i}x_j + \mathbf{j}y_j + \mathbf{k}z_j = r(\phi_j, z)(\mathbf{i}\sin\phi_j + \mathbf{j}\cos\phi_j) + \mathbf{k}z(\phi_j), \tag{3.1}$$

where, ϕ_j is the radial immersion angle of point P on flute number j. With the first flute as the reference edge, the radial immersion angle of the j-th cutting edge at axial elevation z is expressed as,

$$\phi(z) = \phi + (j-1)\phi_p - \psi(z), \tag{3.2}$$

where, ϕ is the immersion angle of the reference edge and ϕ_p is the pitch angle defined as $\phi_p = 2\pi/N$ for a cutter of N uniformly spaced teeth.

The distance $r(z)$ and radial lag angle $\psi(z)$ are both a function of the geometry of the cutter. Hence the tool is divided into three different zones: cone, arc, and taper zones (Engin, 2001a) and corresponding expressions are summarised as follows:

- Cone Zone

$$\begin{aligned} r(z) &= \frac{z}{\tan\alpha}, & \psi(z) &= \frac{\tan i_0}{\cos\alpha}\log\frac{z}{\tan\alpha} \\ \kappa(z) &= \alpha, & -i(z) &= i_0 \end{aligned} \tag{3.3a}$$

- Arc Zone

$$\begin{aligned} r(z) &= R_r + R_c\sqrt{1-(1-E)^2}, & \psi(z) &= (1-E)\tan i_0, \\ \kappa(z) &= \arcsin\sqrt{1-E^2}, & E(z) &= \frac{(R_z - z)}{R_c}, \\ i(z) &= \arctan\left(\frac{(r(z)-R_r)\tan i_0}{R}\right) \end{aligned} \tag{3.3b}$$

- Taper Zone

$$r(z) = N_r + (z - N_z)\tan\beta, \qquad \kappa(z) = \frac{\pi}{2} - \beta,$$

Constant Helix

$$i(z) = i_0, \qquad \psi^{(0)}(z) = \frac{\tan i_0}{\sin\beta}\log r(z), \tag{3.3c}$$

Constant Lead

$$i_s = \arctan\left(\frac{2\pi N_r}{lead \cdot \cos\beta}\right), \qquad \psi^{(s)}(z) = \frac{\tan i_s}{N_r}(z - N_z)$$

where $\alpha, \beta, z, R_c, R_r, R_z, N_r, N_z, M_r,$ and M_z shown in Figure 3.1 and R is the cutter radius, $lead$ is the lead distance of the tool, i_0 is the helix angle at the small cone zone, which is assumed to be constant; the helix angle is shown in Figure 3.3. $\psi^{(0)}$ and $\psi^{(s)}$ corresponds to the lag angles for cutters grounded with a constant helix angle (with variable lead) and those grounded with constant lead (with variable helix angle) (Engin, 2001a).

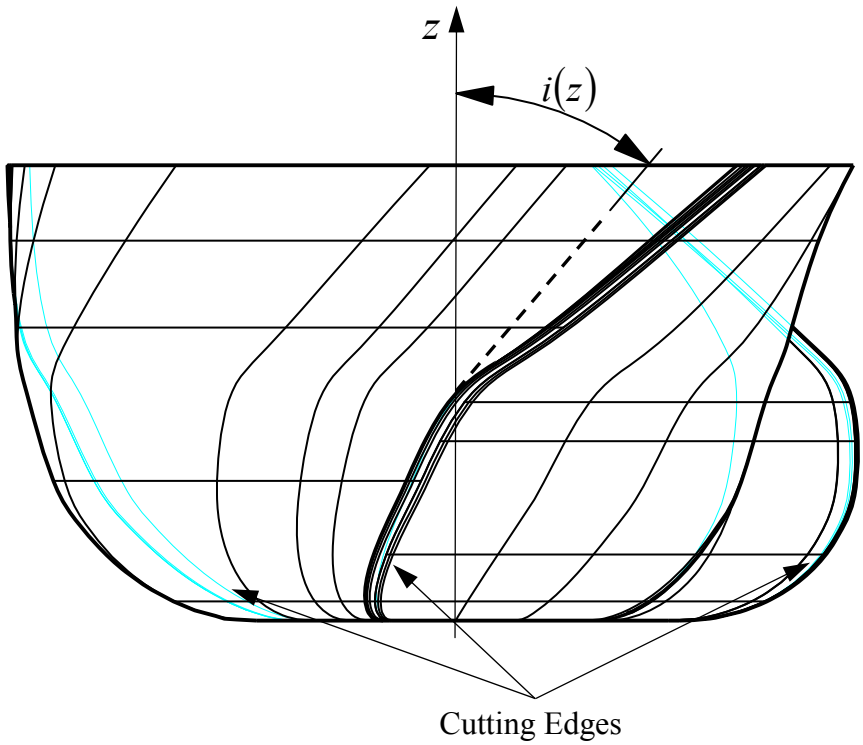

Figure 3.3. Helix angle of a general end milling tool.

3.3. Mechanistic Cutting Force Model

In this section, the analytical modelling of the milling cutting force is presented. The 'Linear Edge-Force' mechanistic model is explained briefly and used in modelling the cutting force, with experimental results used to validate its accuracy. An improvement to the model is proposed which would better model nonlinear influence imposed by 'size effects'. The model's formulations are systematically given.

3.3.1. Linear Edge-Force Model

Based on Kline's work (1982a, 1982b), the tool is discretized along the axis into segments, $\mathrm{d}z$ as shown in Figure 3.2 and the differential tangential $(\mathrm{d}F_t)$, radial $(\mathrm{d}F_r)$ and axial $(\mathrm{d}F_a)$ cutting forces acting on the infinitesimal cutting edge segment are given (Engin, 2001a) by,

$$\mathrm{d}F_{tj}(\phi_j,\kappa) = K_{te}\mathrm{d}S + K_{tc}h(\phi_j,\kappa)\mathrm{d}b, \tag{3.4a}$$

$$\mathrm{d}F_{rj}(\phi_j,\kappa) = K_{re}\mathrm{d}S + K_{rc}h(\phi_j,\kappa)\mathrm{d}b, \tag{3.4b}$$

$$\mathrm{d}F_{aj}(\phi_j,\kappa) = K_{ae}\mathrm{d}S + K_{ac}h(\phi_j,\kappa)\mathrm{d}b, \tag{3.4c}$$

where, $\mathrm{d}b = \mathrm{d}z/\sin\kappa$ is the chip width, $\mathrm{d}S$ is the length of the cutting edge, and ϕ_j is the radial immersion angle of the cutting edge j as shown in Figure 3.2. The coefficients $K_{\bullet c}$ are cutting force coefficients due to the shear force and $K_{\bullet e}$ are edge force coefficients due to the ploughing force of the tool edge and flank rubbing on the workpiece.

The undeformed chip thickness as defined by Martellotti (1941) can be expressed as,

$$h = s_t \sin\phi_j \sin\kappa, \tag{3.5}$$

while the edge length $\mathrm{d}S$ can be derived from equation (3.1) (Engin, 2001a) as,

$$\mathrm{d}S = |\mathrm{dr}| = \mathrm{d}\phi\sqrt{r^2(\phi) + (r'(\phi))^2 + (z'(\phi))^2}, \tag{3.6}$$

where the differentials $r'(\phi)$ and $z'(\phi)$ are with respect to ϕ.

The cutting forces in the cylindrical coordinates are transformed into global Cartesian coordinates (feed (X), normal, (Y) and axial (Z) directions defined in Figure 3.2) by multiplying by the transfer matrix,

$$\begin{bmatrix} \mathrm{d}F_{xj}(\phi_j, z) \\ \mathrm{d}F_{yj}(\phi_j, z) \\ \mathrm{d}F_{zj}(\phi_j, z) \end{bmatrix} = \begin{bmatrix} -\cos\phi_j & -\sin\kappa\sin\phi_j & -\cos\kappa\sin\phi_j \\ \sin\phi_j & -\sin\kappa\cos\phi_j & -\cos\kappa\cos\phi_j \\ 0 & \cos\kappa & -\sin\kappa \end{bmatrix} \times \begin{bmatrix} \mathrm{d}F_{tj}(\phi_j, z) \\ \mathrm{d}F_{rj}(\phi_j, z) \\ \mathrm{d}F_{aj}(\phi_j, z) \end{bmatrix} \tag{3.7}$$

Therefore the average milling forces for one tooth period, is defined as,

$$\overline{F_q} = \frac{1}{\phi_p}\int_{\phi_{start}}^{\phi_{exit}}\int_{z_1}^{z_2} \mathrm{d}F_q(\phi, \mathrm{z})\,\mathrm{d}z\,\mathrm{d}\phi, \tag{3.8}$$

where, $\phi_p = 2\pi/N$, $q = x, y, z$, ϕ_{start} and ϕ_{exit} are the entry and exit radial immersion angles, respectively (Figure 3.4) and the discretization $\mathrm{d}z$ is shown in Figure 3.2.

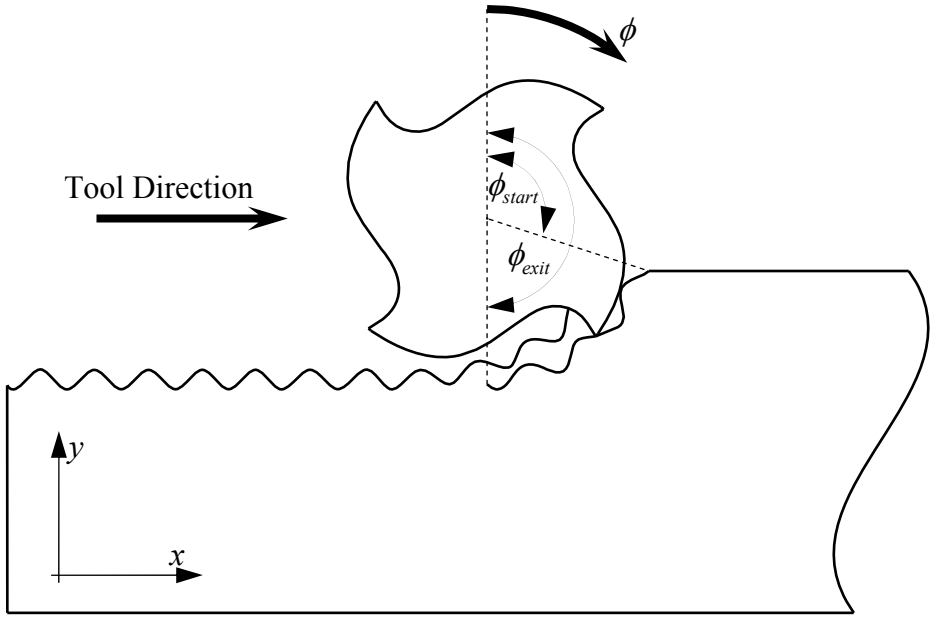

Figure 3.4. Cutter's entry and exit angles for downmilling.

If there is a helix angle, runout or the tool is not a flat end tool, then the chip load at the different disk segments are not the same. When there is a helix or corner radius, the analytical derivation of dS in equation (3.4) is slightly more complicated. The tool used in this section has a fairly large helix angle and a corner radius. Gradisek proposed a uniformed approach to obtaining the cutting force coefficients for general end mill, which is adopted and summarised here.

Following the first integration, equations (3.4) are simplified to,

$$\begin{bmatrix} F_x(\phi) \\ F_y(\phi) \\ F_z(\phi) \end{bmatrix} = \begin{bmatrix} -K_{tc}h\cos(\phi) & -K_{rc}h\sin(\phi) & -K_{ac}h\sin(\phi) \\ K_{tc}h\sin(\phi) & -K_{rc}h\cos(\phi) & -K_{ac}h\cos(\phi) \\ 0 & -K_{ac}h & K_{rc}h \end{bmatrix} \begin{bmatrix} A_1 \\ A_2 \\ A_3 \end{bmatrix} + \begin{bmatrix} -K_{te}\cos(\phi) & -K_{re}\sin(\phi) & -K_{ae}\sin(\phi) \\ K_{te}\sin(\phi) & -K_{re}\cos(\phi) & -K_{ae}\cos(\phi) \\ 0 & -K_{ae} & K_{re} \end{bmatrix} \begin{bmatrix} B_1 \\ B_2 \\ B_3 \end{bmatrix}, \tag{3.9}$$

where, parameters A and B are dependent on the tool geometry and differ along the tool axis for tool without a flat-end. These parameters are defined by the following integrals,

$$A_1 = \int_{z_1}^{z_2} \mathrm{d}z, \qquad A_2 = \int_{z_1}^{z_2} \sin(\kappa(z))\,\mathrm{d}z, \qquad A_3 = \int_{z_1}^{z_2} \cos(\kappa(z))\,\mathrm{d}z(z), \tag{3.10a}$$

$$B_1 = \int_{z_1}^{z_2} \mathrm{d}S(z), \quad B_2 = \int_{z_1}^{z_2} \sin(\kappa(z))\,\mathrm{d}S(z), \quad B_3 = \int_{z_1}^{z_2} \cos(\kappa(z))\,\mathrm{d}S(z) \tag{3.10b}$$

Numerical integration of the B parameters would be required, if the tool is not a flat-end tool as explained by Gradisek et al. (2004). This is due to the complex nature of the edge length, dS of the cutting segment, which varies with elevation z. The instantaneous forces are then averaged over radial immersion angle yielding,

$$\begin{bmatrix} \overline{F_x} \\ \overline{F_y} \\ \overline{F_z} \end{bmatrix} = \frac{s_t}{\phi_p} \begin{bmatrix} -C_4A_1 & -C_5A_2 & -C_5A_3 \\ C_5A_1 & -C_4A_2 & -C_4A_3 \\ 0 & C_2A_3 & -C_2A_2 \end{bmatrix} \begin{bmatrix} K_{tc1} \\ K_{rc1} \\ K_{ac1} \end{bmatrix} + \frac{1}{\phi_p} \begin{bmatrix} -C_3B_1 & -C_2B_2 & -C_2B_3 \\ C_2B_1 & -C_3B_2 & -C_3B_3 \\ 0 & C_1B_3 & -C_1B_2 \end{bmatrix} \begin{bmatrix} K_{te} \\ K_{re} \\ K_{ae} \end{bmatrix}, \tag{3.11}$$

where,

$$C_1 = \int_{\phi_{start}}^{\phi_{exit}} \mathrm{d}\phi = \phi\Big|_{\phi_{start}}^{\phi_{exit}}, \qquad C_2 = \int_{\phi_{start}}^{\phi_{exit}} \sin(\phi)\,\mathrm{d}\phi = -\cos(\phi)\Big|_{\phi_{start}}^{\phi_{exit}},$$

$$C_3 = \int_{\phi_{start}}^{\phi_{exit}} \cos(\phi)\,\mathrm{d}\phi = \sin(\phi)\Big|_{\phi_{start}}^{\phi_{exit}}, \quad C_4 = \int_{\phi_{start}}^{\phi_{exit}} \sin(\phi)\cos(\phi)\,\mathrm{d}\phi = \frac{1}{2}\sin^2(\phi)\Big|_{\phi_{start}}^{\phi_{exit}}, \quad (3.12)$$

$$C_5 = \int_{\phi_{start}}^{\phi_{exit}} \sin^2(\phi)\,\mathrm{d}\phi = -\frac{1}{2}\sin(\phi)\cos(\phi) + \frac{1}{2}\phi\Big|_{\phi_{start}}^{\phi_{exit}}$$

The final step is to extract the six cutting coefficients in equation (3.11). There are however only 3 equations available. In order to obtain a closed-form expression for the cutting force coefficients, the relationship between the cutting force and the feed per tooth is used. As mentioned earlier, in mechanistic modelling the cutting force is assumed to be proportional to the chip load, hence chip thickness. Therefore in the case of milling it is assumed that the average cutting force per tooth is a linear function of the feed, s_t. This is also dependent on the assumption that the deflections during the experiment are negligible and the cutting process is stable. Therefore, the average cutting force can be defined as,

$$\overline{F}_q = \overline{F}_{qc} \cdot s_t + \overline{F}_{qe}, \tag{3.13}$$

where, $(q = x, y, z)$

Therefore equations (3.11) and (3.13) can be used to obtain a closed-form expression for the cutting force coefficients (Gradisek, 2004) as,

$$K_{tc} = \frac{\phi_p\left(\overline{F}_{yc}C_5 - \overline{F}_{xc}C_4\right)}{\left(C_4^2 + C_5^2\right)A_1}, \tag{3.14a}$$

$$K_{rc} = \frac{\phi_p\left(A_3\overline{F}_{zc}\left(C_5^2 + C_4^2\right) - A_2C_2\left(C_4\overline{F}_{yc} + C_5\overline{F}_{xc}\right)\right)}{C_2\left(C_5^2 + C_4^2\right)\left(A_3^2 + A_2^2\right)}, \tag{3.14b}$$

$$K_{ac} = \frac{-\phi_p\left(A_2\overline{F}_{zc}\left(C_5^2 + C_4^2\right) + A_3C_2\left(C_4\overline{F}_{yc} + C_5\overline{F}_{xc}\right)\right)}{C_2\left(C_5^2 + C_4^2\right)\left(A_3^2 + A_2^2\right)}, \tag{3.14c}$$

$$K_{te} = \frac{\phi_p\left(\overline{F}_{ye}C_2 - \overline{F}_{xe}C_3\right)}{\left(C_2^2 + C_3^2\right)B_1}, \tag{3.14d}$$

$$K_{re} = \frac{\phi_p \left(B_3 \overline{F}_{ze} \left(C_2^2 + C_3^2 \right) - B_2 C_1 \left(C_3 \overline{F}_{ye} + C_2 \overline{F}_{xe} \right) \right)}{C_1 \left(C_2^2 + C_3^2 \right) \left(B_3^2 + B_2^2 \right)}, \tag{3.14e}$$

$$K_{ae} = \frac{-\phi_p \left(B_2 \overline{F}_{ze} \left(C_3^2 + C_2^2 \right) + B_3 C_1 \left(C_2 \overline{F}_{xe} + C_3 \overline{F}_{ye} \right) \right)}{C_1 \left(C_2^2 + C_3^2 \right) \left(B_3^2 + B_2^2 \right)}, \tag{3.14f}$$

where, $\phi_p = \dfrac{2\pi}{N}$

Time Domain Simulations

Once the cutting coefficients have been obtained, they can be validated by comparing the predicted cutting force for given cutting condition with experimentally measured cutting forces. Although the coefficients were obtained using a spreadsheet program, running the mechanistic model would either require some programming or the use of available commercial software like CutPro. For this section, the mechanistic model was programmed using Fortran Language in order to validate the coefficients obtained using the approach presented by Gradisek (2004). The cutter geometry and cutting conditions are given in Table 3.1. Apart from the discretisation along the tool axis, the time domain discretisation is in the terms of the rotation of the cutting edges about the cutter axis. A quick convergence study was carried out to identify the optimum discretisation gradation, whilst keeping the simulation timely efficient. The rotation in degrees of the cutting edges used was 0.5^o, whilst the tool was discretized along the axis with a disc thickness 0.01% of the axial depth of cut.

Table 3.1. Tool Geometry and Cutting Conditions

Tool Radius (mm)	10.00
Helix Angle (Degs)	54.39
Corner Radius, R_c (mm)	5.00
R_r (mm)	5.00
R_z (mm)	5.00
H (mm)	5.00
α, β (Degs)	0.00
Radial Immersion, r_{doc} (mm)	10.00
Spindle Speed (rpm)	4420.0

The workpiece and tool were assumed to be perfectly rigid, thus no vibrations were modelled in the simulations similar to the assumption that the deflections are negligible.

The Mechanistic Calibration Experiment

The experiment to obtain the cutting force coefficient was carried out on a ‘‘Marwin MPS’’ with Steptec spindle 27,000 rpm and 75kW, while the cutting force measurements were taken using a ‘‘Kistler dynamometer - 9255B’’ and sampled at a frequency of 50 kHz using a ‘‘LDS Sigma 90-8 scope’’. This sampling frequency meant data was sampled ever 0.5304^{o} of tool rotation. The Kistler dynamometer has an ‘Fx’ and ‘Fy’ force range of -20kN to 20kN, ‘Fz’ force range of -10kN – 40kN and an accuracy of ±0.5%. The experiment was carried out using Alusol (5% concentration) mixed with deionised water coolants. The feedrates used are given in Appendix A and were repeated for all axial depths of cuts ranging from 0.5 to 6.0mm at intervals of 0.5mm. The spindle speed of 4420rpm used in this experiment was based on the magnitudes of the transfer functions between the impact force and the dynamometer measurements in the principal directions, Y obtained through a quick test known as ‘‘reliability test’’. The transfer function reflects the dynamic response of the force sensor, which is dependent on its dynamic properties. The reliability test is explained in Appendix A. The milling orientation used was down-milling.

Modelling and Experimental Assumptions

The definition of chip thickness in equation (3.5) would be inaccurate if there is any relative displacement between the tool and workpiece caused by vibrations. Therefore the cuttings conditions were carefully taken to ensure there was no chatter and to minimize vibrations in the tool and workpiece. However there is always some level of vibration, which comes from mechanical vibrations caused by the machine and slight vibrations from the dynamic nature of the cutting process. These were assumed to be negligible.

The effects the coolant has on the cutting forces was neglected and not included in the model. The coolant was delivered to the cutting region through jets, which would have an impact on the cutting forces measured by the dynamometer. The coolant would also change the temperature of the workpiece and the tool through heat transfer. The effect this has on the machining process (hence cutting forces) was not included in the model.

Experimental Results

For the axial depth of cut of 5.5mm, the average cutting forces are plotted against the feeds per tooth in Figure 3.5. It can be seen that the assumption that the average cutting force per tooth is a linear function of the feed, s_t is of satisfactory accuracy, although F_y is seen to fit more accurately than F_x and F_z. From these results, the six cutting force coefficients were derived using the approach presented by Gradisek (Gradisek, 2004). The point of intersection at y-axis is used to extract the edge force coefficients (due to the ploughing forces) while the slope of the graph is used to extract the cutting force coefficients (due to the shearing of the material).

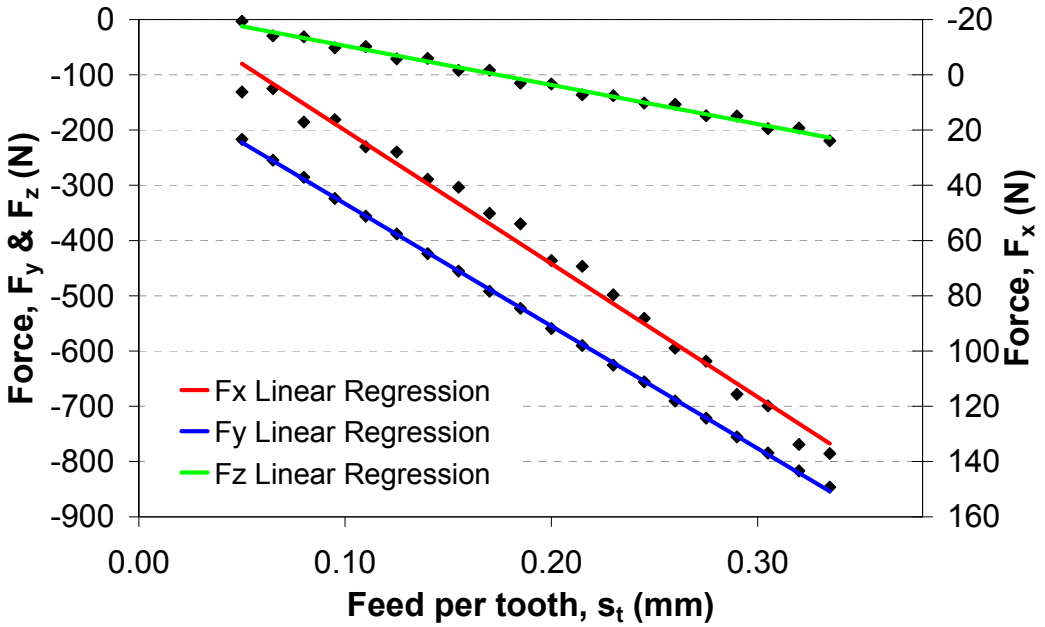

Figure 3.5. Distribution of average measured cutting forces (F_x, F_y, F_z) for 5.5mm axial depth of cut.

The cutting force coefficients obtained for the different axial depths of cuts are shown in Table 3.2. These coefficients are plotted against axial depth of cut in Figures 3.6 – 3.11. The data is fitted using the least squares method to a polynomial expression as follows:

$$K_{tc} = 14.904a^2 - 174.116a + 1157.763, \quad (3.15a)$$

$$K_{te} = 0.261a^2 - 7.520a + 43.438, \quad (3.15b)$$

$$K_{rc} = -47.240a^2 + 560.282a - 915.486, \quad (3.15c)$$

$$K_{re} = -2.254a^2 + 29.082a - 88.682, \quad (3.15d)$$

$$K_{ac} = -13.360a^2 - 82.679a + 976.504, \quad (3.15e)$$

$$K_{ae} = -1.387a^2 - 0.020a + 50.149, \quad (3.15f)$$

where, a is the axial depth of cut.

Plots of these polynomial fittings are shown in Figures 3.6 – 3.11. These polynomial expressions are essential when the cutting coefficients of any axial depth are required. The 'R-squared' value is known as the coefficient of determination and it is the square of the data correlation coefficient (Edwards, 1976). Its value ranges from 0 to 1, where 1 is for perfect curve fitting.

Table 3.2. Mechanistically Calibrated Cutting Force Coefficients

Axial Depth of Cut (mm), a	K_{tc} (N/mm^2)	K_{te} (N/mm)	K_{rc} (N/mm^2)	K_{re} (N/mm)	K_{ac} (N/mm^2)	K_{ae} (N/mm)
0.50	981.697	32.550	-691.073	-70.800	880.899	44.867
1.00	1088.489	45.195	-433.896	-72.246	936.369	55.764
1.50	975.489	35.695	-146.049	-50.058	865.708	48.976
2.00	867.092	29.704	88.704	-37.148	739.643	44.362
2.50	801.097	25.519	242.768	-28.240	655.208	40.384
3.00	772.410	21.860	364.955	-22.105	586.352	37.275
3.50	703.360	22.402	433.296	-14.195	502.936	36.906
4.00	711.859	17.792	504.703	-11.289	488.636	29.436
4.50	672.627	17.202	568.484	-7.990	385.403	28.664
5.00	612.805	7.356	719.912	3.097	154.528	4.967
5.50	657.990	9.317	758.064	3.929	93.674	5.179
6.00	679.603	11.488	778.744	4.736	33.244	6.129

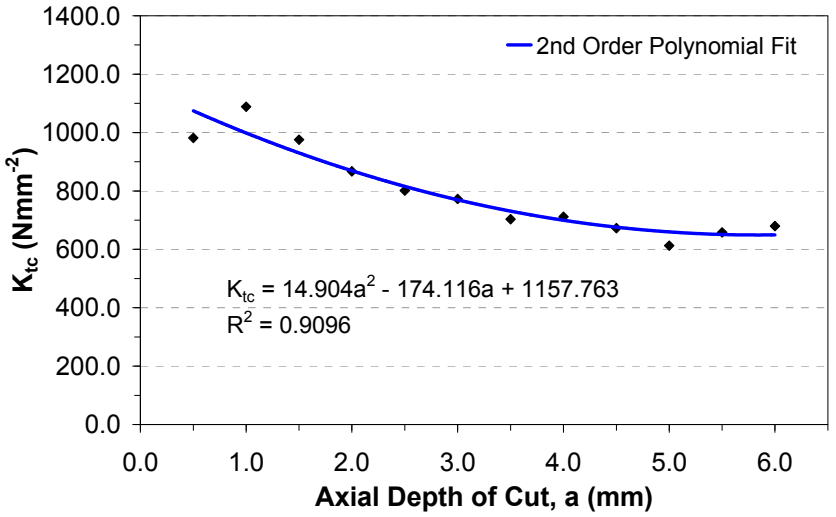

Figure 3.6. Tangential Cutting Force Coefficient, K_{tc}.

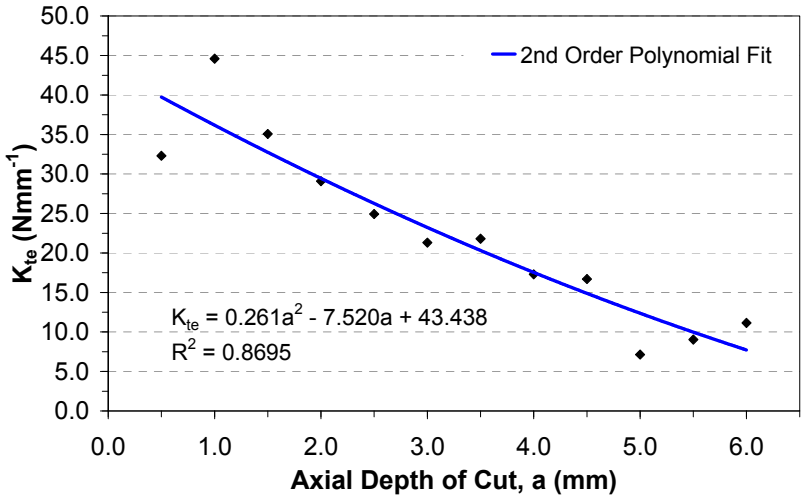

Figure 3.7. Tangential Edge Force Coefficient, K_{te}.

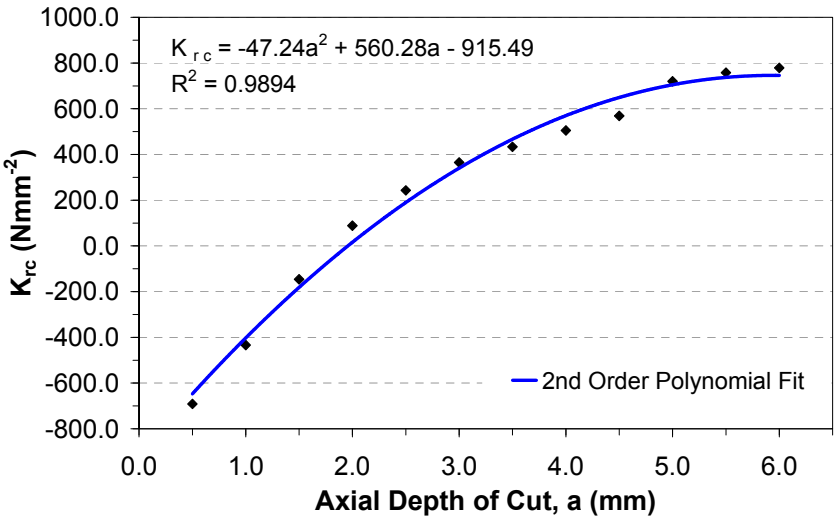

Figure 3.8. Radial Cutting Force Coefficient, K_{rc}.

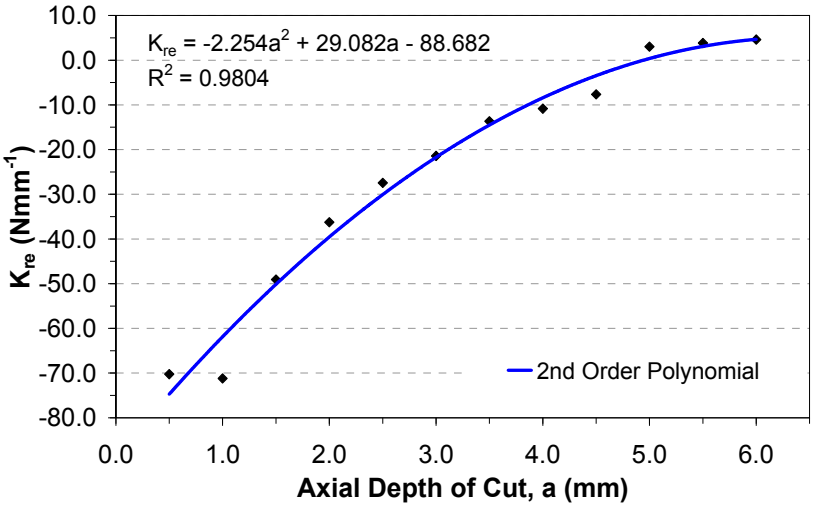

Figure 3.9. Radial Edge Force Coefficient, K_{re}.

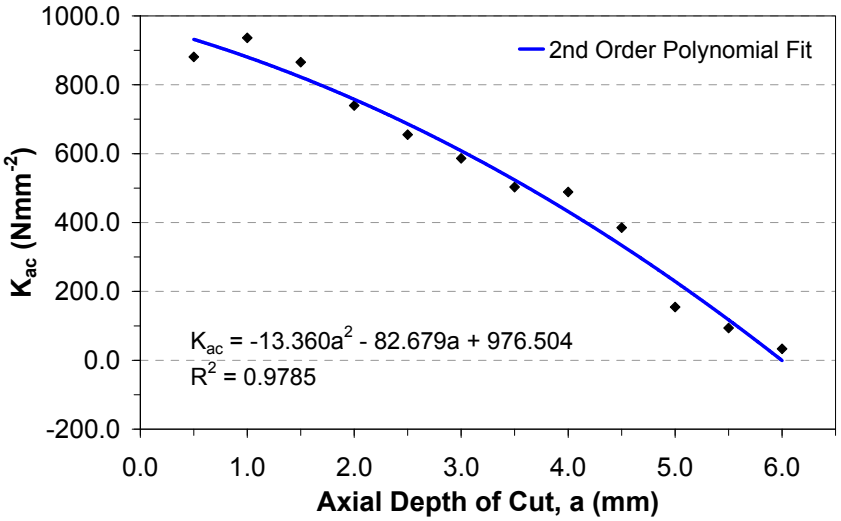

Figure 3.10. Axial Cutting Force Coefficient, K_{ac}.

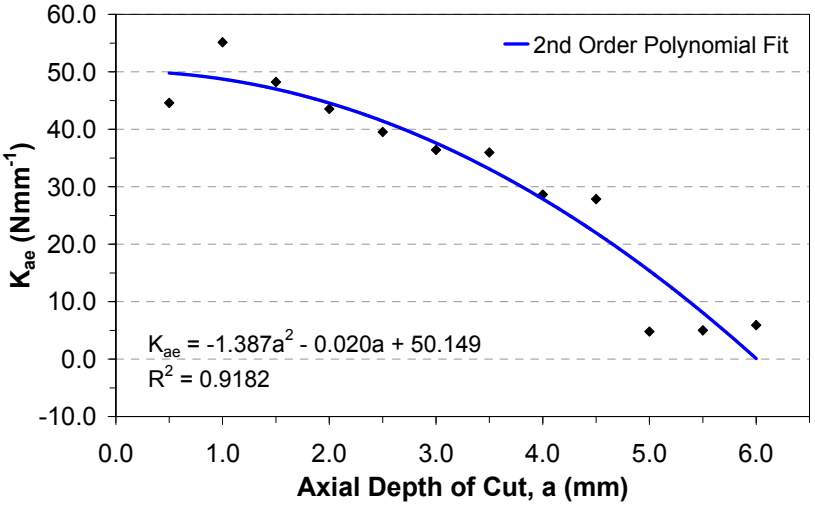

Figure 3.11. Axial Edge Force Coefficient, K_{ae}.

The correlation coefficient gives the quality of a least squares fitting compared to the original data (Wolfram Research, 2008). The R-squared value is simply defined (Press, 1992) as,

$$R^2 \equiv 1 - \frac{\sum_i^n \left(y_i - y_{pi}\right)^2}{\sum_i^n \left(y_i - \bar{y}_i\right)^2}, \tag{3.16}$$

where, y_i is the original data, and y_{pi} is the predicted data. Some discrepancies can be seen at the beginning (0.5mm and 1.0mm) and at the end (5.0mm and 6.0mm). At the small axial depth of cuts of 0.5mm and 1.0mm, the discrepancies are most likely from the tool coming out of cut due to the axial depth of cut being too small for a good engagement. After the 5.0mm axial depth of cut the cutting edge engaged now includes the part of the tool outside the corner radius (there is no taper zone) and it would appear that there seems to be a new trend evolving that would perhaps be better revealed by performing deeper tests and starting the curve fitting from 5.0mm data points. Hence the curve fitting for the data points 0.5mm – 5.0mm is used in Chapters 5 and 6.

Cutting Force Coefficient Validation

The cutting force coefficients shown in Table 3.2 were used to predict the cutting forces at different cutting conditions using the Fortran program as shown in Figures 3.12 – 3.14 in comparison to respective measured cutting forces. The discrepancy in the trough of both the measured cutting forces F_y and F_z is due to the assumption that the tool and the workpiece are rigid and during the simulations at these tool rotations the tooth completely disengaged from the workpiece due to the tool geometry. In reality, there will always be (though usually very small and negligible) a static deflection, which can cause the tool to be constantly engaged with the workpiece depending on the direction of the deflection. This is also noticeable in the measured F_x cutting forces. The extra frequency apart from the tooth passing frequency in the experimental force F_z could be due to tool vibration. The simulations did not take into account any tool or workpiece vibration.

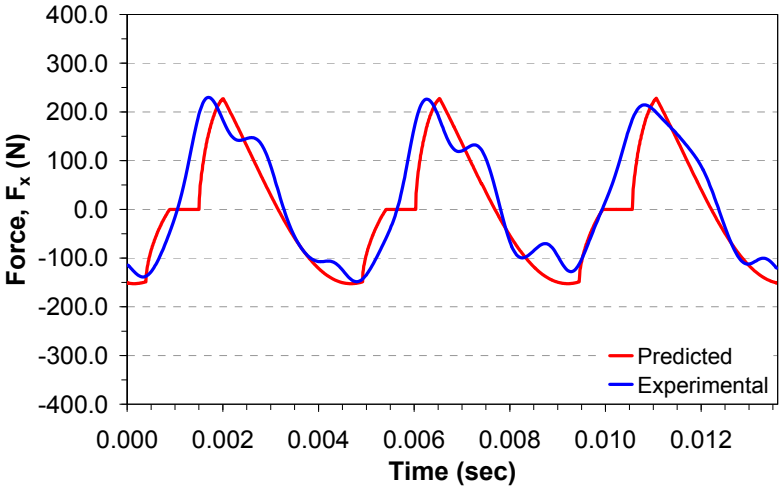

(a) Fx

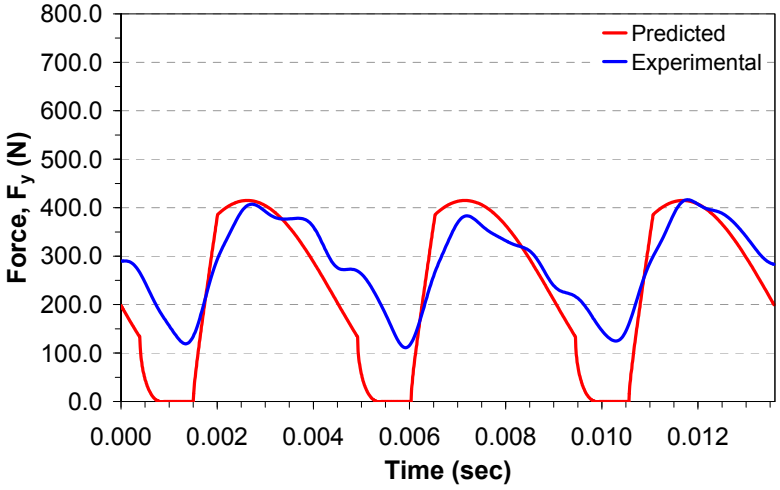

(b) Fy

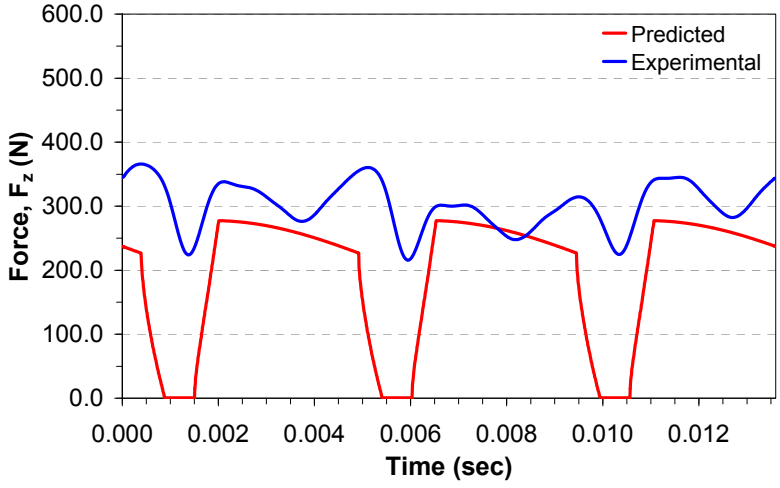

(c) Fz

Figure 3.12. Experimental and prediction forces for 2.5mm axial depth of cut and 0.110mm feed per tooth.

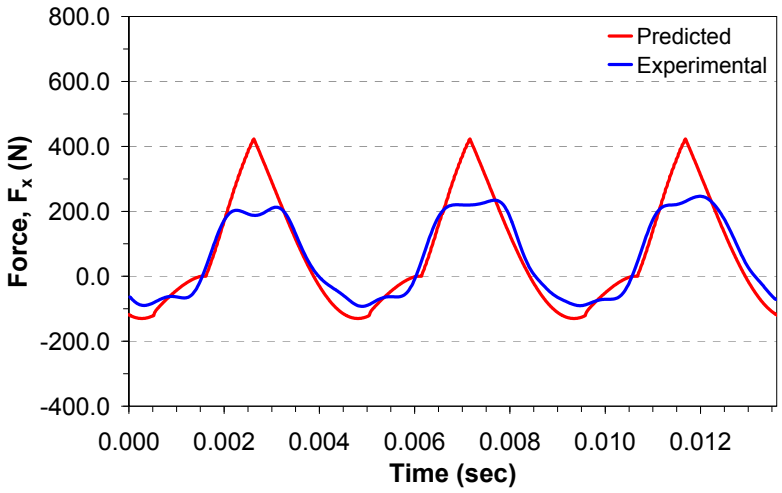

(a) Fx

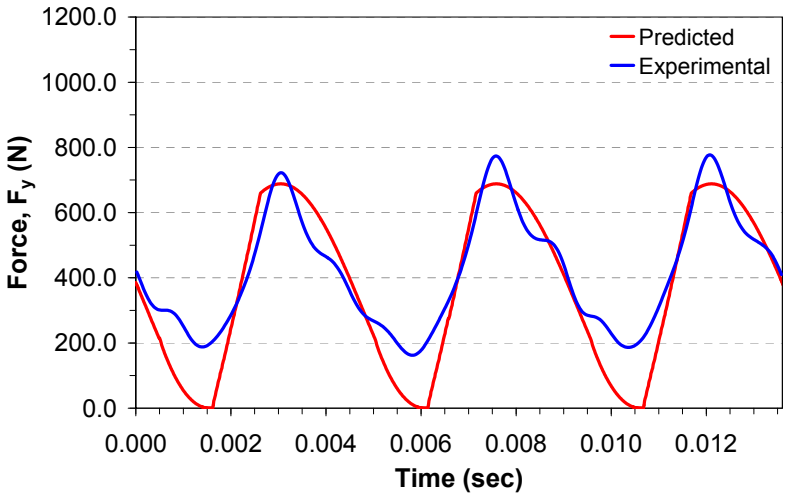

(b) Fy

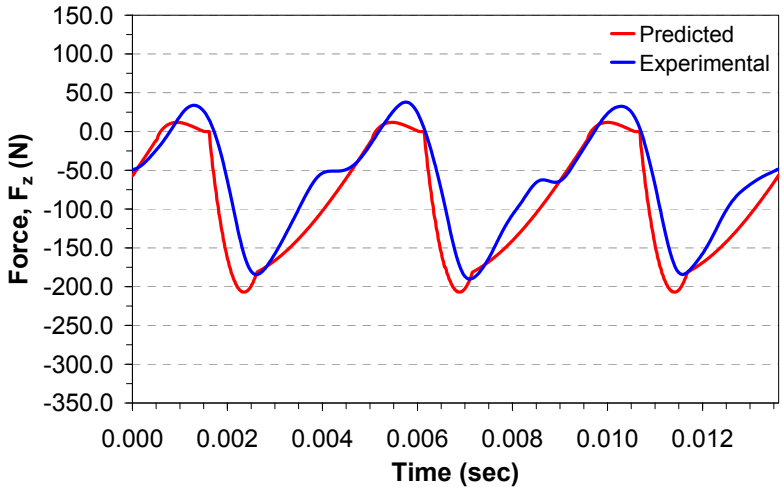

(c) Fz

Figure 3.13. Experimental and prediction forces for 5.0mm axial depth of cut and 0.170mm feed per tooth.

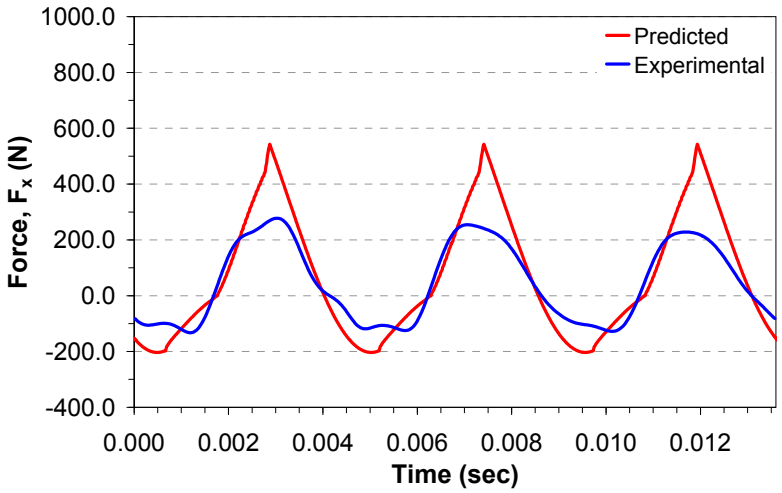

(a) Fx

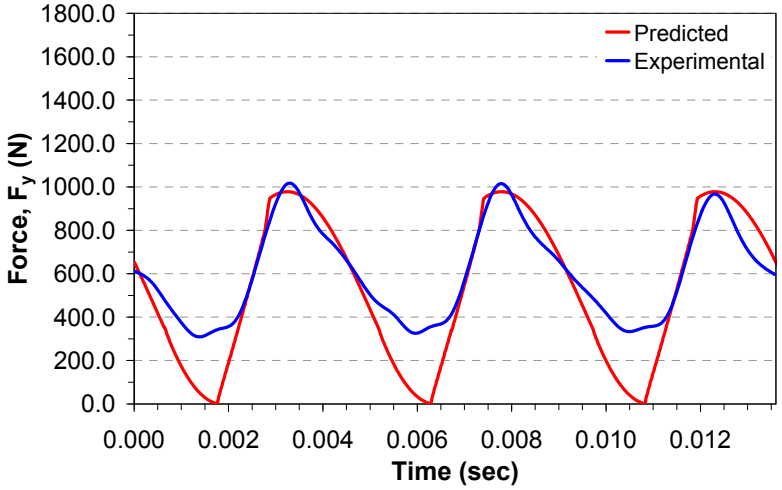

(b) Fy

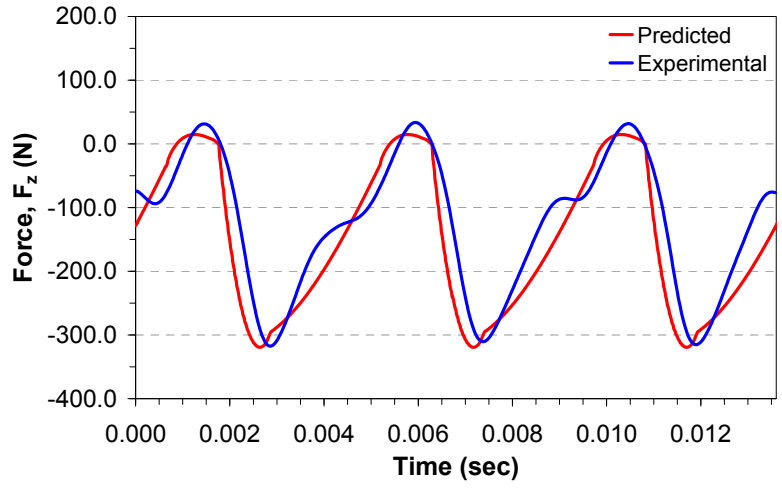

(c) Fz

Figure 3.14. Experimental and prediction forces for 6.0mm axial depth of cut and 0.1850mm feed per tooth.

3.3.2. Higher Order / Non-Linear Edge-Force Model

The mechanistic approach in the previous section assumes a linear relationship between the cutting force and feed (equation 3.13). However this is only accurate for an end tool with a perfectly sharp cutting edge. For a sharp tool having a good deep engagement, a very good linear relationship would be obtained. An example is shown in Figure 3.5, for a tool having an edge radius well below 10-20 microns. On the other hand, when the engagement is shallow or if the tool is very blunt this linear relationship would not be as accurate due to the influence of size effects (Boothroyd, 1975; Wan, 2007; Ranganath, 2007), which is discussed in more detail in the next section. For cases where the size effects can not be ignored, the linear edge force model would give inaccurate results when used to predict cutting forces for varied cutting conditions, hence a nonlinear model is proposed.

The mechanistic model can be improved by assuming a nonlinear relationship between the cutting force and the feed. Therefore equations (3.4 a, b & c) becomes,

$$\mathrm{d}F_{tj}\left(\phi_j,\kappa\right)=K_{tc3}h^3\left(\phi_j,\kappa\right)\mathrm{d}z+K_{tc2}h^2\left(\phi_j,\kappa\right)\mathrm{d}z+K_{tc1}h\left(\phi_j,\kappa\right)\mathrm{d}z+K_{te}\mathrm{d}S, \quad (3.17a)$$

$$\mathrm{d}F_{rj}\left(\phi_j,\kappa\right)=K_{rc3}h^3\left(\phi_j,\kappa\right)\mathrm{d}z+K_{rc2}h^2\left(\phi_j,\kappa\right)\mathrm{d}z+K_{rc1}h\left(\phi_j,\kappa\right)\mathrm{d}z+K_{re}\mathrm{d}S, \quad (3.17b)$$

$$\mathrm{d}F_{aj}\left(\phi_j,\kappa\right)=K_{ac3}h^3\left(\phi_j,\kappa\right)\mathrm{d}z+K_{ac2}h^2\left(\phi_j,\kappa\right)\mathrm{d}z+K_{ac1}h\left(\phi_j,\kappa\right)\mathrm{d}z+K_{ae}\mathrm{d}S \quad (3.17c)$$

Therefore by following the same steps as the mechanistic model described in the previous section, the average milling force for one tooth period expressed as (equation 3.8),

$$\overline{F}_q=\frac{1}{\phi_p}\int_{\phi_{entry}}^{\phi_{exit}}\int_{z_1}^{z_2}\mathrm{d}F_q\left(\phi,\mathrm{z}\right)\mathrm{d}\phi$$

This gives,

$$\begin{bmatrix}\overline{F_x}\\ \overline{F_y}\\ \overline{F_z}\end{bmatrix} = \frac{s_t^3}{\phi_p}\begin{bmatrix}-D_7A_1 & -D_4A_2 & -D_4A_3\\ D_4A_1 & -D_7A_2 & -D_7A_3\\ 0 & D_3A_3 & -D_3A_2\end{bmatrix}\times\begin{bmatrix}K_{tc3}\\ K_{rc3}\\ K_{ac3}\end{bmatrix}+ \frac{s_t^2}{\phi_p}\begin{bmatrix}-D_6A_1 & -D_3A_2 & -D_3A_3\\ D_3A_1 & -D_6A_2 & -D_6A_3\\ 0 & D_2A_3 & -D_2A_2\end{bmatrix}\times\begin{bmatrix}K_{tc2}\\ K_{rc2}\\ K_{ac2}\end{bmatrix}+ \frac{s_t}{\phi_p}\begin{bmatrix}-D_5A_1 & -D_2A_2 & -D_2A_3\\ D_2A_1 & -D_5A_2 & -D_5A_3\\ 0 & D_1A_3 & -D_1A_2\end{bmatrix}\times\begin{bmatrix}K_{tc1}\\ K_{rc1}\\ K_{ac1}\end{bmatrix}+ \begin{bmatrix}-D_9B_1 & -D_1B_2 & -D_1B_3\\ D_1B_1 & -D_9B_2 & -D_9B_3\\ 0 & D_8B_3 & -D_8B_2\end{bmatrix}\times\begin{bmatrix}K_{te}\\ K_{re}\\ K_{ae}\end{bmatrix}, \tag{3.18}$$

where,

$$D_1 = \int_{\phi_{start}}^{\phi_{exit}} \sin(\phi)\,\mathrm{d}\phi = -\cos(\phi)\Big|_{\phi_{start}}^{\phi_{exit}}, \tag{3.19a}$$

$$D_2 = \int_{\phi_{start}}^{\phi_{exit}} \sin^2(\phi)\,\mathrm{d}\phi = -\frac{1}{2}\sin(\phi)\cos(\phi) + \frac{1}{2}\phi\Big|_{\phi_{start}}^{\phi_{exit}}, \tag{3.19b}$$

$$D_3 = \int_{\phi_{start}}^{\phi_{exit}} \sin^3(\phi)\,\mathrm{d}\phi = -\frac{1}{3}\sin^2(\phi)\cos(\phi) - \frac{2}{3}\cos(\phi)\Big|_{\phi_{start}}^{\phi_{exit}}, \tag{3.19c}$$

$$D_4 = \int_{\phi_{start}}^{\phi_{exit}} \sin^4(\phi)\,\mathrm{d}\phi = -\frac{1}{4}\sin^3(\phi)\cos(\phi) - \frac{3}{8}\sin(\phi)\cos(\phi) + \frac{3}{8}\phi\Big|_{\phi_{start}}^{\phi_{exit}}, \tag{3.19d}$$

$$D_5 = \int_{\phi_{start}}^{\phi_{exit}} \sin(\phi)\cos(\phi)\,\mathrm{d}\phi = \frac{1}{2}\sin^2(\phi)\Big|_{\phi_{start}}^{\phi_{exit}}, \tag{3.19e}$$

$$D_6 = \int_{\phi_{start}}^{\phi_{exit}} \sin^2(\phi)\cos(\phi)\,\mathrm{d}\phi = \frac{1}{3}\sin^3(\phi)\Big|_{\phi_{start}}^{\phi_{exit}}, \tag{3.19f}$$

$$D_7 = \int_{\phi_{start}}^{\phi_{exit}} \sin^3(\phi)\cos(\phi)\,\mathrm{d}\phi = \frac{1}{4}\sin^4(\phi)\Big|_{\phi_{start}}^{\phi_{exit}}, \tag{3.19g}$$

$$D_8 = \int_{\phi_{start}}^{\phi_{exit}} \mathrm{d}\phi = \phi\big|_{\phi_{start}}^{\phi_{exit}}, \tag{3.19h}$$

$$D_9 = \int_{\phi_{start}}^{\phi_{exit}} \cos(\phi)\,\mathrm{d}\phi = \sin(\phi)\big|_{\phi_{start}}^{\phi_{exit}} \tag{3.19i}$$

By assuming a nonlinear relationship between cutting force (using a third-order polynomial expression), the average cutting force can be defined as,

$$\overline{F}_q = \overline{F}_{qc3} \cdot s_t^3 + \overline{F}_{qc2} \cdot s_t^2 + \overline{F}_{qc1} \cdot s_t + \overline{F}_{qe}, \tag{3.20}$$

where, $(q = x, y, z)$.

This can then be related to equations (3.19a – 3.19i), which finally yields the cutting coefficients definitions as,

$$K_{tc1} = \frac{\phi_p\left(\overline{F}_{yc1}D_2 - \overline{F}_{xc1}D_5\right)}{\left(D_5^2 + D_2^2\right)A_1}, \tag{3.21a}$$

$$K_{rc1} = \frac{\phi_p\left[A_3\overline{F}_{zc1}\left(D_2^2 + D_5^2\right) - A_2D_1\left(D_5\overline{F}_{yc1} + D_2\overline{F}_{xc1}\right)\right]}{D_1\left(D_2^2 + D_5^2\right)\left(A_3^2 + A_2^2\right)}, \tag{3.21b}$$

$$K_{ac1} = \frac{-\phi_p\left[A_2\overline{F}_{zc1}\left(D_2^2 + D_5^2\right) + A_3D_1\left(D_5\overline{F}_{yc1} + D_2\overline{F}_{xc1}\right)\right]}{D_1\left(D_2^2 + D_5^2\right)\left(A_3^2 + A_2^2\right)}, \tag{3.21c}$$

$$K_{tc2} = \frac{\phi_p\left(\overline{F}_{yc2}D_3 - \overline{F}_{xc2}D_6\right)}{\left(D_3^2 + D_6^2\right)A_1}, \tag{3.21d}$$

$$K_{rc2} = \frac{\phi_p\left[A_3\overline{F}_{zc2}\left(D_3^2 + D_6^2\right) - A_2D_2\left(D_3\overline{F}_{xc2} + D_6\overline{F}_{yc2}\right)\right]}{D_2\left(D_3^2 + D_6^2\right)\left(A_3^2 + A_2^2\right)}, \tag{3.21e}$$

$$K_{ac2} = \frac{-\phi_p\left[A_2\overline{F}_{zc2}\left(D_3^2 + D_6^2\right) + A_3D_2\left(D_3\overline{F}_{xc2} + D_6\overline{F}_{yc2}\right)\right]}{D_2\left(D_3^2 + D_6^2\right)\left(A_3^2 + A_2^2\right)}, \tag{3.21f}$$

$$K_{tc3} = \frac{\phi_p\left(\overline{F}_{yc3}D_4 - \overline{F}_{xc3}D_7\right)}{\left(D_4^2 + D_7^2\right)A_1}, \tag{3.21g}$$

$$K_{rc3} = \frac{\phi_p \left[A_3 \overline{F}_{zc3} \left(D_4^2 + D_7^2 \right) - A_2 D_3 \left(D_4 \overline{F}_{xc3} + D_7 \overline{F}_{yc3} \right) \right]}{D_3 \left(D_4^2 + D_7^2 \right) \left(A_3^2 + A_2^2 \right)}, \tag{3.21h}$$

$$K_{ac3} = \frac{-\phi_p \left[A_2 \overline{F}_{zc3} \left(D_4^2 + D_7^2 \right) + A_3 D_3 \left(D_7 \overline{F}_{yc3} + D_4 \overline{F}_{xc3} \right) \right]}{D_3 \left(D_4^2 + D_7^2 \right) \left(A_3^2 + A_2^2 \right)} \tag{3.21i}$$

The edge force coefficients K_{te}, K_{re}, K_{ae} are the same as the linear mechanistic model equation (3.14 d, e & f). Although the modified mechanistic model introduces six more coefficients, its results would capture nonlinear relationship between feed and cutting forces more accurately. Therefore, for tool with a blunt cutting edge (e.g. honed tools), or when machining with small feed (e.g. in micromachining), the proposed nonlinear mechanistic model could give more accurate cutting force predictions.

Validation

Though a very sharp tool was used in the experimental carried out, the accuracy of the developed higher-order force model is still demonstrated in the predicted cutting forces for axial depth of cut 2.0mm in Figure 3.15. The discrepancies due to the simulations not including static deflection are again seen the comparisons. The cutting force coefficients identified using equations (3.21a – 3.21i) are given in Tables 3.3a and 3.3b

Table 3.3a. Mechanistically Calibrated Higher-Order Cutting Force Coefficients

Axial Depth of Cut (mm), a	K_{tc3} (N/mm^2)	K_{tc2} (N/ mm^2)	K_{tc1} (N/mm^2)	K_{rc3} (N/ mm^2)	K_{rc2} (N/mm^2)	K_{rc1} (N/ mm^2)
0.50	4116.11	-3521.45	1697.37	-9488.44	7645.99	-2198.43
1.00	3945.48	-3917.91	1942.65	-5491.22	5367.23	-1571.10
1.50	4697.96	-3945.12	1775.32	-5323.96	4347.53	-987.59
2.00	6814.69	-4734.37	1725.84	-2754.28	2274.28	-336.78
2.50	6172.25	-4240.64	1562.13	-2637.08	2181.60	-164.86
3.00	1121.77	-1628.27	1167.41	-3853.77	2734.88	-115.37
3.50	-4448.96	589.50	887.37	-6899.24	3967.31	-159.90
4.00	-1563.26	-256.65	917.52	-4979.18	3179.34	-18.56
4.50	-232.33	-963.08	977.26	-2327.22	1519.65	332.35
5.00	948.53	-845.80	792.46	66.13	-24.49	733.88
5.50	-248.44	-239.30	760.03	-335.94	312.51	700.41
6.00	387.03	-584.61	833.89	-192.27	357.34	698.08

Table 3.3b. Mechanistically Calibrated Higher-Order Cutting Force Coefficients

Axial Depth of Cut (mm), a	K_{ac3} (N/mm^2)	K_{ac2} (N/mm^2)	K_{ac1} (N/mm^2)	K_{te} (N/ mm)	K_{re} (N/mm)	K_{ae} (N/ mm)
0.50	2197.48	-2575.46	1530.58	26.52	-57.39	38.11
1.00	3023.28	-3152.74	1703.82	35.50	-58.61	45.37
1.50	2341.79	-2664.75	1530.21	25.99	-39.37	38.71
2.00	3142.22	-2803.22	1374.12	19.60	-31.39	34.03
2.50	3672.91	-3202.30	1358.75	16.40	-22.63	29.10
3.00	3887.38	-3116.36	1233.92	16.02	-15.72	27.22
3.50	811.30	-1866.47	1030.93	17.57	-7.58	27.27
4.00	3034.07	-2795.83	1102.09	13.63	-4.83	19.71
4.50	1743.46	-2033.54	877.20	12.19	-5.39	20.02
5.00	-636.74	304.89	122.90	4.66	2.38	4.74
5.50	-2251.18	1243.11	-90.18	6.96	4.15	6.94
6.00	-1201.43	583.25	-37.54	8.39	5.40	6.43

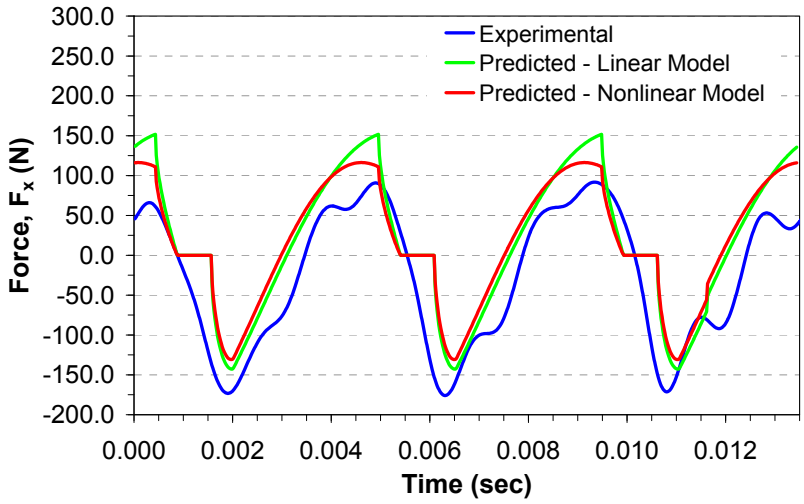

(a) Fx

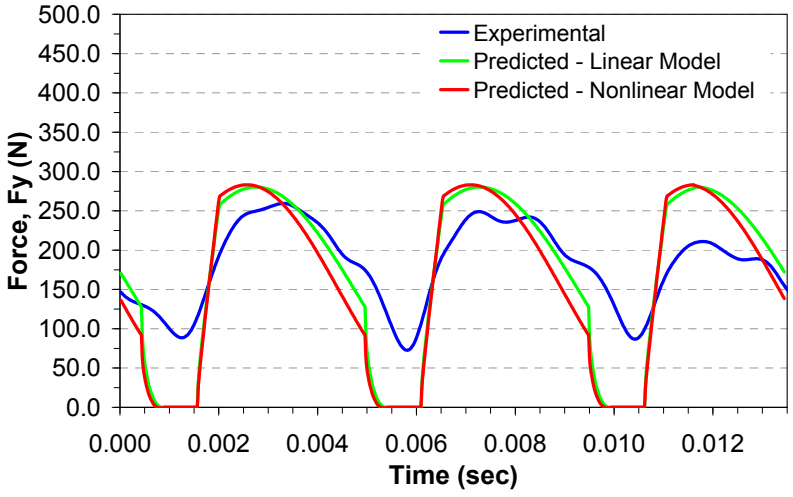

(b) Fy

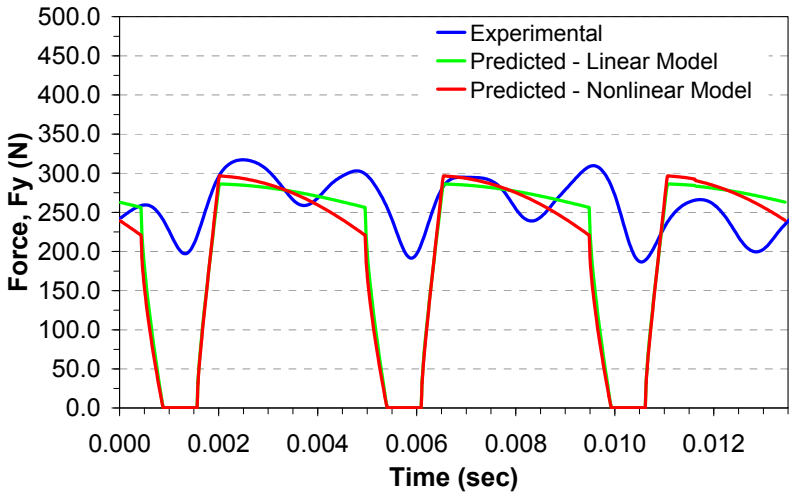

(c) Fz

Figure 3.15. Experimental and prediction forces for 2.0mm axial depth of cut and 0.050mm feed per tooth.

3.4. Finite Element Modelling of Milling Cutting Forces and Cutting Force Coefficients

This section, demonstrates the use of an efficient and accurate numerical tool (i.e. FEA) in simulating the cutting process and determining both the average and instantaneous cutting force coefficients (used in linear edge and exponential force models respectively). The main advantage of this approach compared to other available methods is that it reduces the need for experimental calibrations. In this approach, an Arbitrary Lagrangian Formulation (ALE) was employed in the FEM simulations, which combines advantages of both Lagrangian and Eulerian formulations into a single model. Cutting force predictions using evaluated coefficients are shown to match experimental results with satisfactory accuracy.

3.4.1. Model Formulation

The approach in this section was presented by Adetoro et al. (2008, 2009a) and its application is demonstrated by predicting the cutting forces for a flat end milling tool with no tool runout. With the presence of runout and corner radius, the chip load would not be constant for each discretized disk (Figure 3.2). For a flat end mill, the average forces per tooth period obtained from equation (3.8) can be defined (Altintas, 2000) as,

$$\overline{F}_x = \frac{Nas_t}{8\pi}\left[K_{tc}\cos 2\phi - K_{rc}\left(2\phi - \sin 2\phi\right)\right] - \frac{Na}{8\pi}\left[K_{te}\sin\phi - K_{re}\cos\phi\right]_{\phi_{start}}^{\phi_{exit}}, \qquad (3.22a)$$

$$\overline{F}_y = \frac{Nas_t}{8\pi}\left[K_{tc}\left(2\phi - \sin 2\phi\right) + K_{rc}\cos 2\phi\right] - \frac{Na}{2\pi}\left[K_{te}\cos\phi + K_{re}\sin\phi\right]_{\phi_{start}}^{\phi_{exit}}, \qquad (3.22b)$$

$$\overline{F}_z = \frac{Na}{2\pi}\left[-K_{ac}s_t\cos\phi + K_{ae}\phi\right]_{\phi_{start}}^{\phi_{exit}} \qquad (3.22c)$$

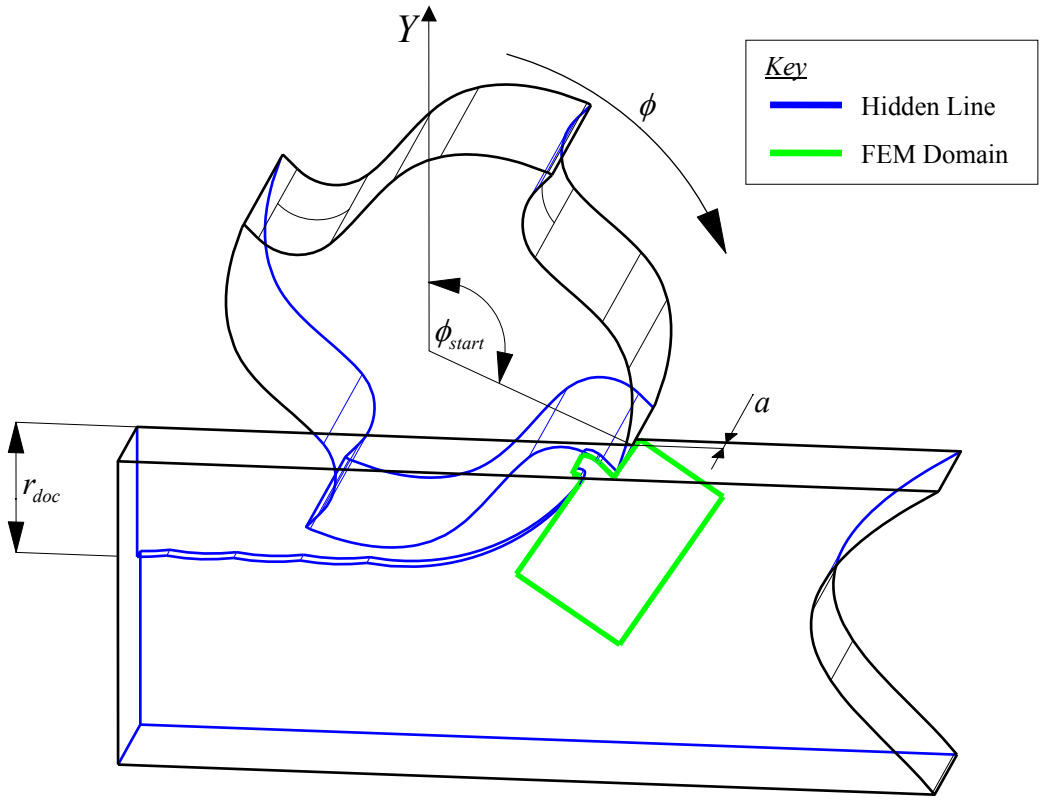

Figure 3.16. Workpiece and cutter showing FEM model.

3.4.2. Simulation

Even though the proposed approach is suitable for any general end mills, it is demonstrated here using a tool with zero helix angle and the results compared with experimental data for a tool with small helix angle. The approach involves modelling the cutting process at different angles of rotation to obtain the instantaneous cutting forces at these respective angles for a given feedrate. The full results obtained for a particular feedrate can be further used to predict the cutting forces for smaller feedrates without additional simulation. This is required for average cutting force coefficients as explained in previous section. When the helix angle is small, the tool would experience very little cutting force along its z-axis, therefore the domain can be simulated using plane strain elements.

The angle of rotation or radial immersion angle ϕ_j, and undeformed chip thickness h, are shown in Figure 3.2. The entry angle of the tool for downmilling can be expressed as,

$$\phi_{entry} = \pi - \arccos\left(1 - \frac{r_{doc}}{R}\right), \tag{3.23}$$

where, r_{doc} is the radial depth of cut and R is the tool radius.

The exit angle for down milling is π according to the convention used in equation (3.23). Therefore, using the undeformed chip thickness h (for a specific angle) from equation (3.5), the cutting process is simulated and the instantaneous radial and tangential cutting forces (in cylindrical coordinate) are obtained for that angle. The reaction forces on the tool obtained from the FEM results are obviously the cutting forces required. Finally, the cutting forces in Cartesian coordinate system (global) can be resolved by a transformation matrix using equation (3.7), where the axial immersion angle, κ is zero for a flat end tool.

The relative speed between the cutting edge and the workpiece is defined as,

$$\upsilon = \Omega \cdot \pi \cdot 2R, \tag{3.24}$$

where Ω is the spindle speed.

3.4.3. Extracting Average Cutting Force Coefficients

The coefficients used in the linear edge-force model are at times referred to as average cutting force coefficients as they are assumed to be constant with change in chip thickness. This is because in the linear edge-force model, the forces due to shearing and ploughing/rubbing are separated out. Using the linear relationship assumption between the cutting forces in global coordinates and the feed per tooth, s_t in equation (3.13), three more equations are obtained to transform equation (3.25) into a closed-form expression.

For example, the entry angles in Figure 3.16 of the tool for downmilling are determined using equation (3.23), while the exit angle for down milling is π. Hence, using the boundary conditions (entry angle = 1.97 rads and exit angles = π) and ignoring coefficients for z-axis, the four average cutting coefficients in equation (3.22 a & b) can be expressed as,

$$K_{tc} = \frac{1}{Na}\left(7.4674 \cdot \overline{F}_{yc} + 7.9133 \cdot \overline{F}_{xc}\right), \tag{3.25a}$$

$$K_{rc} = \frac{1}{Na}\left(7.9133 \cdot \overline{F}_{yc} - 7.4674 \cdot \overline{F}_{xc}\right), \tag{3.25b}$$

$$K_{te} = -\frac{1}{Na}\left(4.7989 \cdot \overline{F}_{xe} + 3.1416 \cdot \overline{F}_{ye}\right), \tag{3.25c}$$

$$K_{re} = \frac{1}{Na}\left(3.1416 \cdot \overline{F}_{xe} - 4.7989 \cdot \overline{F}_{ye}\right) \tag{3.25d}$$

Therefore, to calculate the average cutting force coefficients the global cutting forces at different feeds are required as this is used to obtain the relationship between the feed and cutting forces (in global coordinates) in equation (3.14). To calculate this, let us assume the FEM simulation was conducted for a feed per tooth of $37.5\,\mu m$. Assuming the radial depth of cut is the tools radius, the undeformed chip thickness at the entry angle would be $37.5\,\mu m$ (using equations 3.5 and 3.23). The forces (in both local and global coordinates) at this entry angle are obtained using FEM simulations as explained earlier. The tool is then rotated through various angles and the cutting forces obtained for each respective angle until it is past its exit angle. This will define the full cutting force for the tooth period using a feed per tooth of $37.5\,\mu m$ and more importantly the relationship between both the tangential and radial forces and *h*.

To use the obtained results to calculate the cutting forces for a smaller feed per tooth of $20.0\,\mu m$, the undeformed chip thickness corresponding to $20.0\,\mu m$ is calculated. By keeping the radial depth of the tool radius constant (as the tool radius), this would give an undeformed chip thickness of $20.0\,\mu m$. Then the tangential and radial cutting forces for this thickness/angle and all subsequent angles can be obtained using the relationship between the tangential and radial forces and *h* obtained earlier. The least squares method is used to fit the relationship (between the tangential and radial forces and the chip thickness) to a 2nd-order polynomial model. This is then used to predict the corresponding forces for any undeformed chip thickness hence any angle or rotation. Care should be taken however, to ensure the FEM simulations cover the maximum and the

smallest undeformed chip thicknesses as much as possible in order to make the polynomial approximation as accurate as possible.

The simulation process can however be made more efficient by simulating only the maximum and smallest undeformed chip thickness (corresponding to tool entry and tool exit) and then only a few (1 or 2) chip thicknesses in-between. Depending on the edge radius of the tool however, if there is a considerable influence of size effect, then more than two or three points in between the entry and exit might be required to fully capture the nonlinear relationship between chip thickness and predicted cutting forces. The steps for extracting both the average and instantaneous cutting force coefficients are shown in Figure 3.14.

3.4.4. Instantaneous Cutting Force Coefficients

Similar to the linear edge-force model is the 'exponential' force model. In the exponential force model or 'lumped mechanism' model (Wan, 2007), the effects of the shearing on the rake face and the rubbing at the cutting edge are modelled by a single coefficient. This coefficient is also referred to as exponential cutting force coefficient. Wan et al. studied efficient calibration of instantaneous cutting force coefficients (Wan, 2007) and in their model they separated the cutting force into a nominal component with no runout influence and perturbation component influenced by cutter runout. The FEM approach presented in the previous section is used to extract the cutting force coefficient corresponding to the nominal component of the cutting force.

In the exponential cutting force model, the edge or ploughing force terms in equations (3.4 a, b & c) are dropped giving,

$$\mathrm{d}F_{tj}\left(\phi_j\right) = K_{tc} h \,\mathrm{d}b, \tag{3.26a}$$

$$\mathrm{d}F_{rj}\left(\phi_j\right) = K_{rc} h \,\mathrm{d}b, \tag{3.26b}$$

$$\mathrm{d}F_{aj}\left(\phi_j\right) = K_{ac} h \,\mathrm{d}b, \tag{3.26c}$$

This relationship and the coefficients are readily available from the FEM results. As a matter of fact, the main characteristic of the proposed model is the fact that the milling forces obtained are a collection of instantaneous cutting forces from instantaneous uncut chip thicknesses. This is another advantage this approach gives over the use of experimental results, as the cutting forces in their polar coordinates are readily obtained for each instantaneous chip thickness. This directly shows the ‘‘size effects’’ caused by the ploughing forces at the cutting edge. As explained by Yun and Cho (2001), the difficulty experienced in experimental methods to calibrating exponential cutting force coefficients is that, the measured cutting forces cannot be decomposed into the corresponding components for each discretized disk, which obviously is not the case with the FEM approach. It should be noted however that $\mathrm{d}F_{a,j}(\phi_j)$ was ignored as the helix angle was assumed to be small enough for its influence to be ignored. Hence, the tangential, radial and axial cutting forces from FEM simulations are fitted with 2nd-order polynomials as follows,

$$\mathrm{d}F_{tj}(\phi_j) = \left(C_{t3}h^2 + C_{t2}h + C_{t1}\right)\mathrm{d}b, \tag{3.27a}$$

$$\mathrm{d}F_{rj}(\phi_j) = \left(C_{r3}h^2 + C_{r2}h + C_{r1}\right)\mathrm{d}b, \tag{3.27b}$$

$$\mathrm{d}F_{aj}(\phi_j) = \left(C_{a3}h^2 + C_{a2}h + C_{a1}\right)\mathrm{d}b, \tag{3.27c}$$

where the constants C_{p3}, C_{p2} and C_{p1} $(p = t, r \text{ and } a)$ are extracted using least squares method. Therefore, the exponential cutting force coefficients are simply obtained by dividing equations (3.27 a, b and c) through by $h(\phi_j)\mathrm{d}b$ to obtain,

$$K_p = C_{p3}h + C_{p2} + \frac{C_{p1}}{h}, \qquad (p = t, r, a), \tag{3.28}$$

This allows for the calculation of the instantaneous/exponential cutting coefficient for any uncut chip thickness, h. It should be noted that $\mathrm{d}b = \mathrm{d}z$ when helix angle is ignored or assumed to be zero and it is the axial depth of cut used in the simulations.

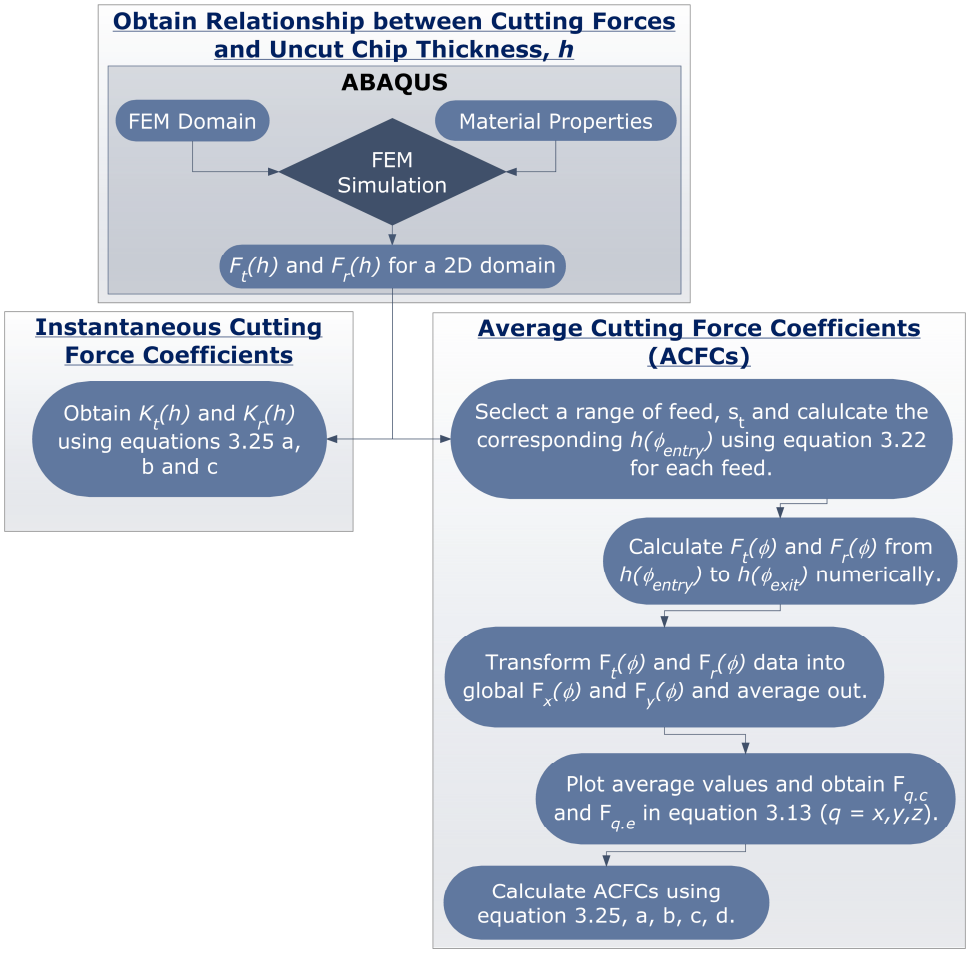

Figure 3.17. Steps for estimating average and instantaneous cutting force coefficients.

3.4.5. The Finite Element Model

Finite Element Mesh

The geometry was simplified to a 2-dimensional domain to reduce its computational cost. Running it as a 3-dimensional domain would demand large computational resources. Pednekar et al. (2004) reported a three-dimensional simulation using ALE adaptive meshing, taking eight days to run using four 1.3GHz processors. The workpiece was modelled using four-node bilinear (CPE4R) isoparametric quadrilateral elements and a plane strain assumption for the deformations. A comparison between plane strain, plane stress and 3-D models was reported by Pednekar et al. (2004) as shown in Figure 3.18. The tool was modelled as a rigid body due to its relatively high stiffness. A penalty

tangential behaviour was adopted to model the friction between the tool and the chip. A friction coefficient of approximately 0.11 reported by Itoigawa et al. (2006) for lubricated machining was used.

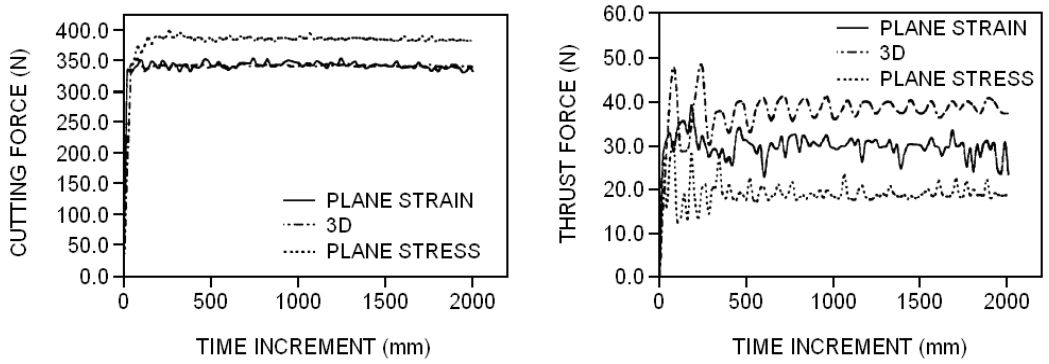

Figure 3.18. (a) cutting force and (b) thrust force comparison between 2D plane strain and stress and 3-D models, by Pednekar et al. (2004).

Explicit Dynamic Analysis

The explicit dynamic analysis algorithm used in all the simulations was originally developed for high speed dynamic problems. It also handles complex contact and material properties very well. In this algorithm, the equation of motion (Hibbitt, 2006),

$$[M]\{\ddot{u}\}+[C]\{\dot{u}\}+[K]\{u\}=\{P\}, \tag{3.29}$$

for the domain is integrated using the explicit central difference integration rule,

$$\dot{u}^{(i+1/2)}=\dot{u}^{(i-1/2)}+\frac{\Delta t^{(i+1)}-\Delta t^{i}}{2}\cdot\ddot{u}^{(i)}, \tag{3.30}$$

$$u^{(i+1)}=u^{(i)}+\Delta t^{(i+1)}\cdot\dot{u}^{(i+1/2)}, \tag{3.31}$$

where $[M]$ is the lumped mass matrix, $[K]$ is the stiffness matrix, $\{P\}$ is the applied load vector, u is the displacement, the superscript (i) is the increment number, while $(i+1/2)$ and $(i-1/2)$ are the mid-increment values, Δt is the time increment and $\dot{u}$ is the velocity vector while $\ddot{u}$ is the acceleration vector.

The explicit method determines the solution by explicitly advancing the kinematic state from the previous increment as opposed to an iterative process (Hibbitt, 2006). In the first increment, the accelerations are defined as,

$$\ddot{u}^{(i)} = \left[M\right]^{-1} \cdot \left\{P^{(i)}\right\}, \tag{3.32}$$

where the lumped mass matrix is a diagonal element matrix, which makes the process computationally efficient.

The central difference operator is not self-starting since the value of the mean velocity $\dot{u}^{(-1/2)}$ is not defined. Therefore, the initial values (unless otherwise specified) for the velocity and acceleration are set to zero. Hence the following condition is specified,

$$\dot{u}^{\left(+\frac{1}{2}\right)} = \dot{u}^{(0)} + \frac{\Delta t^{(0)}}{2}\ddot{u}^{(0)} \tag{3.33}$$

Substituting equation (3.33) into (3.30) gives an expression for $\dot{u}^{(-1/2)}$ as,

$$\dot{u}^{\left(-\frac{1}{2}\right)} = \dot{u}^{(0)} - \frac{\Delta t^{(0)}}{2}\ddot{u}^{(0)} \tag{3.34}$$

These provide the nodal calculations and element calculations are performed using the strain rate to calculate the strain increments and the stresses from constitutive equations. The explicit algorithm was the preferred method as it has the advantages of computational efficiency when dealing with large deformation and highly non-linear problems as machining. In addition to its efficiency, its inbuilt ALE adaptive meshing formulation is robust (Hibbitt, 2006).

Arbitrary Lagrangian-Eulerian (ALE) Adaptive Meshing

The ALE adaptive meshing feature was used in all the simulations, to simulate chip separation and to maintain a high-quality mesh through out the analysis. In ALE adaptive meshing, the mesh can be converted to a pure Eulerian or pure Lagrangian formulation or can be assigned a different motion, at which

point it is termed ‘‘Sliding’’ (Hibbitt, 2006). The ALE adaptive meshing formulation on Abaqus performs two steps:

- Meshing. During this stage, a new mesh is created at a set number of simulation increment intervals. This frequency was set to one by default due to the Eulerian region defined (Figure 3.19) and also spatial mesh constraints. During the meshing stage, the new mesh is found by sweeping iteratively over the domain and moving nodes to satisfy the specified meshing objective. There are two types of meshing objectives, which the algorithm takes as priority when creating a new mesh. The first is a uniform mesh smoothing objective, where the aim is to keep mesh distortion to a minimal, while improving element aspect ratios. This is better suited for domains without Eulerian boundary regions. The second objective is a graded mesh smoothing objective, where the aim is to keep the initial mesh gradation constant. This obviously is better suited for domains with one or more Eulerian boundary regions. Though element distortion is minimized, the aspect ratio is approximately kept the same. In a typical sweep when creating the new mesh, a node is moved by a fraction of the characteristic length of its surrounding elements. There are three smoothing methods used to determine the new location of the nodes. These smoothing methods are: volume smoothing, Laplacian smoothing and equipotential smoothing. The default smoothing method is volume smoothing, which was adopted in all the simulations carried out. In the volume smoothing, a new node location is obtained by computing a volume-weighted average of the element centres in the elements surrounding the node. Laplacian on the other hand, calculates the new location using the average of the position of each of the adjacent nodes connected by an element edge to the node in question. While equipotential smoothing is more complex, as it is a high-order method that relocates a node using weighted average of the positions of the nearest eight nodes (for 2D domain) and eighteen nodes (for 3D domain). To improve the mesh quality of ‘‘Sliding regions’’ a mesh sweep was performed three times.
- Advection step. At this stage, the material and element variables from the previous mesh are remapped/transferred to the new mesh. The second-order

advection based on the work of Van Leer (1971), which uses the concept of upwind scheme was employed by default for the simulations. First, a linear distribution of the variable, φ in each old element is obtained in a process called 'flux-limiting' (Hibbitt, 2006). Secondly, these distributions are integrated over each new element. Finally, the value of the variable for the new element is obtained by dividing the value of each integral by the new element volume. During the mesh motion, the state variables are conserved including the mass and energy (Pantale, 2004) i.e.,

$$\frac{D\varphi}{Dt} = \frac{\partial \varphi}{\partial t} + \hat{\upsilon}_i \frac{\partial \varphi}{\partial x} = 0, \tag{3.35}$$

where $\hat{\upsilon}_i$ is the mesh velocity and i is the increment number.

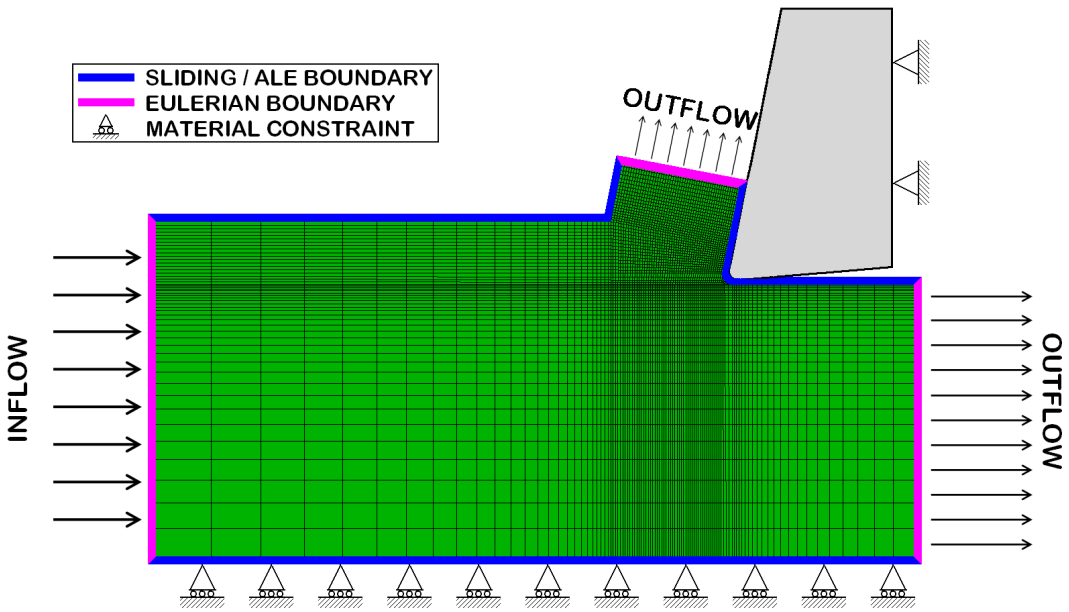

Figure 3.19. The ALE region boundaries and boundary conditions.

3.4.6. Model Geometry and Boundary Conditions

The geometry of the domain according to the study carried out by Ko et al. (Ko, 2002) is given in Tables 3.4 and 3.5. The specified mesh regions and boundary conditions applied to the workpiece and cutter are shown in Figure 3.19.

Table 3.4. HSS end-mill tool geometry with four flutes

HSS end mill with four flutes	
Tool diameter, $D\,(\mu\text{m})$	10,000.0
Rake angle (Deg.)	11.0
Helix angle (Deg.)	0.0
Clearance angle (Deg.)	5.0
Edge radius, $r_{edge}\,(\mu\text{m})$	5.0

Table 3.5. Cutting conditions

Aluminium 2014-T6	
Axial depth, a (μm)	500.0
Radial depth, $r_{doc}\,(\mu\text{m})$	3,000.0
Entry angle (rads)	1.97
Exit angle (rads)	π
Feed, $s_t\,(\mu\text{m})$	37.5
Spindle speed (rev/min)	1000.0

Boundary Conditions

The boundary conditions applied to the material and also to the mesh are shown in Figure 3.20. The mesh boundary conditions are either spatially stationary, (Eulerian region), sliding (ALE region) or fixed to material (Lagrangian region).

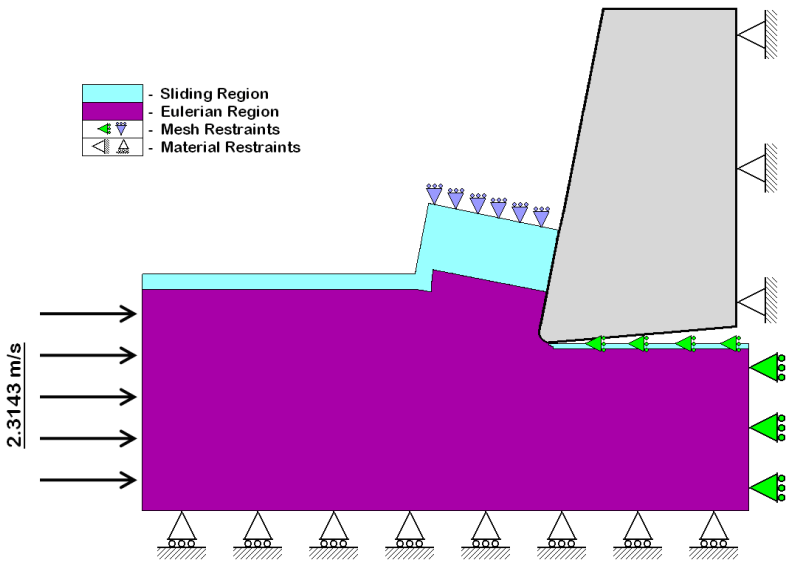

Figure 3.20. Mesh and material boundary conditions.

Material Properties

The material used in the simulation was Aluminium 2014-T6 and its properties are given in Tables 3.6 & 3.7.

Table 3.6. Material Elastic Properties

Aluminium 2014-T6 - Elastic Properties	
Density, ρ $\left(\mathrm{Kgm}^{-3}\right)$	2800
Young's Modulus, E (Pa) e+10	6.98203
Poisson Ratio	0.33425

Table 3.7. Material Plastic Properties

Yield Stress, S (Pa) e+08	**Plastic Strain, ε**
3.2400	0.0
3.5370	0.00056
3.6887	0.00096
3.7714	0.00136
3.8404	0.00176
3.8611	0.00216
3.8818	0.00236
3.9024	0.00276
3.9300	0.00316
3.9507	0.00336
3.9748	0.00376
3.9921	0.00416
4.0231	0.00456
4.0334	0.00496
4.0472	0.00536
4.0507	0.00576
4.0334	0.00496
4.0472	0.00536
4.0507	0.00576

Modelling Assumptions

During machining as explained earlier the tool and workpiece experience different vibrations, which can grow significantly in what is called regenerative

chatter. This in turn affects the undeformed chip thickness. In the simulations, it was assumed that the cutting process was stable and vibrations were negligible, an assumption made when conducting calibration experiments.

The actual tool modelled has a helix angle of 30 degrees, however due to such a small axial depth of cut of 0.5mm it was assumed to be zero. In order to model a tool with helix angle, a three-dimensional domain would be required.

When simulating the end milling cutting process as a two-dimensional domain, the friction experienced on the end face of a flat end-mill rubbing against the surface perpendicular to the tool axis is not included in the simulations.

The cutting edge was modelled as perfectly round with a radius of $5\,\mu m$. The actual edge radius of the tool can only be obtained by measuring it directly from the tool or obtaining it from the manufacturers. Strenkowski et al. measured an average edge radius of $50\,\mu m$ (Strenkowski, 2002), while Ranganath et al. (2007) measured radiuses ranging from $15\,\mu m$ to $72\,\mu m$. This however can quickly create errors in the result as shown in the next section. Moreover, during machining, there is the chance of erosion of the cutting edge, thereby changing its original shape.

Tool runout was ignored in the model. Tool runout would cause variations in the peak in the force measured. Another factor that could affect the similarities of the measured cutting forces per flute is the fact that the flutes might not exactly be of the same geometry and also the pitch angles might vary slight. However, the tool flutes were assumed to be perfectly identical.

3.4.7. Results and Discussions

The simulations were conducted successfully and an example of the steady stress state of the workpiece is shown in Figure 3.21. The primary and secondary shear zones are seen with the highest stress area and the residual stress is seen trailing further along the machined surface. From these simulations the cutting forces in directions 1 and 2 (refer to Figure 3.21) in the local coordinates which correspond to the tangential and radial cylindrical coordinates respectively, are

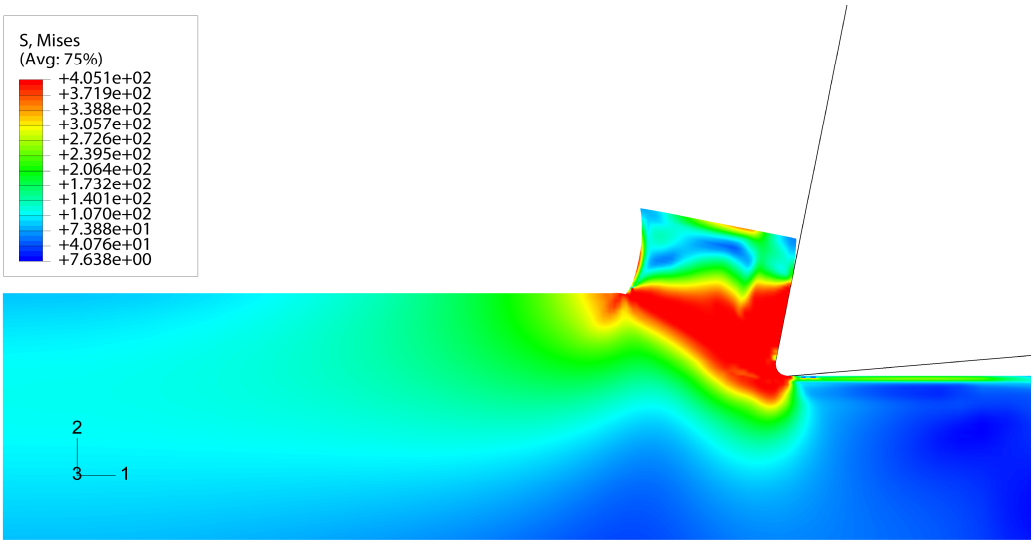

Figure 3.21. von Mises stress distribution for the milling simulation.

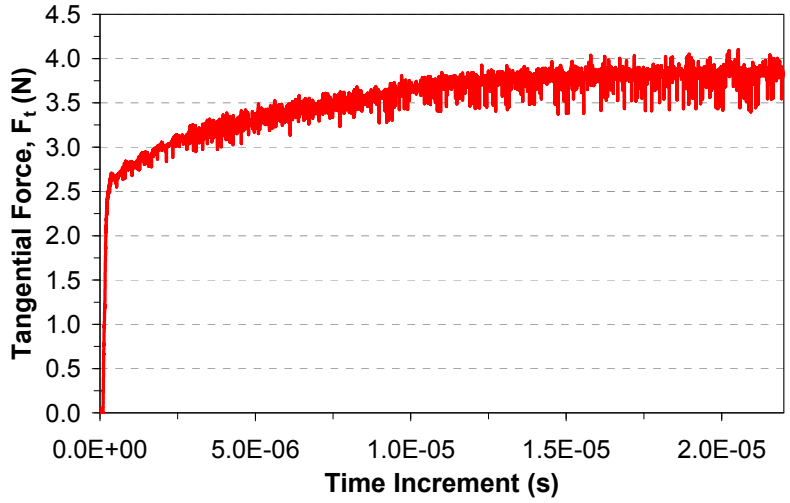

(a) Tangential force

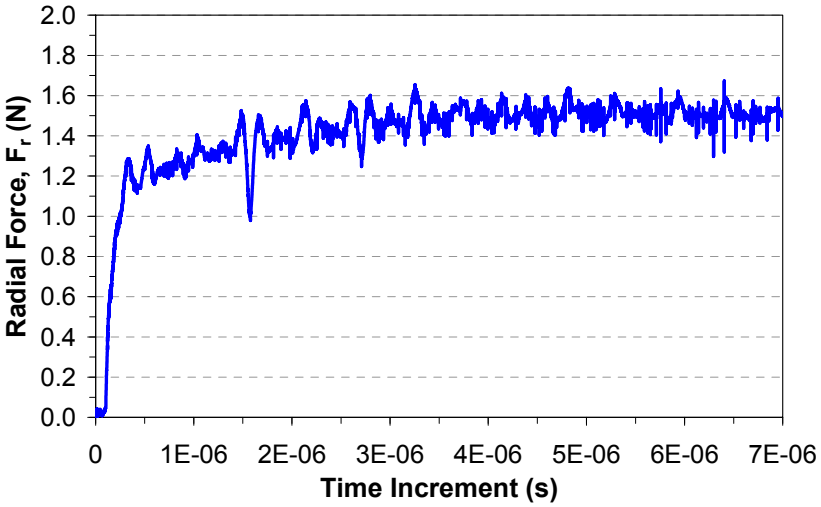

(b) Radial force

Figure 3.22. Convergence of forces on FEM.

collated and shown in Table 3.8. Figures 3.22 a and b show the convergence of the cutting forces in the simulation for $h = 10.602\mu m$.

A plot of these forces against the undeformed chip thickness, h gives an indication of the effect the edge radius has on the cutting force 'size effects' (Figure 3.23 a and b). The ploughing or rubbing of the edge radius adds to the residual stress clearly visible on the machined surface. To further show the influence the edge radius has on the force, it was changed from $5\,\mu m$ to $7.5\,\mu m$. The influence of the larger edge radius can be seen to have increased with the increase in the radius, especially the tangential cutting force, where the curve is seen to approach a constant tangential cutting force value as the chip thickness approaches zero. This graph is actually the relationship described in exponential cutting force model in equation (3.26).

Table 3.8. FEA and calculated cutting force results for feed, $s_t = 37.50\mu m$

ϕ (deg)	ϕ (rads)	$h\,(\mu m)$	Tangential Force, $F_t(N)$	Radial Force, $F_r(N)$	$F_x(N)$	$F_y(N)$
0.0	5.12	34.369	11.047	0.719	4.419	10.125
1.0	5.14	34.102	10.960	0.721	4.559	9.967
2.0	5.16	33.825	10.873	0.724	4.694	9.807
3.0	5.18	33.537	10.784	0.729	4.825	9.644
4.0	5.19	33.239	10.694	0.735	4.951	9.479
5.0	5.21	32.931	10.604	0.742	5.072	9.312
7.5	5.25	32.117	10.369	0.764	5.353	8.881
10.0	5.30	31.242	10.121	0.790	5.598	8.432
12.5	5.34	30.308	9.855	0.818	5.804	7.965
15.0	5.39	29.316	9.568	0.846	5.966	7.480
17.5	5.43	28.268	9.256	0.874	6.082	6.977
20.0	5.47	27.166	8.920	0.901	6.149	6.462
25.0	5.56	24.810	8.187	0.957	6.139	5.417
30.0	5.65	22.265	7.403	1.027	5.957	4.395
35.0	5.73	19.550	6.604	1.114	5.635	3.443
40.0	5.82	16.687	5.787	1.206	5.182	2.575
45.0	5.91	13.696	4.892	1.308	4.554	1.787
50.0	6.00	10.602	3.843	1.536	3.686	1.086

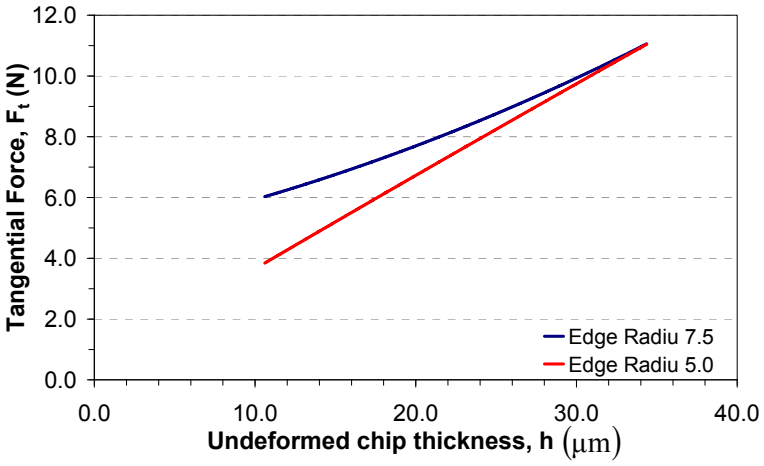

(a) Tangential force

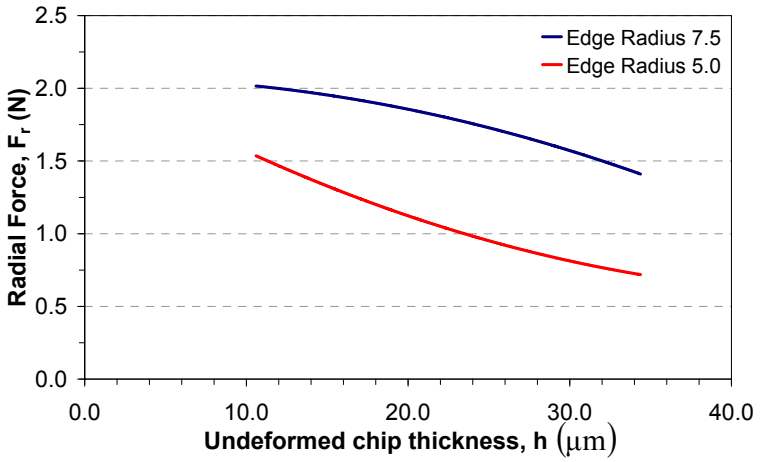

(b) Radial force

Figure 3.23. Cutting forces showing effects of edge radius.

Obtaining Instantaneous Cutting Force Coefficients

Using the cutting force expression in equations (3.25) and (3.26 a, b, and c), the instantaneous uncut chip thickness, *h* (given in Table 3.8) and the corresponding tangential and radial forces, the instantaneous cutting force coefficients are extracted. It should be noted however that the proposed approach is demonstrated here with the cutting edge radius of 5.0 μm assumed. With this edge radius being the cause of the size effect, its accurate measurement is required for the extraction of precise instantaneous cutting force coefficients. For completion, the cutting forces for smaller uncut thickness are extrapolated using a second order polynomial curve fitting of the data given in Table 3.8 and the extracted instantaneous cutting force coefficients are plotted in Figures 3.24 a and b.

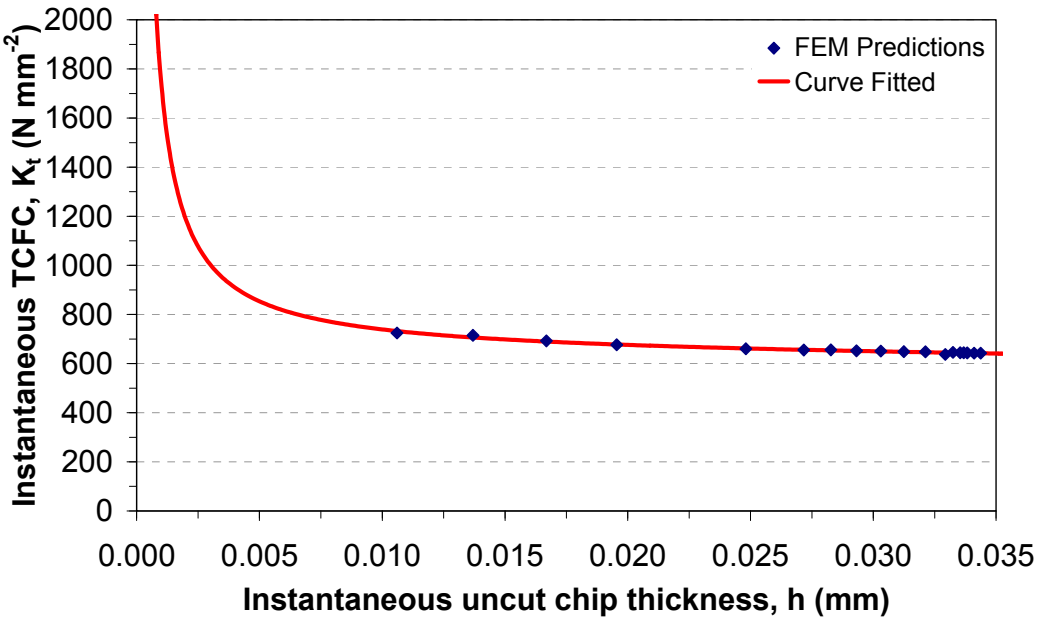

(a) Instantaneous Tangential CFC

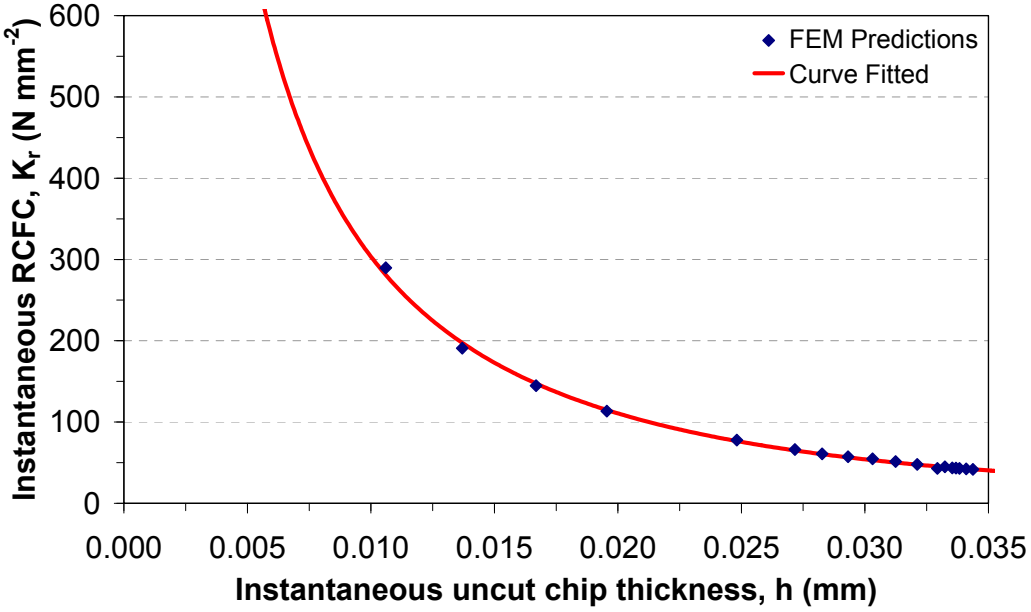

(b) Instantaneous Radial CFC

Figure 3.24. Instantaneous Cutting Force Coefficients.

The expression for the instantaneous cutting force coefficients in equation (3.28) are fitted to the FEM results as shown in Figure 3.24, where,

$$K_p = C_{p1} h + C_{p2} + \frac{C_{p3}}{h}, \qquad (p = t, r),$$

and C_{p1}, C_{p2}, C_{p3} are constants obtained using least squares method as,

$C_{t1} = -757.9939,$ $C_{r1} = 1167.9507,$

$C_{t2} = 635.9116,$ $C_{r2} = -117.2510,$

$C_{t3} = 1.1078,$ $C_{r3} = 4.0915$

The instantaneous cutting force coefficients were also obtained by Wan et al. (2007), however with the use of experimental results.

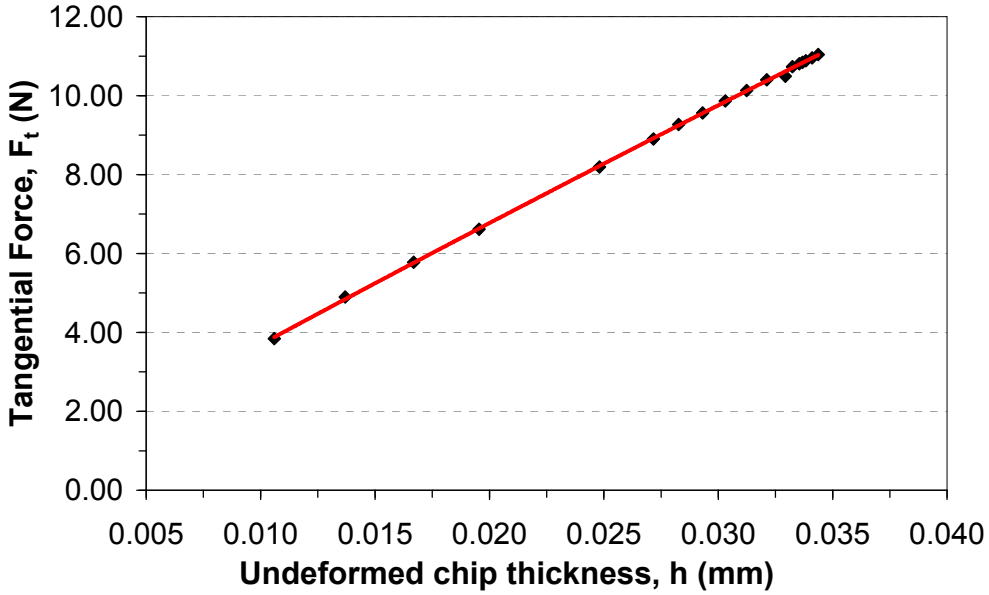

(a) Tangential force

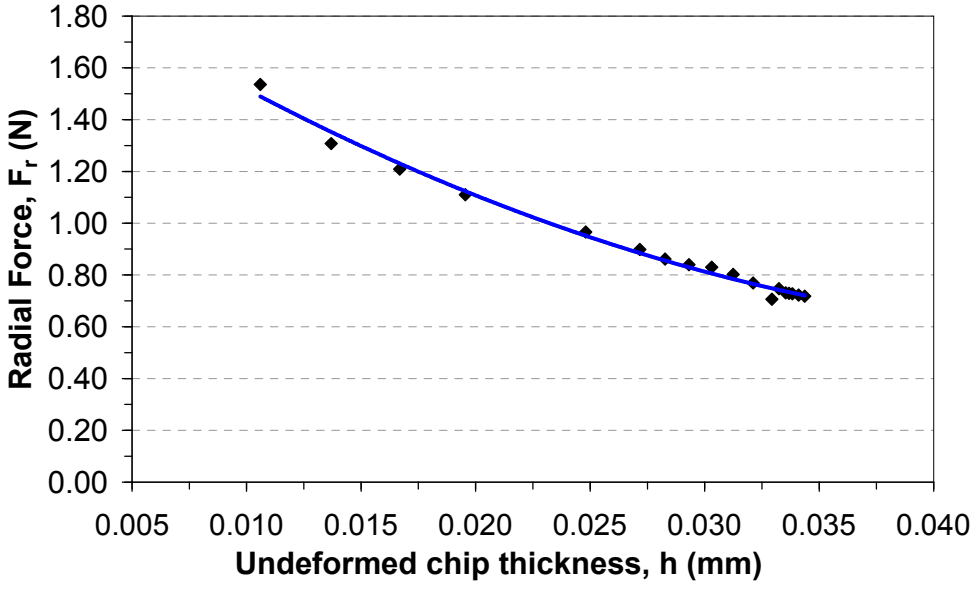

(b) Radial

Figure 3.25. Radial and Tangential forces against undeformed chip thickness.

Obtaining Average Cutting Force Coefficients

Figure 3.25 shows the radial and tangential forces plotted against the undeformed chip thickness. This is therefore used to calculate the cutting force for different smaller feeds as explained in section 3.4.2 and the steps laid out in the flow chart in Figure 3.17. Following the classical approach used for the mechanistic model (detailed in section 3.3.1), the relationship between the forces and the feed per tooth is obtained by taking an average of the cutting forces over the tooth period according to equation (3.9). In the classical approach detailed in section 3.3.1, the cutting forces are sampled over many tooth periods and averaged out for different feedrates. In this case the cutting forces for a tooth period are first calculated by using the FEM results in Table 3.8. This is simply done by fitting a curve to the FEM results as shown in Figure 3.25 and simply calculating the cutting forces for all tool rotation angles ϕ, required for the tooth period; this is then averaged out to obtain the average cutting forces for the corresponding feed used in equation (3.5). Figure 3.26 shows the average cutting forces in Cartesian global coordinates against the feed, s_t. This relationship is different from the one in Figure 3.25 as they are in different coordinates system.

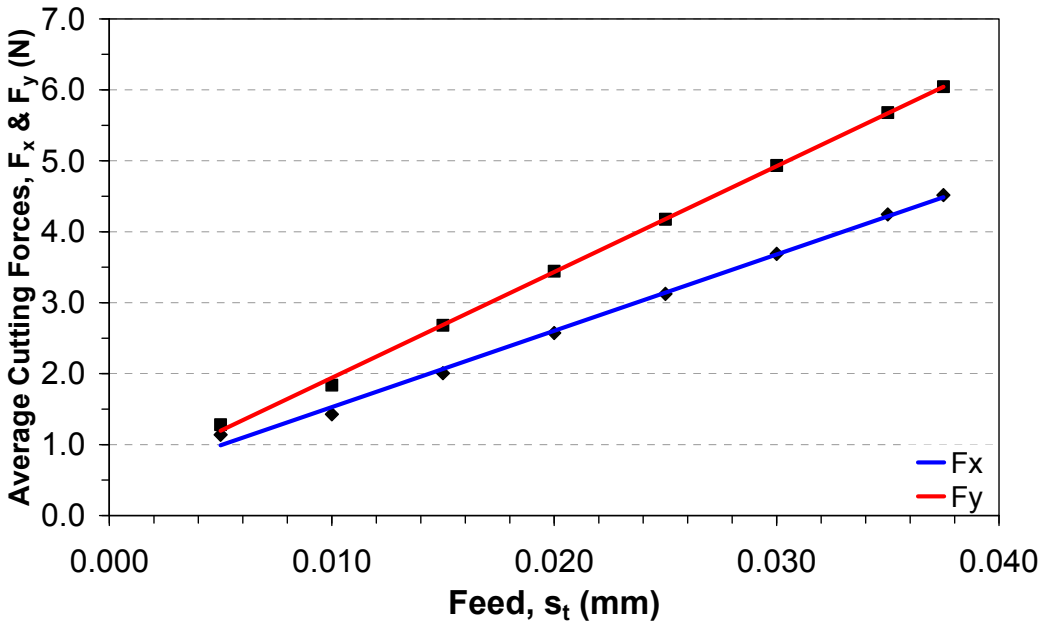

Figure 3.26. Average cutting forces from FEM results.

Hence from the two linear systems of equations (3.13) and (3.22), the force coefficients are obtained in equation (3.25) as,

$K_{te} = 1.35\ \text{Nm}^{-2}$, $K_{tc} = 1729.101\ \text{Nm}^{-2}$,

$K_{re} = 1.288\ \text{Nm}^{-2}$, $K_{rc} = 746.332\ \text{Nm}^{-2}$.

FEM Cutting Force Coefficients Validation

To validate the coefficients, the linear Edge-Force model was programmed in FORTRAN. Quick analytical simulations were carried out using the cutting conditions similar to the ones reported by Ko et al. (2002) and the results are shown in comparison in Figures 3.27 – 3.29.

The trend and also the magnitudes of the experimental results reported by Ko et al. (2002) are clearly reflected in the predictions obtained using the coefficients extracted from the FEM simulations. This was assuming the coefficients were not dependent on the axial depth of cut, which should be the case for a flat end-milling tool with a small constant helix angle. It is obvious that the accuracy of the average cutting force coefficients, $K_{\bullet c}$, is mainly dependent on the slope of the graph in Figure 3.26; while the accuracy of the edge force coefficients, $K_{\bullet e}$ is dependent on the point the graph crosses the y-axis. There are slight over estimations on the Fy's. It is however believed that this is due to the helix angle not being equal to zero on the actual tool as assumed in the FEM models. From these results it is evident that with just the relationship between both the tangential and radial forces and the instantaneous uncut chip thickness, the average cutting force coefficients can be extracted with satisfactory accuracy. To model the variations observed in the peaks the tool runout parameters as defined by Wan (2007) are required. In fact, the approach proposed here deals with the terms in the cutting force model that are not influenced by the tool runout. These terms were separated by Wan et al. (2007). The main difference in this approach compared to other available methods is that it does not require experimental results and yet includes the ploughing forces.

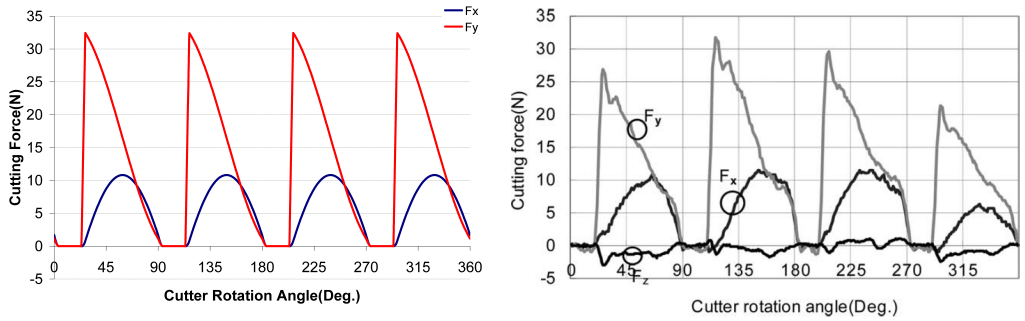

(a) (b)

Figure 3.27. (a) Predicted and (b) experimental cutting forces for feed per tooth 0.0375mm, r_{doc} = 3.0mm, a = 0.5mm, Ω = 1000rpm by (Ko, 2002).

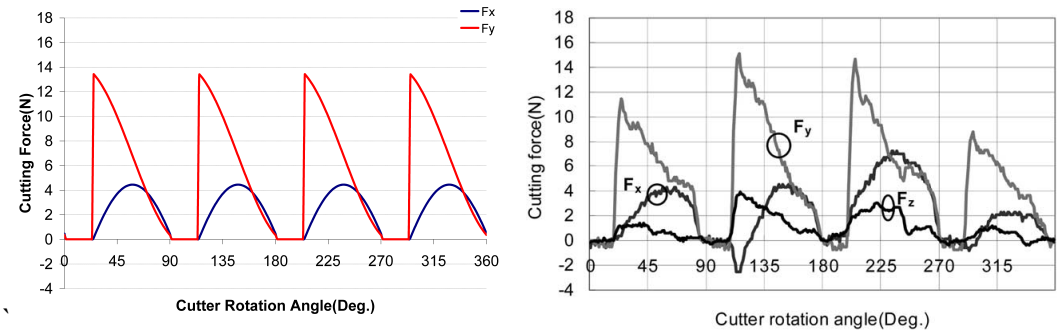

(a) (b)

Figure 3.28. (a) Predicted and (b) experimental cutting forces for feed per tooth 0.0375mm, r_{doc} = 3.0mm, a = 0.2mm, Ω = 1000rpm by (Ko, 2002).

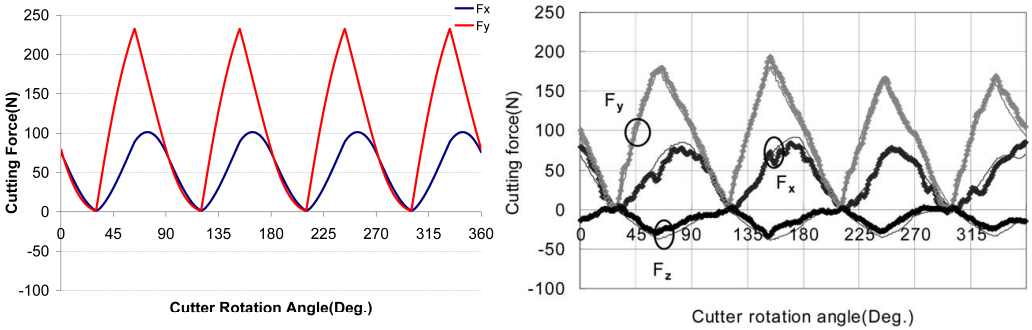

(a) (b)

Figure 3.29. (a) Predicted and (b) experimental cutting forces for feed per tooth 0.0375mm, r_{doc} = 2.5mm, a = 5.0mm, Ω = 2000rpm by (Ko, 2002).

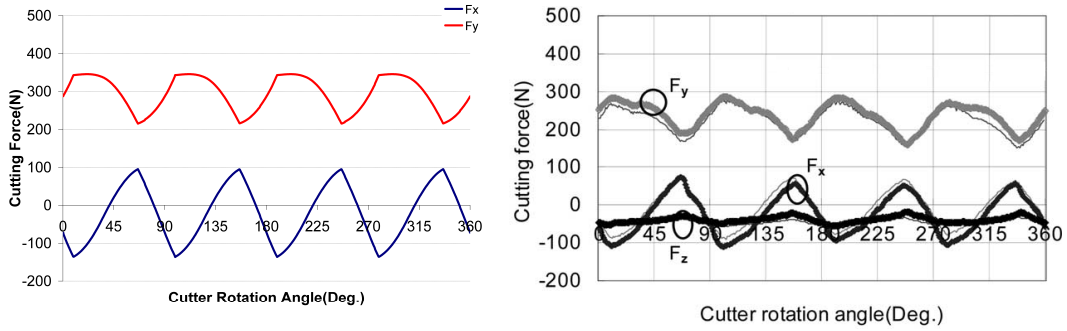

(a) (b)

Figure 3.30. (a) Predicted and (b) experimental cutting forces for feed per tooth 0.0375mm, r_{doc} = 7.0mm, a = 5.0mm, Ω = 1000rpm by (Ko, 2002).

3.5. Summary

In this chapter, the linear edge force model was investigated and used to calibrate the cutting force coefficients for the tool to be used through the course of this thesis. The accuracies of the coefficients were shown in predicted cutting forces. Improvements to the linear edge force model were presented to better model the influence of the size effects and comparisons with experimental results were shown. An FEM approach to extracting the cutting force coefficients in milling was later presented with experimental comparisons. These comparisons show satisfactory accuracies.

Chapter 4

Tool and Workpiece Dynamics

4.1. Introduction

The tool and workpiece dynamics define the structure's behaviour under dynamic loadings. The dynamics consist of its damping, stiffness and mass parameters. Damping is the dissipative factor present in every real-life system/structure. Its influence is more important in some structural analyses than others, hence its neglect or imprecision in these analyses can render these analyses unacceptable; while in other analyses, the analyst might get away by applying an approximate damping ratio of 0.05 or less. Unlike the well developed mass/inertia and stiffness forces, the damping forces are at present extracted through experiments known as modal testing/analysis. This is because the physics behind the damping forces are not fully understood especially for a wide range of systems. It is however always desirable for an analyst to be able to predict the damping ratio (either analytically or numerically) for any given geometry without having to rely solely on experimental results.

Numerous studies in which the approximation of the damping parameters is not acceptable and are identified experimentally are reported in the literature. Of these studies are the studies on the dynamic modelling of metal cutting process. Due to the dynamic nature of the process, a complete and accurate modelling of

the workpiece and tool vibrations experienced during metal cutting process would require the use of accurate damping parameters as reported by (Tobias, 1958, Budak, 1998). Other studies requiring the damping parameters include studies on blast and accidental impact modelling and so on (Kaewunruen, 2005).

A significant contribution at the early development of modal analysis was proportional damping model. It was first proposed by Lord Rayleigh in 1878, where he indicated that if the viscous damping matrix is proportional to mass and stiffness matrices (the damping forces are proportional to the kinetic and potential energies of the system) then it can be expressed (Rayleigh, 1878) as,

$$[C] = \alpha_0 [M] + \alpha_1 [K], \tag{4.1}$$

where α_0 and α_1 are real positive constants. The model is termed 'Rayleigh damping' or 'classical damping'. The significance of this model is that the damped system would have the same mode shapes compared to its undamped counterpart, thus the system is said to possess 'classical normal modes'. In proportional damping model the viscous damping matrix in the same manner as the mass and stiffness matrices, can be generalized using the system's modal matrix or eigenvectors, $\{\Psi\}$. This considerably simplifies the dynamic analysis by allowing the multi degree of freedom (MDoF) system to be represented by a series of uncoupled single degree of freedom (SDoF) systems.

The equation of motion for a multi degree of freedom (MDoF) system can be expressed as,

$$[M]\{\ddot{x}(t)\} + [C]\{\dot{x}(t)\} + [K]\{x(t)\} = \{F(t)\}, \tag{4.2}$$

where $[M]$ is the mass matrix, $[C]$ is the viscous damping matrix, $[K]$ is the stiffness matrix, $\{\ddot{x}(t)\}$, $\{\dot{x}(t)\}$, $\{x(t)\}$ $\{F(t)\}$ are the acceleration, velocity, displacement and excitation force vectors respectively.

In 1960, Caughey and O'Kelly (1960) provided a generalization of Rayleigh's condition for discrete systems in form of the series,

$$[C] = [M]\sum_{u=0}^{L-1} \alpha_u \left([M]^{-1}[K]\right)^u, \tag{4.3}$$

where L is the number of identified modes used in the curve fitting, α_u are real positive constants obtained through using experimentally identified damping parameters. The Rayleigh damping model is the first two series of the expansion. In 1965, Caughey and O'Kelly (1965) derived the condition which the system matrix must satisfy for the system to have classical normal modes. In this condition, it is said that a system defined by equation (4.2) can possess classical normal modes if and only if the system matrices satisfy the following relationship,

$$[K][M]^{-1}[C] = [C][M]^{-1}[K] \tag{4.4}$$

Based on this result, they also proved that the series expansion in equation (4.3) is the necessary and sufficient condition for the existence of classical normal modes. Based on the limitation posed for systems with a singular mass matrix, the three matrices can be treated as equal and can be interchanged as reported in (Adhikari, 2000) as,

$$[K][C]^{-1}[M] = [M][C]^{-1}[K], \tag{4.5}$$

$$[M][K]^{-1}[C] = [C][K]^{-1}[M] \tag{4.6}$$

The dynamic parameters for a structure are identified through modal testing and used in different time and frequency domain analysis. Frequency domain analyses are general preferred due to their computational time compared to time domain analyses. The required computational time is usually much shorter compared to time domain analysis, owing mainly to the lack of spatial and time discretisation. This efficient computational time coupled with the publication of Cooley and Turkey's invented Fast Fourier Transform (FFT) algorithm (Cooley, 1965), the frequency response of a structure can be computed from the measurement of given input and output responses. The first method of experimental modal analysis was however proposed by Kennedy and Pancu (1947), though the proposed method was largely forgotten until the invention of the FFT algorithm by Cooley. There has been other different modal testing

methods proposed, however one of the most common involves the excitation of the structure using an instrumented hammer and measurement of the response with the use of a transducer (either laser based vibration transducers or accelerometers). The impact excitation and the vibration response of the structure are measured and transformed into 'frequency response functions' (FRFs) using a Fourier Analyzer. Subsequently, the structure's dynamic parameters are extracted from the measured FRF. Great contributions on the identification of the dynamic parameters are reported by (Ewins, 1984, Allemang, 1986, Mitchell, 1986), with a good review of the developments reported by (Brown, 1982).

Other notable developments are methods proposed to reduce or eliminate the systematic and noise errors which adversely affect measured FRFs (Sanliturk, 2005). One of these systematic errors is the so called 'mass loading effect' which occurs when an accelerometer is used as the transducer. The accelerometer directly changes the dynamics of the system and causes the measured resonant frequencies to deviate from their correct values. Methods of correcting of the mass loading effects on the direct FRFs are reported by (Ewins, 1984, Cakar, 2005).

The frequency response function (FRF) or 'transfer function' (TF) is used in a wide range of studies on the analysis of dynamic response of linear systems, including the milling process. The transfer function is used along with the cutting force model as explained later to predict stability margins in milling. The accuracy of the predicted stable region relies on the transfer function identified at the cutter-workpiece contact zone.

Thus this chapter is structured as follows; the experimental method for structural damping identification is discussed and a new numerical approach for its prediction is proposed in the second section; a new FEM and Fourier approach to identifying the structures transfer function is presented in section three; while the applications of both the proposed approach to predicting damping and also the presented FE approach are shown for thin wall machining in section four. A brief review of the well developed model for predicting stable margins due to Hopf bifurcations is also given in section three. A more in-depth review of this model is later given in subsequent chapters.

4.2. Prediction and Modelling of Damping Parameters

In this section, a novel approach proposed by Adetoro et al. (2009a) that uses identified damping parameters for a known geometry to predict the damping parameters for any given geometry with a different thickness is discussed. This approach eliminates the need for experimental modal analysis otherwise used to identify these damping parameters. It is envisaged that this approach would further lead to the understanding of the physics behind the damping forces, as it identifies certain trends in the effect the geometry has on the damping parameters. A modelling approach similar to Caughey's series is proposed, to better model the damping parameters. The prediction and damping models are validated using experimentally identified damping parameters and time domain finite element (FE) simulations of dynamic vibrations for various examples.

4.2.1. Experimental Modal Analysis

If its assumed that the undamped MDoF system in equation (4.2) is excited sinusoidally by a set of forces, $\{f(t)\}$ all at the same frequency, ω but with different amplitudes and phases and assuming a solution $\{x(t)\}$ exists (Ewins, 1984) of the form,

$$\{x(t)\} = \{X\}e^{i\omega t}, \qquad i = \sqrt{-1}, \tag{4.7}$$

where ω is the natural frequency of the system and $\{X\}$ is a constant, then (4.2) is expressed as,

$$\left([K] - \omega^2[M]\right)\{\Psi\} = \{0\}, \tag{4.8}$$

which represents an eigenvalue problem, where ω_n^2 is the eigenvalue (undamped natural frequency squared) and $\{\Psi\}$ is the eigenvector. The characteristic equation of the system is simply,

$$\left|[K] - \omega_n^2[M]\right| = 0 \tag{4.9}$$

The stiffness and mass matrices are currently in their spatial coordinates and using the extracted eigenvectors, the spatial models can be transformed into their modal model in generalised coordinates. This is done by pre-multiplying the matrices by the transpose of the eigenvectors and post multiplying by the eigenvectors. This transformation from the spatial coordinates into the generalized coordinates is one of the main advantages of modal analysis as it can be used to uncouple the equation of motion (equation 4.2) for large system. The uncoupled modes can subsequently be treated in the same way as a single degree of freedom (SDoF) system. This is known as the orthogonality property of an undamped MDoF system or system with proportional damping. The orthogonality property also allows for modal superposition which is later used in FEM simulations.

The equation of motion is also represented in Laplace transform domain as follows,

$$\left([M]s^2+[C]s+[K]\right)\left\{\tilde{X}(s)\right\}=\left\{\tilde{F}(s)\right\}, \tag{4.10}$$

or,

$$[D(s)]\left\{\tilde{X}(s)\right\}=\left\{\tilde{F}(s)\right\} \tag{4.11}$$

Hence, the receptance frequency response function (FRF) of the system is defined as,

$$[G(s)]=[D(s)]^{-1}, \tag{4.12}$$

which rearranges to,

$$[G(s)]=\frac{\text{adj}[D(s)]}{\det[D(s)]}, \tag{4.13}$$

where $G(s)$ is the transfer function (TF) matrix of the system and for a single degree of freedom, $\det[D(s)]$ is known as the 'characteristic equation' of the system (He, 2001). The 'characteristic equation' is shared by each element in the transfer function matrix. Therefore, the transfer function matrix can be expressed by its partial fraction expansion as (He, 2001),

$$G_{rl}(s) = \sum_{p=1}^{L} \left(\frac{R_{rlp}^{+}}{s - s_p^{+}} + \frac{R_{rlp}^{-}}{s - s_p^{-}} \right), \tag{4.14}$$

where the complex roots are given as,

$$s_p^{+}, s_p^{-} = -\zeta_p \omega_{np} \pm \sqrt{1 - \zeta_p^2}\, \omega_{np} i \tag{4.15}$$

where ζ_p is the damping ratio, where only underdamped cases are studied in this thesis (i.e. $\zeta_p < 1$), p is known as the mode number. The complex roots s_p^{+} and s_p^{-} and the complex residues R_{rlp}^{+} and R_{rlp}^{+} are a conjugate pair. The residues are obtained from the partial fraction expansions as detailed by He and Fu (He, 2001).

Hence,

$$G_{rl}(s) = \sum_{p=1}^{L} \left[\frac{(\alpha_{rlp} + \beta_{rlp} s)}{(s^2 + 2\zeta_p \omega_{np} s + \omega_{np}^2)} \right], \tag{4.16}$$

where L is the total number of modes identified experimentally, ω_n is the natural frequency of the system, α_{rlp} and β_{rlp} are constants obtained experimentally reflecting the residue of mode p at row r and column l. They are required when extracting the mode shapes experimentally. The mode shapes are however the eigenvectors in equation (4.8), therefore the experimental approach to extracting them is not covered in this thesis. Altintas however proposed an approach in which they can be collected into a residue matrix $[R]_p$ for each mode in order to calculate the mode shapes (Altintas, 2000).

To experimentally measure the direct transfer function G_{rr}, the system is excited at point r (using an instrumented hammer), whilst the accelerometer is placed at point r. Using a Fourier analyser, the accelerance frequency response function (FRF) is extracted for each impact test. This is simply the division of the Fourier transform of the measured time domain input force $f(t)$ and acceleration $\ddot{x}(t)$ i.e.,

$$A(\omega) = \frac{\ddot{X}(\omega)}{F(\omega)} \tag{4.17}$$

The use of accelerometer as the transducer alters the frequency response, hence the error induced in the measured direct FRF is corrected using the expression given by (Cakar, 2005),

$$A_{new}(\omega) = \frac{A(\omega)}{1 - m_{accel} A(\omega)}, \tag{4.18}$$

where $A_{new}(\omega)$ is the accelerance without the effect of the accelerometer mass, and m_{accel} is the mass of the accelerometer.

The FRF or TF is simply the imaginary axis, $i\omega$-axis in the s-plane (i.e. $s = i\omega$). Hence from equation (4.7) we have that,

$$x(t) = Xe^{i\omega t}, \tag{4.19}$$

$$\ddot{x}(t) = (i\omega)^2 Xe^{i\omega t} = -\omega^2 x(t), \tag{4.20}$$

Therefore, the receptance FRF, $G(\omega)$ in terms of accelerance FRF is expressed as,

$$G(\omega) = \frac{X(\omega)}{F(\omega)} = \frac{A_{new}(\omega)}{-\omega^2} \tag{4.21}$$

This gives the transfer function element G_{rr} in equation (4.16), where $s = i\omega$. All the elements in the matrix $[G(\omega)]$ share the same denominator of $\det[D(s)]$. Therefore, assuming there are two modes within the range of frequency extracted by the Fourier Analyzer (i.e. $L = 2$), the direct transfer function can be defined using equation (4.16) as,

$$G_{rr}(s) = \left[\frac{\alpha_{rr1} + \beta_{rr1} s}{s^2 + 2\zeta_1 \omega_{n1} s + \omega_{n1}^2}\right]_{\text{mode 1}} + \left[\frac{\alpha_{rr2} + \beta_{rr2} s}{s^2 + 2\zeta_2 \omega_{n2} s + \omega_{n2}^2}\right]_{\text{mode 2}}, \qquad s = i\omega \tag{4.22}$$

The experimental measurements are analysed using a modal analysis system, which scans the transfer function data for the two amplitudes

corresponding to these modes and the corresponding two frequencies at which the real part of the transfer function is zero. These two frequencies are the natural frequencies of the system. Then the modal analysis system fits a curve to the data with a denominator having a (2×2)-order polynomial, which is then converted to 2 independent second order differential equations according to equation (4.22). Therefore the numerical values of the natural frequency, damping and residue for each mode can be estimated (Allemang, 1986).

To measure element G_{rr}, location r is excited whilst keeping the accelerometer measurement point fixed at l, thereby giving one row or column of the transfer function matrix. The transfer function matrix obtained is symmetric for a linear system. Altintas detailed a method for constructing the full modal matrix of the structure using only one row or column identified experimentally (Altintas, 2000).

4.2.2. Proportional Damping

From Caughey and O'Kelly's condition (explained in section 4.1), for a system to possess classical normal modes we have the conditions given in equations (4.4, 4.5 and 4.6). Therefore using the procedure described in section 4.2.1, the dynamic parameters identified for Case 1C are given in Table 4.3. To experimentally obtain the system's mass, stiffness and damping matrices, the modal matrix or mode shapes are required. Using the experimentally identified residues in equation (4.22), the modal matrix for unity modal mass can be calculated as explained by Altintas (2000). Therefore, the modal mass matrix is simply an identity matrix and the modal stiffness and modal damping are defined as,

$$K_p = \omega_{np}^2, \tag{4.23}$$

$$C_p = 2\omega_{np}\zeta_p \tag{4.24}$$

The modal mass, stiffness and damping matrices are then transformed to spatial coordinates using the modal matrix or mode shapes. This is done by simply

pre-multiplying the matrices by the modal matrix and post multiplying by the transpose of the modal matrix. Therefore equations (4.4), (4.5) and (4.6) are used to show that the system possess classical normal modes in Appendix B and hence that the damping is proportional.

4.2.3. Proposed Damping Prediction Approach

Damping Ratio

The approach discussed in this section was proposed by Adetoro et al. (2009a). It is a quick, simple and yet significantly accurate approach to predicting the damping ratio in terms of the frequency for a given wall using the known damping ratios of a wall with same height (provided only the wall thickness is changed). From a range of extracted structural dynamics, it was discovered that there was a certain trend between the different damping ratios for different wall thicknesses. It was found that a new set of parameters, $\overline{\zeta}_p$ and $\overline{\omega}_p$, can be defined as follows,

$$\overline{\zeta}_p = \frac{\zeta_p^a}{t_a}, \tag{4.25}$$

for damping ratio and

$$\overline{\omega}_p = \frac{\omega_{np}^a}{t_a}, \tag{4.26}$$

for natural frequency, where t_a is the reference current wall thickness, ζ_p^a is the modal damping ratio and ω_p^a is the natural frequency for the reference wall respectively. These parameters ($\overline{\zeta}_p$ and $\overline{\omega}_p$) are then used to predict the damping ratio, ζ_p^b in terms of frequency, ω_p^b for any new geometry (provided only the wall thickness is changed) by simply multiplying $\overline{\zeta}_p$ and $\overline{\omega}_p$ by the new wall thickness t_b as follows,

$$\zeta_p^b = \overline{\zeta}_p \cdot t_b, \tag{4.27}$$

$$\omega_p^b = \overline{\omega}_p \cdot t_b \tag{4.28}$$

It should be noted that ζ_p^b and ω_p^b are not necessarily the precise modal damping and natural frequencies of the new wall. Studying the series in equation (4.3) propose by Caughey (Caughey, 1960), the zeroth order approximation gives,

$$[C_0] = \alpha_0 [M], \tag{4.29}$$

which is not realistic as there the stiffness term has to always exist in what ever level of approximation, hence in an attempt to preserve the stiffness and mass terms a new series is proposed, which is defined as,

$$\zeta_p = \frac{1}{2} \sum_{u=1}^{L/2} \left(\alpha_{2u-1} \cdot \omega_n^{-u} + \alpha_{2u} \cdot \omega_n^{u} \right), \tag{4.30}$$

where the first term expands out to,

$$\zeta = \frac{1}{2} \left(\frac{\alpha_1}{\omega_n} + \alpha_2 \omega_n \right) \tag{4.31}$$

Noting from single degree of freedom systems (He, 2001) that,

$$\omega_n^2 = \frac{K_p}{M_p}, \tag{4.32}$$

$$\zeta_p = \frac{C_p}{2\sqrt{K_p M_p}}, \tag{4.33}$$

where C_p, K_p, and M_p are the modal damping, stiffness and mass respective. This is obtained when the equation of motion of a multi-degree of freedom (equation 4.2) is uncoupled using the eigenvectors obtained from undamped case in the eigenproblem in equation (4.8) as (He, 2001) follows,

$$\boldsymbol{\Psi}^T [M] \, \boldsymbol{\Psi} \cdot \ddot{\mathbf{q}} + \boldsymbol{\Psi}^T [C] \, \boldsymbol{\Psi} \cdot \dot{\mathbf{q}} + \boldsymbol{\Psi}^T [K] \, \boldsymbol{\Psi} \cdot \mathbf{q} = \mathbf{f}, \tag{4.34}$$

where **q** and **f** are the displacement and force vectors respectively in the transformed co-ordinate.

This transforms the whole multi-degree of freedom system into L number of single degree of freedom systems, which are uncoupled. Hence,

$$C_p = \mathbf{\Psi}^T [C] \mathbf{\Psi}, \tag{4.35a}$$

$$M_p = \mathbf{\Psi}^T [M] \mathbf{\Psi}, \tag{4.35b}$$

$$K_p = \mathbf{\Psi}^T [K] \mathbf{\Psi} \tag{4.35c}$$

Therefore, equation (4.31) can be written for the first series as,

$$C_p = \alpha_1 M_p + \alpha_2 K_p, \tag{4.36}$$

which, shows that both mass and stiffness retained in the first series. Expanding the proposed series gives,

$$C_p = \alpha_1 M_p + \alpha_2 K_p + \alpha_3 M_p^{1.5} + \alpha_4 K_p^{1.5} + \alpha_5 M_p^2 + \alpha_6 K_p^2 + \ldots \tag{4.37}$$

Therefore by dividing equation (4.30) through by the wall thickness t_a, as done in equations (4.25) and (4.26) we obtain the following series expansion,

$$\overline{\zeta} = \frac{1}{2} \sum_{u=1}^{L/2} \left(\alpha_{2u-1} \cdot \overline{\omega}^{-u} + \alpha_{2u} \cdot \overline{\omega}^{u} \right), \tag{4.38}$$

where constants α_{2u-1} and α_{2u} are real constants obtained using least squares method. This series expands out in the form,

$$\overline{\zeta} = \frac{1}{2} \left(\frac{\alpha_1}{\overline{\omega}} + \alpha_2 \overline{\omega} + \frac{\alpha_3}{\overline{\omega}^2} + \alpha_4 \overline{\omega}^2 + \frac{\alpha_5}{\overline{\omega}^3} + \alpha_6 \overline{\omega}^3 + \ldots \right) \tag{4.39}$$

Therefore, by dividing the different numerically extracted natural frequencies in equation (4.9) for each identified mode for the new wall thickness by t_b to obtain $\overline{\omega}$ in equation (4.30) and then multiplying the calculated $\overline{\zeta}$ by t_b, the corresponding damping for that mode is obtained.

Damping Matrix

The damping ratio, ζ_p^b in terms of frequency can be readily used directly by most commercial Finite Element (FE) packages, however the damping matrix $[C]$ in equation (4.2) is sometimes required. To obtain the damping matrix, the numerically extracted natural frequency of the new structure for each mode is divided by the wall's thickness t_b, to obtain $\overline{\omega}$ and used in equation (4.38), to calculate $\overline{\zeta}$, which is then multiplied back by the wall's thickness t_b, to obtain the new modal damping ratio for the corresponding mode.

The modal damping C_p is simply calculated in a similar fashion to SDoF using equation (4.33). The damping matrix $[C]$ is finally obtained by pre-multiplying by the modal matrix and then post-multiplying by the transpose of the modal matrix or eigenvectors obtained in equation (4.9). This orthogonal property only applies to systems that possess classical normal modes or proportional damping.

4.2.4. Time Domain Simulation in FEA

The transient modal dynamic analysis on Abaqus was used to validate the proposed approach to predicting damping ratios. Being a very well developed model, the modal dynamic analysis gives the response of a defined domain as a function of time for a given time dependent loading. The response obtained is the linear response of the structure, which is easily extracted once the modes of the system are available. The modes are extracted in a frequency extraction analysis, which utilizes the Lanczos algorithm due to the size of the eigenproblem in equation (4.9). The algorithm is detailed by Grimes et al. (1994) and in Abaqus user manual (Hibbitt, 2006).

The library of elements available in Finite Element Method is well documented in the literature on the Finite Element Method, however for completeness the formulation of the elements used during this thesis are discussed briefly here.

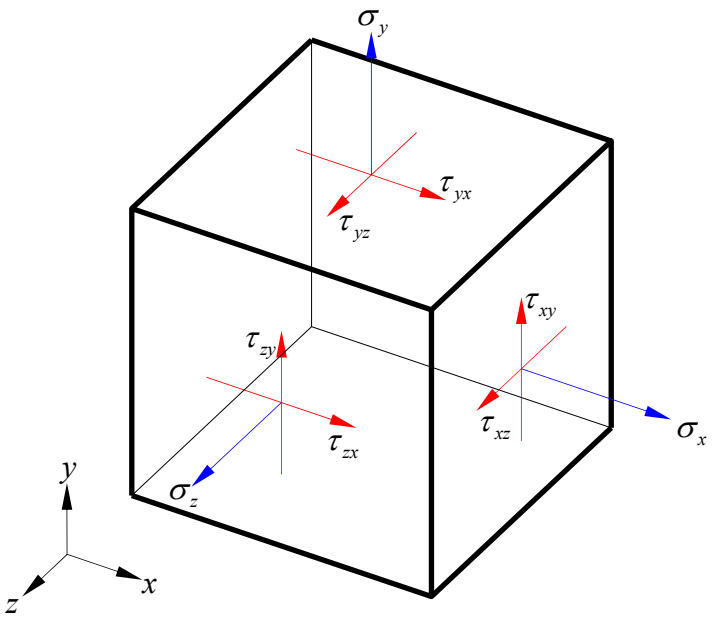

Figure 4.1. 3-D state of stress.

Element Formulation

Isoparametric elements are used through out this thesis, in proposed Finite Element models/simulations. The isoparametric elements use mathematical mapping from a coordinate system called the 'natural' or 'isoparametric' coordinate system to the other called the 'physical' coordinate system. The physical coordinate system is the system in which the domain is defined, i.e. X, Y, Z, (Figure 4.1); while the isoparametric interpolation is defined in terms of the natural element coordinates, i.e. ξ, η, ζ, (Figure 4.2). Second order 20-node brick isoparametric element is used through the course of this thesis. However to demonstrate the element formulation, an 8-node element is described here. The 20-node brick element used in the FEM simulations uses the 'Serendipity' shape function for its interpolations based on corner and midside nodes only.

The stresses acting on a unit volume are shown in Figure 4.1 and their equations of equilibrium are obtained as,

$$\frac{\partial \sigma_x}{\partial x} + \frac{\partial \tau_{xy}}{\partial y} + \frac{\partial \tau_{xz}}{\partial z} = 0, \tag{4.20a}$$

$$\frac{\partial \tau_{yx}}{\partial x} + \frac{\partial \sigma_y}{\partial y} + \frac{\partial \tau_{yz}}{\partial z} = 0, \tag{4.40b}$$

$$\frac{\partial \tau_{zx}}{\partial x} + \frac{\partial \tau_{zy}}{\partial y} + \frac{\partial \sigma_z}{\partial z} = 0, \tag{4.40c}$$

where $\tau_{xy} = \tau_{yx}$ $\tau_{xz} = \tau_{zx}$ and $\tau_{yz} = \tau_{zy}$.

The constitutive equation for an isotropic material is defined (Kwon, 1997) as,

$$\{\sigma\} = [D]\{\varepsilon\}, \tag{4.41}$$

where the stress and strain tensors are,

$$\{\sigma\} = \{\sigma_x \quad \sigma_y \quad \sigma_z \quad \tau_{xy} \quad \tau_{yz} \quad \tau_{zx}\}^T,$$

$$\{\varepsilon\} = \{\varepsilon_x \quad \varepsilon_y \quad \varepsilon_z \quad \gamma_{xy} \quad \gamma_{yz} \quad \gamma_{zx}\}^T,$$

and the elastic matrix $[D]$ is obtained as,

$$[D] = \frac{E}{(1+\nu)(1-2\nu)} \begin{bmatrix} 1+\nu & \nu & \nu & 0 & 0 & 0 \\ \nu & 1+\nu & \nu & 0 & 0 & 0 \\ \nu & \nu & 1+\nu & 0 & 0 & 0 \\ 0 & 0 & 0 & \frac{1-2\nu}{2} & 0 & 0 \\ 0 & 0 & 0 & 0 & \frac{1-2\nu}{2} & 0 \\ 0 & 0 & 0 & 0 & 0 & \frac{1-2\nu}{2} \end{bmatrix}, \tag{4.42}$$

where E is the material's modulus of elasticity and ν is the Poisson's ratio.

For small displacement assumption, the strain vector is defined as,

$$\begin{Bmatrix} \varepsilon_x \\ \varepsilon_y \\ \varepsilon_z \\ \gamma_{xy} \\ \gamma_{yz} \\ \gamma_{zx} \end{Bmatrix} = \begin{Bmatrix} \frac{\partial u}{\partial x} \\ \frac{\partial v}{\partial y} \\ \frac{\partial w}{\partial z} \\ \frac{\partial u}{\partial y} + \frac{\partial v}{\partial x} \\ \frac{\partial v}{\partial z} + \frac{\partial w}{\partial y} \\ \frac{\partial w}{\partial x} + \frac{\partial u}{\partial z} \end{Bmatrix}, \tag{4.43}$$

where u, v and w are displacements in the X, Y and Z global directions respectively.

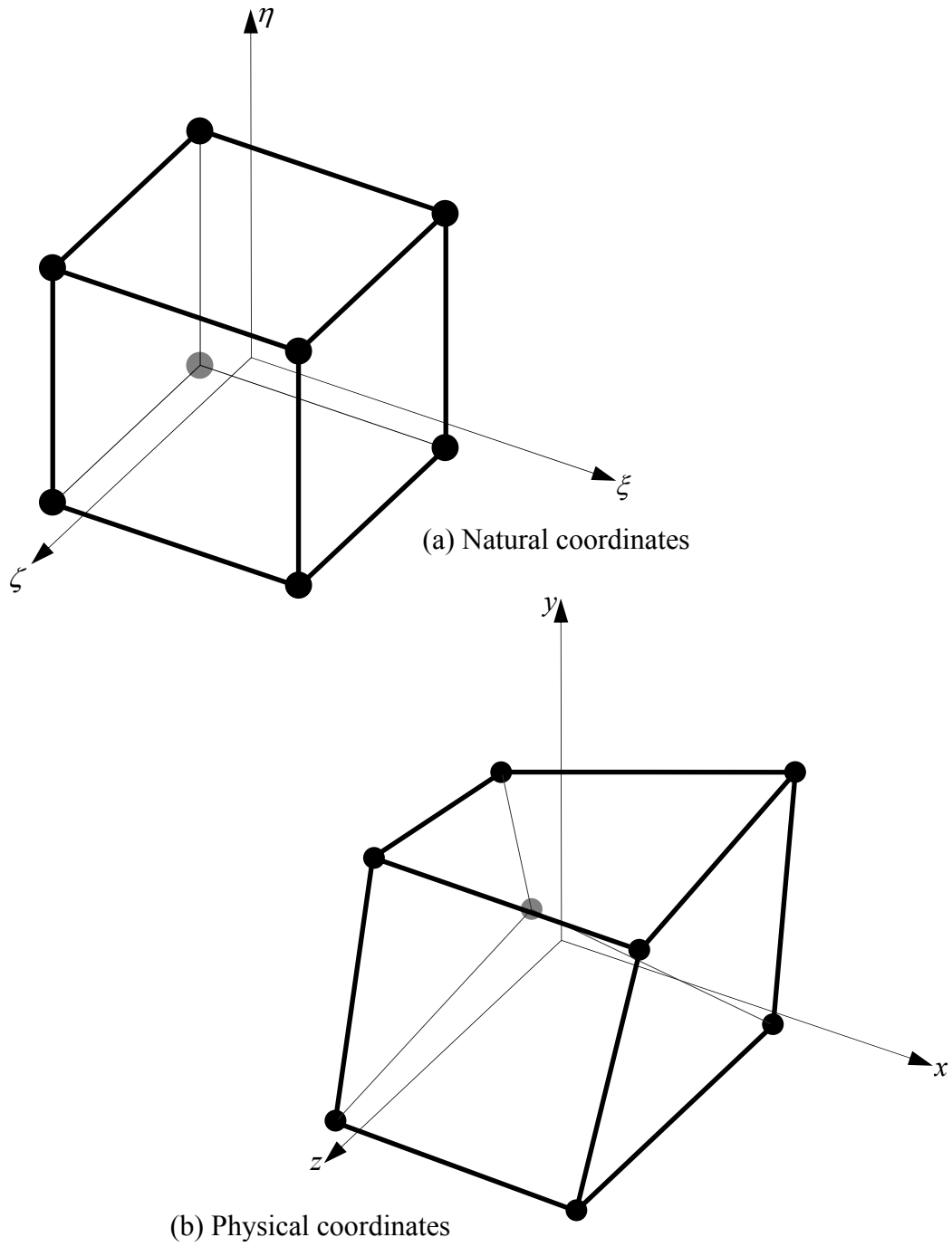

(a) Natural coordinates

(b) Physical coordinates

Figure 4.2. 3-D isoparametric solid element.

Therefore in the mathematical isoparametric mapping for an 8-node brick element (shown in Figure 4.2), the two coordinate (natural and physical) systems are defined in relation to each other as follows,

$$u = \sum_{i=1}^{8} u_i N_i(\xi,\eta,\zeta), \qquad v = \sum_{i=1}^{8} v_i N_i(\xi,\eta,\zeta), \qquad w = \sum_{i=1}^{8} w_i N_i(\xi,\eta,\zeta), \tag{4.44}$$

where $(u_i,\ v_i,\ w_i)$ are nodal values in the global coordinate system $(x,\ y,\ z)$, N_i are the shape functions and they are given below for a 8-node brick element (Kwon, 1997) and in Appendix B for a 20-node brick element, where $(-1 \le \xi,\eta,\zeta \le 1)$.

$$N_1 = \frac{1}{8}(1-\xi)(1-\eta)(1-\zeta), \qquad N_2 = \frac{1}{8}(1+\xi)(1-\eta)(1-\zeta),$$

$$N_3 = \frac{1}{8}(1+\xi)(1+\eta)(1-\zeta), \qquad N_4 = \frac{1}{8}(1-\xi)(1+\eta)(1-\zeta),$$

$$N_5 = \frac{1}{8}(1-\xi)(1-\eta)(1+\zeta), \qquad N_6 = \frac{1}{8}(1+\xi)(1-\eta)(1+\zeta),$$

$$N_7 = \frac{1}{8}(1+\xi)(1+\eta)(1+\zeta), \qquad N_8 = \frac{1}{8}(1-\xi)(1+\eta)(1+\zeta), \tag{4.45}$$

Therefore equation (4.44) is arranged in matrix form as,

$$\begin{Bmatrix} u \\ v \\ w \end{Bmatrix} = \begin{bmatrix} N_1 & 0 & 0 & N_2 & 0 & 0 & \dots & \dots & \dots & N_8 & 0 & 0 \\ 0 & N_1 & 0 & 0 & N_2 & 0 & 0 & \dots & \dots & \dots & N_8 & 0 \\ 0 & 0 & N_1 & 0 & 0 & N_2 & 0 & 0 & \dots & \dots & \dots & N_8 \end{bmatrix} \cdot \begin{Bmatrix} u_1 \\ v_1 \\ w_1 \\ u_2 \\ v_2 \\ w_2 \\ \cdot \\ \cdot \\ \cdot \\ u_8 \\ v_8 \\ w_8 \end{Bmatrix} \tag{4.46}$$

$$= [N]\{d\},$$

where d is the nodal displacement vector.

When the shape functions are used for both geometric mapping and also the nodal variable interpolation within the element, the element is called

isoparametric. The shape function $N_i(\xi,\eta,\zeta)$, is such that it has a unity value only at the node, i and zero at other nodes in the element.

Therefore by substituting equation (4.46) into (4.43) we obtain,

$$\{\varepsilon\} = [B]\{d\}, \tag{4.47}$$

in which,

$$[B] = \begin{bmatrix} \frac{\partial N_1}{\partial x} & 0 & 0 & \dots & \frac{\partial N_7}{\partial x} & 0 & 0 & \frac{\partial N_8}{\partial x} & 0 & 0 \\ 0 & \frac{\partial N_1}{\partial y} & 0 & 0 & \dots & \frac{\partial N_7}{\partial y} & 0 & 0 & \frac{\partial N_8}{\partial y} & 0 \\ 0 & 0 & \frac{\partial N_1}{\partial z} & 0 & 0 & \dots & \frac{\partial N_7}{\partial z} & 0 & 0 & \frac{\partial N_8}{\partial z} \\ \frac{\partial N_1}{\partial y} & \frac{\partial N_1}{\partial x} & 0 & \frac{\partial N_2}{\partial y} & \frac{\partial N_2}{\partial x} & 0 & \dots & \frac{\partial N_8}{\partial y} & \frac{\partial N_8}{\partial x} & 0 \\ 0 & \frac{\partial N_1}{\partial z} & \frac{\partial N_1}{\partial y} & 0 & \frac{\partial N_2}{\partial z} & \frac{\partial N_2}{\partial y} & 0 & \dots & \frac{\partial N_8}{\partial z} & \frac{\partial N_8}{\partial y} \\ \frac{\partial N_1}{\partial z} & 0 & \frac{\partial N_1}{\partial x} & \frac{\partial N_2}{\partial z} & 0 & \frac{\partial N_2}{\partial x} & \frac{\partial N_3}{\partial z} & 0 & \dots & \frac{\partial N_8}{\partial x} \end{bmatrix} \tag{4.48}$$

Though the formulation for a linear element is shown in this section, the actual simulations were carried out using higher-order quadratic solid elements (20-nodes shown in Appendix B). They both follow the same formulation steps. Though the quadratic element does feature many more matrix elements (i.e. 60×60), it is however more accurate as depicted in the results in Chapter 3 and in subsequent Chapters.

Stiffness Matrix

Therefore the stiffness matrix for the element is obtained using,

$$[K] = \int_{Vol} [B]^T [D][B] \mathrm{d}x\mathrm{d}y\mathrm{d}z = \int_{-1}^{1}\int_{-1}^{1}\int_{-1}^{1} [B]^T [D][B] \det[J] \mathrm{d}\xi \mathrm{d}\eta \mathrm{d}\zeta, \tag{4.49}$$

where $[K]$ is the element's stiffness matrix, $[J]$ is the Jacobian of the transformation from the physical coordinate (x,y,z), to the natural coordinate (ξ,η,ζ).

From equation (4.48), the derivatives, $\partial N_1(\xi,\eta,\zeta)/\partial x$, $\partial N_1(\xi,\eta,\zeta)/\partial y$ and $\partial N_1(\xi,\eta,\zeta)/\partial z$, can be obtained using the chain rule (Kwon, 1997) as follows,

$$\frac{\partial}{\partial \xi} = \frac{\partial x}{\partial \xi}\frac{\partial}{\partial x} + \frac{\partial y}{\partial \xi}\frac{\partial}{\partial y} + \frac{\partial z}{\partial \xi}\frac{\partial}{\partial z}, \tag{4.50a}$$

$$\frac{\partial}{\partial \eta} = \frac{\partial x}{\partial \eta}\frac{\partial}{\partial x} + \frac{\partial y}{\partial \eta}\frac{\partial}{\partial y} + \frac{\partial z}{\partial \eta}\frac{\partial}{\partial z}, \tag{4.50b}$$

$$\frac{\partial}{\partial \zeta} = \frac{\partial x}{\partial \zeta}\frac{\partial}{\partial x} + \frac{\partial y}{\partial \zeta}\frac{\partial}{\partial y} + \frac{\partial z}{\partial \zeta}\frac{\partial}{\partial z}, \tag{4.50c}$$

which can be written in matrix form (Kwon, 1997) as,

$$\begin{Bmatrix} \frac{\partial}{\partial \xi} \\ \frac{\partial}{\partial \eta} \\ \frac{\partial}{\partial \zeta} \end{Bmatrix} = \begin{bmatrix} \frac{\partial x}{\partial \xi} & \frac{\partial y}{\partial \xi} & \frac{\partial z}{\partial \xi} \\ \frac{\partial x}{\partial \eta} & \frac{\partial y}{\partial \eta} & \frac{\partial z}{\partial \eta} \\ \frac{\partial x}{\partial \zeta} & \frac{\partial y}{\partial \zeta} & \frac{\partial y}{\partial \zeta} \end{bmatrix} \begin{Bmatrix} \frac{\partial}{\partial x} \\ \frac{\partial}{\partial y} \\ \frac{\partial}{\partial z} \end{Bmatrix} \tag{4.51}$$

The Jacobian matrix is defined as,

$$[J] = \begin{bmatrix} \frac{\partial x}{\partial \xi} & \frac{\partial y}{\partial \xi} & \frac{\partial z}{\partial \xi} \\ \frac{\partial x}{\partial \eta} & \frac{\partial y}{\partial \eta} & \frac{\partial z}{\partial \eta} \\ \frac{\partial x}{\partial \zeta} & \frac{\partial y}{\partial \zeta} & \frac{\partial y}{\partial \zeta} \end{bmatrix}, \tag{4.52}$$

while its inverse is used in equation (4.51) to obtain the derivatives in the physical coordinates, (i.e. the derivatives of the shape functions with respect to x, y and z). The elements in the Jacobian matrix are simply defined as,

$$\frac{\partial x}{\partial \xi} = \sum_{i=1}^{8} \frac{\partial N_i}{\partial \xi} x_i, \qquad \frac{\partial y}{\partial \xi} = \sum_{i=1}^{8} \frac{\partial N_i}{\partial \xi} y_i, \qquad \frac{\partial z}{\partial \xi} = \sum_{i=1}^{8} \frac{\partial N_i}{\partial \xi} z_i, \tag{4.53a}$$

$$\frac{\partial x}{\partial \eta} = \sum_{i=1}^{8} \frac{\partial N_i}{\partial \eta} x_i, \qquad \frac{\partial y}{\partial \eta} = \sum_{i=1}^{8} \frac{\partial N_i}{\partial \eta} y_i, \qquad \frac{\partial z}{\partial \eta} = \sum_{i=1}^{8} \frac{\partial N_i}{\partial \eta} z_i, \tag{4.53b}$$

$$\frac{\partial x}{\partial \zeta} = \sum_{i=1}^{8} \frac{\partial N_i}{\partial \zeta} x_i, \qquad \frac{\partial y}{\partial \zeta} = \sum_{i=1}^{8} \frac{\partial N_i}{\partial \zeta} y_i, \qquad \frac{\partial z}{\partial \zeta} = \sum_{i=1}^{8} \frac{\partial N_i}{\partial \zeta} z_i, \tag{4.53c}$$

where x_i, y_i, z_i are the nodal coordinates for each node i.

Therefore equation (4.53) is simply calculated and the inverse of the Jacobian matrix is obtained numerically. The integration in equation (4.49) is performed for all the simulations on Abaqus using Gauss integration as its efficient and well suited for the polynomial interpolations. Though reduced integration is available on Abaqus, a full integration was adopted in the simulations using modal analysis to prevent hourglass modes in the solution of the eigenvalue problem.

Mass Matrix

The two main common mass matrices used in FEM are lumped and consistent mass matrix. Archer (1963, 1965) developed the consistent mass matrix and is defined as,

$$[M] = \int_{Vol} \rho [N]^T [N] \mathrm{d}V, \tag{4.54}$$

where $[M]$ is the mass matrix and ρ s the mass density. Equation (4.54) can also be solved using Gauss' Integration just like in stiffness matrix.

The lumped mass matrix was developed earlier than the consistent matrix (Kwon, 1997) and preferred for its computational advantages, as it is a diagonal matrix. For the 8-node element discussed above, the lumped element mass matrix would simply be,

$$[M] = \frac{\rho V}{8}[I], \tag{4.55}$$

where V is the element's volume and $[I]$ is a (24×24) identity matrix.

Kwon and Bang (1997) described an approach to extract it from consistent matrix. This simply involves, adding all the diagonal components of the consistent mass matrix corresponding to the translational degrees of freedom and then

dividing the diagonal components by the summation. Then finally multiply by the element's total mass. The off-diagonals elements are simply equated to zero.

Transient Modal Dynamic Analysis

When the model is projected onto the eigenmodes used for the system's dynamic representation (i.e. uncoupling the system's stiffness, mass and damping matrices as in equation 4.34), its uncoupled equation of motion at time t is (Hibbitt, 2006) obtained by substituting equations (4.32, 4.33) into (4.34) as follows,

$$\ddot{q}_p + 2\zeta_p \omega_{np} q_p + \omega_{np}^2 q_p = f_{t-\Delta t} + \frac{\Delta f}{\Delta t}\Delta t, \tag{4.56}$$

where p is the mode number, q_p is the amplitude of the response of mode p, $\omega_{n,p}$ is the undamped natural frequency of mode p, Δf is the change in f over the time increment, Δt assuming the excitation varies linearly within each increment and ζ_p is the damping ratio for mode p. The solution is given (Hibbitt, 2006) in the form,

$$\begin{Bmatrix} q_{t+\Delta t} \\ \dot{q}_{t+\Delta t} \end{Bmatrix} = \begin{bmatrix} a_{11} & a_{12} \\ a_{21} & a_{22} \end{bmatrix} \begin{Bmatrix} q_t \\ \dot{q}_t \end{Bmatrix} + \begin{bmatrix} b_{11} & b_{12} \\ b_{21} & b_{22} \end{bmatrix} \begin{Bmatrix} f_t \\ f_{t+\Delta t} \end{Bmatrix}, \tag{4.57}$$

where, $i,l = 1,2$, a_{il} and b_{il} are constants, which are dependent on the three different cases of non-rigid body motion. These cases are based on the oscillation modes - underdamped, critical damping and overdamped.

For the underdamped case, the constants are given as follows (Hibbitt, 2006);

$$a_{11} = \exp\left(-\zeta\omega_n \Delta t\right)\left(\frac{\zeta\omega_n}{\omega_d}\sin\omega_d \Delta t + \cos\omega_d \Delta t\right), \tag{4.58a}$$

$$a_{12} = \exp\left(-\zeta\omega_n \Delta t\right)\frac{1}{\omega_d}\sin\omega_d \Delta t, \tag{4.58b}$$

$$a_{21} = -\exp(-\zeta\omega_n \Delta t)\frac{\omega}{\sqrt{1-\zeta^2}}\sin\omega_d \Delta t, \tag{4.58c}$$

$$a_{22} = \exp(-\zeta\omega_n \Delta t)\left(\cos\omega_d \Delta t - \frac{\zeta\omega_n}{\omega_d}\sin\omega_d \Delta t\right), \tag{4.58d}$$

$$\begin{aligned} b_{11} = -\exp(-\zeta\omega_n \Delta t)\Bigg[&\left(\frac{\zeta}{\omega_n\omega_d} + \frac{2\zeta^2-1}{\omega_n^2\omega_d\Delta t}\right)\sin\omega_d\Delta t \\ &+ \left(\frac{1}{\omega_n^2} + \frac{2\zeta}{\omega_n^3\Delta t}\right)\cos\omega_d\Delta t\Bigg] + \frac{2\zeta}{\omega_n^3\Delta t}, \end{aligned} \tag{4.59a}$$

$$b_{12} = \exp(-\zeta\omega_n \Delta t)\left[\left(\frac{2\zeta^2-1}{\omega_n^2\omega_d\Delta t}\right)\sin\omega_d\Delta t + \left(\frac{2\zeta}{\omega_n^3\Delta t}\right)\cos\omega_d\Delta t\right] + \frac{1}{\omega_n^2} - \frac{2\zeta}{\omega_n^3\Delta t}, \tag{4.59b}$$

$$\begin{aligned} b_{21} = -\exp(-\zeta\omega_n \Delta t)\Bigg[&\left(\frac{2\zeta^2-1}{\omega_n^2\omega_d\Delta t} + \frac{\zeta}{\omega_n\omega_d}\right)\left(\omega_d\cos\omega_d\Delta t - \zeta\omega_n\sin\omega_d\Delta t\right) \\ &- \left(\frac{1}{\omega_n^2} + \frac{2\zeta}{\omega_n^3\Delta t}\right)\left(\omega_d\sin\omega_d\Delta t + \zeta\omega_n\cos\omega_d\Delta t\right)\Bigg] - \frac{1}{\omega_n^2\Delta t}, \end{aligned} \tag{4.59c}$$

$$\begin{aligned} b_{22} = -\exp(-\zeta\omega_n \Delta t)\Bigg[&\left(\frac{2\zeta^2-1}{\omega_n^2\omega_d\Delta t}\right)\left(\zeta\omega_n\sin\omega_d\Delta t - \omega_d\cos\omega_d\Delta t\right) \\ &+ \left(\frac{2\zeta}{\omega_n^3\Delta t}\right)\left(\omega_d\sin\omega_d\Delta t + \zeta\omega_n\cos\omega_d\Delta t\right)\Bigg] + \frac{1}{\omega_n^2\Delta t}, \end{aligned} \tag{4.59d}$$

where $\omega_d = \omega_n\sqrt{1-\zeta^2}$, which is the damped natural frequency.

Since the time integrations is done in generalized coordinates, the response of the physical variables are obtained through summation (Altintas, 2000),

$$u = \sum_p^N \boldsymbol{\psi}_\mathbf{p} q_p, \tag{4.60a}$$

$$v = \sum_p^N \boldsymbol{\psi}_\mathbf{p} \dot{q}_p, \tag{4.60b}$$

where $\boldsymbol{\psi}_\mathbf{p}$ are the eigenvector corresponding to the mode p, u is the displacement in nodal coordinates and v is the velocity in nodal coordinates.

The Finite Element Model

The workpiece material used in the FEM model is ‘‘Aluminium Alloy 7010 T7651’’. The material properties required for generating the stiffness and mass matrices are: Density, ρ = 2.823×10^{3} (Kg m^{-3}), Young’s Modulus, E = 69.809 (GPa) and Poisson Ratio, ν = 0.337. Three different types of workpiece were used in the finite element analysis (FEA). The dimensions are shown in Figure 4.3 and the corresponding wall heights, *H* and thicknesses, *W* are given in Tables 4.1, 4.2, 4.3, 4.4, and 4.5 along with their experimentally identified damping ratios. The damping parameters for Case 1A (Table 4.1) and Case 2A (Table 4.4) are to be used to predict the damping parameters, ζ_p^b for the remaining structures (Cases 1B, 1C and 2B) using the proposed approach in equation (4.27). The damping parameters predicted, ζ_p^b and the force data, $f(t)$ measured by the instrumented hammer (in time domain) during impact tests were used in each corresponding FE analysis.

The workpiece was bolted at the back surface to a milling machine during the impact tests, hence in the FEM simulations it was assumed to be perfectly clamped (characterised by stiffness values of 1×10^{36} for the corresponding degrees of freedom) and that the resonant frequency of the machine is much higher than the excited frequencies during impact tests.

Table 4.1. Case 1A, *H = 30mm*, *W = 4.5mm*

Mode Number, p	**Natural Frequency,** ω_{np} **(Hz)**	**Modal Damping Ratio,** ζ_p **(%)**
1	4.1900×10^{03}	2.9639×10^{-02}
2	4.3516×10^{03}	1.9803×10^{-02}
3	4.8717×10^{03}	1.0514×10^{-02}
4	5.4475×10^{03}	8.8120×10^{-03}
5	6.2813×10^{03}	7.1132×10^{-03}
6	7.3331×10^{03}	4.3088×10^{-03}
7	8.6491×10^{03}	4.9493×10^{-03}

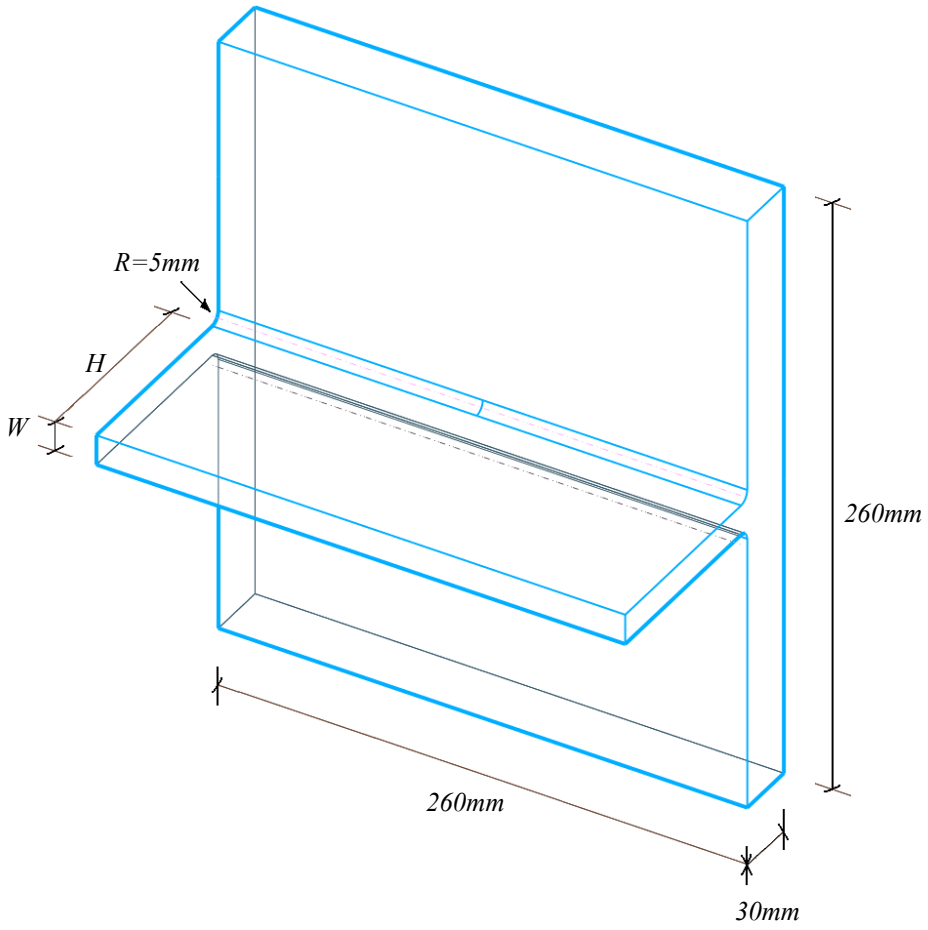

Figure 4.3. Workpiece dimensions.

Table 4.2. Case 1B, $H = 30mm$, $W = 3.0mm$

Mode Number, p	Natural Frequency, ω_{np} (Hz)	Modal Damping Ratio, ζ_p (%)
1	2.8299×10^{03}	2.5093×10^{-02}
2	3.1979×10^{03}	4.2365×10^{-03}
3	3.4036×10^{03}	3.4138×10^{-03}
4	3.7928×10^{03}	5.6309×10^{-03}
5	4.3637×10^{03}	5.6441×10^{-03}

Table 4.3. Case 1C, $H = 30mm$, $W = 1.5mm$

Mode Number, p	Natural Frequency, ω_{np} (Hz)	Modal Damping Ratio, ζ_p (%)
1	1.3181×10^{03}	3.0010×10^{-02}
2	1.6038×10^{03}	2.4222×10^{-03}
3	1.7067×10^{03}	2.4937×10^{-03}
4	1.9071×10^{03}	2.5882×10^{-03}
5	2.1948×10^{03}	1.6691×10^{-03}

Table 4.4. Case 2A, *H = 70mm*, *W = 7.5mm*

Mode Number, p	Natural Frequency, ω_{np} (Hz)	Modal Damping Ratio, ζ_p (%)
1	1.2725×10^{03}	1.6636×10^{-02}
2	1.4651×10^{03}	1.4675×10^{-02}
3	2.9977×10^{03}	8.3671×10^{-03}
4	2.0140×10^{03}	1.0525×10^{-02}
5	4.3787×10^{03}	5.8279×10^{-03}

Table 4.5. Case 2B, *H = 70mm*, *W = 3.5mm*

Mode Number, p	Natural Frequency, ω_{np} (Hz)	Modal Damping Ratio, ζ_p (%)
1	5.7573×10^{02}	9.2024×10^{-03}
2	6.5420×10^{02}	6.0351×10^{-03}
3	8.9132×10^{02}	5.1987×10^{-03}
4	1.2789×10^{03}	6.0564×10^{-03}
5	1.8500×10^{03}	3.2948×10^{-03}

4.2.5. Validation

Damping Ratio for Case 1

Using the experimental modal analysis explained in section 4.2.1, the different damping ratios are extracted for the Cases 1A, 1B and 1C as given in Tables 4.1, 4.2 and 4.3, respectively. The proposed approach uses the damping ratio obtained from one geometry (Case 1A) to predict the damping for any given geometry with only the thickness changed (Case 1B) and (Case 1C). Using the least squares method, the damping ratios identified for Case 1A (see Table 4.1) were used to extract the coefficients in equation (4.38) as follows,

$\alpha_1 = -1.1272\times10^{4}$, $\alpha_4 = -1.8055\times10^{-6}$, $\alpha_7 = 3.0997\times10^{12}$,

$\alpha_2 = 3.6932\times10^{-3}$, $\alpha_5 = -1.2188\times10^{10}$,

$\alpha_3 = 1.8194\times10^{7}$, $\alpha_6 = 2.8190\times10^{-10}$

The curve fitting is compared with the calculated $\overline{\zeta}_p$ and $\overline{\omega}_p$ in Figure 4.4. From this curve fitting, the damping for a new wall thickness can be predicted as shown in Figures 4.5(b) and 4.5(c) for Cases 1B and Case 1C respectively using equations (4.27 and 4.28).

The experimental data for each geometry (Tables 4.1, 4.2 and 4.3) was used to extract the coefficients α_u in Rayleigh's damping model and Caughey's series in equations (4.1 and 4.3). By transforming Rayleigh's damping model (equation 4.1) into generalized coordinates using equation (4.35) and substituting in equations (4.32 and 4.33) it can be expressed as,

$$\zeta_p = \left(\frac{\alpha_0}{\omega_{n,p}} + \alpha_1 \omega_{n,p} \right), \tag{4.61}$$

while Caughey's series can be expressed in generalized coordinates as,

$$\zeta_p = \left(\frac{\alpha_0}{\omega_{n,p}} + \alpha_1 \omega_{n,p} + \alpha_2 \omega_{n,p}^3 + \alpha_3 \omega_{n,p}^5 + \ldots \right) \tag{4.62}$$

Hence using least square method, the experimental damping ratios for each geometry in Tables 4.1, 4.2, and 4.3 were used to extract the coefficients for each corresponding geometry.

The damping ratio curve fittings using both Rayleigh and Caughey's series are compared with the damping ratios from the proposed series in Figures 4.5(a), 4.5(b) and 4.5(c). The comparison between the proposed damping prediction approach, Caughey's series curve fitting and experimental data is seen to be satisfactory. Though it should be noted that to obtain Caughey's series curve, the experimental data is required for each geometry in order to obtain the coefficients. The coefficients identified for Rayleigh damping model and Caughey's series are given or each geometry in Tables 4.6, 4.7 and 4.8.

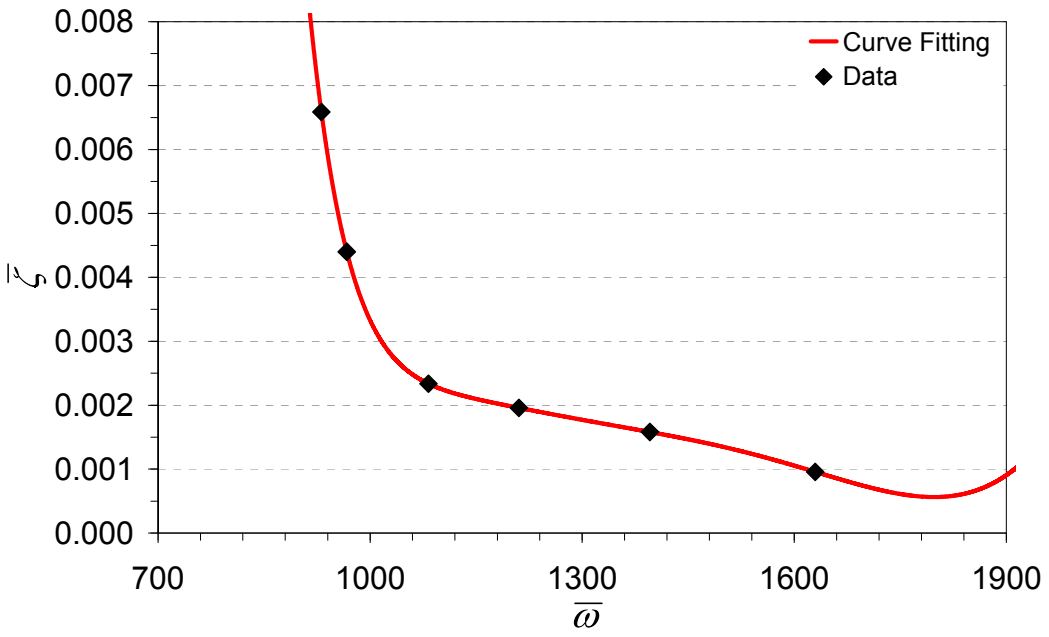

Figure 4.4. Comparison between curve fitting using proposed series and $\overline{\zeta}_p$.

Table 4.6. Case 1A, *H = 30mm, W = 4.5mm (Rayleigh and Caughey's Damping Constants)*

	α_0	α_1	α_2	α_3	α_4
Rayleigh	1.1445×10^{03}	-1.4440×10^{-06}			
Caughey's Series	9.8711×10^{03}	-9.5707×10^{-05}	3.4716×10^{-12}	-5.3111×10^{-20}	2.8810×10^{-26}

Table 4.7. Case 1B, *H = 30mm, W = 3.0mm (Rayleigh and Caughey's Damping Constants)*

	α_0	α_1	α_2	α_3	α_4
Rayleigh	7.6520×10^{01}	-3.8016×10^{-06}			
Caughey's Series	2.5645×10^{03}	-7.4519×10^{-04}	8.0026×10^{-11}	-3.746×10^{-18}	6.4637×10^{-26}

The proposed approach apart from predicting the damping ratio can be used to give a rough estimate of the frequency range of the most significant modes, when performing a finite element analysis (FEA) or an impact test by using the calculated ω_p^b.

Table 4.8. Case 1C, *H = 30mm, W = 1.5mm (Rayleigh and Caughey's Damping Constants)*

	α_0	α_1	α_2	α_3	α_4
Rayleigh	5.0647×10^{03}	-1.2563×10^{-05}			
Caughey's Series	8.3362×10^{02}	-1.0084×10^{-03}	4.5089×10^{-10}	-8.7757×10^{-17}	6.2665×10^{-24}

Taking $\overline{\omega}_1 = 882\,\text{Hz}$ for example, it will become $\omega_1^b = 6615\,\text{Hz}$ for a 7.5mm thick wall using equation (4.28). Using FEM, the first natural frequency is calculated to be 6588.4 Hz, hence ω_1^b can be used as a rough estimate of the minimum frequency of interest and knowledge of the minimum frequency can be used to reduce the computational time.

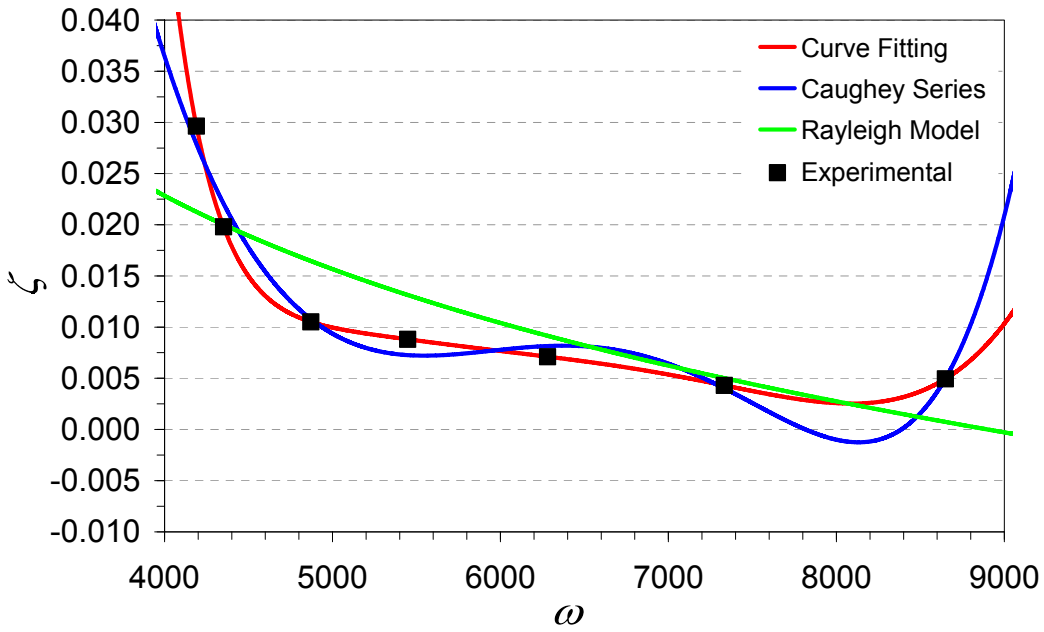

(a) Case 1A

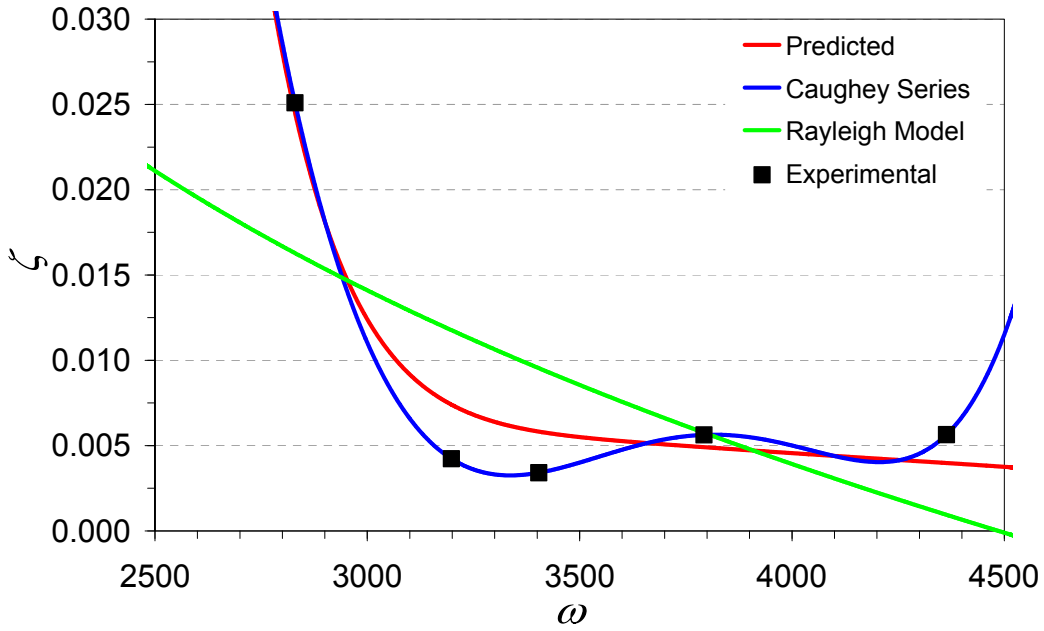

(b) Case 1B

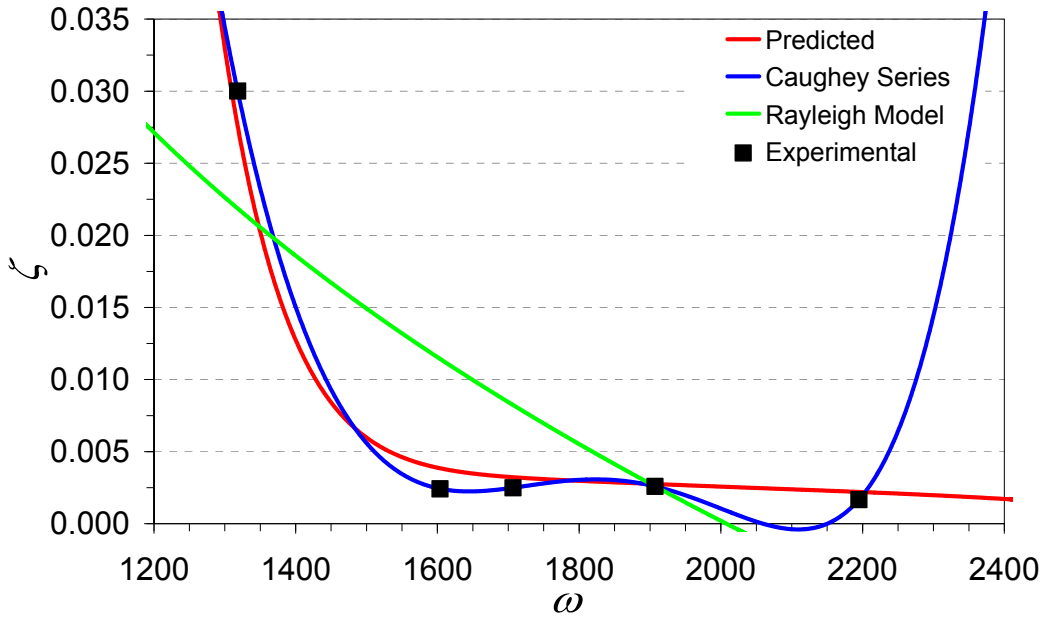

(c) Case 1C

Figure 4.5. Comparison between predicted damping ratios (using the proposed approach), curve fittings (using Caughey's series and Rayleigh's damping model) and experimental damping ratios: (a) Case 1A; (c) Case 1B; (c) Case 1C.

Similarly, by using the maximum frequency of the dominant modes in equation (4.28) ω_p^b can be taken as a rough estimate of the maximum frequency of the dominant modes for the new structure.

Damping Ratio for Case 2

A wall section with a different height of 70mm (Case 2) was further used to validate the proposed approach. The different damping ratios extracted for Case 2A and Case 2B are given in Table 4.4 and 4.5. Using the least squares method, the damping ratios identified for Case 2A were used to extract the coefficients in equation (4.38) as follows,

$$\alpha_1 = 3.68005 \times 10^{-1}, \qquad \alpha_2 = 3.04763 \times 10^{-7},$$

while the curve fitting is compared with the calculated $\overline{\zeta}_p$ and $\overline{\omega}_p$ in Figure 4.6. From this curve fitting, the damping for a new wall thickness can be predicted as shown in Figure 4.7(b) for Case 2B using equations (4.27 and 4.28).

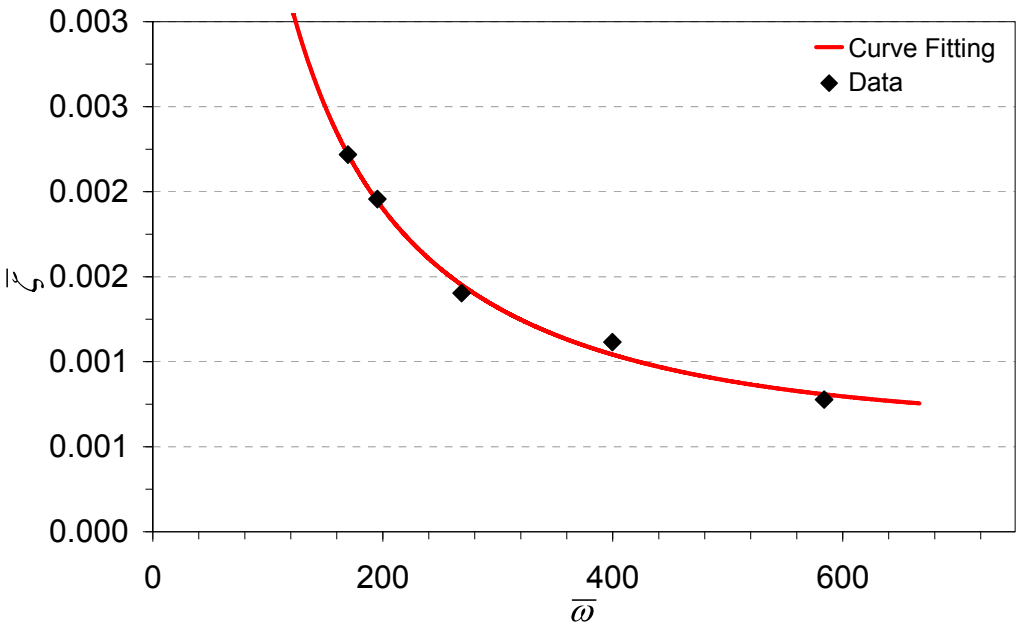

Figure 4.6. Comparison between curve fitting using proposed series and $\overline{\zeta}_p$.

Rayleigh and Caughey's series coefficients extracted using damping parameters in Tables 4.4 and 4.5 are given in Tables 4.9 and 4.10. The damping ratio curve fittings using both Rayleigh and Caughey's series are also compared with the damping ratio curve fitting from the proposed series in Figures 4.7(a) and 4.7(b). The comparison between the proposed damping prediction approach, Rayleigh model and experimental data is satisfactory. The comparison between the proposed series damping model (equation 4.30) and Rayleigh's model in Figure 4.7(a) are exactly the same, because the first term in the series in equation (4.38) is equivalent to Rayleigh's model, when $\overline{\zeta}_p$ and $\overline{\omega}_p$ are converted back into the $\overline{\zeta}_p^b$ and $\overline{\omega}_p^b$. This further shows the accuracy of the proposed approach as the results for Case 2B were fully predicted as opposed to curve fitted.

Table 4.9. Case 2A, *H = 70mm, W = 7.5mm (Rayleigh and Caughey's Damping Constants)*

	α_0	α_1	α_2	α_3
Rayleigh	4.1401×10^{01}	6.0953×10^{-07}		
Caughey's Series	2.2405×10^{01}	-9.8966×10^{-07}	2.1526×10^{-13}	-8.0922×10^{-21}

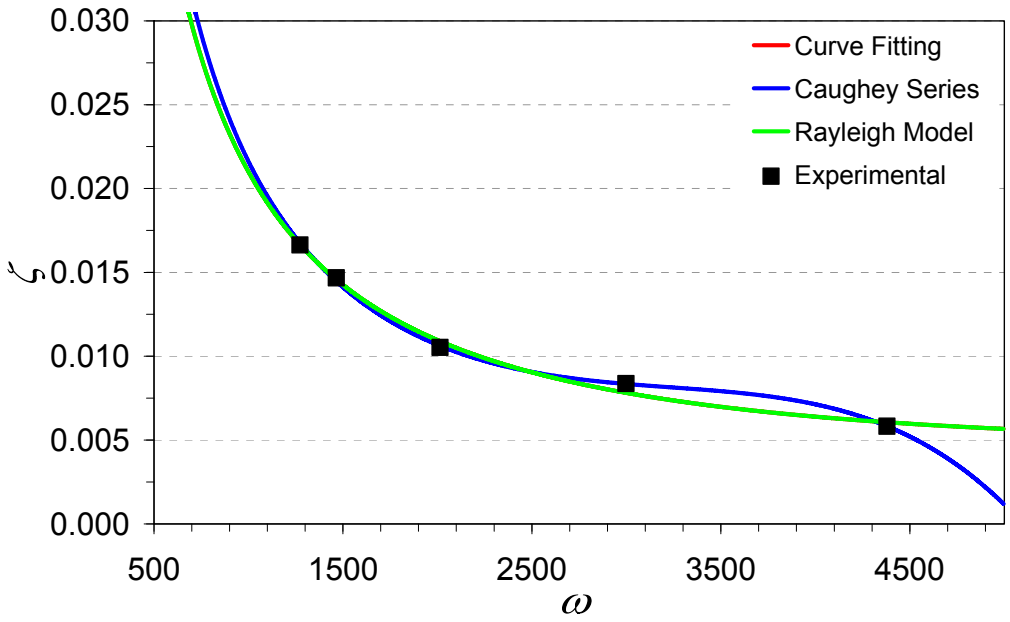

(a) – Case 2A

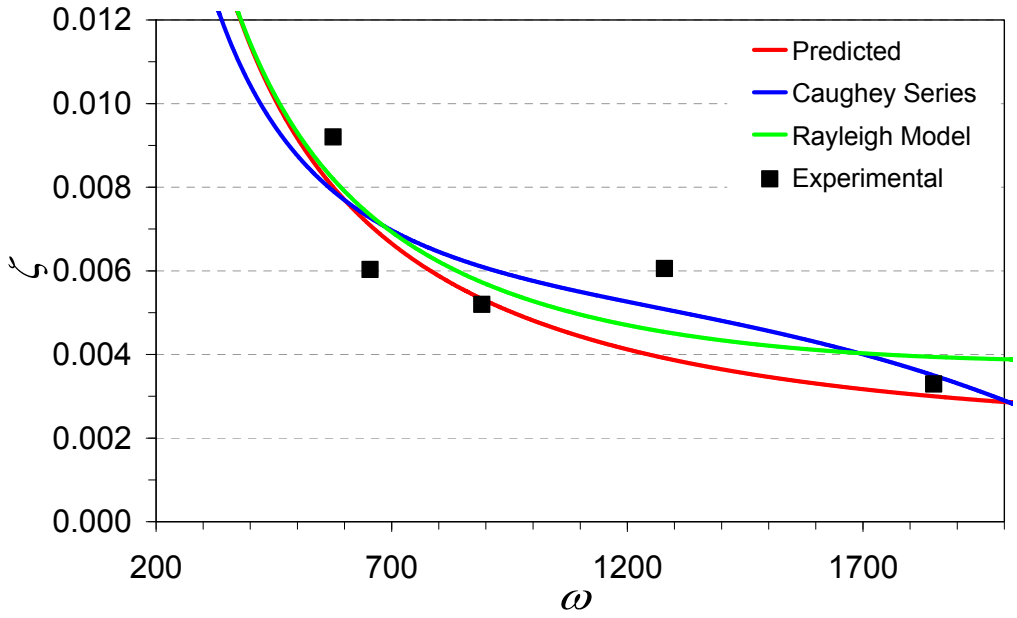

(b) – Case 2B

Figure 4.7. Comparison between predicted damping ratios (using the proposed approach), curve fittings (using Caughey's series and Rayleigh's damping model) and experimental damping ratios: (a) Case 2A; (c) Case 2B.

Table 4.10. Case 2B, *H = 70mm*, *W = 3.5mm (Rayleigh and Caughey's Damping Constants)*

	α_0	α_1	α_2
Rayleigh	8.8871	1.6646×10^{-06}	
Caughey's Series	3.7947	2.4528×10^{-06}	-4.8788×10^{-13}

Time Domain – Case 1

Cases 1B and 1C were simulated in a commercial FEM package (Abaqus) using the simulation approach explained in section 4.2.4. Two different simulations were performed for each structure. In the first simulation (for each case), the damping ratios extracted experimentally were used directly. This simulation shows how accurate the actual FEM predictions are compared to experimental results. In the second simulation (for each case), the predicted damping ratios using the new approach discussed in this section were used. It should be noted that this second simulation requires no experimental input/data as all the material properties are known and the damping ratios are predicted using the proposed approach. The input force in time domain $f(t)$ used in equation (4.56) in both simulations, was the impact force measured using the instrumented hammer for each corresponding structure.

The damping ratio ζ_p in equation (4.56), for the first simulation was the experimental damping ratio for each natural frequency (Tables 4.2 and 4.3); and in the second simulation corresponds to the predicted damping ratio, ζ_p^b (Figures 4.5(b) and 4.5(c)), where ω_p^b is the numerically identified natural frequency for the structure. The damping ratios are defined in Abaqus in terms of their corresponding frequencies. The acceleration at the same accelerometer location (as it was during the experimental impact testing) was monitored in the FE analyses and is compared with acceleration measured during the experiments.

Comparison between the FEM modal analysis and the experimental results is satisfactory as shown in Figures 4.8(a) and 4.8(b). The comparison between the FEM results when using experimental damping ratios and when using predicted damping ratios show a very good match, see Figures 4.8(a) and 4.8(b).

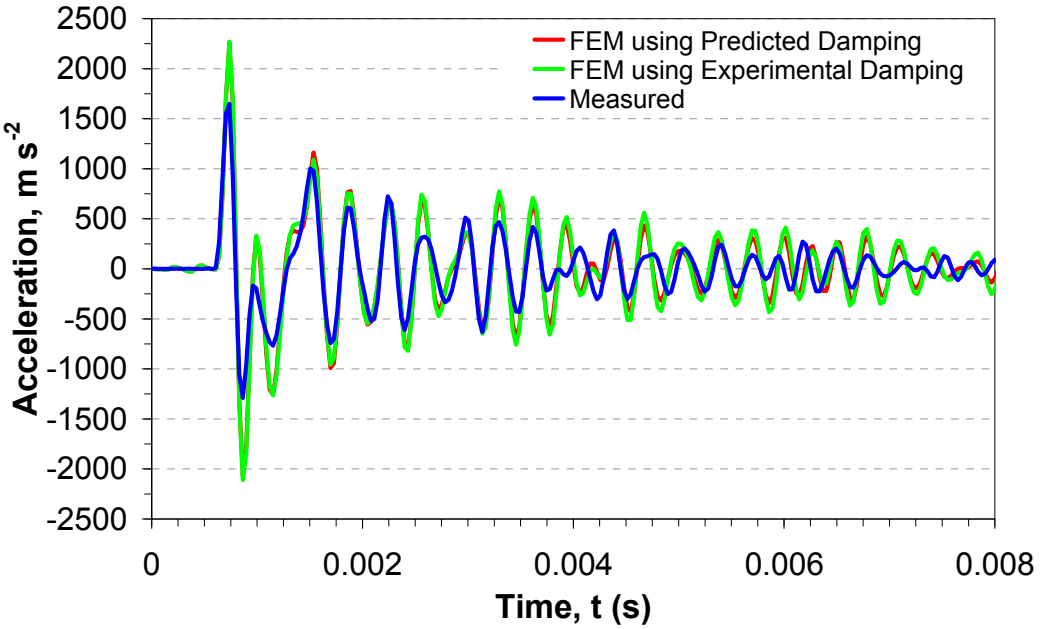

(a) Case 1B

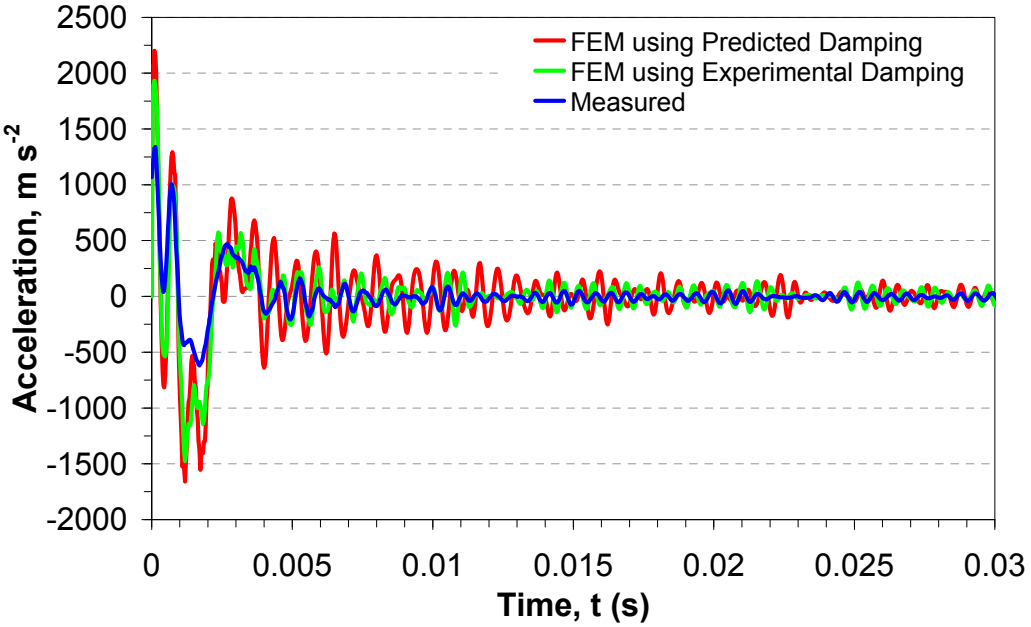

(b) Case 1C

Figure 4.8. Comparison between FEM predicted acceleration for both simulations and experimentally measured acceleration.

Time Domain – Case 2

Likewise for Case 2B, the experimentally identified damping ratios and damping ratio predicted (using the proposed approach) were used in FEM simulations and comparisons to experimental results are shown in Figure 4.9 to further show the accuracy of the predicted damping ratios.

The possibilities of predicting the damping ratio for any given structure with only a change in just its height was also investigated. However the results, although inconclusive show a possible new set of parameters of the kind,

$$\overline{\zeta}_h = \zeta_p^a \cdot h_a, \tag{4.63}$$

$$\overline{\omega}_h = \omega_{n,p}^a \cdot h_a \tag{4.64}$$

Further experimental tests would however be required to further investigate any possible relationship.

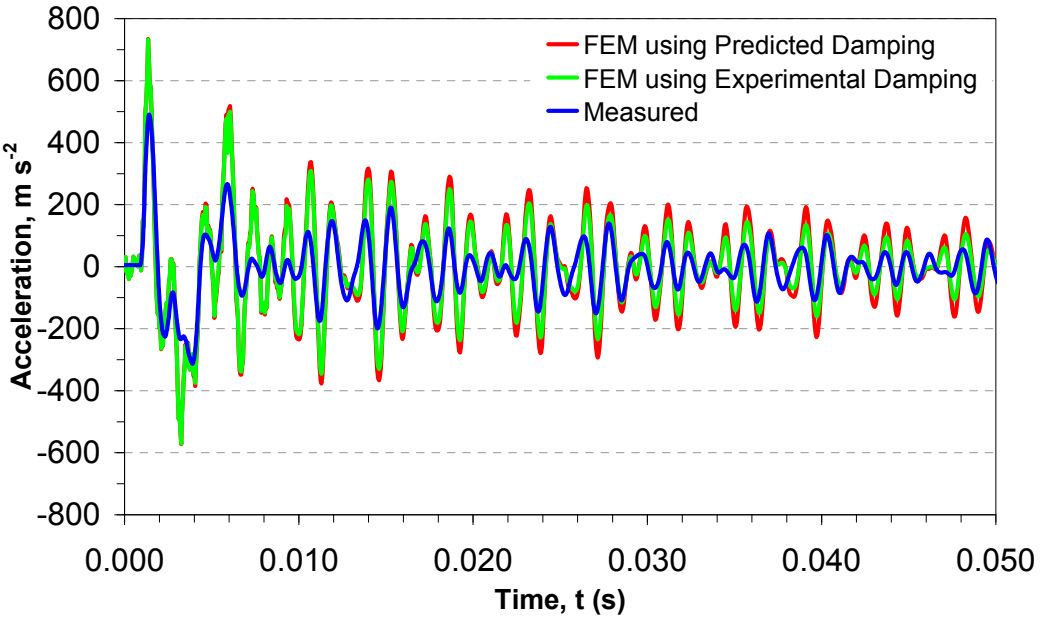

Figure 4.9. Comparison between FEM predicted acceleration for both simulations and experimentally measured acceleration.

4.3. FEM Approach to Stability Lobes Prediction

This section presents a Finite Element Analysis (FEA) and Fourier transform approach to obtain a structure's frequency response function (FRF). The aim of this approach is to eliminate the need for the classical impact experimental approach used in extracting structure's FRF. The numerical and experimental FRFs are used to obtain stable regions in the machining of thin walled structure. Examples are compared with experimental results and a satisfactory agreement is observed.

4.3.1. Chatter Stability Model

The FEM approach presented in this section was proposed by Adetoro et al. (2009b). The stability model used in this section is the 2-D model proposed by Altintas and Budak (1995) as summarized below. The periodic milling forces excite the cutter and the workpiece causing two orthogonal dynamic displacements x and y in the global axis. This generates undulations on the machined surface and each tooth removes the undulations generated by the previous tooth (Figure 4.11). Therefore leading to a modulated chip thickness as opposed to a static chip thickness (Figure 4.10), which can be expressed as,

$$h_j(\phi) = s_t \sin\phi_j + \left(\upsilon_{jc}^0 - \upsilon_{jw}^0\right) - \left(\upsilon_{jc} - \upsilon_{jw}\right), \tag{4.65}$$

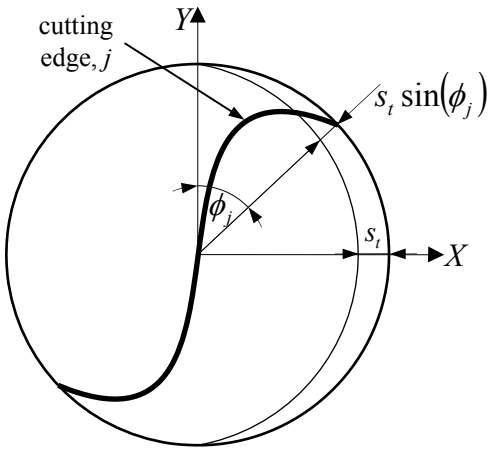

Figure 4.10. Static milling model.

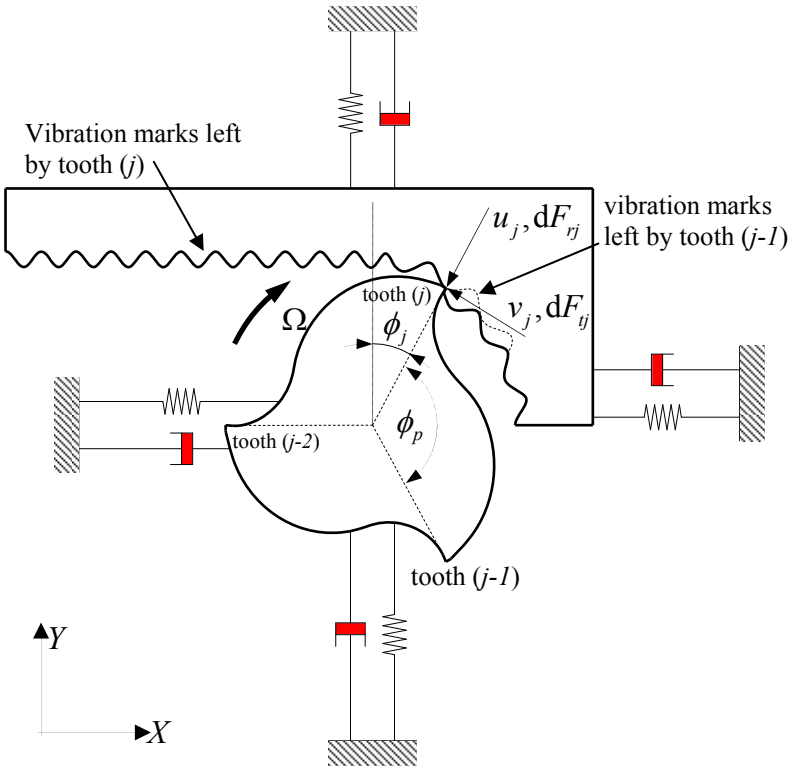

Figure 4.11. Dynamic Milling Model.

where s_t is the feed per tooth, $\left(\upsilon_{jc}^0, \upsilon_{jc}\right)$ and $\left(\upsilon_{jw}^0, \upsilon_{jw}\right)$ are the dynamic displacement of the cutter and workpiece at the previous and present tooth periods respectively, $\phi_j = j\phi_p + \Omega t$ is the angular immersion of tooth j (see Figure 4.11) for a cutter (Ω if the angular speed), with constant pitch angle $\phi_p = 2\pi/N$ (N is the number of teeth).

The dynamic displacements in the chip thickness direction due to tool and workpiece vibrations are defined as,

$$\upsilon_{j\beta} = -x_\beta \sin\phi_j - y_\beta \cos\phi_j \quad (\beta = c, w), \tag{4.66}$$

where c and w indicate the cutter and workpiece respectively, x_β, y_β and x_β^0, y_β^0 are the dynamic displacements in the global axis for the current and previous tooth periods respectively.

By eliminating the static part (Figure 4.10) in equation (4.65), the dynamic chip thickness in milling is defined as,

$$h_j(\phi) = \Delta x \sin\phi_j - \Delta y \cos\phi_j, \tag{4.67}$$

where,

$$\begin{aligned} \Delta x &= \left(x_c - x_c^0\right) - \left(x_w - x_w^0\right), \\ \Delta y &= \left(y_c - y_c^0\right) - \left(y_w - y_w^0\right) \end{aligned} \tag{4.68}$$

Therefore, the dynamic forces on tooth j (using ''Exponential Force Coefficient Model'', (Budak, 1994)) in the tangential and radial directions can be defined as,

$$\begin{aligned} F_{tj}(\phi) &= K_t a h_j(\phi), \\ F_{rj}(\phi) &= K_r F_{tj}(\phi), \end{aligned} \tag{4.69}$$

where a is the axial depth of cut (ADOC), and K_t and K_r are the tangential and radial cutting force coefficients respectively. By substituting equation (4.67) into (4.69) and resolving in the global directions, the following expression is obtained (Altintas, 1995, Budak, 2006) as:

$$\begin{Bmatrix} F_x \\ F_y \end{Bmatrix} = \frac{1}{2} a K_t \begin{bmatrix} a_{xx} & a_{xy} \\ a_{yx} & a_{yy} \end{bmatrix} \begin{Bmatrix} \Delta x \\ \Delta y \end{Bmatrix}, \tag{4.70}$$

where,

$$a_{xx} = \sum_{j=0}^{N-1} g_j \left[-\sin\phi\cos\phi - \left(\sin^2\phi\right) K_r \right] \tag{4.71a}$$

$$a_{xy} = \sum_{j=0}^{N-1} g_j \left[-\cos^2\phi - \left(\sin\phi\cos\phi\right) K_r \right] \tag{4.71b}$$

$$a_{yx} = \sum_{j=0}^{N-1} g_j \left[\sin^2\phi\sin\gamma - \left(\sin\phi\cos\phi\right) K_r \right] \tag{4.71c}$$

$$a_{yy} = \sum_{j=0}^{N-1} g_j \left[\sin\phi\cos\phi - \left(\cos^2\phi\right) K_r \right] \tag{4.71d}$$

where, $\left.\begin{aligned} g(\phi_j) &= 1 \leftarrow \phi_{start} < \phi_j < \phi_{exit} \\ g(\phi_j) &= 0 \leftarrow \phi_j < \phi_{start} \quad \text{or} \quad \phi_j > \phi_{exit} \end{aligned}\right\}$

a_{xy} are the periodic directional cutting coefficients and they depend on the angular position of the cutter and the radial cutting force coefficient K_r (refer to Chapter 5), thereby making equation (4.70) a function of time,

$$\{F(t)\} = \frac{1}{2} a K_t [A(t)]\{\Delta(t)\}, \tag{4.72}$$

where, $\{\Delta(t)\} = \{\Delta x, \quad \Delta y, \quad \Delta z\}^T$. $[A(t)]$ is periodic at the tooth passing frequency $\omega_T = N\Omega$, therefore its Fourier series expansion is used for the solution of the system. The average value in the Fourier series expansion (single frequency solution) of the time varying directional coefficients is used in this section. Reference should be made to Chapter 5 for more detail on the model as a three-dimensional model is outlined. Therefore, the average Fourier term $[A_o]$ of the Fourier series expansion (Altintas, 2001) can be defined as,

$$\begin{aligned} [A_o] &= \frac{1}{T}\int_0^T [A(t)]\mathrm{d}t \\ &= \frac{1}{\phi_p}\int_{\phi_{start}}^{\phi_{exit}} [A(\phi)]\,\mathrm{d}\phi = \frac{N}{4\pi}[\alpha], \end{aligned} \tag{4.73}$$

and the evaluated elements of the directional factor matrix, $[\alpha]$ are given as follows:

$$\alpha_{xx} = \left[\cos 2\phi + K_r(\sin 2\phi - 2\phi)\right]_{\phi_{start}}^{\phi_{exit}}, \tag{4.74a}$$

$$\alpha_{xy} = \left[-\sin 2\phi + 2\phi + K_r \cos 2\phi\right]_{\phi_{start}}^{\phi_{exit}}, \tag{4.74b}$$

$$\alpha_{yx} = \left[-\sin 2\phi - 2\phi + K_r \cos 2\phi\right]_{\phi_{start}}^{\phi_{exit}}, \tag{4.74c}$$

$$\alpha_{yy} = \left[-\cos 2\phi - K_r(\sin 2\phi + 2\phi)\right]_{\phi_{start}}^{\phi_{exit}}, \tag{4.74d}$$

Hence, equation (4.72) reduces to,

$$\{F(t)\} = \frac{N}{8\pi} a K_t [A_0]\{\Delta(t)\}, \tag{4.75}$$

where $[A_0]$ is the time invariant, but immersion dependent directional cutting coefficient matrix.

The vibration vectors at the present time t and previous tooth periods $(t-T)$ are defined as,

$$\begin{aligned}\{r\} &= \{x(t), \quad y(t), \quad z(t)\}^T \\ \{r_0\} &= \{x(t-T), \quad y(t-T), \quad z(t-T)\}^T\end{aligned} \tag{4.76}$$

By using the transfer function at the cutter-workpiece contact zone, the vibration vectors are defined in frequency domain as,

$$\left.\begin{aligned}\{r(i\omega)\} &= [G(i\omega)]\{F\}e^{i\omega t} \\ \{r_0(i\omega)\} &= e^{-i\omega T}\{r(i\omega)\}\end{aligned}\right\} \tag{4.77}$$

Therefore, the displacement/regenerative vector in equation (4.72) is defined as,

$$\{\Delta(t)\} = \{(x-x_0), \quad (y-y_0), \quad (z-z_0)\}^T, \tag{4.78}$$

and in frequency domain, using equation (4.77) as,

$$\{\Delta(i\omega)\} = (1-e^{-i\omega T})[G(i\omega)]\{F\}e^{i\omega t} \tag{4.79}$$

where, $[G(i\omega)]$ is the transfer function (TF) matrix of the structure. Hence, equation (4.75) becomes an eigenvalue problem defined as,

$$\{F\}\mathrm{e}^{i\omega_c t} = \frac{N}{8\pi} aK_t[A_0](1-\mathrm{e}^{-i\omega_c T})[G(i\omega_c)]\{F\}\mathrm{e}^{i\omega_c t}, \tag{4.80}$$

The transfer function matrix $[G(i\omega_c)]$ is the main focus of this section. It is defined as,

$$[G(i\omega_c)] = [G_c(i\omega_c)] + [G_w(i\omega_c)], \tag{4.81}$$

where,

$$[G_{\beta xx}(i\omega_c)] = \begin{bmatrix} G_{\beta xx}(i\omega_c) & G_{\beta xy}(i\omega_c) \\ G_{\beta yx}(i\omega_c) & G_{\beta yy}(i\omega_c) \end{bmatrix}, \qquad (\beta = c, w) \tag{4.82}$$

Equation (4.80) has a non-trivial solution if and only if its determinant is zero,

$$\det[[I]+\Lambda[G_0(i\omega_c)]]=0, \tag{4.83}$$

where, $[G_0]=[A_0][G]$ is known as the oriented transfer function. The eigenvalues is defined as,

$$\Lambda=-\frac{N}{8\pi}K_t a\left(1-\mathrm{e}^{-i\omega_c T}\right) \tag{4.84}$$

Solving equation (4.83) numerically will give eigenvalues with complex and real parts $(\Lambda=\Lambda_R+i\Lambda_I)$, and from Euler's formula, $\mathrm{e}^{-i\omega_c T}=\cos\omega_c T-i\sin\omega_c T$. When this is substituted into equation (4.84), the complex part has to vanish (i.e. $\Lambda_I(1-\cos\omega_c T)=\Lambda_R\sin\omega_c T$) because the axial depth of cut a is a real value. Therefore,

$$\kappa=\frac{\Lambda_I}{\Lambda_R}=\frac{\sin\omega_c T}{1-\cos\omega_c T}=\tan\psi, \tag{4.85}$$

where ψ is the phase shift of the eigenvalues. From this expression the relationship between the frequency and the spindle speed is obtained (Altintas, 1995) as follows;

$$\begin{aligned}
&\omega_c T=\varepsilon+2k\pi,\\
&\varepsilon=\pi-2\psi,\\
&\psi=\tan^{-1}\kappa,\\
&n=\frac{60}{NT},
\end{aligned} \tag{4.86}$$

where ε is the phase difference between the inner and outer undulations, k is an integer corresponding to the number of vibration waves within a tooth period and n is the spindle speed (rpm). Substituting equation (4.85) into (4.84) and the final expression for chatter free axial depth of cut becomes,

$$a_{\lim}=-\frac{4\pi\Lambda_R}{NK_t}\left(1+\kappa^2\right) \tag{4.87}$$

Therefore for a given chatter frequency, ω_c the eigenvalues are obtained from equation (4.83), which allows for the critical depth of cut to be calculated

using equation (4.87) and finally the spindle speed using equation (4.86) for different number of vibration waves, k. This is repeated for various frequencies around the structures dominant modes.

4.3.2. State Space Approach to the System's Transfer Function

The element formulation was discussed in section 4.2.4 and the stiffness and mass matrices can be used to define the domain with very good accuracy. This however comes at the cost of large matrices sizes as large as 30000×30000. It is for this reason that FEM commercial packages are well suited with some optimization algorithm or the other embedded within the code to deal with the large matrices encountered.

While most commercial packages can be used to obtain very good results in structural analysis, it is always desirable to write a program that is tailored towards analysing a main process. This allows for quicker modelling time as the options that are not pertaining to the process wouldn't necessarily be included in the program. Furthermore, a much simplified user interface would then be made possible. Most especially for real end users like machinists working on the 'shop floor'. There have been various commercial software packages of this nature, for example 'Metalmax', 'CutPro' and 'ShopPro', that aim to analyse different aspects of milling, from experimental modal analysis, to cutting force modelling and so on.

With the system matrix available and dynamic parameters known, in order to obtain the system's transfer function using any Finite Element Method (FEM) approach, the location of the input would have to be changed and the FEM simulation re-run to obtain the response of the system to an input force. This approach in itself is capable of attaining accurate results (as demonstrated in Case studies in section 4.3) and even in modelling the change in dynamics along a thin wall in Chapter 6. However, in order to further simplify the process, a new 'State Space' approach to obtaining the system's transfer function is proposed.

Model Formulation

The state-space is an alternate approach to defining the relationship between the input and output of a system using state variables. The state variables are a set of numbers, with sufficient information to allow computation of system behaviour at any future given time. The state space is summarised below, while an in-depth study can be found in (Timothy, 1968). The standard second-order differential equation of motion given in equation (4.2) is used for its formulation.

Since the vector $\mathbf{x}$ in equation (4.2) is completely defined by the initial conditions $\mathbf{x_0}$ and $\dot{\mathbf{x}}_\mathbf{0}$ and input $\mathbf{F}$, we define the column vector $\mathbf{y}(t_0) = \mathbf{y}_0$. Hence,

$$\mathbf{y}_\mathbf{0} = \begin{pmatrix} \mathbf{x_0} \\ \dot{\mathbf{x}}_\mathbf{0} \end{pmatrix} \tag{4.88}$$

A unique output solution $\mathbf{x}$ is determined by $\mathbf{F}$ and $\mathbf{y}_0$, therefore,

$$\mathbf{y} = \begin{pmatrix} \mathbf{y_1} \\ \mathbf{y_2} \end{pmatrix}, \tag{4.89}$$

can be defined as a state vector, while,

$$\left.\begin{aligned} \dot{\mathbf{y}}_\mathbf{1} &= \dot{\mathbf{x}} = \mathbf{y_2}, \\ \dot{\mathbf{y}}_\mathbf{2} &= \ddot{\mathbf{x}} \end{aligned}\right\} \tag{4.90}$$

Therefore by substituting for $\ddot{\mathbf{x}}$ in equation (4.2) the following is (Timothy, 1968) obtained,

$$\dot{\mathbf{y}}_\mathbf{2} = \mathbf{M}^{-1}\mathbf{F} - \left(\mathbf{M}^{-1}\mathbf{C}\right)\mathbf{y_2} - \left(\mathbf{M}^{-1}\mathbf{K}\right)\mathbf{y_1} \tag{4.91}$$

Hence,

$$\begin{pmatrix} \dot{\mathbf{y}}_\mathbf{1} \\ \dot{\mathbf{y}}_\mathbf{2} \end{pmatrix} = \begin{pmatrix} \mathbf{0} & \mathbf{I} \\ -\mathbf{M}^{-1}\mathbf{K} & -\mathbf{M}^{-1}\mathbf{C} \end{pmatrix} \begin{pmatrix} \mathbf{y_1} \\ \mathbf{y_2} \end{pmatrix} + \begin{pmatrix} \mathbf{0} \\ \mathbf{M}^{-1}\mathbf{I} \end{pmatrix} \mathbf{F}, \tag{4.92}$$

which is known as the system or state equation, where $\mathbf{I}$ is an identity matrix. Just like before, the solution is uniquely determined by $\mathbf{F}$ and $\mathbf{y}_0$, as a result the output equation is,

$$\mathbf{x} = \begin{pmatrix} \mathbf{I} & \mathbf{0} \end{pmatrix} \begin{pmatrix} \mathbf{y}_1 \\ \mathbf{y}_2 \end{pmatrix} \tag{4.93}$$

Therefore, the 'state vectors' in equations (4.90) and (4.91) for the differential system in equation (4.2) are generally written (Jaymin, 2001) as,

$$\dot{\mathbf{y}} = [\mathbf{A}]\mathbf{y} + [\mathbf{B}]\mathbf{F}, \tag{4.94}$$

$$\mathbf{x} = [\mathbf{C}]\mathbf{y} + [\mathbf{D}]\mathbf{F}, \tag{4.95}$$

where, for n state variables, i inputs, l outputs, $[\mathbf{A}]$ is the $n \times n$ system/state matrix, $[\mathbf{B}]$ is the $n \times i$ input matrix, $[\mathbf{C}]$ is the $l \times n$ output matrix, $[\mathbf{D}]$ is the $l \times i$ coupling matrix between inputs and outputs (for simplicity this is taken as null), $\mathbf{F}$ is the $i \times 1$ input/control vector, $\mathbf{x}$ is the $l \times i$ output vector, $\mathbf{y}$ is the $n \times 1$ state vector.

Using this approach, the response for any desired output point can be obtained for any specified input point. It also easily allows for multiple input and output as well. The input point and output point can be easily changed according to where the force is acting or where the response is required.

The System's Transfer Function

To obtain the transfer function from the state space equations, it is simply defined in Laplace transform domain, while ignoring the initial conditions (He, 2001) as,

$$s\tilde{\mathbf{y}}(s) = \mathbf{A}\tilde{\mathbf{y}}(s) + \mathbf{B}\tilde{\mathbf{f}}(s), \tag{4.96a}$$

$$s\tilde{\mathbf{y}}(s) - \mathbf{A}\tilde{\mathbf{y}}(s) = \mathbf{B}\tilde{\mathbf{f}}(s), \tag{4.96b}$$

$$\tilde{\mathbf{y}}(s)(s\mathbf{I} - \mathbf{A}) = \mathbf{B}\tilde{\mathbf{f}}(s), \tag{4.96c}$$

$$\tilde{\mathbf{y}}(s) = (s\mathbf{I} - \mathbf{A})^{-1}\mathbf{B}\tilde{\mathbf{f}}(s), \tag{4.96d}$$

$$\tilde{\mathbf{x}}(s) = \mathbf{C}\tilde{\mathbf{y}}(s) + \mathbf{D}\tilde{\mathbf{f}}(s) \tag{4.97}$$

Therefore,

$$\tilde{\mathbf{x}}(s) = [\mathbf{C}](s\mathbf{I} - \mathbf{A})^{-1}\mathbf{B}\tilde{\mathbf{f}}(s) + \mathbf{D}\tilde{\mathbf{f}}(s), \tag{4.98a}$$

$$\mathbf{G}(s) = [\mathbf{C}](s\mathbf{I} - \mathbf{A})^{-1}\mathbf{B} + \mathbf{D} \tag{4.98b}$$

The transfer function is defined over the complex Laplace plane, s as described in previous section. The frequency response function (FRF) or transfer function is simply the $i\omega$ – axis in the s – plane $(\text{i.e. } s = i\omega)$. Therefore, the system's transfer function is defined in state space representation as,

$$\mathbf{G}(i\omega) = [\mathbf{C}]((i\omega)\mathbf{I} - \mathbf{A})^{-1}\mathbf{B} + \mathbf{D} \tag{4.99}$$

The steps for deriving the system stiffness and mass matrices (K and M) are given in section 4.2.4, while the new approach to model and/or predict proportional damping proposed in section 4.2.3 can be used to obtain the damping matrix.

Much efforts were made to use various available approximation methods to help reduce or to solve very large matrices. However it was either too computationally slow to implement the method or the solutions obtained were highly sensitive to the approximations introduced. Due to the nature of the solution sought (i.e. prediction of stable margins), errors in the extracted system's dynamics can very quickly render the approach useless/unproductive. Hence a simple FEM approach is thus proposed in conjunction with discrete Fourier transform.

4.3.3. Fourier Approach to the System's Transfer Function

To obtain the transfer function of the system, the time domain response to a dynamic loading was obtained using the modal dynamic analysis on Abaqus described in section 4.2.4. Therefore the dynamic response (output) for the workpiece to the dynamic loading (input) is obtained from equation (4.60a).

The system's frequency response function (FRF), is simply the ratio of the Fourier transform of the output/dynamic response over the input/dynamic loading (in the case of a system with single input and output) i.e.,

$$G_{\beta nq}(\omega)=\frac{X_{\beta nq}(\omega)}{F_{pnq}(\omega)} \qquad (p=c,w),(n=x,y),(q=x,y) \tag{4.100}$$

The discrete Fourier transform (DFT) algorithm is adopted, which is defined (Smith, 1997) as,

$$\begin{aligned} \mathrm{Re}\,G[\Theta] &= \sum_{\tau=0}^{M-1} h[\tau]\cos\left(\frac{2\pi\Theta t}{M}\right), \\ \mathrm{Im}\,G[\Theta] &= -\sum_{\tau=0}^{M-1} h[\tau]\sin\left(\frac{2\pi\Theta t}{M}\right) \end{aligned} \tag{4.101}$$

where Θ runs from 0 to $M/2$, $\mathrm{Re}\,G[\Theta]$ and $\mathrm{Im}\,G[\Theta]$ are the real and imaginary parts of the frequency domain signal and $h[\tau]$ is the time domain signal.

The corresponding frequencies are defined as,

$$\omega=\frac{k\cdot f}{M-1}, \tag{4.102}$$

were ω is the frequency, f is the sampling frequency.

4.3.4. The Finite Element Model

The workpiece material used in the FEM model is Aluminium Alloy 7010 T7651 and its properties are given in section 4.2.4. The three different types of workpiece in Tables 4.1, 4.2 and 4.3 were used in the finite element analysis (FEA). The dimensions are shown in Figure 4.3 and the different thicknesses, (W) are given in Tables 4.1, 4.2 and 4.3 respectively. The damping ratios, ζ_p used in equation (4.29) were identified through impact tests and are given in Tables 4.1, 4.2 and 4.3.

The assumptions made in the finite element analysis (FEA) are as follows:

- The workpiece was bolted at the back surface during the impact tests and in the FEM this was assumed to be clamped.
- The workpiece was bolted to the milling machine during the impact test and it was assumed that the natural frequencies of the machine are very high compared to that of the workpiece, hence their influence can be ignored in the FEM analysis.
- The mass of the accelerometer was assumed to be a point mass added to the FEM model. Although the addition of the point mass was only done at this stage to validate the proposed approach to extracting the structures transfer function. When this approach is later used in section 4.4 to show the application of previous damping prediction approach in section 4.3, the accelerometer mass is not added.

4.3.5. Results

Extracting the Workpiece Transfer Function

For Case C, the measured input force from the impact test was used as the input force (in time domain) in the FEM modal analysis. The predicted

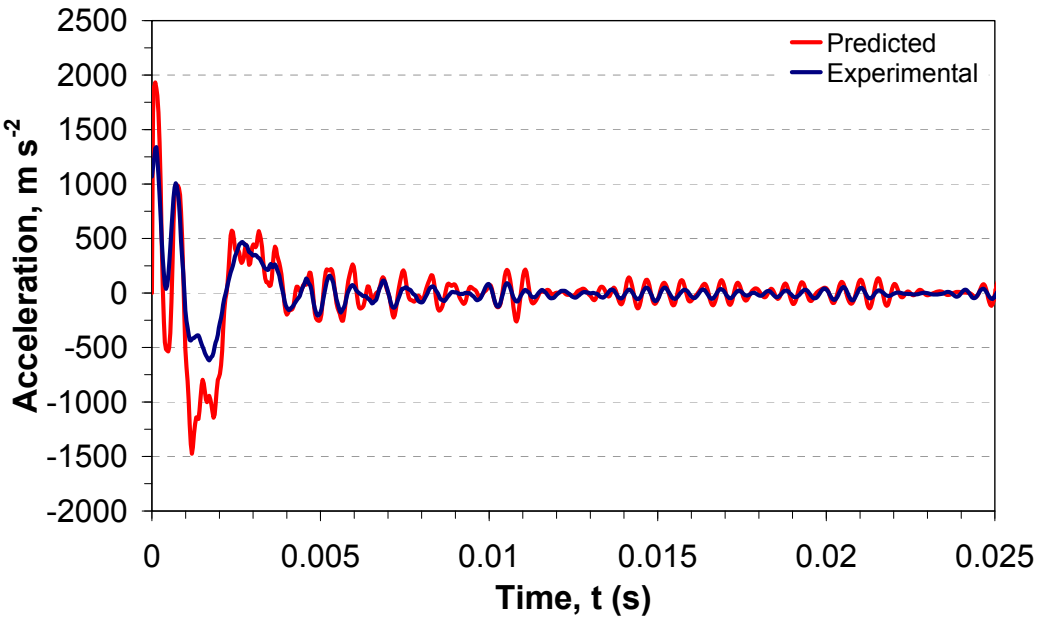

Figure 4.12. Predicted and measured acceleration for Case C.

acceleration (in time domain) is shown in comparison to the experimental acceleration from the accelerometer (during the impact test) in Figure 4.12. The predicted FRF (using the approach in section 2) and experimental FRF, are compared in Figures 4.13a and 4.13b respectively. The agreement between the experimental results and the predictions is satisfactory.

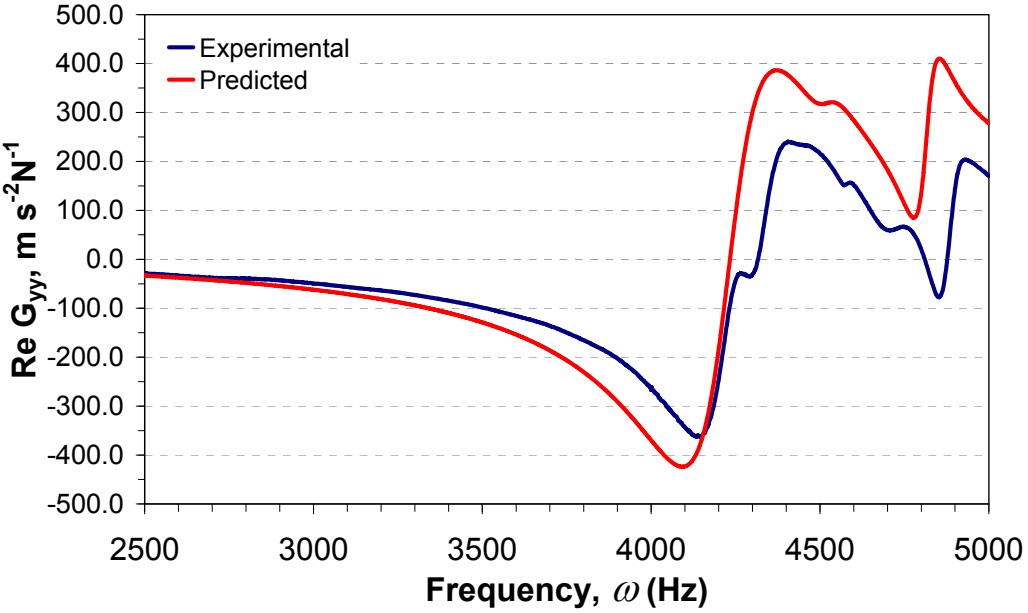

(a) Real G_{wyy}

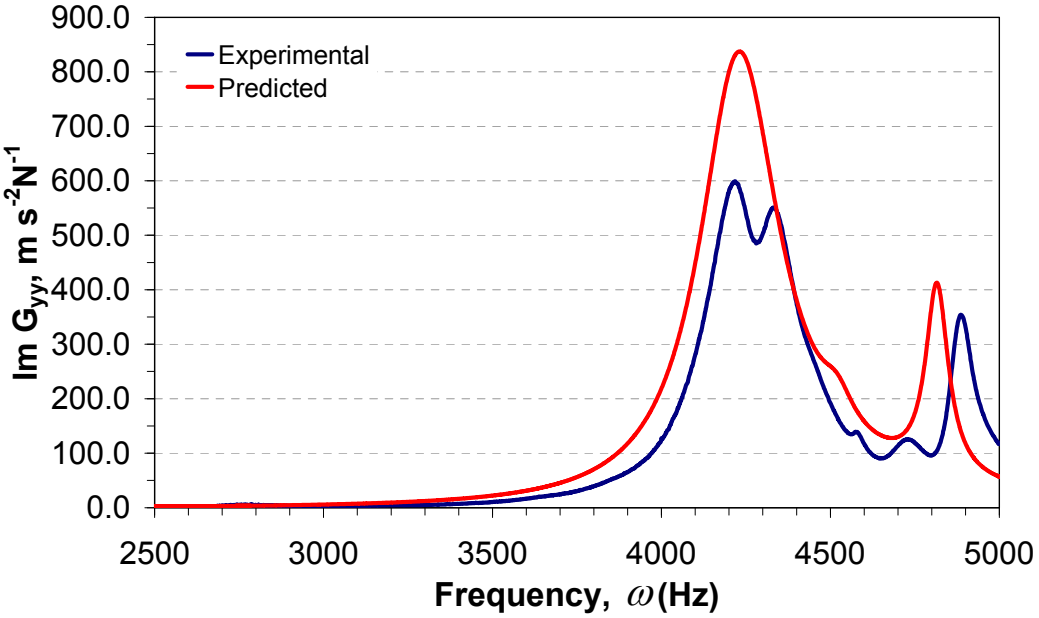

(b) Imag G_{wyy}

Figure 4.13. Predicted and measured FRFs for Case A.

For Cases B and C, the input force (in time domain) used in the FEM modal analysis was a Dirac delta function. The predicted and experimental FRFs are compared in Figures 4.14 and 4.15. The agreement between the experimental results and the predictions is satisfactory. It should be noted that though the frequency response of the workpiece are identified only in the normal direction (*Y*), they can equally be extracted for the feed and axial directions (*X* and *Z*).

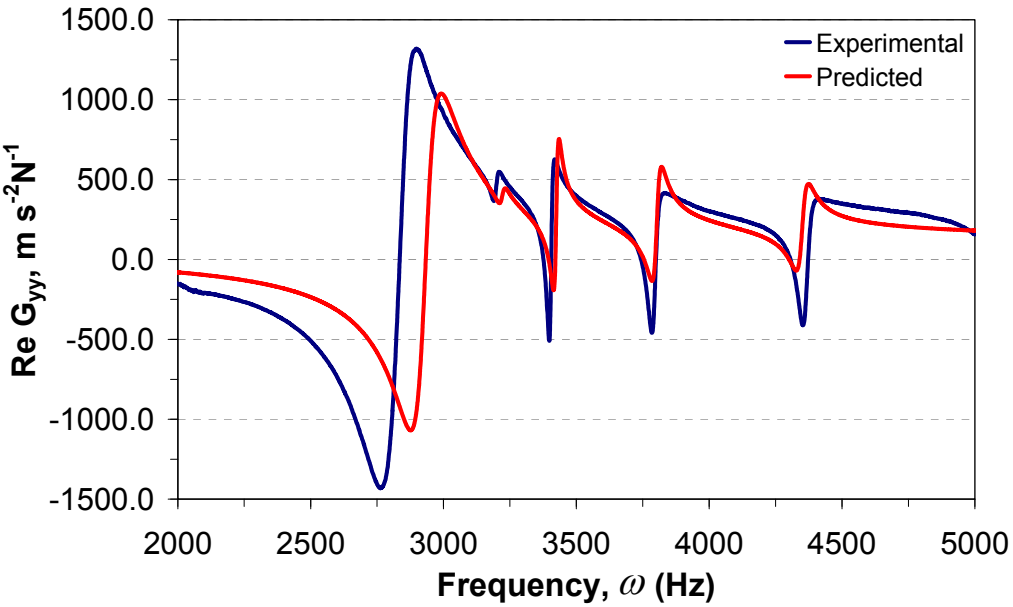

(a) Real G_{wyy}

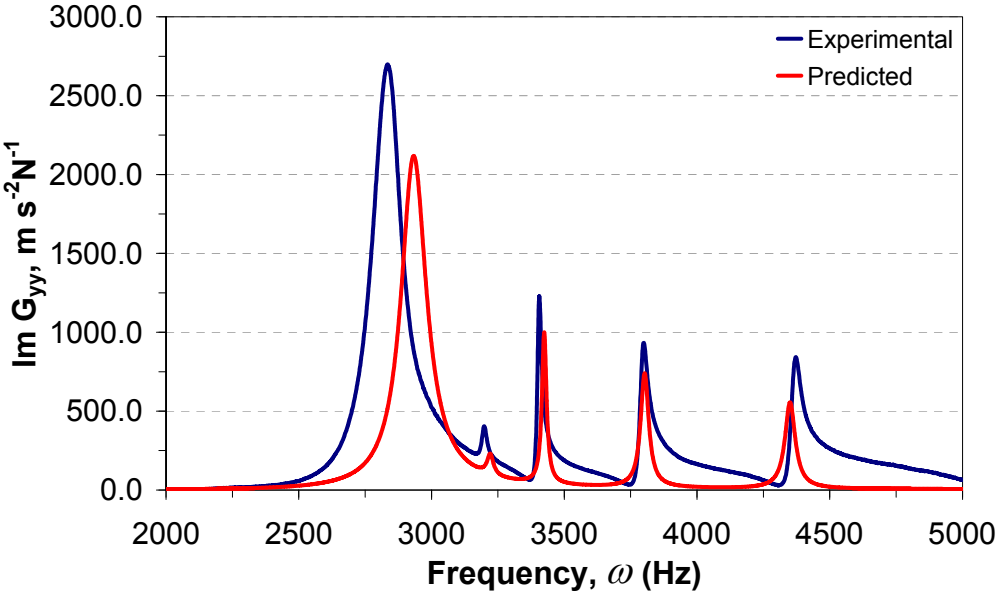

(b) Imag G_{wyy}

Figure 4.14. Predicted and measured FRFs for Case B.

The results here are used to validate the presented approach. Moreover, an advantage this approach presents is actually in the fact that the FRF for the system can be identified in any specified spatial direction. Whilst experimentally, extracting the FRF for a structure can be challenging depending on the geometry of the structure.

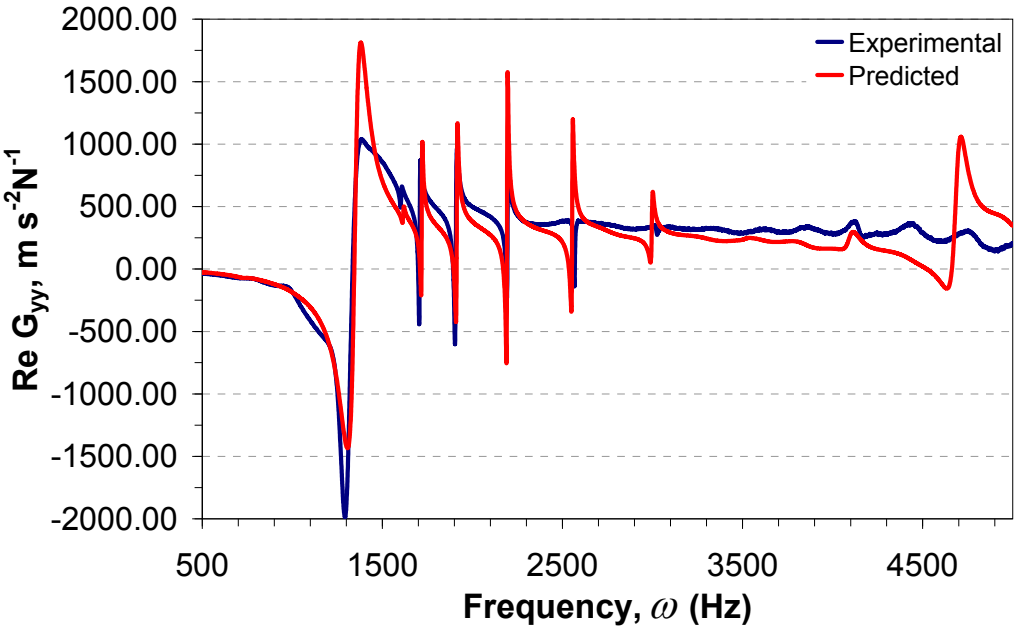

(a) Real G_{wyy}

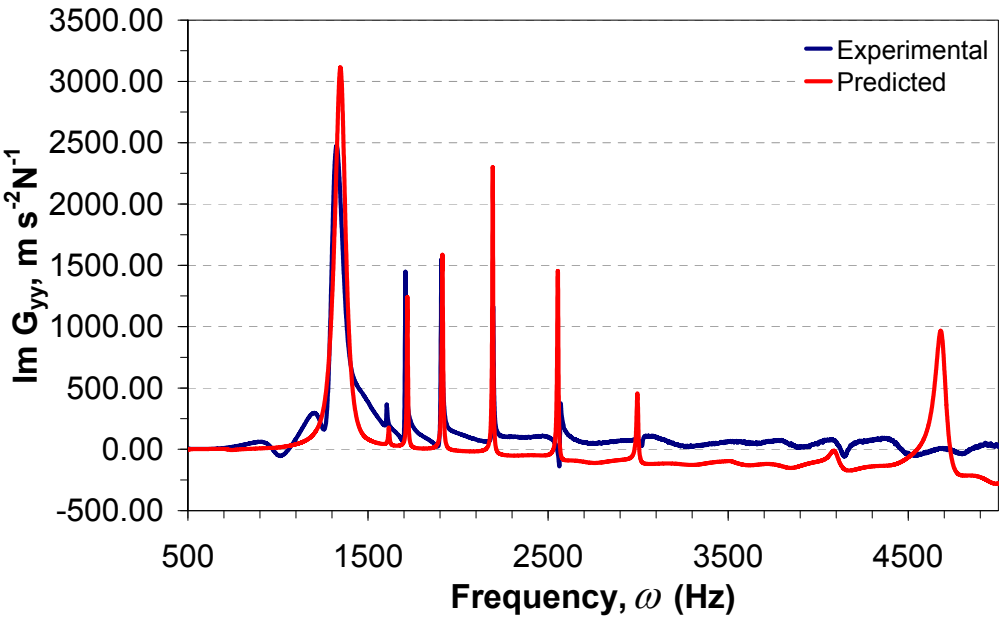

(b) Imag G_{wyy}

Figure 4.15. Predicted and measured FRFs for Case C.

Chatter Stability Lobes

The stability lobe model described in section 4.3.1 was programmed using Matlab. Using both the predicted and experimental FRFs, the stability lobes were generated for the three different types of workpiece using the cutting conditions listed in Table 4.11. The cutting force coefficients were assumed as constant and their values given in Table 4.11 were calibrated in Chapter 3, where ‘‘RCFC’’ and ‘‘TCFC’’ are the radial and tangential cutting force coefficients respectively. The axial depth of cut they correspond to are given in Table 4.11. Due to the nonlinear behaviours or the cutting force coefficients an average is normally used; however in Chapter 5, an approach that accurately predicts the stability lobes with nonlinear coefficients is developed. In the transfer function matrix $[G(i\omega_c)]$, the elements for the $G_{pxx}(i\omega_c)$, $G_{pxy}(i\omega_c)$ and $G_{pyx}(i\omega_c)$ are given small values (1E-16) as only the direct transfer function $G_{pyy}(i\omega_c)$ was extracted. The predicted and experimental results are compared in Figures. 4.16(a), 4.16(b) & 4.16(c) for the three different workpiece.

The slight discrepancy in the predicted natural frequency (frequency at which FRF real is zero and imaginary is maximum) can be seen in the slight shift in the spindle speed calculated in the stability lobes. The natural frequency predicted affects the stable tooth passing frequency ω_T calculated in the stability lobes, hence the slight differences seen in the spindle speeds. The predicted stable axial depth of cuts in Figures 4.16(b) and 4.16(c) are slightly higher than the experimental stable ADOC and this is due to the FEM model being too stiff. This can be caused by the boundary condition assumption stated in section 4.3.4, where the back surface was assumed to be perfectly clamped.

Table 4.11. Cutting conditions and cutting force coefficients

	Workpiece A	**Workpiece B**	**Workpiece C**
RCFC, K_r	1.1459	0.3030	-0.7040
TCFC, K_t **(MPa)**	679.6021	801.0970	981.6966
Axial Depth of Cut, (mm)	6.00	2.50	0.50
Radial Depth of Cut, (mm)	2.00	1.00	0.50

In the FEM stiffness matrix, the diagonal elements corresponding to these degrees of freedom are therefore given a very high value (1E+36) and the degrees of freedom at this surface are not included in the simulation. A more accurate approach would require knowledge of the friction at the boundary between the machine and the workpiece.

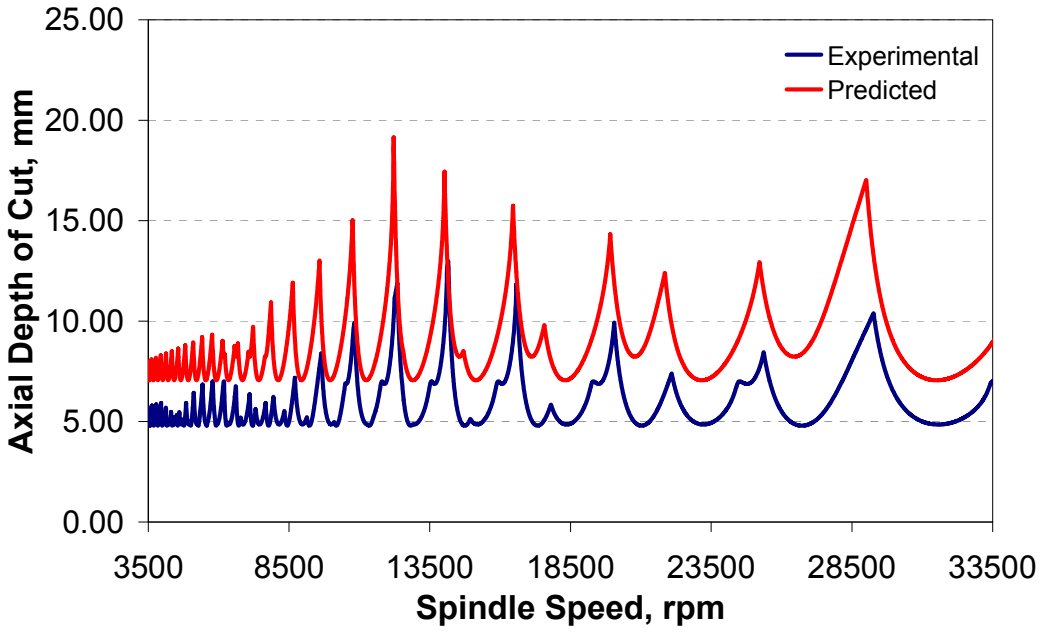

(a) Case A

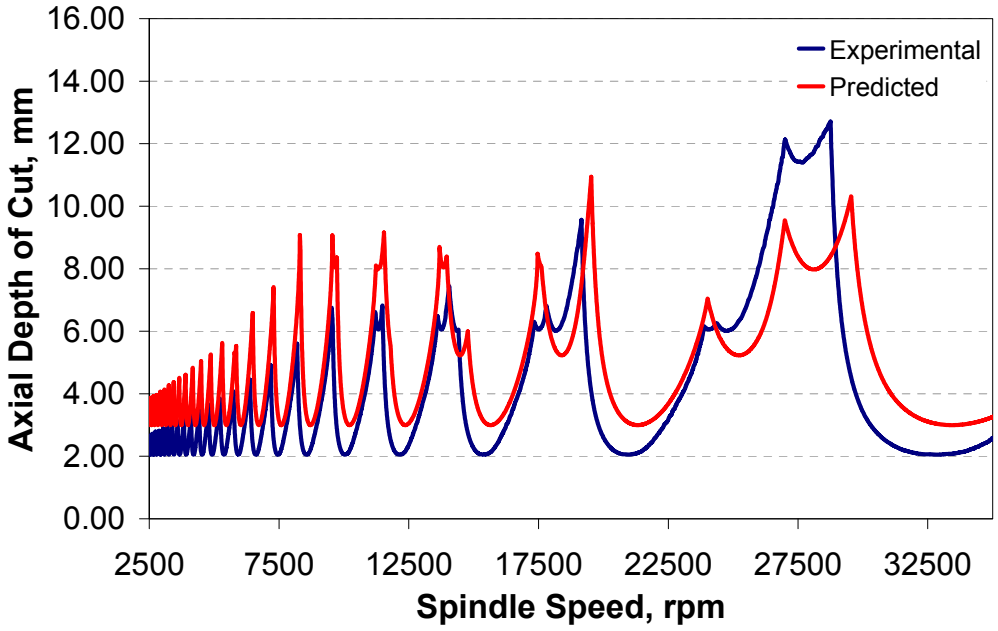

(b) Workpiece B

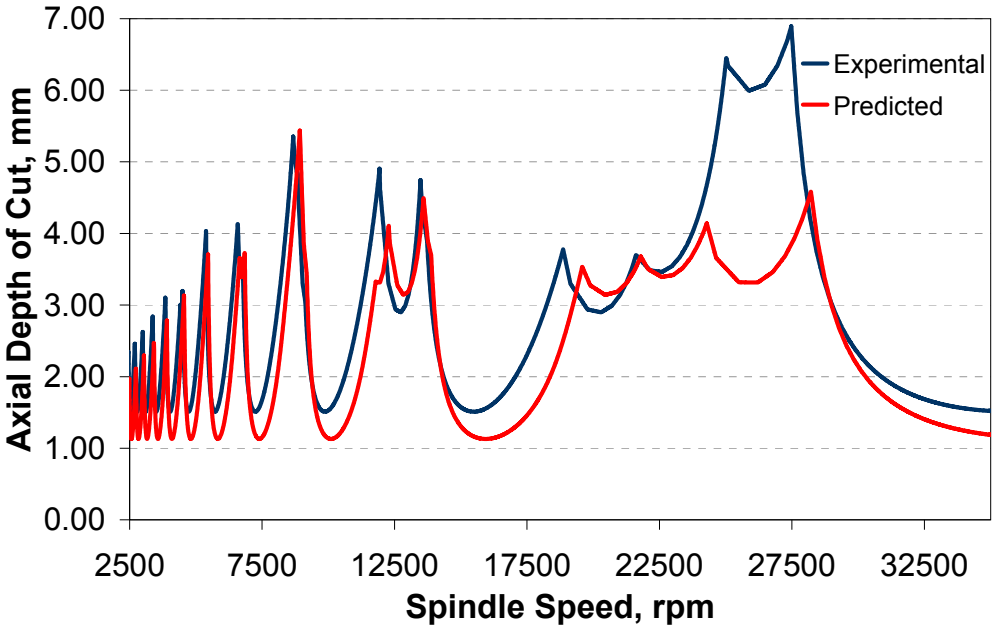

(b) Workpiece C

Figures 4.16. Stability lobes comparison.

4.4. Numerical Prediction of Stable Margins in Thin Wall Machining

In this section, the above proposed approach to damping prediction and modelling, the FEM and Fourier approach for extracting structure's FRF presented are applied to thin wall machining stable margin prediction. It is shown in this chapter that only one experimental tap test result is required during thin wall machining. This is because the damping parameters required for subsequent wall thicknesses can be predicted using the proposed approach. An example of predicted stable regions using both experimental and numerical FRF's gave a good comparison. Though the damping model is believed to be at a development stage its direct application is clearly shown in this section.

4.4.1. Damping Prediction Applications

When machining a wall section, the materials are taken off in layers which change the workpiece's geometry and hence its damping parameters. An approach that identifies a certain trend in the changes the workpiece thickness has on the damping parameter was proposed in section 4.2. This approach defines the damping parameters of a wall section as a function of another similar wall with a different thickness. When machining a simple wall section as shown in Figure 4.3, the wall thickness progressively gets thinner until the desired thickness is acquired. To fully implement the well developed stability lobe model summarised in section 4.3.1, the damping parameters are required, most especially when machining thin walled structures. Hence, the proposed approach can be directly used to predict the damping parameters as the workpiece thickness reduces, while mass and stiffness parameters can be modelled numerically with satisfied accuracy.

During process planning, the damping parameters for the starting wall thickness can be extracted by performing a single tap test experiment, which is used in the prediction of the starting wall's stable margins. Based on the radial depth of cut used in the calculation of the stable margins, the new wall thickness

is known. This can then be used in equations (4.27 and 4.28) to predict what the damping parameters for the next wall would be, where $\overline{\zeta}_p$ and $\overline{\omega}_p$ are obtained using equations (4.25 and 4.26) using the experimental tap test results. These damping parameters are subsequently used in the finite element approach (as explained in section 4.3) to predict the transfer function. Hence, the stable margins for the next wall can be calculated using this predicted transfer function without any experimental tests conducted.

During the design stage, with the knowledge of the damping parameters for the initial workpiece, the final optimum design can be obtained based on a trade off between weight and machinability. Though information about the weight is simply calculated, information about the machinability is dependent on the stable regions predicted for the wall thicknesses after the initial wall thickness. Therefore this approach can also be used at this stage without the need to carry out cumbersome machining tests.

To fully apply the predicted damping parameters, the finite element approach presented in section 4.3 is required. This approach deals with the stiffness and mass parameters along with the damping parameters by predicting the systems frequency response function (section 4.3.2). Therefore the stable margin can be predicted for thinner walls.

4.4.2. Results

To show this application, the damping parameters for Case 2B predicted in section 4.2.5 are used to extract the stability lobes and compared with stability lobes obtained using experimentally identified damping parameters. Using the damping parameters predicted in Figure 4.7(b), the FEM and Fourier approach (section 4.3.2), the frequency response function is extracted and shown in Figure 4.17. This frequency response function is solely based on prediction and a good comparison is seen with experimentally identified FRFs'.

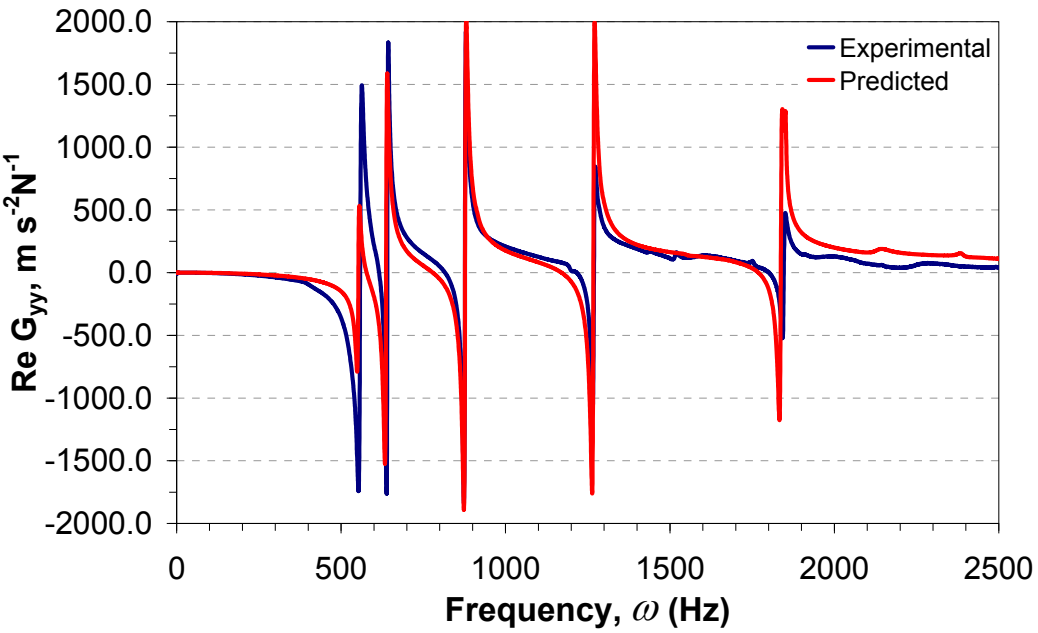

(a) Real G_{wyy}

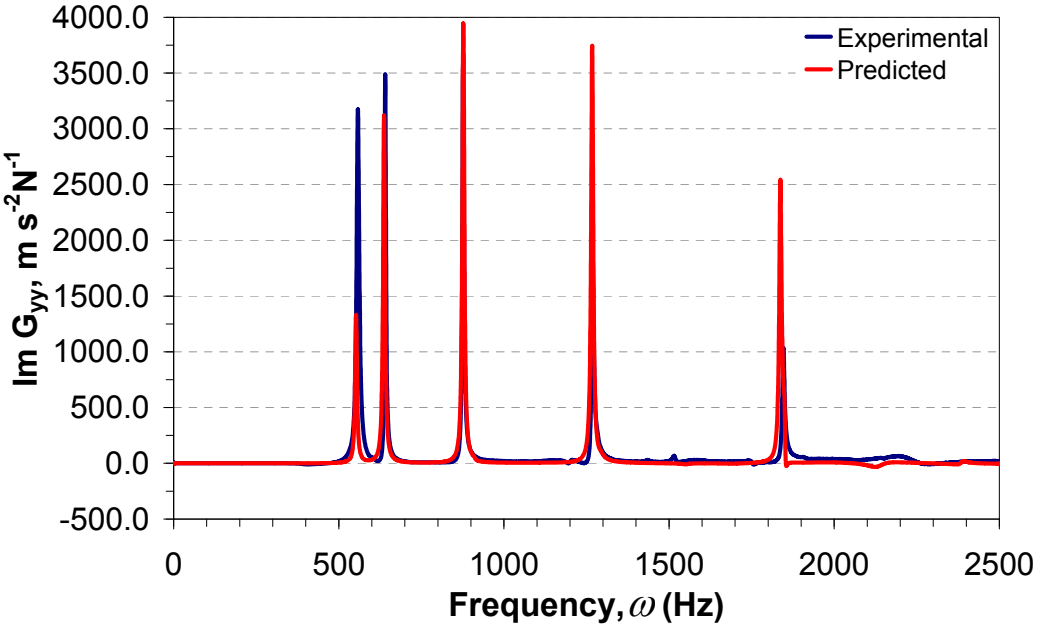

(b) Imag G_{wyy}

Figure 4.17. Predicted and measured FRFs for Case 2B.

The identified frequency response function (FRF) of the workpiece was used to extract the stable margins using the approach briefly summarised in section 4.3.1 as shown in Figure 4.18. The cutting force coefficients are again assumed as constant and the coefficients for an axial depth of cut of 0.50mm were

used. As detailed in Chapter 3 the tangential cutting force coefficient = 981.6966 (Nmm^{-2}), while the ratio of the radial to the tangential cutting force coefficients = -0.7040. A radial depth of cut of 0.50mm was used in the stability lobes model.

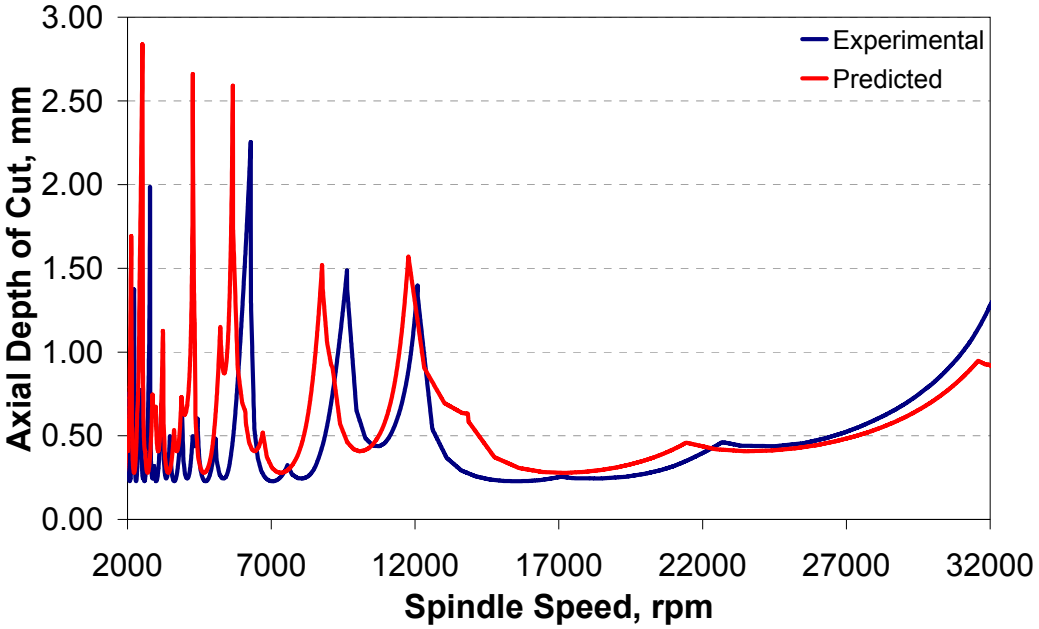

Figures 4.18. Stability lobes comparison for Case 2B.

4.5. Summary

In this chapter, different aspects of tool and workpiece structural dynamics have been covered. A new approach to predict and model the damping parameters for thin walls was proposed. Different numerical methods to obtain the system's transfer function were introduced, with the aim to reduce the reliance on experimentally results. The models were experimentally validated, except for the State Space approach. This approach was only introduced without any results due to limitations imposed by available computer resources. The damping model proposed was also compared with existing models.

Chapter 5

Tool Chatter

5.1. Introduction

Even after such an extensive research into chatter vibration, it still is (as stated by Taylor just over a century ago) one of the most obscure and delicate of all problems facing the machinist (1907). It certainly undermines and reduces productivity and surface quality in manufacturing. It could also increase the cost through possible machine or tool damage. It is because of these effects that it has been the topic of several studies over the years. The stability lobes/chart approach is more practical from the stance of a machinist, while its extraction can be somewhat tedious. The predicted stable region relies on the transfer function identified at the cutter-workpiece contact zone. The classical approach to obtaining this transfer function is through impact test, though an FEM approach was proposed in Chapter 4.

The prediction of stable conditions in the form of charts started when, Tobias (1958) and Tlusty (1963) simultaneously made the remarkable discovery that the main source of self-excited regenerative vibration/chatter was not related to the presence of negative process damping as it was previously assumed. However, it is related to the structural dynamics of the machine tool-workpiece system and the feedback response between subsequent cuts. Their model is only

applicable to orthogonal metal cutting where the directional dynamic milling coefficients are constant and not periodic. Other studies on the stability of orthogonal metal cutting were reported by Merritt (1965).

After various attempts to model the stability margin for milling whilst respecting the varying directional cutting coefficients (Slavicek, 1965; Vanherck 1967; Sridhar, 1968a, 1968b; Hohn, 1968; Optiz, 1968, 1970; Tlusty, 1970), Altintas and Budak (1995, 1994, 1996a, 1996b, 1998a, 1998b) later proposed an analytic approach to predict stability margin. Perhaps, the first analytical approach in which the zeroth order term in the Fourier series expansion (single frequency solution or zeroth order approximation) of the time varying coefficients was adopted. The analytical model was later extended to include three directions by Altintas (2001), where the axial immersion angle was assumed to be constant. Except for flat end mills however, the axial immersion angle, is a function of the axial depth of cut. Campa et al. (2007) later proposed an averaging approach to calculating the axial immersion angle in order to solve the stability model analytically. However, the axial immersion angle was still assumed to be a constant. This is the main analytical approach generally used in predicting stable cutting conditions in machining (Bravo, 2005; Solis, 2004; Lacerda, 2004).

Davies (2000) and Endres (2000) showed on the other hand that the classical chatter stability model, which neglects the degree of intermittent process, cannot accurately predict the stability lobes at low radial immersion milling operations; for which they showed the presence of additional lobes around high spindle speed ranges that may be effective during thin wall machining. The study by Davies led to two types of vibrations, which are generally known as Hopf and Flip bifurcations. The same problem was studied by (Insperger, 2000; Insperger, 2004; Stepan, 2005; Gradisek, 2005). Merdol and Altintas (2004) further extended the multi-frequency model by Budak and Altintas (1998a), to predict the added lobes due highly intermittent milling process.

One of the major drawbacks from the models proposed in the literature is that they assume the cutting force coefficients are constant. As shown in Chapter 3, the cutting force coefficients for a general end mill are a function of the axial depth of cut. The cutting force coefficients have also been reported as a variable

of the axial depth of cut by (Lim, 1995; Gadalla, 1997; Engin, 1999, 2001; Altintas, 2000, 2001; Gradisek, 2004), where the calibrated coefficients are generally fitted quite accurately with a polynomial expression. Hence, to better model the cutting forces in the stability lobe model, this non-linearity would have to be modelled. Although the majority of these studies have been carried out using a flat end mill, for which the cutting coefficients can be assumed to be constant as shown in Chapter 3. However when modelling the stability margin for a general end mill (e.g. bull nose or ball end milling tool), the non-linearity of the cutting force coefficients and axial immersion can not be ignored. The axial immersion was used in Chapter 3 to resolve the cutting forces into their radial and axial components.

Therefore this chapter is structured as follows; improvements to the zeroth order approximation when predicting stable cutting conditions for corner radius end mills and a numerical approach to obtaining more accurate results are proposed. The numerical approach obtains more accurate results by modelling the cutting force more accurately using the non-linear cutting force coefficients and the axial immersion angle dependent on the axial depth of cut. The results are validated extensively using experimental results towards the end of the section. The extended multi-frequency model by Merdol (2004) is further improved in this chapter; first by developing the formulation for a three-dimensional system and then by including the non-linearity of the cutting force coefficients and the axial immersion, thereby producing more accurate stability margin predictions. Although the process was not highly intermittent and the results obtained do not depict any added lobes, it however confirms the accuracy of the developed formulation.

5.2. Improved Stability Lobes Prediction using Non-linear Cutting Force Coefficients

This section presents improvements to the well developed stability lobe model summarised in Chapter 4 by considering the cutting force coefficients and axial immersion angle as a variable along the axial depth of cut. The cutting force coefficients which help to model the cutting forces in the stability lobes are a variable along the axial depth of cut. Therefore an algorithm that predicts stable axial depth of cuts for different spindle speed whilst using non-linear cutting force coefficients is proposed. The results obtained for tool dynamic vibrations are validated extensively using experimental results and a very good agreement is seen.

5.2.1. The Chatter Stability Model

The stability model used in this section is similar to the model proposed by Altintas (2001) and was recently proposed by Adetoro et al. (2009). Modifications to this model in a three dimensional orientation are presented in this section. The periodic milling forces excite the cutter and the workpiece in the feed, normal and spindle axis directions, causing three orthogonal dynamic displacements (x), (y) and (z) respectively in the global axis. This generates undulations on the machined surface and each tooth removes the undulations generated by the previous tooth (Figure 5.2), therefore leading to a modulated chip thickness, which can be expressed (Budak, 1998) as,

$$h_j(\phi_j,\gamma) = s_t \sin\phi_j + \left(\upsilon_{jc}^0 - \upsilon_{jw}^0\right) - \left(\upsilon_{jc} - \upsilon_{jw}\right), \tag{5.1}$$

where s_t is the feed per tooth (Figure 5.1), $\left(\upsilon_{jc}^0, \upsilon_{jc}\right)$ and $\left(\upsilon_{jw}^0, \upsilon_{jw}\right)$ are the dynamic displacement of the cutter and workpiece at the previous $(t-T)$ and present t tooth periods respectively, $\phi_j = j\phi_p + \Omega t$ is the angular immersion of tooth j (see Figure 5.2) for a cutter (Ω if the angular speed), with constant pitch

angle $\phi_p = 2\pi/N$ (N is the number of teeth). This modulated chip thickness shown in Figure 5.2 is the practical model as opposed to the chip thickness in the static model in Figure 5.1.

The dynamic displacements in the chip thickness direction due to tool and workpiece vibrations can be resolved into its components as,

$$\upsilon_{j\beta} = \left(x_\beta \sin\phi_j + y_\beta \cos\phi_j\right)\sin\left(\bar{\gamma}\right) - z_\beta \cos\left(\bar{\gamma}\right) \qquad (\beta = c, w), \tag{5.2a}$$

and

$$\upsilon^0_{j\beta} = \left(x^0_\beta \sin\phi_j + y^0_\beta \cos\phi_j\right)\sin\left(\bar{\gamma}\right) - z^0_\beta \cos\left(\bar{\gamma}\right) \qquad (\beta = c, w), \tag{5.2b}$$

where c and w indicate the cutter and workpiece respectively, $\bar{\gamma}$ is the axial immersion angle shown in Figure 5.2, a is axial depth of cut, x_β, y_β and x^0_β, y^0_β are the dynamic displacements in the global axis for the current and previous tooth periods respectively.

The axial immersion, $\bar{\gamma}$ is variable along the tool axis direction. An average method for calculating the axial immersion, $\bar{\gamma}$ was proposed by Campa et al. (2007) in an attempt to solve the stability problem analytically. Altintas suggests assuming the axial immersion, $\bar{\gamma}$ to be acting at the middle of the maximum axial depth of cut. Being able to define a maximum axial depth of cut is however arbitrary.

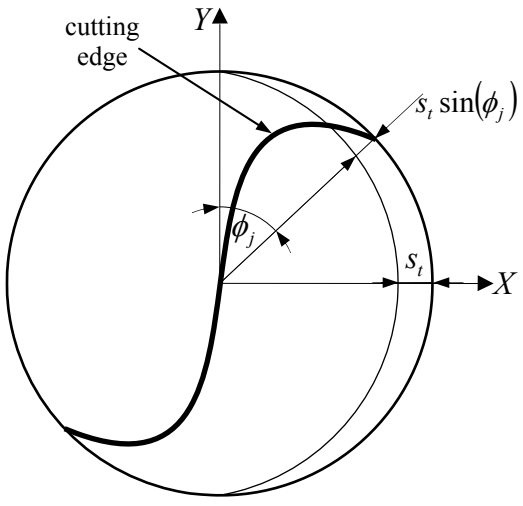

Figure 5.1. Static milling model.

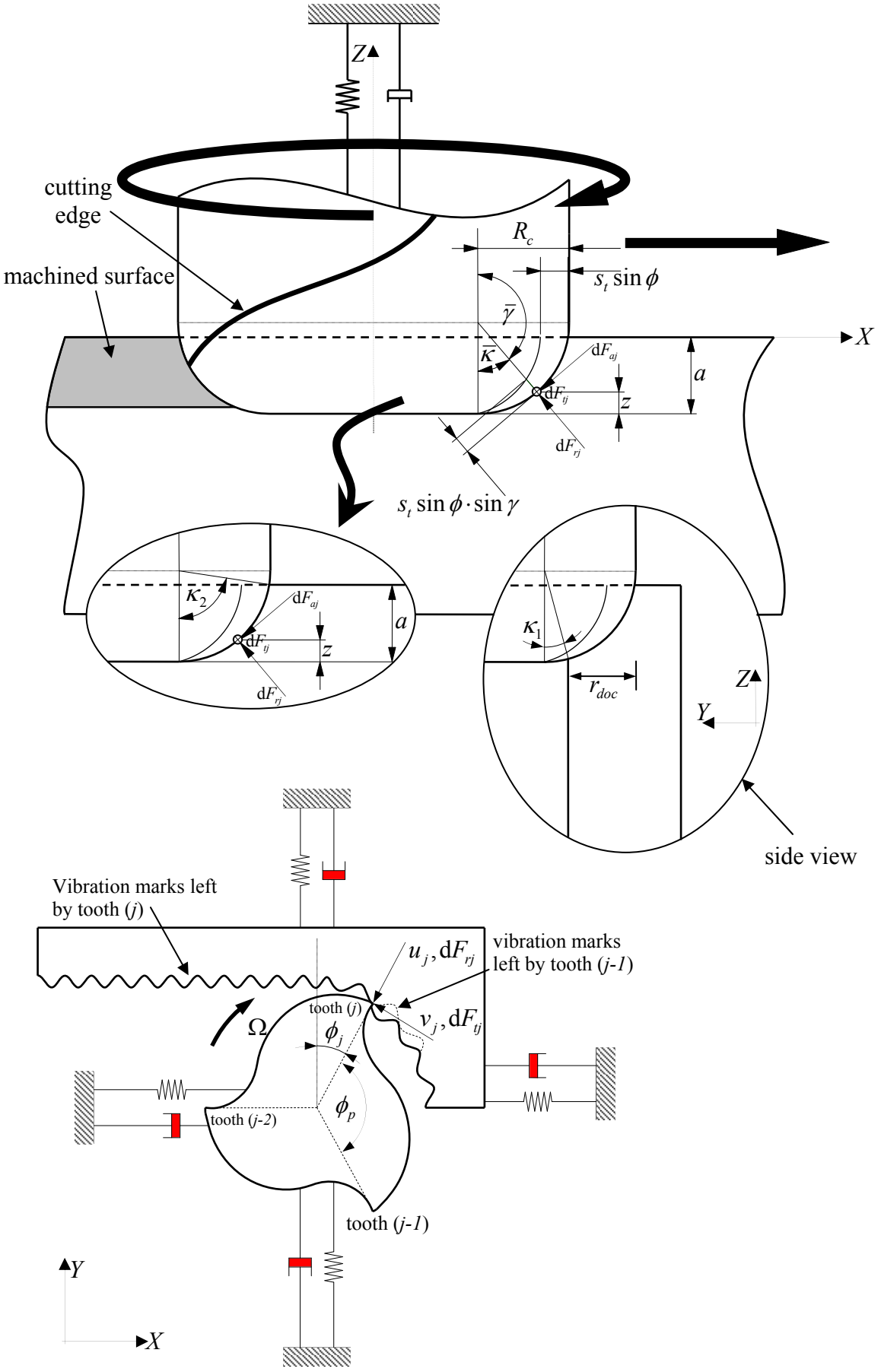

Figure 5.2. Dynamic milling model.

The axial immersion can be defined in terms of the axial depth of cut for bull nose tools as,

$$\bar{\gamma} = \pi - \bar{\kappa}, \tag{5.3}$$

where,

for $a \leq R_c$,

$$\bar{\kappa} = \left[\kappa_1 + \left(\frac{\kappa_2 - \kappa_1}{2} \right) \right], \tag{5.4}$$

$$\kappa_2 = \arcsin\left(\sqrt{1 - \left[\frac{R_z - a}{R_c} \right]^2} \right), \tag{5.5}$$

for radial depth of cut, $r_{doc} > R_c$,

$$\kappa_1 = 0,$$

for radial depth of cut, $r_{doc} \leq R_c$,

$$\kappa_1 = \arctan\left(\frac{R_c - r_{doc}}{\sqrt{R_c^2 - \left[R_c - r_{doc} \right]^2}} \right) \tag{5.6}$$

Though the definition of the axial immersion above is an average value, it can however be shown to give good results within the corner radius. The parameters κ_1, κ_2, κ and R_c are illustrated in Figure 5.2 and κ_1 is the axial immersion angle at the lowest point of intersection of the tool and the workpiece.

Therefore by eliminating the static part in equation (5.1), the dynamic chip thickness in milling is defined as,

$$h_j\left(\phi_j, \bar{\gamma}\right) = \left[\left(\Delta x \sin\phi_j + \Delta y \cos\phi_j \right) \sin\bar{\gamma} - \Delta z \cos\bar{\gamma} \right] g\left(\phi_j\right), \tag{5.7}$$

where,

$$\begin{aligned}\Delta x &= \left(x_c - x_c^0\right) - \left(x_w - x_w^0\right),\\ \Delta y &= \left(y_c - y_c^0\right) - \left(y_w - y_w^0\right),\\ \Delta z &= \left(z_c - z_c^0\right) - \left(z_w - z_w^0\right),\end{aligned} \tag{5.8}$$

and $g\left(\phi_j\right)$ determines whether the tooth is in or out cut, i.e.,

$$\left.\begin{aligned} g\left(\phi_j\right) &= 1 \leftarrow \phi_{start} < \phi_j < \phi_{exit}\\ g\left(\phi_j\right) &= 0 \leftarrow \phi_j < \phi_{start} \quad \text{or} \quad \phi_j > \phi_{exit}\end{aligned}\right\} \tag{5.9}$$

Therefore, the dynamic forces on tooth j in the tangential, radial and axial directions can be defined as,

$$\begin{aligned}F_t^j\left(\phi,\bar{\gamma},a\right) &= K_t(a)ah_j\left(\phi_j,\bar{\gamma}\right),\\ F_r^j\left(\phi,\bar{\gamma},a\right) &= K_r(a)ah_j\left(\phi_j,\bar{\gamma}\right),\\ F_a^j\left(\phi,\bar{\gamma},a\right) &= K_a(a)ah_j\left(\phi_j,\bar{\gamma}\right),\end{aligned} \tag{5.10}$$

where, K_t, K_r and K_a are the tangential, radial and axial cutting force coefficients respectively, a is the axial depth of cut.

This force definition is similar to the linear force model proposed by Budak (1996) with the exception of the edge/ploughing. The edge/ploughing forces are much like the static part of equation (5.1); they do not contribute to dynamic chatter. The linear force model introduces six coefficients as explained in Chapter 3, comprising of three cutting force coefficients, K_{tc}, K_{rc}, K_{ac} and three edge/ploughing force coefficients, K_{te}, K_{re}, K_{ae}. Where K_t, K_r and K_a in equation (5.10) correspond to the tangential, radial and axial cutting force coefficient, K_{tc}, K_{rc}, K_{ac} respectively.

The linear force model's cutting force and edge force coefficients are a function of the axial depth of cut, a as shown in the calibrated coefficients in section 3.3.1 for a tool with a corner radius (refer to Chapter 3). The non-linearity of the cutting force coefficients have also been reported by (Engin, 2001 and Gradisek, 2004). However for simplicity, like the axial immersion γ, the cutting force coefficients, K_t, K_r and K_a are assumed to be constant and an average

value is used as has been reported in numerous studies on stability lobe prediction. However to further improve the stability lobe model, they are considered as a non-linear function of the axial depth of cut here. To model the non-linearity of the cutting force coefficients, a polynomial expression is usually fitted to the data using least squares method as reported by Gadalla (1997) and Altintas (2001). Hence by substituting equation (5.7) into equation (5.10) and resolving in the global directions, the following expression is obtained:

$$\begin{Bmatrix} F_x \\ F_y \\ F_z \end{Bmatrix} = \begin{bmatrix} -\cos\phi_j & -\sin\gamma\sin\phi_j & -\cos\gamma\sin\phi_j \\ \sin\phi_j & -\sin\gamma\cos\phi_j & -\cos\gamma\cos\phi_j \\ 0 & \cos\gamma & -\sin\gamma \end{bmatrix} \begin{Bmatrix} F_t^j \\ F_r^j \\ F_a^j \end{Bmatrix}. \tag{5.11}$$

Substituting equation (5.10) into equation (5.11) and summing the forces from all the teeth and displacements gives the total dynamic milling forces on the tool using,

$$F_x = \sum_{j=0}^{N-1} F_x^j, \quad F_y = \sum_{j=0}^{N-1} F_y^j, \quad F_z = \sum_{j=0}^{N-1} F_z^j, \tag{5.12}$$

Hence,

$$\{F(t)\} = a[A(t)]\{\Delta(t)\}, \tag{5.13}$$

where $\{F(t)\}$ is the force vector in time domain, $\{\Delta(t)\} = \{\Delta x, \quad \Delta y, \quad \Delta z\}^T$ and $[A]$ contains the time varying directional dynamic milling force coefficients that are also dependent on the axial depth of cut through the cutting force coefficients. The elements in matrix $[A]$ are defined as,

$$a_{xx} = \sum_{j=0}^{N-1} g_j \left[-(\sin\phi\sin\gamma\cos\phi)K_t - (\sin^2\phi\sin^2\gamma)K_r - (\sin^2\phi\sin\gamma\cos\gamma)K_a \right] \tag{5.14a}$$

$$a_{xy} = \sum_{j=0}^{N-1} g_j \left[-(\sin\gamma\cos^2\phi)K_t - (\sin\phi\sin^2\gamma\cos\phi)K_r - (\sin\phi\sin\gamma\cos\phi\cos\gamma)K_a \right] \tag{5.14b}$$

$$a_{xz} = \sum_{j=0}^{N-1} g_j \left[(\cos\phi \cos\gamma) K_t + (\sin\gamma \sin\phi \cos\gamma) K_r + (\sin\phi \cos^2\gamma) K_a \right] \tag{5.14c}$$

$$\begin{aligned} a_{yx} = \sum_{j=0}^{N-1} g_j \Big[& (\sin^2\phi \sin\gamma) K_t - (\sin\phi \sin^2\gamma \cos\phi) K_r \\ & - (\sin\phi \sin\gamma \cos\phi \cos\gamma) K_a \Big] \end{aligned} \tag{5.14d}$$

$$a_{yy} = \sum_{j=0}^{N-1} g_j \left[(\sin\phi \sin\gamma \cos\phi) K_t - (\sin^2\gamma \cos^2\phi) K_r - (\sin\gamma \cos^2\phi \cos\gamma) K_a \right] \tag{5.14e}$$

$$a_{yz} = \sum_{j=0}^{N-1} g_j \left[-(\sin\phi \cos\gamma) K_t + (\sin\gamma \cos\phi \cos\gamma) K_r + (\cos\phi \cos^2\gamma) K_a \right] \tag{5.14f}$$

$$a_{zx} = \sum_{j=0}^{N-1} g_j \left[(\sin\phi \sin\gamma \cos\gamma) K_r - (\sin\phi \sin^2\gamma) K_a \right] \tag{5.14g}$$

$$a_{zy} = \sum_{j=0}^{N-1} g_j \left[(\sin\gamma \cos\phi \cos\gamma) K_r - (\sin^2\gamma \cos\phi) K_a \right] \tag{5.14h}$$

$$a_{zz} = \sum_{j=0}^{N-1} g_j \left[-(\cos^2\gamma) K_r + (\sin\gamma \cos\gamma) K_a \right] \tag{5.14i}$$

The directional coefficient matrix, $[A]$ is periodic at the tooth passing frequency $\omega_T = N\Omega$ and also a function of the axial depth of cut through the cutting force coefficients. Hence to obtain an analytical solution a mono-frequency solution is adopted. This makes the periodic matrix just a function of axial depth of cut, by taking its average Fourier term $[A_o]$ of the Fourier series expansion (Altintas, 2001) as,

$$\begin{aligned} [A_o] &= \frac{1}{T} \int_0^T [A(t)] \mathrm{d}t \\ &= \frac{1}{\phi_p} \int_{\phi_{start}}^{\phi_{exit}} [A(\phi)] \mathrm{d}\phi = \frac{N}{8\pi} [\alpha(a)] \end{aligned} \tag{5.15}$$

and the evaluated elements of the directional factor matrix, $[\alpha]$ are given as follows:

$$\begin{aligned} \alpha_{xx} = \Big[& K_t \sin\bar{\gamma} \cos 2\phi + K_r \sin^2\bar{\gamma} (\sin 2\phi - 2\phi) + \\ & K_a \sin\bar{\gamma} \cos\bar{\gamma} (\sin 2\phi - 2\phi) \Big]_{\phi_{start}}^{\phi_{exit}}, \end{aligned} \tag{5.16a}$$

$$\alpha_{xy} = \left[-K_t \sin\bar{\gamma}\left(\sin 2\phi + 2\phi\right) + K_r \sin^2\bar{\gamma}\cos 2\phi + K_a \sin\bar{\gamma}\cos\bar{\gamma}\cos 2\phi\right]_{\phi_{start}}^{\phi_{exit}}, \quad (5.16b)$$

$$\alpha_{xz} = 2\left[K_t 2\cos\bar{\gamma}\sin\phi - K_r \sin 2\bar{\gamma}\cos\phi - K_a \cos\phi\left(\cos 2\bar{\gamma} + 1\right)\right]_{\phi_{start}}^{\phi_{exit}}, \quad (5.16c)$$

$$\alpha_{yx} = \left[-K_t \sin\bar{\gamma}\left(\sin 2\phi - 2\phi\right) + K_r \sin^2\bar{\gamma}\cos 2\phi + K_a \sin\bar{\gamma}\cos\bar{\gamma}\cos 2\phi\right]_{\phi_{start}}^{\phi_{exit}}, \quad (5.16d)$$

$$\begin{aligned}\alpha_{yy} = \Big[&-K_t \sin\bar{\gamma}\cos 2\phi - K_r \sin^2\bar{\gamma}\left(\sin 2\phi + 2\phi\right) \\ &- K_a \sin\bar{\gamma}\cos\bar{\gamma}\left(\sin 2\phi + 2\phi\right)\Big]_{\phi_{start}}^{\phi_{exit}},\end{aligned} \quad (5.16e)$$

$$\alpha_{yz} = 2\left[K_t 2\cos\bar{\gamma}\cos\phi + K_r \sin 2\bar{\gamma}\sin\phi + K_a \sin\phi\left(\cos 2\bar{\gamma} + 1\right)\right]_{\phi_{start}}^{\phi_{exit}}, \quad (5.16f)$$

$$\alpha_{zx} = 2\left[-K_r \sin 2\bar{\gamma}\cos\phi - K_a \cos\phi\left(\cos 2\bar{\gamma} - 1\right)\right]_{\phi_{start}}^{\phi_{exit}}, \quad (5.16g)$$

$$\alpha_{zy} = 2\left[K_r \sin 2\bar{\gamma}\sin\phi + K_a \sin\phi\left(\cos 2\bar{\gamma} - 1\right)\right]_{\phi_{start}}^{\phi_{exit}}, \quad (5.16h)$$

$$\alpha_{zz} = 2\left[-K_r\phi\left(\cos 2\bar{\gamma} + 1\right) + K_a\phi\sin 2\bar{\gamma}\right]_{\phi_{start}}^{\phi_{exit}} \quad (5.16i)$$

Alternative to the mono-frequency solution is the multi-frequency solution, which considers several terms (Merdol, 2004, Gradisek, 2005). Using the mono-frequency solution in equation (5.15), equation (5.13) is reduced to,

$$\{F(t)\} = \frac{N}{8\pi} a\left[\alpha(a)\right]\{\Delta(t)\}. \quad (5.17)$$

The vibration vectors at the present time t and previous tooth periods $(t-T)$ are defined as,

$$\{r\} = \{x(t), \quad y(t), \quad z(t)\}^T \qquad \{r_0\} = \{x(t-T), \quad y(t-T), \quad z(t-T)\}^T \quad (5.18)$$

Using the transfer function at the cutter-workpiece contact zone, the vibration vectors are defined in frequency domain as,

$$\left.\begin{aligned}\{r(i\omega)\} &= \left[G(i\omega)\right]\{F\}e^{i\omega t} \\ \{r_0(i\omega)\} &= e^{-i\omega T}\{r(i\omega)\}\end{aligned}\right\} \quad (5.19)$$

Therefore, the displacement/regenerative vector,

$$\{\Delta(t)\} = \{(x - x_0), \quad (y - y_0), \quad (z - z_0)\}^T, \quad (5.20)$$

in frequency domain becomes,

$$\{\Delta(i\omega)\} = \left(1 - e^{-i\omega T}\right)[G(i\omega)]\{F\}e^{i\omega t} \tag{5.21}$$

where, the transfer function (TF) matrix $[G(i\omega)]$ is the sum of the 'Frequency Response Function' (FRF) or 'TF' matrixes of the tool/cutter and of the workpiece as follows,

$$[G(i\omega)] = \begin{bmatrix} G_{cxx}(i\omega) & G_{cxy}(i\omega) & G_{cxz}(i\omega) \\ G_{cyx}(i\omega) & G_{cyy}(i\omega) & G_{cyz}(i\omega) \\ G_{czx}(i\omega) & G_{czy}(i\omega) & G_{czz}(i\omega) \end{bmatrix} + \begin{bmatrix} G_{wxx}(i\omega) & G_{wxy}(i\omega) & G_{wxz}(i\omega) \\ G_{wyx}(i\omega) & G_{wyy}(i\omega) & G_{wyz}(i\omega) \\ G_{wzx}(i\omega) & G_{wzy}(i\omega) & G_{wzz}(i\omega) \end{bmatrix}, \tag{5.22}$$

where, c denotes the cutter and w denotes the workpiece. It should be noted that if the directions (x), (y) and (z) are orthogonal to each other, then the cross transfer functions are zero. Hence, equation (5.17) becomes an eigenvalue problem defined as,

$$\{F\} = \frac{N}{8\pi} a\left(1 - \mathrm{e}^{-i\omega_c T}\right)[\alpha(a)][G(i\omega)]\{F\}, \tag{5.23}$$

which has a non-trivial solution if its determinant is zero,

$$\det[[I] + \Lambda[\Phi(i\omega_c, a)]] = 0, \tag{5.24}$$

where, the oriented transfer function $[\Phi] = [\alpha(a)][G(i\omega_c)]$ and the complex eigenvalue, Λ is defined as,

$$\Lambda = \Lambda_R + i\Lambda_i = -\frac{N}{8\pi} a\left(1 - \mathrm{e}^{-i\omega_c T}\right), \tag{5.25}$$

The complex eigenvalue, Λ can be solved if a value is given for the cutting force coefficients, K_t, K_r and K_a. For given cutting coefficients, the eigenvalue becomes a cubic function (Altintas, 2001) expressed as,

$$a_3\Lambda^3 + a_2\Lambda^2 + a_1\Lambda + 1 = 0, \tag{5.26}$$

where,

$$a_3 = \left(-\Phi_{11}\Phi_{22}\Phi_{33}\right)+\left(\Phi_{11}\Phi_{23}\Phi_{32}\right)+\left(\Phi_{21}\Phi_{12}\Phi_{23}\right)-\left(\Phi_{21}\Phi_{13}\Phi_{32}\right) -\left(\Phi_{31}\Phi_{12}\Phi_{23}\right)+\left(\Phi_{31}\Phi_{13}\Phi_{22}\right),$$

$$a_2 = \left(\Phi_{22}\Phi_{33}\right)-\left(\Phi_{23}\Phi_{32}\right)+\left(\Phi_{11}\Phi_{33}\right)+\left(\Phi_{11}\Phi_{22}\right)-\left(\Phi_{21}\Phi_{12}\right)-\left(\Phi_{31}\Phi_{13}\right),$$

$$a_1 = -\left(\Phi_{33}\right)-\left(\Phi_{22}\right)-\left(\Phi_{11}\right),$$

and Φ_{ij} are the elements of the oriented transfer function Φ.

The eigenvalue obtained has a real and an imaginary part, $\left(\Lambda = \Lambda_R + i\Lambda_I\right)$ and from Euler's formula we have that, $\mathrm{e}^{-i\omega_c T} = \cos\omega_c T - i\sin\omega_c T$. When this is substituted into equation (5.25) the following is obtained,

$$\Lambda = \Lambda_R + i\Lambda_I = -\frac{N}{8\pi}a\left(1-\cos\omega_c T + i\sin\omega_c T\right). \tag{5.27}$$

Noting that the division of two complex numbers is given as (Smith, 1997),

$$\mathrm{Re}\,H + i\,\mathrm{Im}\,H = \frac{\mathrm{Re}\,M + i\,\mathrm{Im}\,M}{\mathrm{Re}\,D + i\,\mathrm{Im}\,D} \tag{5.28}$$

where,

$$\mathrm{Re}\,H = \frac{\left(\mathrm{Re}\,M\cdot\mathrm{Re}\,D\right)+\left(\mathrm{Im}\,M\cdot\mathrm{Im}\,D\right)}{\left(\mathrm{Re}\,D\right)^2+\left(\mathrm{Im}\,D\right)^2}, \mathrm{Im}\,H = \frac{\left(\mathrm{Im}\,M\cdot\mathrm{Re}\,D\right)-\left(\mathrm{Re}\,M\cdot\mathrm{Im}\,D\right)}{\left(\mathrm{Re}\,D\right)^2+\left(\mathrm{Im}\,D\right)^2}$$

and after some manipulations, the following is obtained,

$$a = -\frac{4\pi}{N}\left[\frac{\Lambda_R\left(1-\cos\omega_c T\right)+\Lambda_I\sin\omega_c T}{\left(1-\cos\omega_c T\right)} + i\frac{\Lambda_I\left(1-\cos\omega_c T\right)-\Lambda_R\sin\omega_c T}{\left(1-\cos\omega_c T\right)}\right]. \tag{5.29}$$

Since the axial depth of cut a is real number, the imaginary part of equation (5.29) has to vanish (i.e., $\Lambda_I\left(1-\cos\omega_c T\right) = \Lambda_R\sin\omega_c T$). Therefore,

$$\frac{\Lambda_I}{\Lambda_R} = \frac{\sin\omega_c T}{1-\cos\omega_c T} = \tan\psi, \tag{5.30}$$

where, ψ is the phase shift of the eigenvalues. From this expression the relationship between the frequency and the spindle speed is obtained (Altintas, 2001) as follows,

$$\left.\begin{aligned} &\omega_c T = \varepsilon + 2k\pi, \\ &\varepsilon = \pi - 2\psi, \\ &\psi = \tan^{-1}\left(\frac{\Lambda_I}{\Lambda_R}\right), \\ &n = \frac{60}{NT}, \end{aligned}\right\} \tag{5.31}$$

where, ε is the phase difference between the inner and outer undulations, k is an integer corresponding to the number of vibration waves within a tooth period n is the spindle speed (rpm).

Therefore substituting equation (5.30) into the real part of equation (5.29) and an expression for chatter free axial depth of cut is obtained as,

$$a_{\lim} = -\frac{4\pi\Lambda_R}{N}\left(1+\left[\frac{\Lambda_I}{\Lambda_R}\right]^2\right), \tag{5.32}$$

where, there exists a real positive solution if and only if $\Lambda_R < 0$.

For the case where the cutting coefficients and axial immersion are assumed to be constant, the axial depth of cut can be obtained using equation (5.32). However, for the case where the cutting coefficients are dependent on the axial depth of cut, obtaining an analytical solution proved very complicated as the oriented transfer function matrix $[\Phi]$ is complex. Another approach could be to study the numerical nature of the relationship between the directional coefficients matrix $[\alpha(a)]$ and the axial depth of cut, a. An example of this relationship is shown in Figures 5.3, 5.4, 5.5 and 5.6 (considering a 2-dimensional system) and from this a polynomial expression can be fitted as shown in the plots. Therefore equation (5.24) could be written in the form,

$$\det[[I]+\Lambda(P_{\alpha G})] = 0, \tag{5.33}$$

where,

$$P_{\alpha G} = \left(a^6[\alpha_6]+a^5[\alpha_5]+a^4[\alpha_4]+a^3[\alpha_3]+a^2[\alpha_2]+a[\alpha_1]+[\alpha_0]\right)[G(i\omega_c)],$$

and

$$[\alpha_C] = \begin{bmatrix} \alpha_{xxC} & \alpha_{xyC} \\ \alpha_{yxC} & \alpha_{yyC} \end{bmatrix}, \qquad C = 0,1,2....6.$$

The elements of the matrix $[\alpha_{Cnst}]$ contain the constants of the polynomial fitting (example shown in Figures 5.3, 5.4, 5.5 and 5.6) for each corresponding order C.

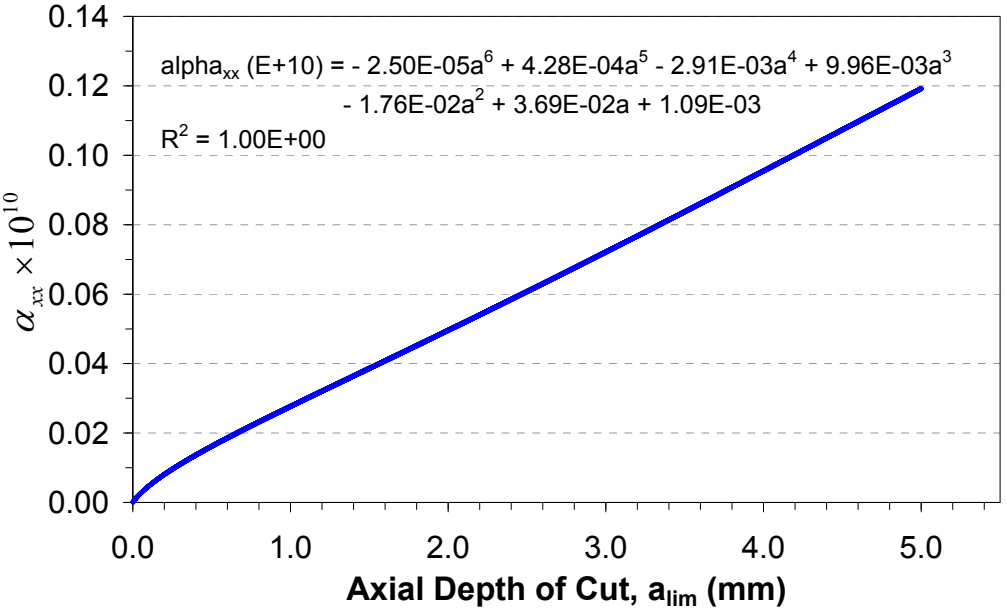

Figure 5.3. Directional coefficient, α_{xx}.

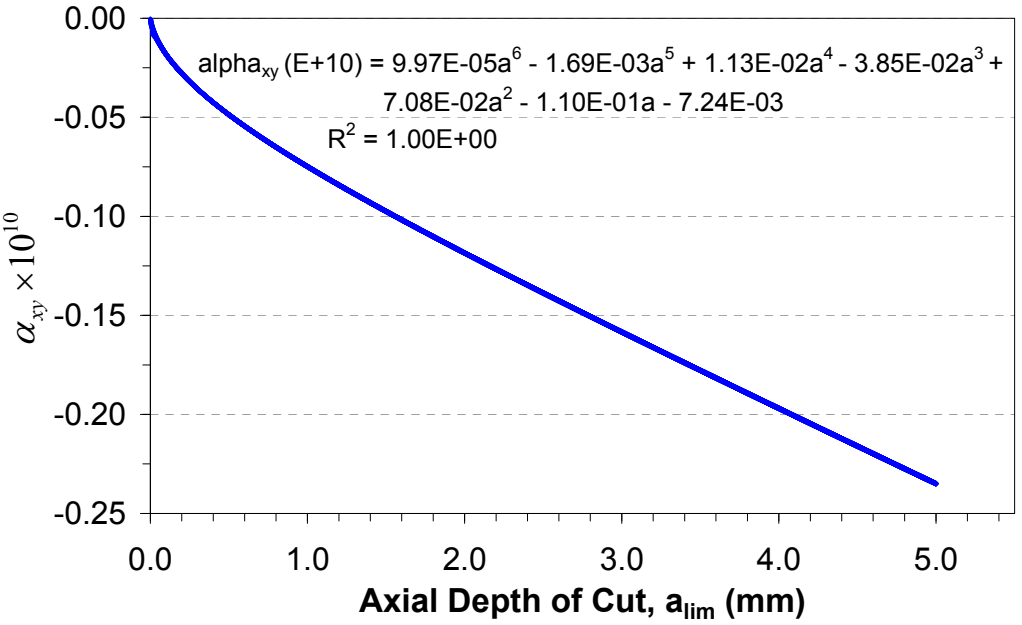

Figure 5.4. Directional coefficient, α_{xy}.

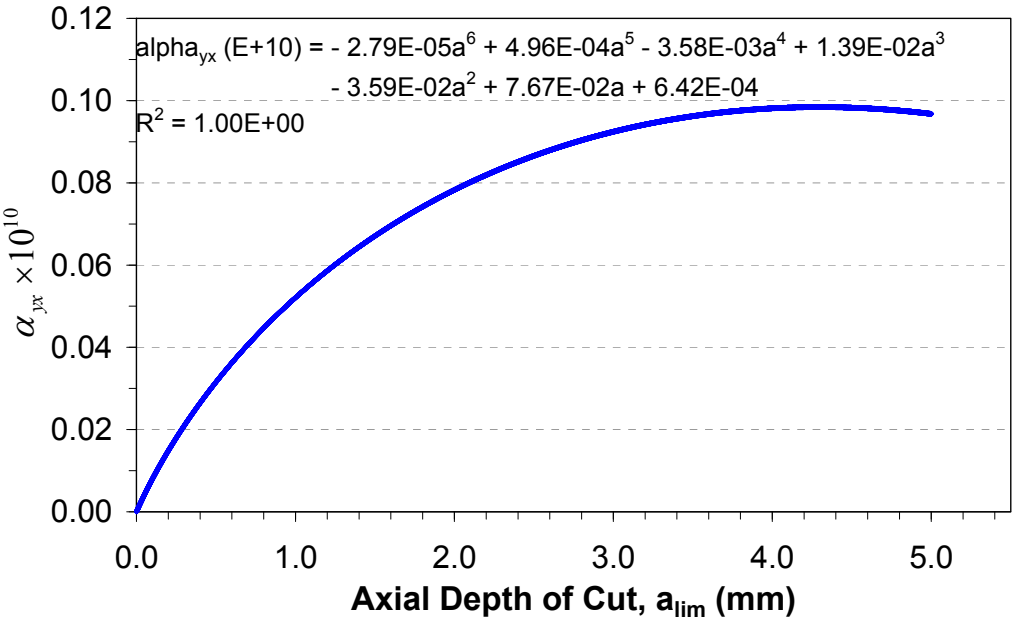

Figure 5.5. Directional coefficient, α_{yx}.

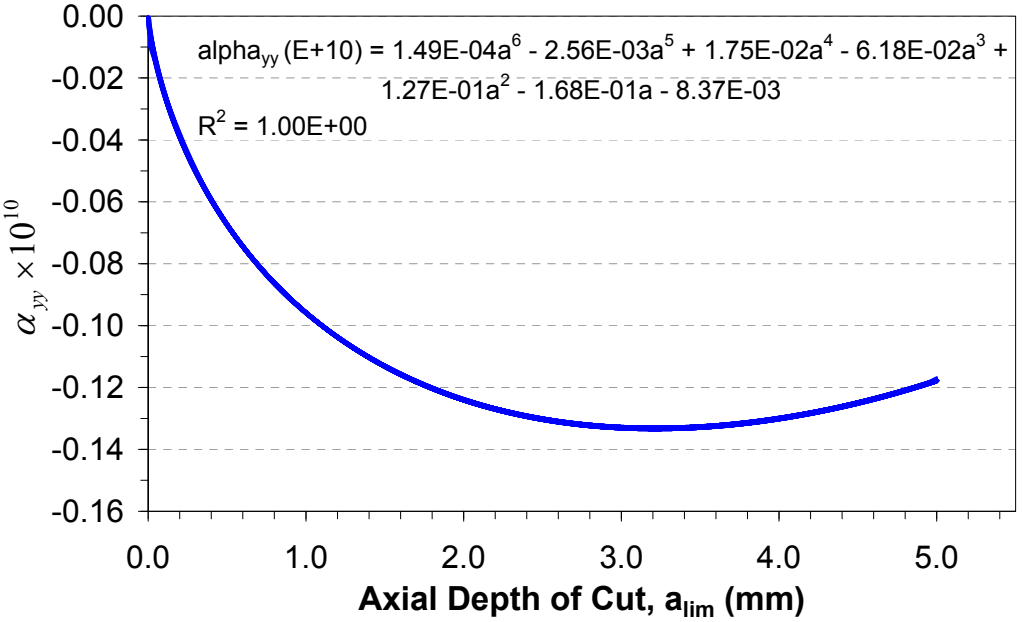

Figure 5.6. Directional coefficient, α_{yy}.

Therefore for example, the sixth order constants in Figures 5.3, 5.4, 5.5 and 5.6 are written out in matrix form $[\alpha_6]$ as,

$$[\alpha_6] = \begin{bmatrix} -2.5041 & 9.9694 \\ -2.7940 & 14.937 \end{bmatrix} \times 10^{-5} \tag{5.34}$$

The accuracy of the curve fitting is shown using the ‘‘R-squared’’ value defined in Chapter 3. There so far isn’t any known solution approach for the non-linear eigenvalue problem in equation (5.33) and an analytical solution was again sought, which still proved to be very complicated when obtaining the expressions. This again is due to the products and divisions of complex numbers. However, being able to solve this semi-numerical approach would be greatly beneficial, as the relationship obtained using polynomial curve fitting in equation (5.33) is dependent on the radial depth of cut only. The radial depth of cut is usually kept constant during machining processes. However, to predict a stable margin a numerical approach is thus proposed, which can be used to obtain very accurate results based on the resolution defined.

5.2.2. Proposed Numerical Approach

The numerical approach simply involves solving equation (5.32) using the cutting coefficients and the axial immersion for different axial depth of cuts and monitoring the error between the axial depth of cut value used to obtain the coefficients and the axial immersion and the obtained axial depth of cut in equation (5.32). When the cutting force coefficients are calibrated and fitted with a polynomial expression, there is a range of axial depth of cut $a_{\min} \le a \le a_{\max}$ within which the curve fitting is accurate. This range is usually the same minimum and maximum axial depths of cut at which the coefficients are calibrated. The same axial depth of cut range applies to the calculated characteristic coefficients in equation (5.26). This same range should be used when numerically seeking a converged solution. The steps of the proposed algorithm are as follows:

1. Select a chatter frequency from transfer functions around a dominant mode

2. Start the numerical approach to calculating stable axial depth of cut:

(A) Using predicted axial depth of cut a^m (where initial values of $a^0 = a_{\min}$), calculate the cutting force coefficients, K_t, K_r, K_a and axial immersion $\bar{\gamma}$

(B) Solve the eigenvalue characteristic equation (5.26)

(C) Calculate the critical depth of cut using equation (5.32)

(D) Subtract the calculated axial depth of cut $a_{\lim}$ from the predicted axial depth of cut a^m to obtain the error as follows

$$\eta^m = a^m - a_{\lim}$$

(E) If $m > 1$, compare the sign of the previous and current axial depth of cut error, η^m and η^{m-1}, else go to (I)

(F) If the signs have changed, a converged axial depth of cut solution can be obtained by means of simple interpolation as follows,

$$a^*_{\lim} = \frac{-\eta^{m-1}}{\eta^m - \eta^{m-1}} \cdot \left(a^m - a^{m-1}\right) + a^{m-1} \tag{5.35}$$

(G) then proceed to step 3

(H) If the signs are unchanged and $a^m < a_{\max}$ then update the predicted axial depth of cut using $a^{m+1} = a^m + \Delta a$, else STOP and go to step 1 as the solution to the chosen chatter frequency is not within the range of the axial depth of cut imposed by the calibrated cutting force coefficients

(I) Go to step (A) with $m = m + 1$, $a^{m-1} = a^m$ and $\eta^{m-1} = \eta^m$

3. Using the converged axial depth of cut solution, $a^*_{\lim}$ calculate the corresponding cutting force coefficients and axial immersion and then solve the eigenvalue characteristic equation, (5.26)

4. Calculate the spindle speed n, using equation (5.31) for each integer number of vibration waves within a tooth period i.e., $k = 0, 1, 2, 3, ...$

5. Repeat the procedure for different chatter frequencies around dominant modes

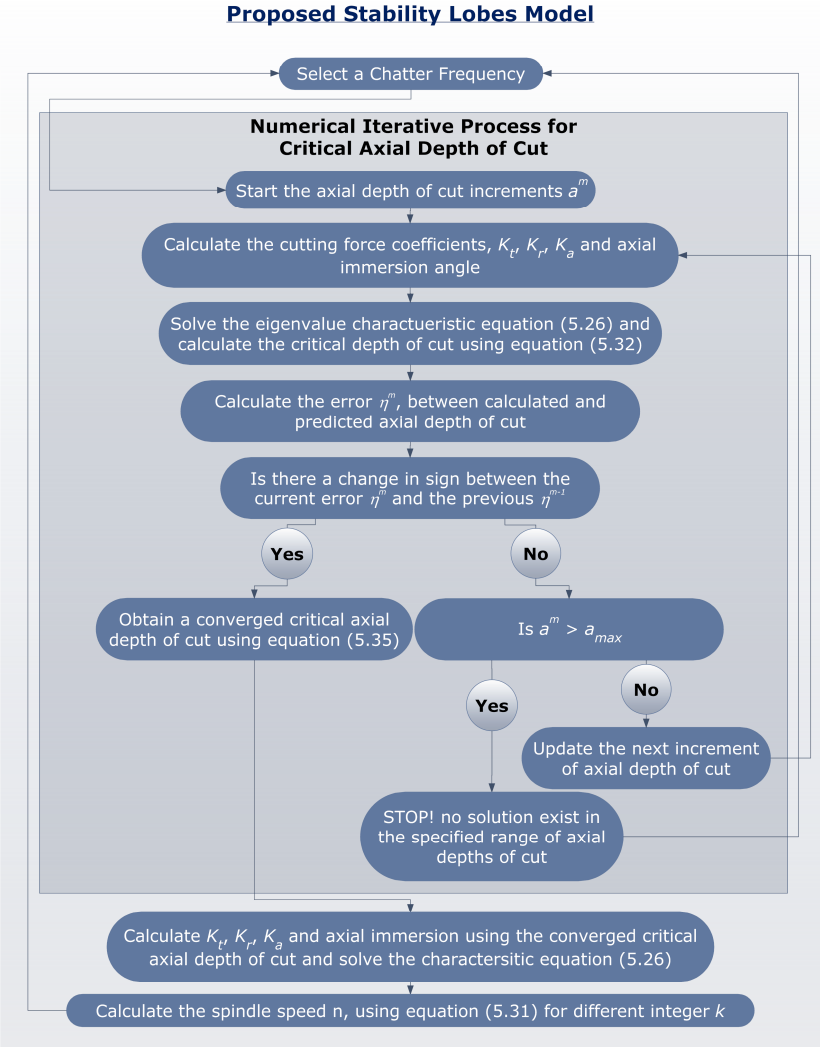

Figure 5.7. Stability model numerical algorithm.

The case where no solution is obtained (step (G)) would rarely occur; however this could happen if the solution being sought is above the maximum axial depth of cut $a_{\max}$. Hence the range for which the cutting coefficient has been calibrated for must be extended, alternatively the axial depth of cut a^m that gives the smallest error η^m can be used. The steps explained above are laid out systematically in Figure 5.7.

5.2.3. System's Transfer Function

During machining both the tool and the workpiece will always exhibit dynamic deflections. However their relative stiffness's would determine the magnitude of these deflections. Therefore, for cases where the stiffness of the tool

is relatively high compared to that of the workpiece (for example when machining a thin walled workpiece), the dynamics of the tool can be ignored. This was also done in Chapter 4, where the tool dynamics was ignored when extracting stable region for thin wall machining. The improvements by Adetoro et al. (2009c) that have been discussed in this chapter are however validated first by considering only the tool's dynamic vibrations/chatter. For these cases the workpiece's stiffness is kept relatively higher than that of the tool (for example machining a block of material), therefore the transfer function of the workpiece can be ignored. The deflections in two main directions are considered in this chapter, therefore the tool's transfer function column and row corresponding to the direction being omitted can be simply removed or the diagonal elements given a relatively small value, but not zero. For completeness (though not necessary) if obtaining the transfer function in a certain direction proves experimentally challenging, the full matrix can still be extracted using the FEM approach presented in Chapter 4.

For the case where only the tool dynamics in the feed (X) and normal (Y) directions are considered, the dynamics extracted experimentally can be assumed to be constant. Therefore following the experimental procedure explained in section 4.2.1, the tools dynamics were extracted experimentally and given in Table 5.1

Table 5.1. Tool dynamic parameters

Direction	Mode	Natural Frequency, ω_n (Hz)	Modal Stiffness, k (10^7 Nm^{-1})	Modal Damping Ratio, ζ (10^{-2} %)
X	1	1306.9361	1.0657	7.9626
	2	1897.8177	5.6677	4.4413
	3	2195.3198	6.6598	5.0610
	4	2686.9228	3.1818	3.6897
Y	1	1262.6637	1.2149	3.4316
	2	2074.2514	2.2493	7.7559
	3	2684.0002	3.1113	2.9063

From these identified dynamic parameters the real and imaginary parts of the transfer function are simply calculated for each mode by sweeping the frequency of interest according to step (1). Therefore using modal superposition, the real part is defined (Budak, 1998b) as,

$$\begin{aligned}\mathrm{Re}\,G(\omega) = &\frac{1}{K_1}\left[\frac{1-(\omega/\omega_{n,1})^2}{\left(1-(\omega/\omega_{n,1})^2\right)^2+\left(2\zeta_1(\omega/\omega_{n,1})\right)^2}\right]_{\text{mode1}} \\ &+\frac{1}{K_2}\left[\frac{1-(\omega/\omega_{n,2})^2}{\left(1-(\omega/\omega_{n,2})^2\right)^2+\left(2\zeta_2(\omega/\omega_{n,2})\right)^2}\right]_{\text{mode2}}+\ldots\end{aligned} \tag{5.36}$$

while the imaginary part is defined as

$$\begin{aligned}\mathrm{Im}(\omega) = &\frac{1}{K_1}\left[\frac{-2\zeta_1(\omega/\omega_{n,1})}{\left(1-(\omega/\omega_{n,1})^2\right)^2+\left(2\zeta_1(\omega/\omega_{n,1})\right)^2}\right]_{\text{mode1}} \\ &+\frac{1}{K_2}\left[\frac{-2\zeta_2(\omega/\omega_{n,2})}{\left(1-(\omega/\omega_{n,2})^2\right)^2+\left(2\zeta_2(\omega/\omega_{n,2})\right)^2}\right]_{\text{mode2}}+\ldots\end{aligned} \tag{5.37}$$

Any extra identified modes for the real and imaginary parts are simply added in the same manner to obtain the numeric values for the transfer function for each frequency.

5.2.4. Experimental Validation

To obtain experimental results to validate the proposed numerical approach, an aluminium milling application with a 3-tooth milling cutter is considered. The workpiece was kept sufficiently rigid in comparison to the tool in order to minimize workpiece vibration. The modal properties of the tool measured using impact tests are given in Table 5.1. The cutting coefficients were calibrated using the approach explained by Gradisek et al. (2004) (see Chapter 3) and fitted with 2nd-order polynomial expressions as shown in Figures 5.8, 5.9, 5.10.

$$\left.\begin{aligned}K_t(\mathrm{a})\ \left[\mathrm{Nmm^{-2}}\right] &= 6.0078a^2-130.8499a+1120.7047,\\ K_r(\mathrm{a})\ \left[\mathrm{Nmm^{-2}}\right] &= -59.2929a^2+618.5384a-965.1056,\\ K_a(a)\ \left[\mathrm{Nmm^{-2}}\right] &= -18.0639a^2-58.9326a+955.4979.\end{aligned}\right\} \tag{5.38}$$

The cutting force coefficients were curve fitted in this section between 0.50mm and 5.00mm as opposed to 0.50mm and 6.00mm in Chapter 3 and it is within this range of axial depth of cut, the cutting force coefficients can predict the cutting forces with reliable accuracy.

Using the proposed algorithm in section 5.2.2, an example of the error calculated in step (2D) and the converged axial depth (approximately 2.0mm) calculated in step (2F) for chatter frequency 1303.5 Hertz are plotted in Figure 5.11.

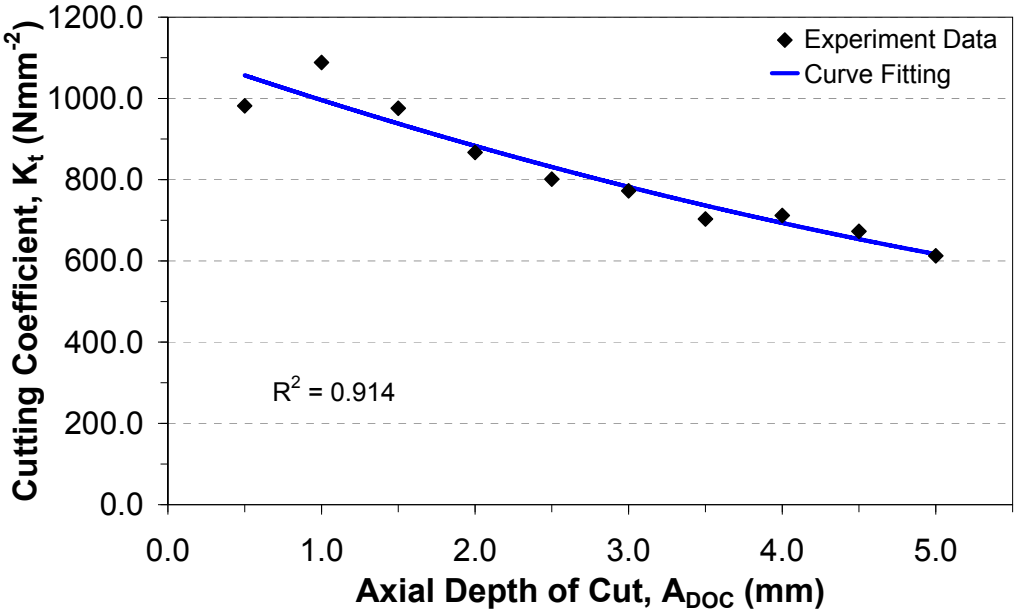

Figure 5.8. Calibrated tangential cutting force coefficient.

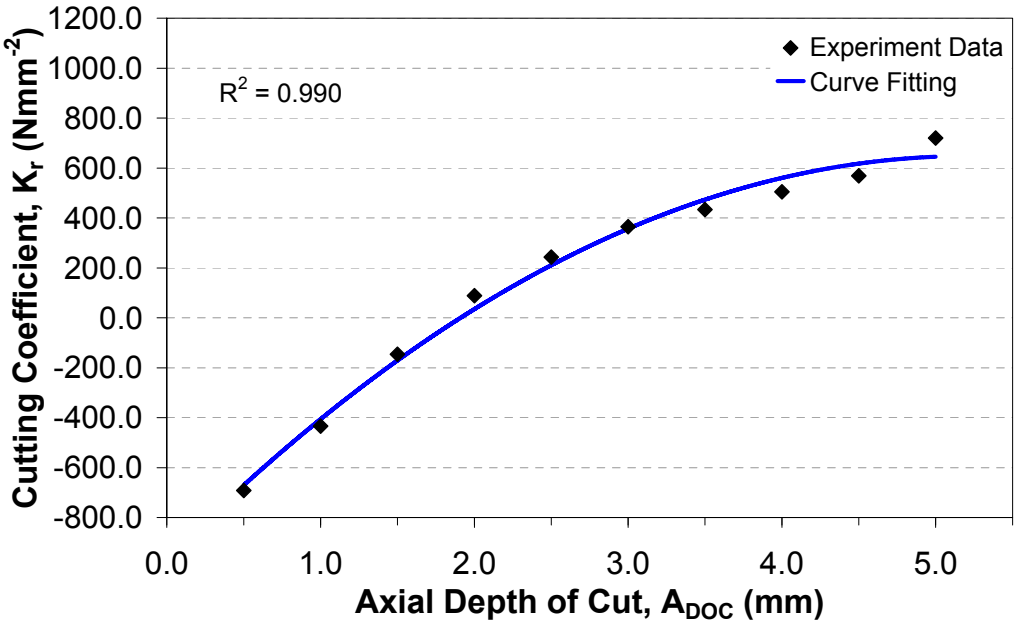

Figure 5.9. Calibrated radial cutting force coefficient.

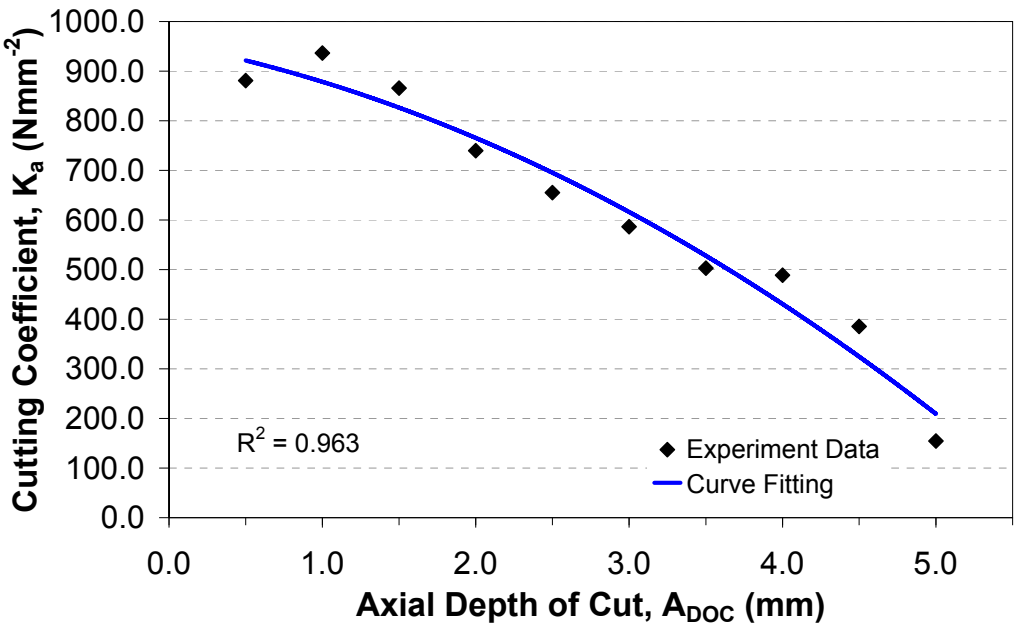

Figure 5.10. Calibrated axial cutting force coefficient.

Being a numerical method, the algorithm proposed in section 5.2.2 can be used to obtain very accurate results depending on the incremental steps used. The smaller the incremental steps, the more accurate the converged axial depth of cut obtained, although the algorithm naturally improves the results through the interpolation done in step (2F).

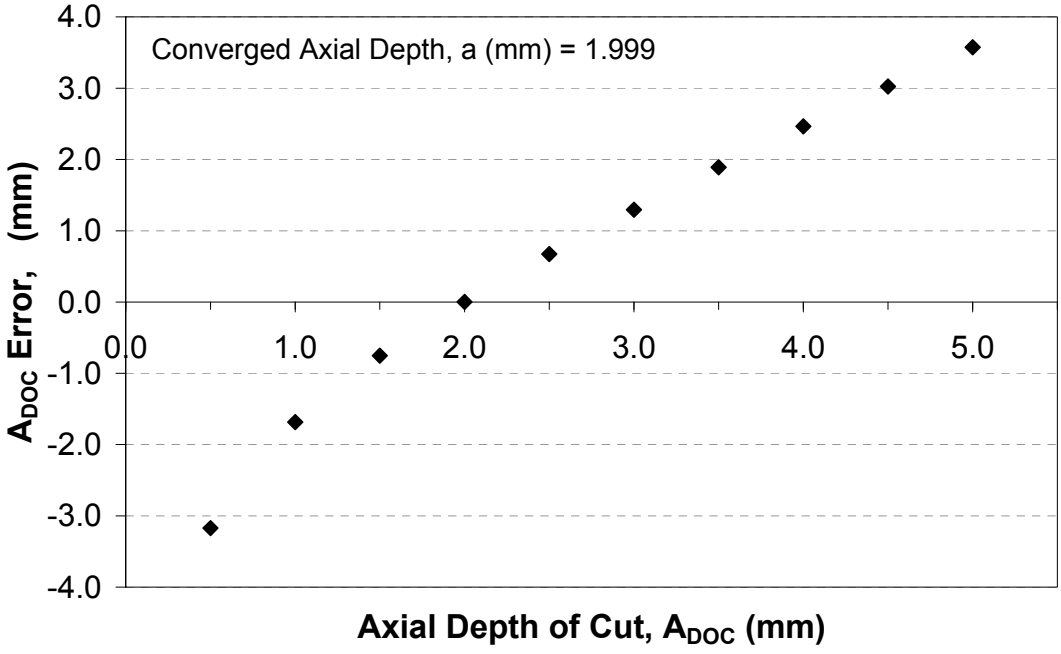

Figure 5.11. Example of algorithm convergence.

Using the proposed approach, the stability lobe diagram for a 19.0mm radial depth of cut and 20.0mm tool diameter is shown in Figure 5.12, where the unstable region is shown in grey. Changing the radial depth of cut would change the directional dynamic milling coefficients as these are a variable of the entry and exit angles used in equation (5.16). The results obtained are compared in Figure 5.12 with results using the currently adopted approach proposed by Altintas (2001) (where the axial immersion is assumed to be constant and acting at $\gamma = \pi/2 + \pi/4$) and also results from a commercial software package. The stability lobes predicted are experimentally verified using a radial depth of cut of 19.00 mm and a feed of 0.20 mm, where the feedrate is simply calculated for each spindle speed. The presence of chatter is monitored by the spectrum of cutting forces measured and tool vibration measured using an accelerometer built in at the back of the spindle. The different experimental results are analysed and grouped into three categories: stable, transition and chatter cuts. The 'transition' cuts were identified as such because slight chatter was either identified in the measured force or the predicted chatter frequency can be seen very slightly in the FFTs. The region predicted to be unstable is in good agreement with the experimental results.

The cutting force and vibration measurements for a series of cutting conditions (indicated in Figure 5.12) are shown in Figures (5.13 - 5.22) to further

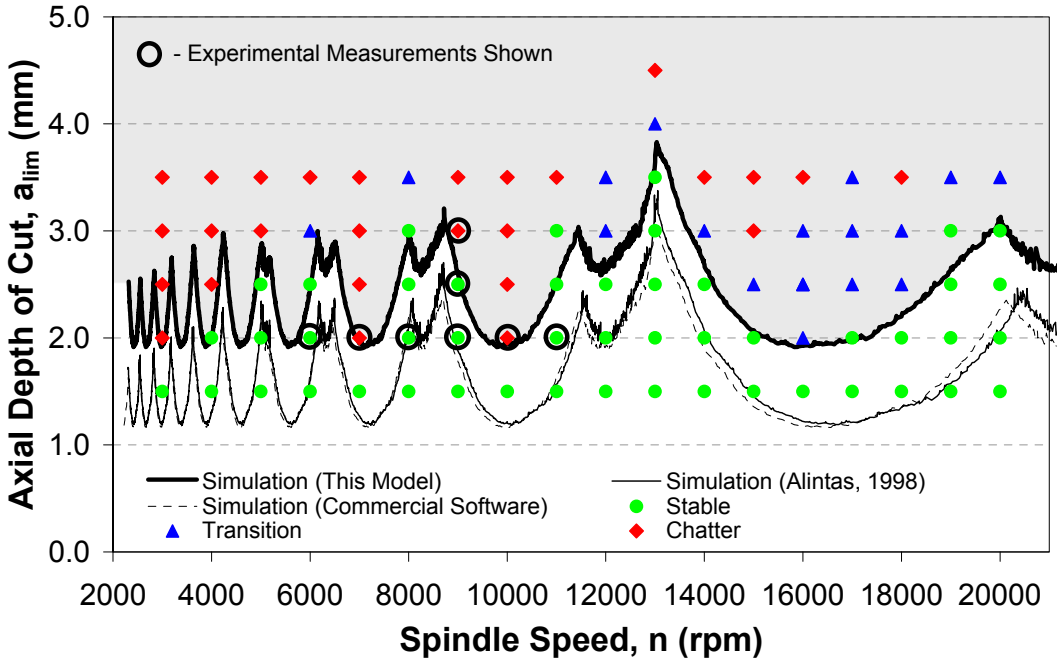

Figure 5.12. Stability margin validation.

show the effects of chatter development and why its early prediction is imperative for efficient machining processes. At a depth of cut of 2.00mm, the stability lobes model proposed by Adetoro et al. (2009) and explained in this section predict stable cutting at spindle speed of 6000 rev/min, chatter at 7000 rev/min and stable cutting again at 8000 rev/min.

The cutting forces measured in the feed direction (X) for spindle speed of 6000 rev/min are shown in Figure 5.13a and the FFT of this data is shown in Figure 5.13b. The cutting force plot shows a stable cut and the FFT shows only the

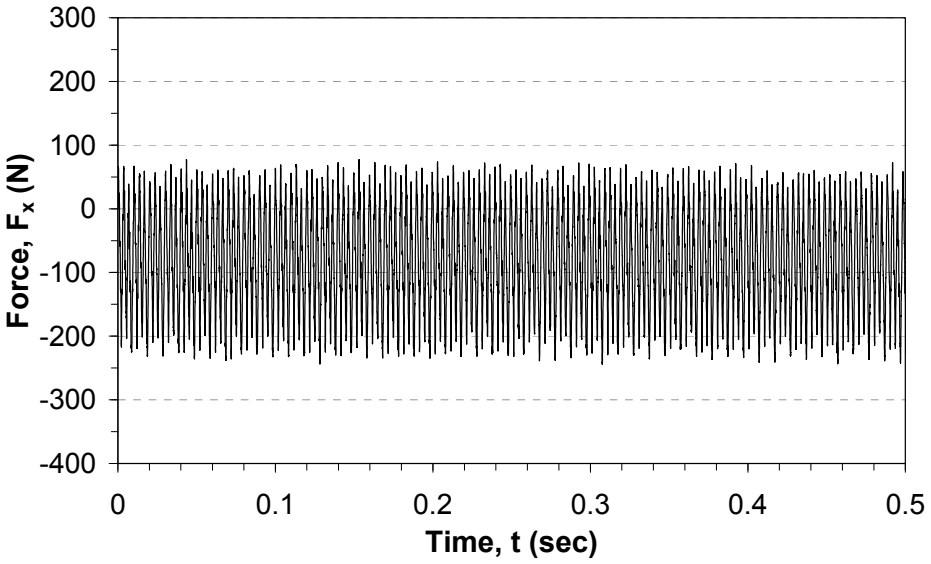

(a)– Measured cutting forces, F_x

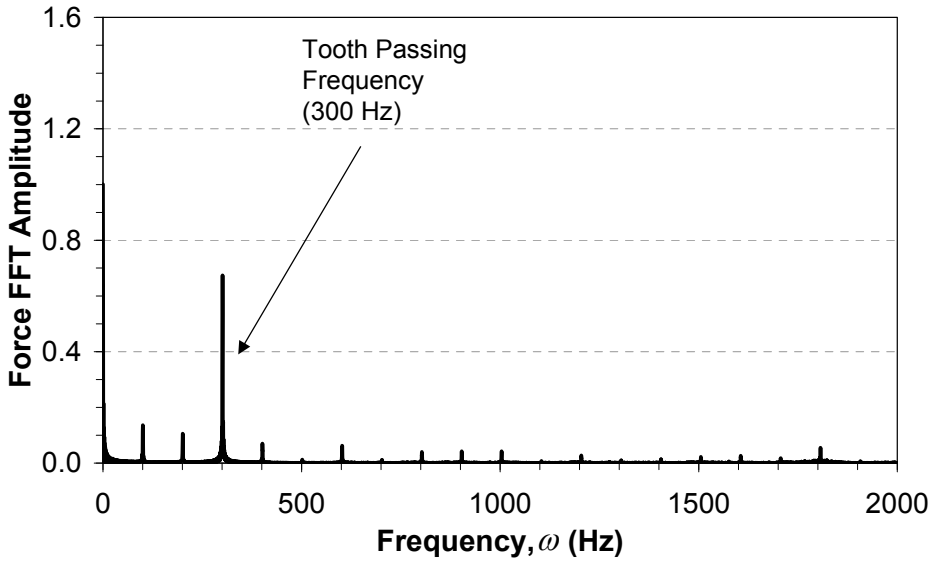

(b) – FFT of measured cutting forces

Figure 5.13. Measurements for 6000 rev/min and 2.0mm axial depth of cut.

presence of the tooth passing frequency, ω_T of 300 Hz and its harmonics. Using the previously adopted approach where the cutting force coefficients are assumed as constant, this cutting condition is predicted as an unstable cutting condition. Therefore this validates the improvements proposed in this section.

The cutting forces for 7000 rev/min are shown in Figure 5.14a and it can be seen that the cutting forces are higher and more unsteady than 6000 rev/min. The FFT of this cutting force data is shown in Figure 5.14b and the chatter frequency at 1266 Hz. The chatter frequency is naturally predicted by the stability model, as

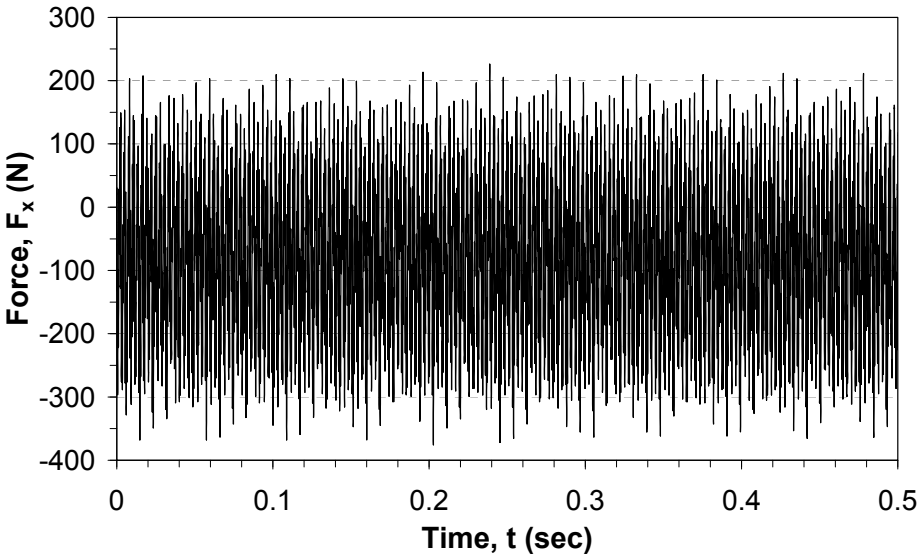

(a) – Measured cutting forces, F_x

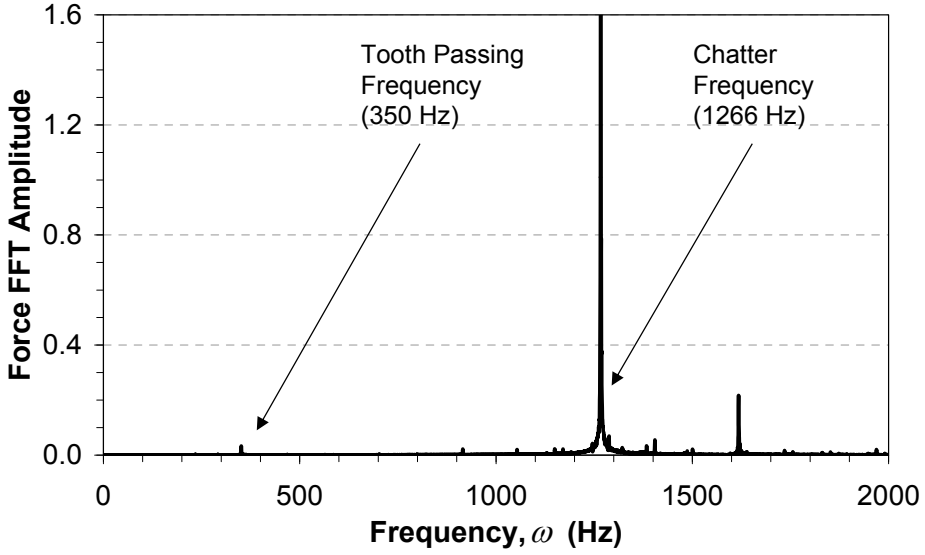

(b) – FFT of measured cutting forces

Figure 5.14. Measurements for 7000 rev/min and 2.0mm axial depth of cut.

the nature of the stability model is actually to assume a chatter frequency (step 1) and then give the stable margin that would initiate this chatter frequency. The chatter frequency predicted for 7000 rev/min was 1276.50 Hz, which further shows the accuracy of the model.

The measured cutting forces for 8000 rev/min are shown in Figure 5.15a and the FFT of this data shown in Figure 5.15b. This shows that the chatter is no longer present and the cutting was stable as predicted in Figure 5.12.

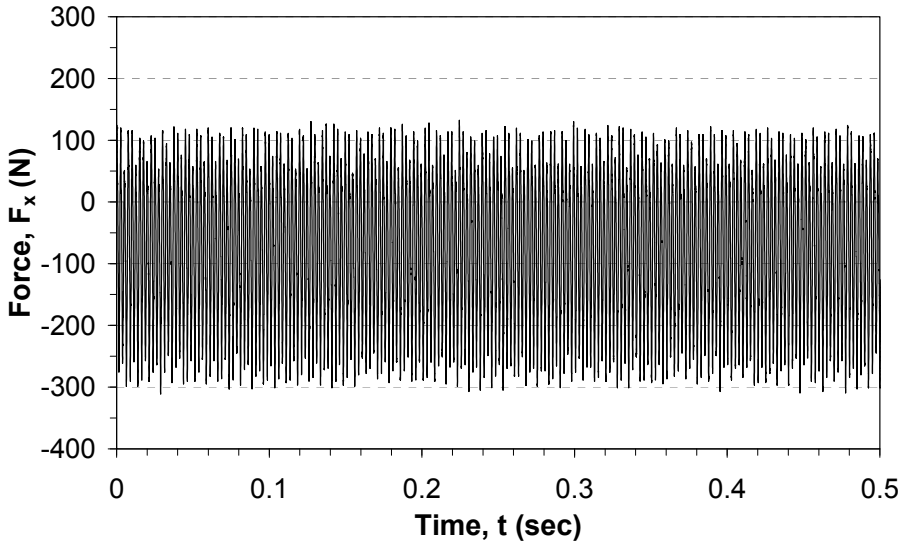

(a) – Measured cutting forces, Fx

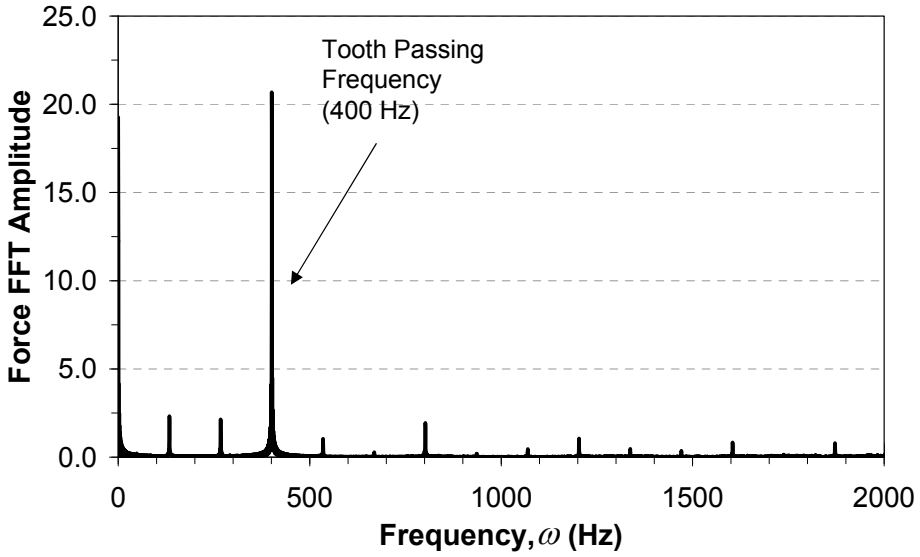

(b) – FFT of measured cutting forces

Figure 5.15. Measurements for 8000 rev/min and 2.0mm axial depth of cut.

Once chatter develops apart from the drastic increase in cutting force, there is the risk of considerable damage to the spindle. The vibrations measured from the accelerometer in-built at the back spindle are shown for 9000 rev/min in Figure 5.16a and the FFT shown in Figure 5.16b. This cutting condition was stable as predicted in Figure 5.12 and the FFT shows only the tooth passing frequency, ω_T (450 Hz) and its harmonics.

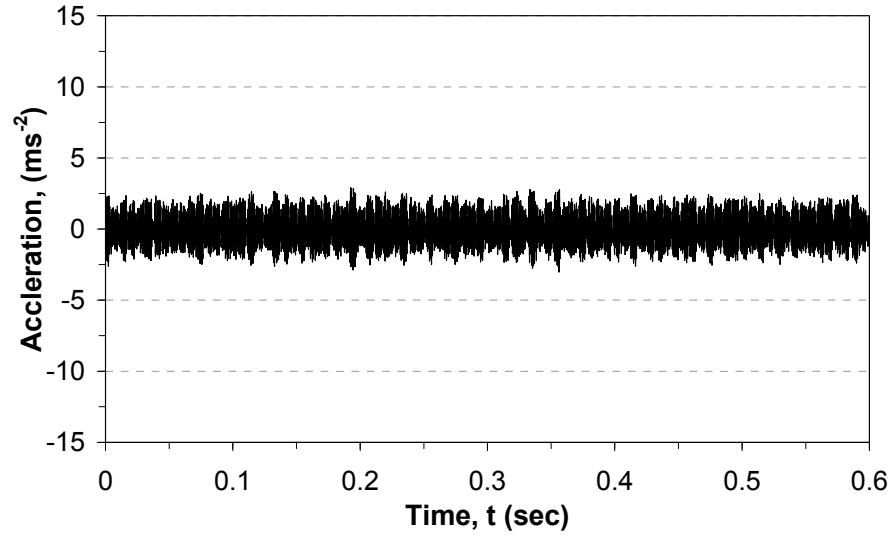

(a) – Measured spindle deflections

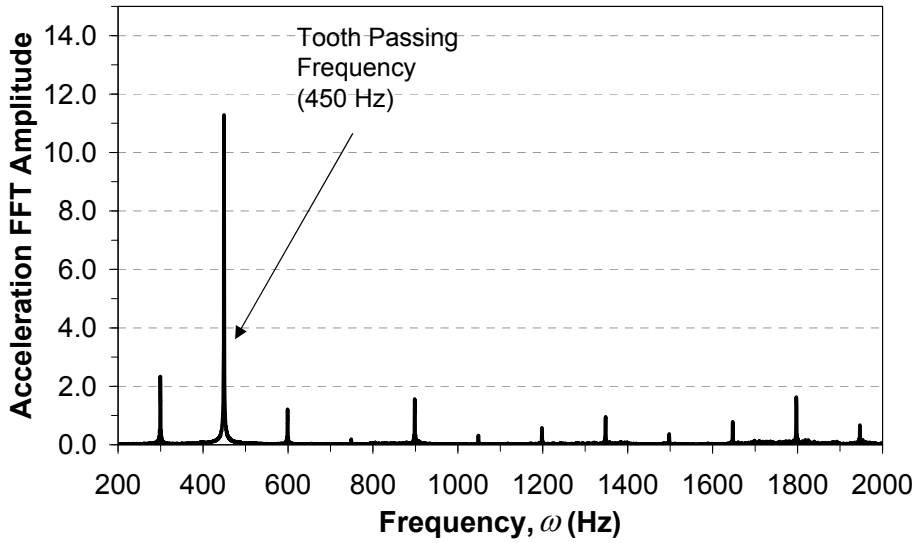

(b) – FFT of vibration data

Figure 5.16. Measurements for 9000 rev/min and 2.0mm axial depth of cut.

The vibrations measured for 10000 rev/min are shown in Figure 5.17a and the FFT in Figure 5.17b. This confirms the prediction for chatter presence. The vibrations are seen to increase quite drastically due to the development of chatter. The FFT also shows the tooth passing frequency, ω_T (500 Hz), its harmonics and an extra frequency at 1278 Hz, which is the chatter frequency. The chatter frequency predicted was 1290.5 Hz.

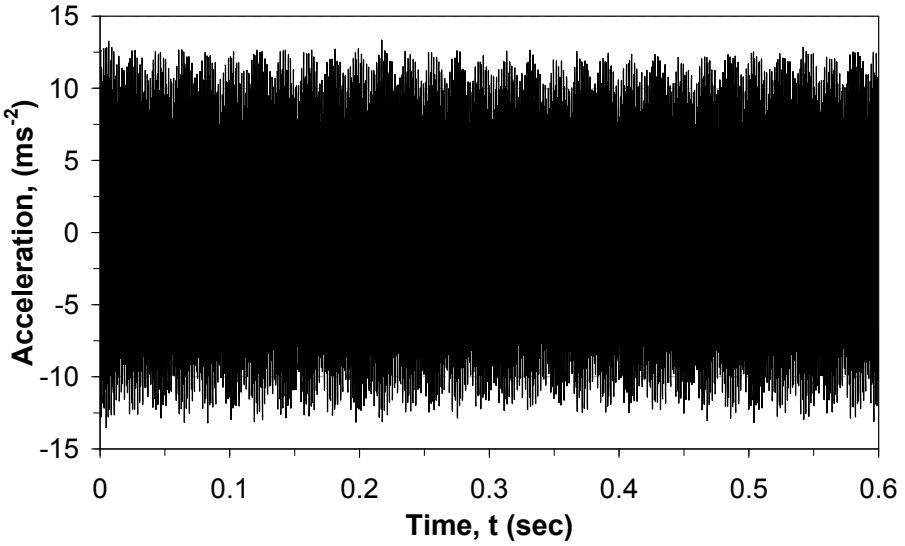

(a) – Measured spindle vibrations

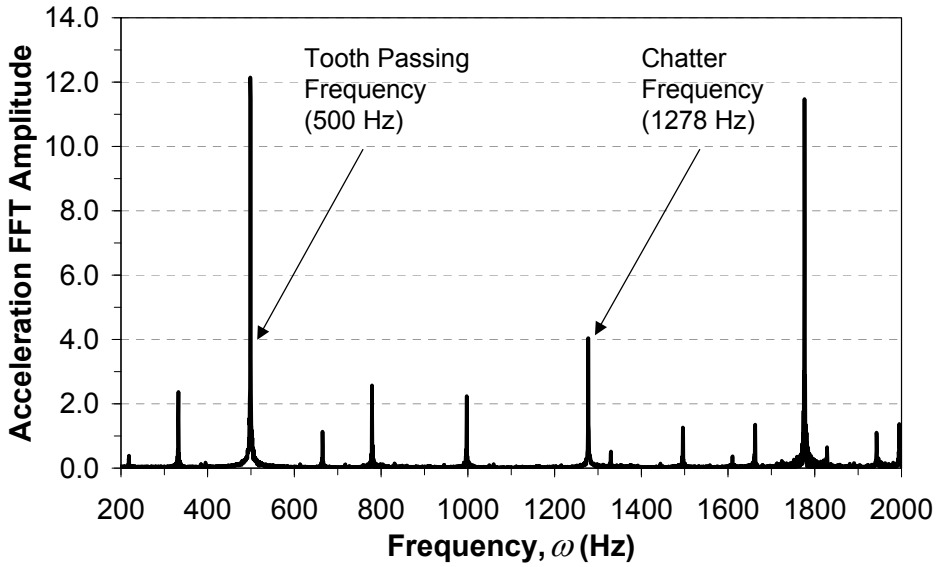

(b) – FFT of vibration data

Figure 5.17. Measurements for 10000 rev/min and 2.0mm axial depth of cut.

The vibrations measured for 11000 rev/min are shown in Figure 5.18a and the FFT in Figure 5.18b. The vibrations are seen to be back to normal magnitude, which confirms the prediction for a stable cutting condition. The FFT also shows only the tooth passing frequency, ω_T (550 Hz) and its harmonics.

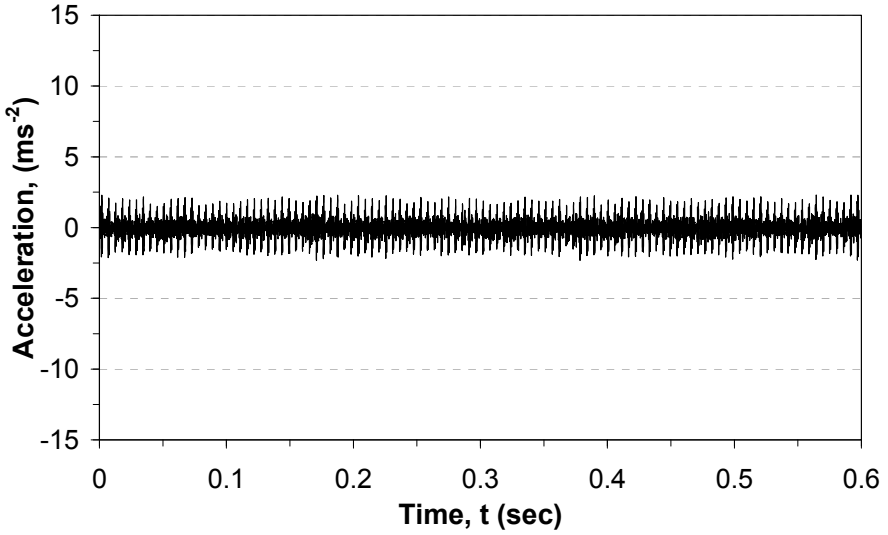

(a) – Measured spindle vibrations

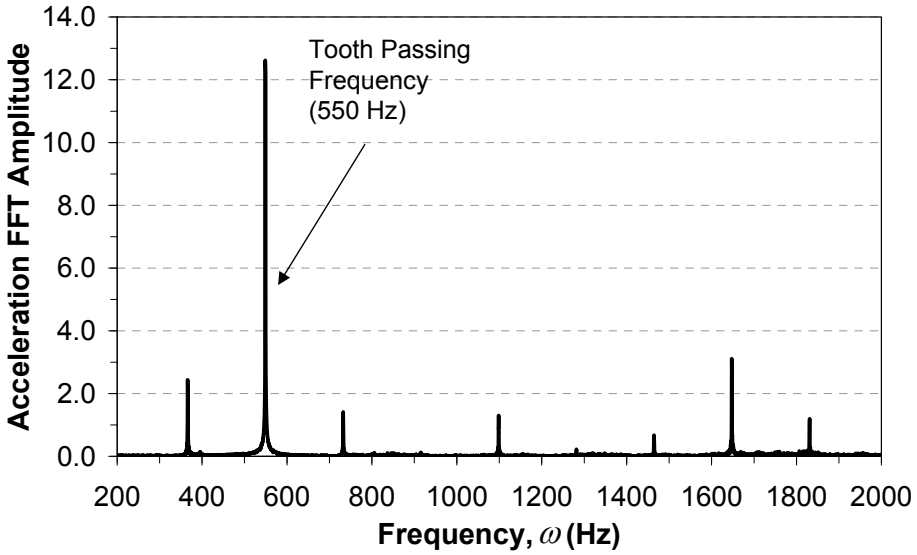

(b) – FFT of vibration data

Figure 5.18. Measurements for 11000 rev/min and 2.0 mm axial depth of cut.

The presented experimental measurements so far show the development of chatter as the spindle speed is changed. To show the development of chatter as the depth of cut is increased, a spindle speed of 9000 rev/min is used. A plot of the

measured cutting forces in the normal direction (Y) for axial depths of cut of 2.00 mm, 2.50 mm and 3.00 mm are shown in Figures 5.19, 5.20 and 5.21. The FFTs of these cutting force data are shown as well. The chatter predicted for 3.00 mm is seen to be present in the experimental cut depicted by the drastic increase in the measured experimental forces (Figure 5.21a).

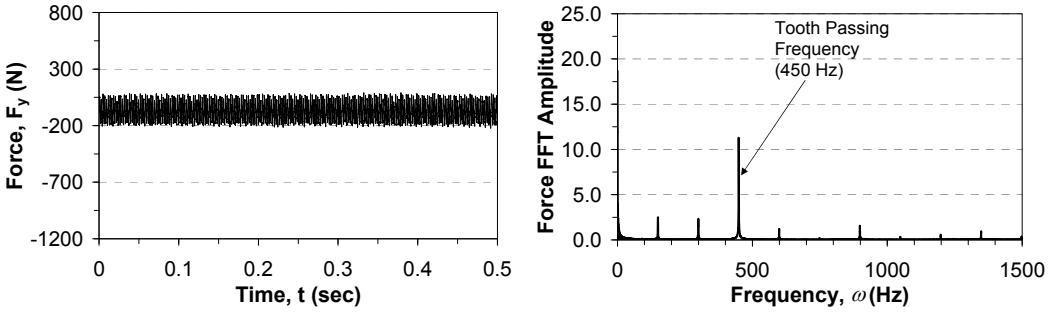

(a) – Measured cutting forces, F_y (b) – FFT of cutting forces

Figure 5.19. Measurements for 9000 rev/min and 2.0 mm axial dept of cut.

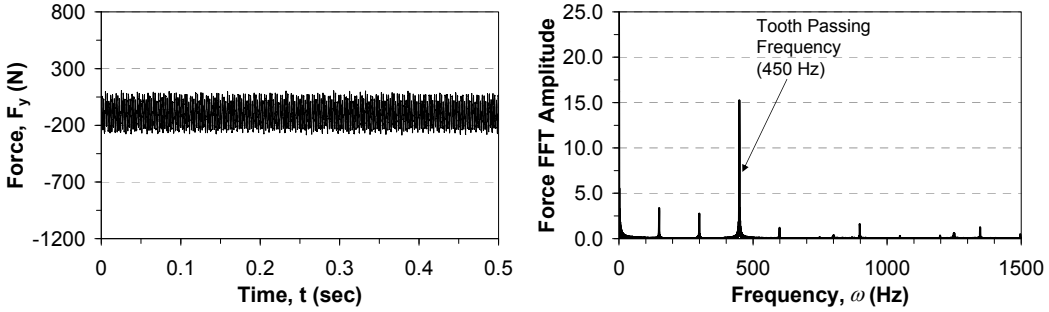

(a) – Measured cutting forces, F_y (b) – FFT of cutting forces

Figure 5.20. Measurements for 9000 rev/min and 2.5 mm axial dept of cut.

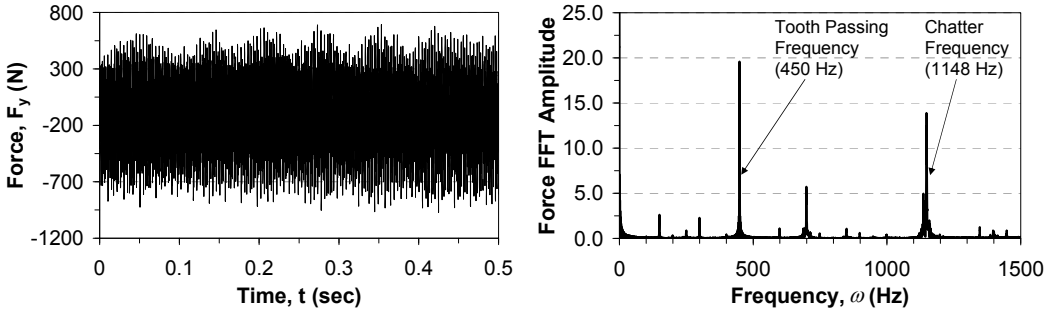

(a) – Measured cutting forces, F_y (b) – FFT of cutting forces

Figure 5.21. Measurements for 9000 rev/min and 3.0 mm axial dept of cut.

The development of the chatter frequency is also clearly seen in the FFTs of the cutting forces (Figures 5.19b, 5.20b and 5.21b). The actual chatter frequency was 1148 Hz compared to 1136 Hz predicted by the proposed stability model. Finally, the effects of chatter are shown in the surface finish of the workpiece in Figures 5.22a and 5.22b. The tooth marks causing the bad surface finish are clearly visible.

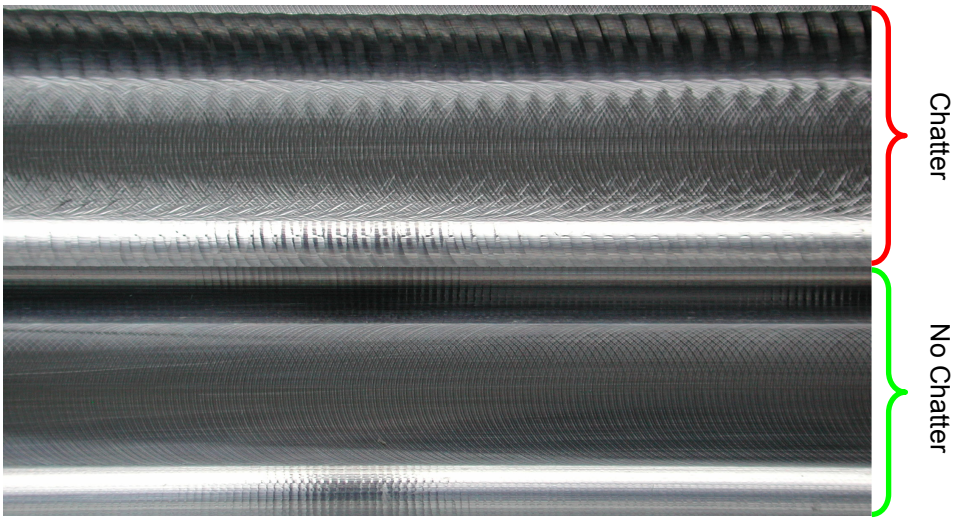

(a) – Plan view

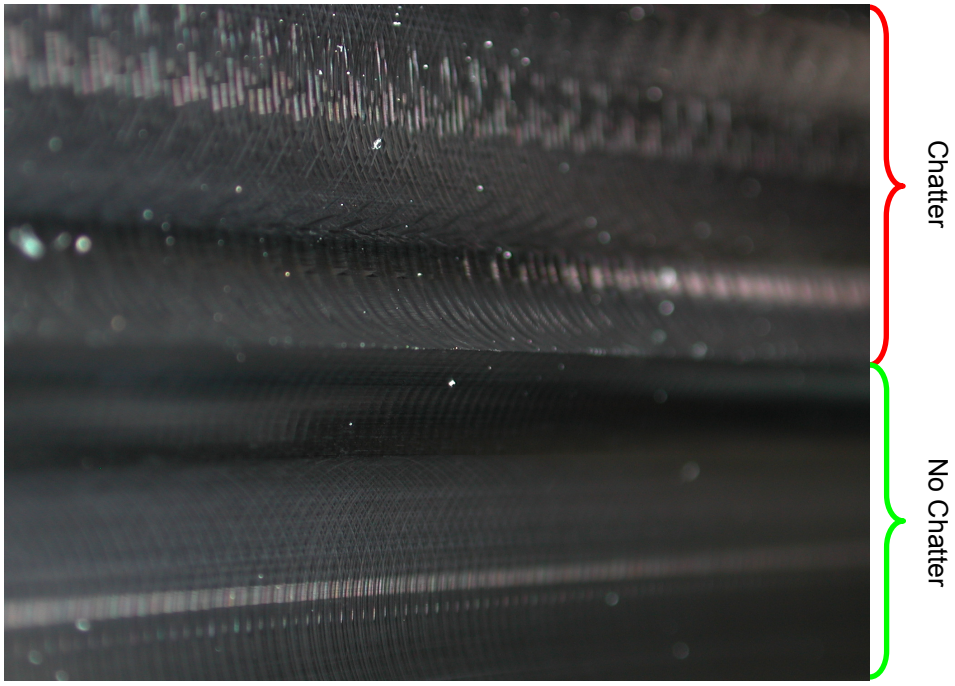

(b) – Side view

Figure 5.22. Plan and side views of two axial depth of cut surface finishes for 9000 rev/min, axial depth of cuts of; 2.50 mm above and 3.00 mm below.

5.3. Floquet Approach to Higher-Order Approximation using Non-linear Cutting Force Coefficients

In this section, a higher order approximation model is developed considering the systems vibrations in three dimensions. This higher order approximation considers the effect of higher harmonics on the stability margin for a milling system. The model takes into account the non-linearity of the cutting force coefficients and the axial immersion when predicting the stability margin.

5.3.1. Model Formulation

The zeroth order approximation presented in the previous section is only able to predict instabilities due to Hopf bifurcations. However for Flip bifurcation, the tooth passing frequency harmonics must be considered. The use of Floquet's theorem to model instabilities due to Flip bifurcations has been reported by Insperger (2003) and (Merdol (2004). Therefore, the model by Merdol is further developed in this section for a three-dimensional system.

It was shown in equation (5.13), that the directional coefficient matrix, $[A]$ is periodic at the tooth passing frequency $\omega_T = N\Omega$ and also a function of the axial depth of cut through the cutting force coefficients and the axial immersion angle. In previous studies it was only considered to be periodic at the tooth passing frequency, ω_T. Therefore the directional matrix $[A]$ can be expanded into the Fourier series,

$$[A(t,a)] = \sum_{r=-\infty}^{\infty} [A_r] e^{ir\omega_T t}, \tag{5.39}$$

where the Fourier series coefficient $[A_r]$ is given by,

$$[A_r] = \frac{1}{T}\int_0^T [A(t,a)] e^{-ir\omega_T t}\, \mathrm{d}t, \quad r = 0, \pm 1, \pm 2, \pm 3... \tag{5.40}$$

From equation (5.1), the angular immersion of tooth j was defined as,

$$\phi_j(t) = j\phi_p + \Omega t \qquad \text{where, } \phi_p = \frac{2\pi}{N}$$

The tooth period and tooth passing frequency are defined respectively as,

$$T = \frac{2\pi}{N\Omega}, \qquad \omega_T = \frac{2\pi}{T} \tag{5.41}$$

Hence,

$$\phi_j(t) = \Omega(jT + t) = \Omega\tau_j, \tag{5.42}$$

and when,

$$\left.\begin{array}{llll} t = 0 & \rightarrow & \tau_j = jT, & \phi_j(0) = j\Omega T = \phi_p \\ t = T & \rightarrow & \tau_j = (j+1)T, & \phi_j(T) = (j+1)\Omega T = (j+1)\phi_p \end{array}\right\} \tag{5.43}$$

The directional matrix $[A]$ as shown in previous section, is only valid when the tool is engaged $(\text{i.e. } \phi_{entry} \le \phi \le \phi_{exit})$ and is periodic at the pitch angle, ϕ_p. Therefore, equation (5.40) can be expressed as,

$$\begin{aligned} [A_r] &= \frac{1}{T}\sum_{j=0}^{N-1}\int_{jT}^{(j+1)T}[A_j(\phi,a)]e^{-irN\phi}\,\mathrm{d}\phi, \\ &= \frac{N}{2\pi}\int_{\phi_{entry}}^{\phi_{exit}}[A(\phi,a)]e^{-irN\phi}\,\mathrm{d}\phi = \frac{N}{16\pi}[\alpha_r(a)], \end{aligned} \tag{5.44}$$

where $[\alpha_r(a)] = \begin{bmatrix} \alpha_{xxr}(a) & \alpha_{xyr}(a) & \alpha_{xzr}(a) \\ \alpha_{yxr}(a) & \alpha_{yyr}(a) & \alpha_{yzr}(a) \\ \alpha_{zxr}(a) & \alpha_{zyr}(a) & \alpha_{zzr}(a) \end{bmatrix}$

By using Euler's formula, which gives the relationship between the complex exponential function and the polar form defined as,

$$\mathrm{e}^{-i\theta} = \cos\theta - i\sin\theta, \tag{5.45}$$

we have the following,

$$\left.\begin{array}{l} b\cdot e^{i\theta} = b(\cos\theta + i\sin\theta), \\ b\cdot e^{-i\theta} = b(\cos\theta - i\sin\theta) \end{array}\right\} \tag{5.46}$$

Therefore, by using equation (5.46), by noting that the reciprocal of the imaginary unit i is $-i$ and after slight manipulations using trigonometry identities, the elements of the directional factor matrix, are given as follows,

$$\begin{aligned}\alpha_{xxr} = -\sin\bar{\gamma}\Bigg(& \frac{2K_t}{p_3}e^{-i(p_3\phi)} - \frac{2K_t}{p_2}e^{-i\cdot(p_2\phi)} - \frac{2\left(K_r - iK_a\right)}{p_1}e^{-i(p_1\phi+\bar{\gamma})} \\ & + \frac{2\left(K_r + iK_a\right)}{p_1}e^{-i(p_1\phi-\bar{\gamma})} + \frac{\left(K_r - iK_a\right)}{p_2}e^{-i(p_2\phi+\bar{\gamma})} - \frac{\left(K_r + iK_a\right)}{p_2}e^{-i(p_2\phi-\bar{\gamma})} \\ & + \frac{\left(K_r - iK_a\right)}{p_3}e^{-i(p_3\phi+\bar{\gamma})} - \frac{\left(K_r + iK_a\right)}{p_3}e^{-i(p_3\phi-\bar{\gamma})}\Bigg)\Bigg|_{\phi_{start}}^{\phi_{exit}}\end{aligned} \tag{5.47a}$$

$$\begin{aligned}\alpha_{xyr} = -\sin\bar{\gamma}\Bigg(& \frac{i4K_t}{p_1}e^{-i(p_1\phi)} + \frac{\left(i2K_t\right)}{p_2}e^{-i(p_2\phi)} + \frac{\left(i2K_t\right)}{p_3}e^{-i(p_3\phi)} \\ & - \frac{\left(iK_r + K_a\right)}{p_2}e^{-i(p_2\phi+\bar{\gamma})} + \frac{\left(iK_r - K_a\right)}{p_2}e^{-i(p_2\phi-\bar{\gamma})} \\ & + \frac{\left(iK_r + K_a\right)}{p_3}e^{-i(p_3\phi+\bar{\gamma})} - \frac{\left(iK_r - K_a\right)}{p_3}e^{-i(p_3\phi-\bar{\gamma})}\Bigg)\Bigg|_{\phi_{start}}^{\phi_{exit}}\end{aligned} \tag{5.47b}$$

$$\begin{aligned}\alpha_{xzr} = -2\cos\bar{\gamma}\Bigg(& \frac{2K_t}{p_4}e^{-i(p_4\phi)} + \frac{2K_t}{p_5}e^{-i\cdot(p_5\phi)} - \frac{\left(iK_r + K_a\right)}{p_4}e^{-i(p_4\phi+\bar{\gamma})} \\ & + \frac{\left(iK_r - K_a\right)}{p_4}e^{-i(p_4\phi-\bar{\gamma})} + \frac{\left(iK_r + K_a\right)}{p_5}e^{-i(p_5\phi+\bar{\gamma})} \\ & - \frac{\left(iK_r - K_a\right)}{p_5}e^{-i(p_5\phi-\bar{\gamma})}\Bigg)\Bigg|_{\phi_{start}}^{\phi_{exit}}\end{aligned} \tag{5.47c}$$

$$\begin{aligned}\alpha_{yxr} = -\sin\bar{\gamma}\Bigg(& -\frac{i4K_t}{p_1}e^{-i(p_1\phi)} + \frac{i2K_t}{p_2}e^{-i(p_2\phi)} + \frac{i2K_t}{p_3}e^{-i(p_3\phi)} \\ & - \frac{\left(iK_r + K_a\right)}{p_2}e^{-i(p_2\phi+\bar{\gamma})} + \frac{\left(iK_r - K_a\right)}{p_2}e^{-i(p_2\phi-\bar{\gamma})} \\ & + \frac{\left(iK_r + K_a\right)}{p_3}e^{-i(p_3\phi+\bar{\gamma})} - \frac{\left(iK_r - K_a\right)}{p_3}e^{-i(p_3\phi-\bar{\gamma})}\Bigg)\Bigg|_{\phi_{start}}^{\phi_{exit}}\end{aligned} \tag{5.47d}$$

$$\begin{aligned}\alpha_{yyr} = -\sin\bar{\gamma}\Bigg(& \frac{2K_t}{p_2}e^{-i(p_2\phi)} - \frac{2K_t}{p_3}e^{-i(p_3\phi)} - \frac{\left(2K_r - i2K_a\right)}{p_1}e^{-i(p_1\phi+\bar{\gamma})} \\ & + \frac{\left(2K_r + i2K_a\right)}{p_1}e^{-i(p_1\phi-\bar{\gamma})} - \frac{\left(K_r - iK_a\right)}{p_2}e^{-i(p_2\phi+\bar{\gamma})} + \frac{\left(K_r + iK_a\right)}{p_2}e^{-i(p_2\phi-\bar{\gamma})} \\ & - \frac{\left(K_r - iK_a\right)}{p_3}e^{-i(p_3\phi+\bar{\gamma})} + \frac{\left(K_r + iK_a\right)}{p_3}e^{-i(p_3\phi-\bar{\gamma})}\Bigg)\Bigg|_{\phi_{start}}^{\phi_{exit}}\end{aligned} \tag{5.47e}$$

$$\alpha_{yzr} = 2\cos\bar{\gamma}\left(\frac{2K_t}{p_4} e^{-i(p_4\phi)} - \frac{2K_t}{p_5} e^{-i(p_5\phi)} - \frac{(K_r - iK_a)}{p_4} e^{-i(p_4\phi+\bar{\gamma})} + \frac{(K_r + iK_a)}{p_4} e^{-i(p_4\phi-\bar{\gamma})} - \frac{(K_r - iK_a)}{p_5} e^{-i(p_5\phi+\bar{\gamma})} + \frac{(K_r + iK_a)}{p_5} e^{-i(p_5\phi-\bar{\gamma})} \right)\Bigg|_{\phi_{start}}^{\phi_{exit}} \tag{5.47f}$$

$$\alpha_{zxr} = -4\sin\bar{\gamma}\left(Ka\sin\bar{\gamma} - Kr\cos\bar{\gamma}\right)\left(\frac{e^{-i(p_5\phi)}}{p_5} - \frac{e^{-i(p_4\phi)}}{p_4} \right)\Bigg|_{\phi_{start}}^{\phi_{exit}} \tag{5.47g}$$

$$\alpha_{zyr} = -4\sin\bar{\gamma}\left(Ka\sin\bar{\gamma} - Kr\cos\bar{\gamma}\right)\left(\frac{i\cdot e^{-i(p_5\phi)}}{p_5} + \frac{i\cdot e^{-i(p_4\phi)}}{p_4} \right)\Bigg|_{\phi_{start}}^{\phi_{exit}} \tag{5.47h}$$

$$\alpha_{zzr} = 8\cos\bar{\gamma}\left(Ka\sin\bar{\gamma} - Kr\cos\bar{\gamma}\right)\left(\frac{i\cdot e^{-i(p_1\phi)}}{p_1} \right)\Bigg|_{\phi_{start}}^{\phi_{exit}} \tag{5.47i}$$

where,

$$p_1 = rN, \qquad p_2 = rN + 2, \qquad p_3 = rN - 2,$$

$$p_4 = rN + 1, \qquad p_5 = rN - 1,$$

and $\alpha_{il,r}$ is a complex conjugate of $\alpha_{il,-r}$ ($i = l = x, y, z$, $r = 0, 1, 2, 3, \ldots.$), the axial immersion angle $\bar{\gamma}$ was defined in section 5.2.1. For the special case of $r = 0$, the directional factor matrix for the zeroth order approximation in equation (5.15) is used.

The displacement and regenerative vector from equation (5.21) can also be defined as

$$\{\Delta(t)\} = \left(1 - e^{-i\omega T}\right)[G(i\omega)]\{F(t)\}, \tag{5.48}$$

which when substituted into the cutting forces expression (equation (5.13)), gives a differential equation with periodic and piecewise continuous coefficients in the form,

$$\{F(t)\} = a\left(1 - e^{-i\omega T}\right)[A(t)][G(i\omega)]\{F(t)\}, \tag{5.49}$$

According to Floquet's theorem (Magnus, 1966), there exists a solution to equation (5.49) in the form,

$$F(t) = e^{\lambda t} P(t) \tag{5.50}$$

where, $P(t)$ is periodic at the tooth period T, λ is the so-called characteristic exponent/Floquet exponent, while $\mu = e^{\lambda t}$ is a characteristic multiplier of the system.

At the stability limit, the tool/workpiece will vibrate at the chatter frequency ω_c, hence $\lambda = i\omega_c$. Therefore there are three cases for the critical characteristics multipliers $\left(\mu = e^{i\omega_c t}\right)$:

- μ is complex and $|\mu| = 1$. This type of instability is called the Hopf (or Neimark-Sacker) bifurcation or Quasi-periodic chatter (Insperger, 2008) and predictions of which were developed in the previous section.
- $\mu = -1$. This type of instability is called period two, period doubling or flip bifurcation (Insperger, 2008).
- $\mu = 1$. This type of instability is a called period one or saddle-node bifurcation. This type of instability cannot arise in milling as shown by Davies (2002) and Insperger (2001).

Therefore, by following solution form in equation (5.50), the dynamic milling force expression (equation 5.13) can be expanded into the Fourier series,

$$P(t) = \sum_{k=-\infty}^{\infty} P_k e^{ik\omega_T t}, \tag{5.51}$$

where, the Fourier coefficient P_k is given by,

$$P_k = \frac{1}{T}\int_0^T P(t) e^{-ik\omega_T t}\, \mathrm{d}t, \quad k = 0, \pm 1, \pm 2, \pm 3... \tag{5.52}$$

Therefore, equation (5.51) is substituted into equation (5.50) to obtain,

$$F(t)=\left(e^{i\omega_c t}\sum_{k=-\infty}^{\infty}P_k e^{ik\omega_T t}\right)=\sum_{k=-\infty}^{\infty}P_k e^{i(\omega_c+k\omega_T)t} \tag{5.53}$$

When this is compared with the differential equation obtained when equation (5.48) is substituted into equation (5.13) we obtain,

$$\sum_{k=-\infty}^{\infty}\left(P_k e^{i(\omega_c+k\omega_T)t}\right)=\Lambda\left(\sum_{r=-\infty}^{\infty}[A_r]e^{ir\omega_T t}\right)\left(\sum_{k=-\infty}^{\infty}P_k e^{i(\omega_c+k\omega_T)t}\cdot[G_k]\right), \tag{5.54}$$

where,

$$[G_k]=[G(i(\omega_c+k\omega_T))], \tag{5.55}$$

and the eigenvalue, Λ is defined as,

$$\Lambda=\frac{a}{2}\left(1-\mathrm{e}^{-i\omega_c T}\right) \tag{5.56}$$

Therefore, by comparing equations (5.54) and (5.51), we have,

$$P(t)=\Lambda\left(\sum_{r=-\infty}^{\infty}[A_r]e^{ir\omega_T t}\right)\left(\sum_{k=-\infty}^{\infty}P_k e^{ik\omega_T t}\cdot[G_k]\right) \tag{5.57}$$

Hence, by multiplying both sides of equation (5.57) by $(1/T)e^{-i\eta\omega_T t}$ and integrating from 0 to T, we obtain,

$$\frac{1}{T}\int_0^T P(t)e^{-i\eta\omega_T t}\,\mathrm{d}t=\Lambda\frac{1}{T}\int_0^T\left(\sum_{r=-\infty}^{\infty}[A_r]e^{ir\omega_T t}\right)\left(\sum_{k=-\infty}^{\infty}[G_k]\cdot P_k e^{-i(\eta-k)\omega_T t}\right)\mathrm{d}t, \tag{5.58}$$

which gives the Fourier spectrum coefficient, of the force term $P(t)$ at harmonics η as,

$$P_\eta=\Lambda\left(\sum_{k=-\infty}^{\infty}[A_{\eta-k}][G_k]\cdot P_k\right), \tag{5.59}$$

where, $\eta, k=0,\pm1,\pm2,\pm3,....,\pm h_r$

Therefore, depending on the number of tooth passing frequency harmonics considered, the algebraic equation in equation (5.59) can be truncated to an

eigenvalue problem, for which a nontrivial solution exists only if its determinant is zero; i.e.,

$$\det\left[\delta_{\eta k} I + \Lambda\left[A_{\eta-k}\right]\left[G_k\right]\right] = 0, \tag{5.60}$$

where, $\delta_{\eta k}$ is the Kronecker delta (i.e. $\delta_{\eta k} = 1$ if $\eta = k$, $\delta_{\eta k} = 0$ if $\eta \neq k$) and I is an identity matrix.

Similar, to the zeroth order approximation presented in the previous section, equation (5.58) is the characteristic equation of the milling system. Approximate roots of this infinite order characteristic equation can be obtained by solving its truncated version. For this characteristic equation, there exists $\left(6h_r + 3\right)$ eigenvalues and when $h_r = 0$, the problem is reduced to the zeroth order approximation presented in the previous section.

Therefore, to predict the stability margin for a given structure (i.e. cutter and workpiece), the dynamic parameters are extracted using either the experimental approach discussed in Chapter 4, or the numerical damping prediction, the FEM and the Fourier methods proposed in Chapter 4. It would be much easier to use the actual modal dynamic parameters (i.e. natural frequency, damping ratios and modal stiffness), like those given in Table 5.1. These dynamic parameters are used in equations (5.36) and (5.37) to calculate the system's transfer function matrix $\left(\left[G_k\right]\right)$ using the different frequency harmonics $\left(\omega_c + k\omega_T\right)$.

For example: for $h_r = 2,$ we have that,

$$\begin{pmatrix} [P_0] \\ [P_{-1}] \\ [P_1] \\ [P_{-2}] \\ [P_2] \end{pmatrix} = \Lambda\boldsymbol{\Gamma} \begin{pmatrix} [P_0] \\ [P_{-1}] \\ [P_1] \\ [P_{-2}] \\ [P_2] \end{pmatrix} \tag{5.61}$$

where,

$$\mathbf{\Gamma} = \begin{bmatrix} \mathbf{A_0G_0} & \mathbf{A_1G_{-1}} & \mathbf{A_{-1}G_1} & \mathbf{A_2G_{-2}} & \mathbf{A_{-2}G_2} \\ \mathbf{A_{-1}G_0} & \mathbf{A_0G_{-1}} & \mathbf{A_{-2}G_1} & \mathbf{A_1G_{-2}} & \mathbf{A_{-3}G_2} \\ \mathbf{A_1G_0} & \mathbf{A_2G_{-1}} & \mathbf{A_0G_1} & \mathbf{A_3G_{-2}} & \mathbf{A_{-1}G_2} \\ \mathbf{A_{-2}G_0} & \mathbf{A_{-1}G_{-1}} & \mathbf{A_{-3}G_1} & \mathbf{A_0G_{-2}} & \mathbf{A_{-4}G_2} \\ \mathbf{A_2G_0} & \mathbf{A_3G_{-1}} & \mathbf{A_1G_1} & \mathbf{A_4G_{-2}} & \mathbf{A_0G_2} \end{bmatrix} \tag{5.62}$$

and,

$$[A_r] = \begin{bmatrix} \alpha_{xxr} & \alpha_{xyr} & \alpha_{xzr} \\ \alpha_{yxr} & \alpha_{yyr} & \alpha_{yzr} \\ \alpha_{zxr} & \alpha_{zyr} & \alpha_{zzr} \end{bmatrix}, \tag{5.63}$$

$$[G_k] = \begin{bmatrix} G_{xxk}(i(\chi)) & G_{xyk}(i(\chi)) & G_{xzk}(i(\chi)) \\ G_{yxk}(i(\chi)) & G_{yyk}(i(\chi)) & G_{yzk}(i(\chi)) \\ G_{zxk}(i(\chi)) & G_{zyk}(i(\chi)) & G_{zzk}(i(\chi)) \end{bmatrix}, \tag{5.64}$$

where, $\chi = \omega_c + k\omega_T$

The eigenvalues obtained have a real and an imaginary part, $(\Lambda = \Lambda_R + i\Lambda_I)$. Therefore, by following the same procedure as in equations (5.27 – 5.31), the axial depth of cut can be defined as,

$$a_{\lim} = -\Lambda_R \left(1 + \left[\frac{\Lambda_I}{\Lambda_R} \right]^2 \right), \tag{5.65}$$

while, the spindle speed can be written in the form,

$$n = \frac{60\omega_c}{N(2\pi k + \varepsilon)}. \tag{5.66}$$

The minimum predicted $a_{\lim}$ for the different harmonics is taken as the corresponding critical axial depth of cut.

5.3.2. Proposed Numerical Approach

The numerical approach for the higher order approximation is very similar to the procedure proposed for the zeroth order approximation, with the exceptions

of the added steps to allow for higher order approximation. The steps of the proposed algorithm are therefore as follows:

1. Specify a spindle speed range of interest and the increment.

2. Specify a chatter frequency range of interest (around the dominant modes of the system).

3. Determine the total number of tooth passing frequency harmonics of interest, h_r. The higher the number of harmonics, the better the higher order approximations will be and also the greater the computation time.

4. Begin the numerical steps by selecting the spindle speed.

5. Select a chatter frequency and calculate the corresponding frequencies of all the harmonics, using $(\omega_c + k\omega_T)$.

6. Calculate the corresponding transfer function matrices, G_k using equations (5.36 and 5.37) for each considered harmonic.

7. Start the numerical approach to calculating stable axial depth of cut:

(A) Using predicted axial depth of cut a^m (where initial values of $a^0 = a_{\min}$), calculate the cutting force coefficients, K_t, K_r, K_a and axial immersion $\bar{\gamma}$

(B) Calculate the elements in matrices, $[A_r]$ using equations (5.47)

(C) Construct the system's oriented transfer function matrix (example of which is shown in equation (5.62) for $h_r = 2$)

(D) Solve the eigenvalue characteristic equation (5.60)

(E) Calculate the critical depth of cut using equation (5.65)

(F) Subtract the calculated axial depth of cut $a_{\lim}$ from the predicted axial depth of cut a^m to obtain the error as follows

$$\eta^m = a^m - a_{\lim}$$

(G) If $m > 1$, compare the sign of the previous and current axial depth of cut error, η^m and η^{m-1}, else go to (K)

(H) If the signs have changed, a converged axial depth of cut solution can be obtained by means of simple interpolation as follows,

$$a^*_{\lim} = \frac{-\eta^{m-1}}{\eta^m - \eta^{m-1}} \cdot a^m \cdot a^{m-1} + a^{m-1} \tag{5.67}$$

(I) Then proceed to step 8

(J) If the signs are unchanged and $a^m < a_{\max}$ then update the predicted axial depth of cut using $a^{m+1} = a^m + \Delta a$, else STOP and go to step 1 as the solution to the chosen chatter frequency is not within the range of the axial depth of cut imposed by the calibrated cutting force coefficients

(K) Go to step (A) with $m = m + 1$, $a^{m-1} = a^m$ and $\eta^{m-1} = \eta^m$

8. Using the converged axial depth of cut solution, $a^*_{\lim}$ calculate the corresponding cutting force coefficients and axial immersion.

9. Calculate the elements in matrices, $[A_r]$ using equations (5.47) and $[G_k]$ using equations (5.36 and 5.37), now using the accurate cutting force coefficients and axial immersion. Then construct the system's oriented transfer function matrix.

10. Solve the eigenvalue characteristic equation (5.60)

11. Calculate the spindle speed using equation (5.66) for each stability lobe $k = 0, 1, 2, 3, \ldots$

12. Repeat the procedure for the different chatter frequencies in the specified range still for the current spindle speed.

13. Increase the spindle speed to the next spindle speed based on the increment specified and repeat step 5 and continue.

These steps are laid out chronologically in Figure 5.23.

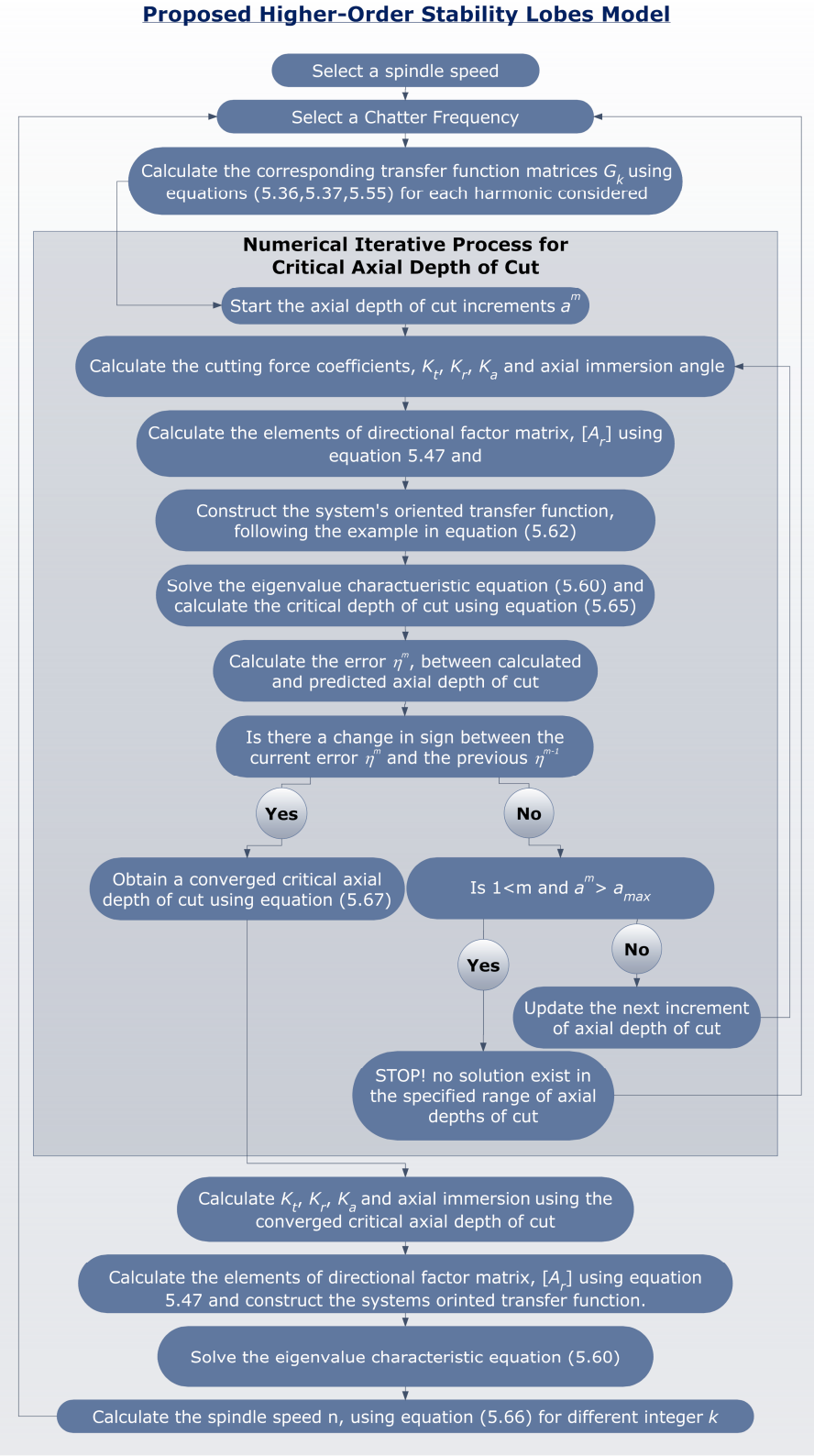

Figure 5.23. Higher-order stability model numerical algorithm.

5.3.3. Validation

The higher approximation approach developed in this section is more suited for a highly intermittent cutting process, which is obtained for very shallow radial depths of cut. However, the model is demonstrated here using a very deep radial depth of cut (19.00mm), which is nearly a full slot. The main purpose of this is to check on the validity of the actual model, since a very good set of accurate results were obtained for the zeroth order approximation.

Therefore, the proposed algorithm was used to predict the stable margin for the cutting process presented in the previous section. A radial depth of cut of 19.00mm, a total of 10 harmonics (i.e. $h_r = 10$), a range of chatter frequencies from 500Hz to 3000Hz was scanned at increments of 0.5Hz. The minimum and maximum natural frequencies of the tool are at 1.2627×10^3 Hz and 2.6869×10^3 Hz respectively, therefore this frequency range covers all the natural frequencies. The numerical solution steps, were coded using Matlab. The predicted stable margin is shown in Figure 5.24 and compared with the previously validated results obtained in section 5.2 on zeroth order approximation.

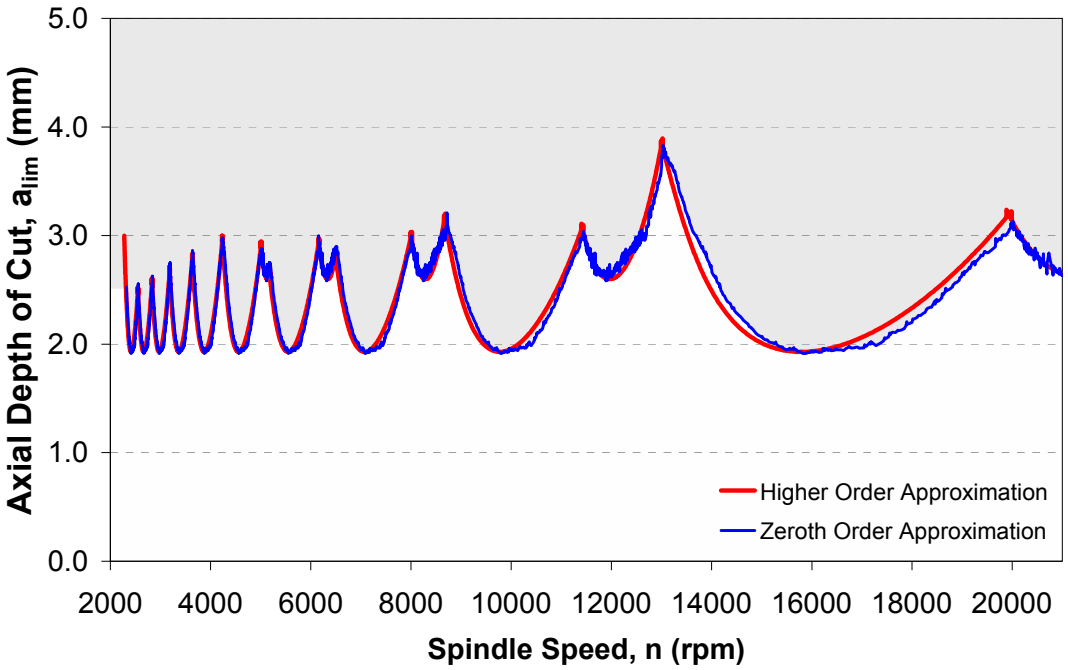

Figure 5.24. Stability Margin Validation.

It can be seen that there is no added stability lobe that arises from an intermittent cutting process. This is because as mentioned earlier the cutting conditions are nearly a full slot, which means that the tool's teeth are constant in engagement. To further demonstrate this, the FFT of the cutting forces and deflection measurements shown in Figures 5.11 – 5.19, shows that although the higher harmonics exist they are not particularly dominant. However the results shown in Figure 5.24, validates the formulation of the model as the results are not seen to deviate from the zeroth order approximation; while the accuracy of the zeroth approximation has been confirmed in the previous section.

5.4. Summary

In this chapter, the stability lobe approach to predicting the Hopf bifurcations in milling processes is discussed and the focus was on tool chatter only by making the workpiece relatively rigid. Improvements to the model are proposed and a numerical algorithm that allows for the extraction of the converged solution was proposed. The cutting force coefficient was successfully adopted into the stability model as a variable of the axial depth of cut. The accuracy attainable by the proposed improvements is clearly seen in the results compared extensively with experimental results. An approach that uses Floquet theorem to predict stable margins, while taking into account the effects of higher harmonics, the non-linearity of coefficients and axial immersion was also developed.

Chapter 6

Thin Walled Workpiece Chatter

6.1. Introduction

Due to weight requirements and the demand for higher efficiency, manufactured parts are being designed with much thinner sections, which greatly reduces the parts' structural stiffness. On the one hand when machining these parts, the need for more accurate stable cutting conditions becomes much more imperative as the development of chatter can greatly reduce the manufacturing efficiency by rendering the whole part unusable. On the other hand, knowledge of the influence the part's design has on the cutting conditions would aid the designers in reaching better and more efficient designs. Chatter as stated by Taylor (1907) is one of the most obscure and delicate of all problems facing the machinist, as it undermines and reduces productivity and surface quality in manufacturing and also increases the cost through possible machine or tool damage. It is because of these effects that it has been the topic of several studies over the years.

The accuracy of the predicted stable region relies on the dynamic parameters identified at the cutter-workpiece contact zone. The classical approach to obtaining the dynamic parameters is through impact tests. Unlike in tool chatter, predicting the stability margin for flexible workpiece parts is more

complex, as the dynamic parameters are not constant along the workpiece and are constantly changing as material is removed and the geometry changes. Attempts were made by Thevenot (2006) to use this varying dynamics in thin wall machining to initiate the variation of the spindle speed along the workpiece in order to improve surface finish. The tendency in this approach however is for new marks to be left on the surface due to the change in cutting conditions as seen from their experimental results. Budak considered the variations in the dynamics of the cutter and the workpiece along the axial direction. Seguy et al. (2008) recently carried out a study to try and include the varying dynamics along a thin wall and thin floor section, but the results show certain discrepancies which could have arisen from the assumptions taken. Adetoro et al. (2009b, 2009g) recently presented a 'finite element analysis' (FEA) approach to identify the systems transfer function at specified locations, which was discussed in Chapter 4.

Thus this chapter is structured as follows; the modifications to the stability lobe model proposed in Chapter 5 and the FEM approach proposed in Chapter 4 are used to include the nonlinear dynamics along a thin wall in the stability lobes prediction. Therefore, the nonlinear cutting coefficients, axial immersion angle and nonlinear dynamics along the workpiece are all included in the stable margin predicted. The accuracy is clear in the comparisons with experimental results. The accuracy also spans to the precise location of chatter development predicted.

6.2. Accurate Prediction of Stability Lobes using Nonlinear Thin Wall Dynamics

This section further presents applications of the improvements proposed in Chapter 5 and also the applications of the Finite Element (FE) and Fourier transform approach in Chapter 4 in thin wall machining. The FE and Fourier approach was used to include the non-linearity of the workpiece dynamics in thin wall machining when predicting stable region. The model and approach are validated extensively using experimental results and very good agreements have been achieved.

The stability lobe model used in this section was described in detail in Chapter 5. It is based on the three dimensional stability model by Altintas (2001). The modifications introduced in Chapter 5 allow for more accurate modelling of the cutting forces using non-linear cutting force coefficients and non-linear axial immersion angle. Reference should be made to Chapter 5, as this model is not detailed in this chapter. The chapter mainly goes on to use this improved model to predict the stable margin for thin walled sections, whilst accommodating the changes in the workpiece dynamics along the tool path.

6.2.1. Varying Workpiece Transfer Function

The tool or cutter's transfer function can be assumed to be constant during the machining process, while the workpiece transfer function however cannot be assumed to be constant. It varies initially along a given tool path and also as material is removed, hence the experimental approach to extracting the transfer function would be challenging. The 'finite element' approach presented in Chapter 4 can be used to identify the workpiece transfer function at a single specified location; since the ideal stable condition when machining a thin wall section, would be a condition that is stable all along the workpiece. Therefore using the previously proposed finite element approach, the system's transfer function is identified at as many locations along the intended tool path as possible

and their corresponding stability margins calculated using the method detailed in Chapter 5. Therefore, by simply superimposing the predicted stability lobes the actual stable cutting region for the given tool path can then be obtained. The lobes have to be superimposed because it is impractical to change the cutting conditions during machining, therefore the chosen cutting conditions at the beginning of cut must be stable for the rest of the tool path. Thevenot (2006) tried the varying spindle sped approach and found that new marks were left on the surface due to the abruptly stopped cutting process. Although the approach proposed here can be used to vary the spindle speed along the tool-path, it is not advised.

6.2.2. The Finite Element Model

The workpiece material used in the FEM model was the same model used in Chapter 4 and is given again here for convenience. The material used during both the experiments and FEM analysis was Aluminium Alloy 7010 T7651. The material properties required for generating the stiffness and mass matrices are: Density - 2.823×10^{3} Kg m-3, Young's Modulus - 69.809 GPa and Poisson Ratio - 0.337. The dimensions of the workpiece are shown in Figure 6.1 and the thickness, (W) = 3.0mm and height (H) = 30.0mm.

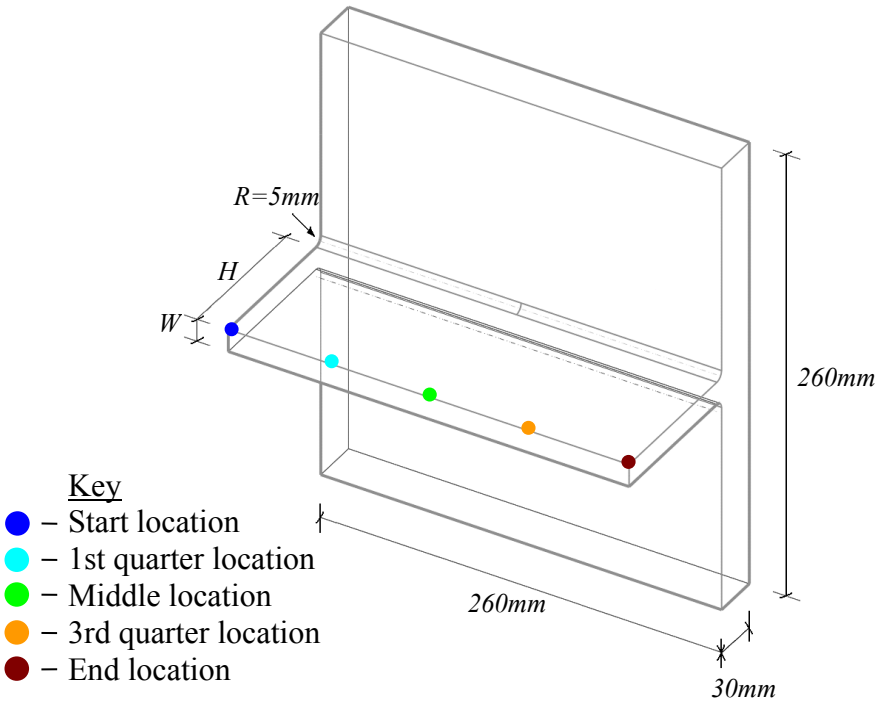

Figure 6.1. Workpiece dimensions.

The assumptions made in the finite element analysis (FEA) are as follows:

- The workpiece was bolted at the back surface during the machining and in the FEM this was assumed to be perfectly clamped.
- It was assumed that the natural frequencies of the machine are very high compared to that of the workpiece, hence their influence can be ignored in the FEM analysis.

6.2.3. The Damping Ratio

The mass or inertia and stiffness forces can be predicted numerically with very good accuracy for any given geometry, material properties and boundary conditions. The damping forces are at present extracted through experiments known as modal testing or analysis, although an approach to predicting the damping ratio for subsequent walls was proposed in Chapter 4. This approach can certainly be incorporated with the method this Chapter presents. Just like the natural frequency, the damping ratio is dependent on the geometry, therefore it can be taken to be constant along the workpiece, although it changes as material is removed. The damping ratios, ζ_l for the cutter and workpiece were identified through impact tests in Chapters 4 and 5 and are given in Tables 6.1 and 6.2 for convenience. The workpiece is excited using an instrumented hammer, whilst the accelerometer is placed on the opposite side of the impact point, to measure the direct transfer function. Using a Fourier analyser, the accelerance frequency response function is extracted for each impact test. This is simply the division of the Fourier transform of the measured time domain input force $f(t)$ and acceleration $\ddot{x}(t)$.

$$Acc(\omega) = \frac{\ddot{X}(\omega)}{F(\omega)}, \tag{5.26}$$

where $Acc(\omega)$ is the accelerance FRF, $\ddot{X}(\omega)$ is the output acceleration signal in frequency domain and $F(\omega)$ is the input force signal in frequency domain. The experimental measurements are analysed using a modal analysis system (a commercial software package called CutPro was used for the solutions in this

paper), which scans the measured transfer function and fits a curve to the data in order to obtain the numerical values of natural frequency and corresponding damping ratios (Gadalla, 1997). The errors induced by the mass of the accelerometer were compensated for using the approach proposed by Cakar and Sanliturk (2005).

6.2.4. Results

Extracting the Workpiece Transfer Function

To obtain experimental results to validate the proposed numerical approach, an aluminium milling application with 3-teeth milling cutter is considered. The finite element approach introduced in Chapter 4 was used to identify the workpiece transfer function at five locations: at the start, a quarter way, half way, three quarter way and finally at the end point. These locations were at 1.00mm, 65.00mm, 130.00mm, 195.0mm, 259.0mm as shown in Figure 6.1 along the cutting path respectively. In Chapter 4, the workpiece was analysed in Case Study 1B, however the transfer function was only extracted at a single point in order to validate the modelling approach. The workpiece transfer function was identified in the normal direction (Y) as the dynamics in the feed direction (X) can be neglected due to its relative magnitude. The workpiece material used in the FEM model is ‘‘Aluminium Alloy 7010 T7651’’. The material properties required for generating the stiffness and mass matrices are: Density, $\rho = 2.823\times10^{3}$ (Kgm^{-3}), Young’s Modulus, $E = 69.809$ (GPa) and Poisson Ratio, $\upsilon = 0.337$.

Table 6.1. Tool Dynamic Parameters in X and Y directions

Direction	Mode	Natural Frequency, ω_n (Hz)	Modal Stiffness, k (10^7 Nm^{-1})	Modal Damping Ratio, ζ (10^{-2} %)
X	1	1306.9361	1.0657	7.9626
	2	1897.8177	5.6677	4.4413
	3	2195.3198	6.6598	5.0610
	4	2686.9228	3.1818	3.6897
Y	1	1262.6637	1.2149	3.4316
	2	2074.2514	2.2493	7.7559
	3	2684.0002	3.1113	2.9063

Therefore by following the detailed Fourier approach presented in Chapter 4, the workpiece's transfer function at the five different locations are extracted from the time domain response of the workpiece to an input force. The different identified transfer functions are shown in Figures 6.2, 6.3, 6.4, 6.5, 6.6 and the dynamic

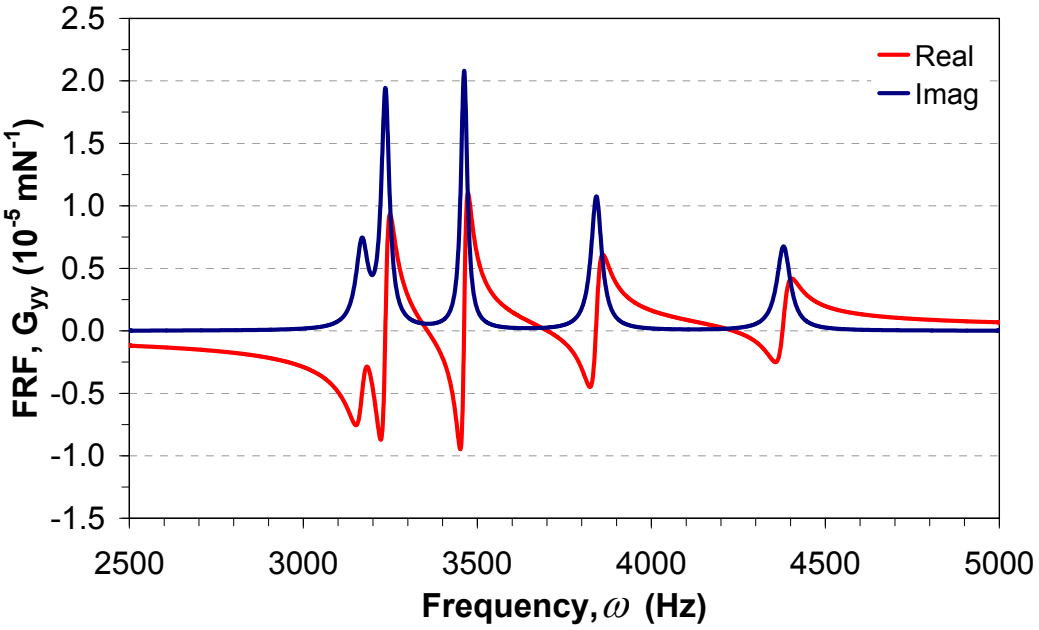

Figure 6.2. FEM identified workpiece varying transfer function at the start location (1.0mm along tool path).

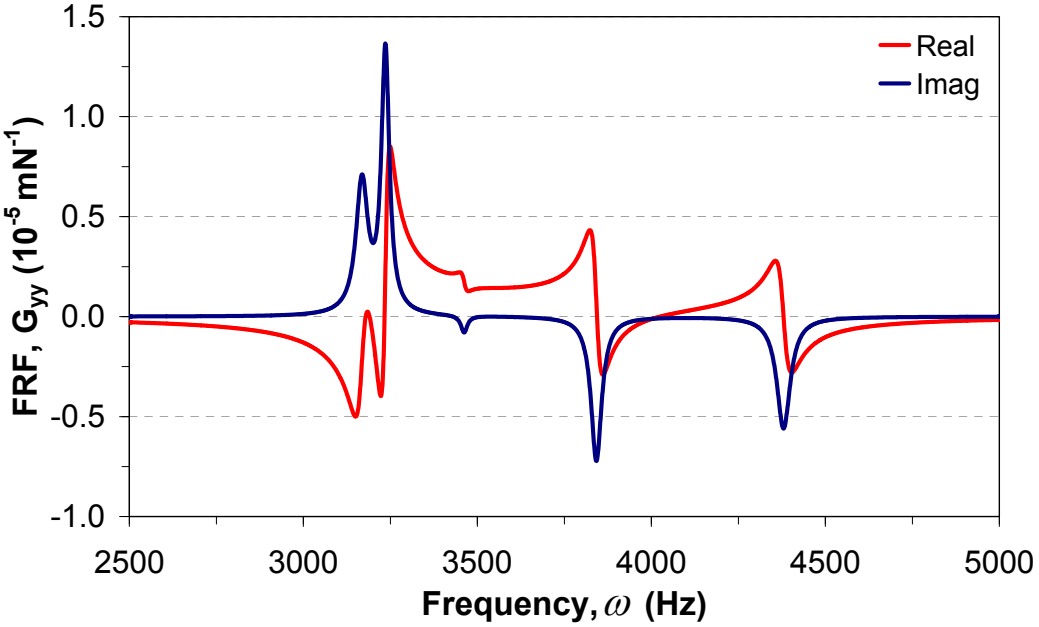

Figure 6.3. FEM identified workpiece varying transfer function at the 1st quarter location (65mm along tool path).

parameters are given in Table 2, where the experimental identified natural frequencies are compared with numerical extracted natural frequencies (the experiments are with the effects of the accelerometer removed). These numerical natural frequencies are obtained using the approach to solving the eigenvalue problem detailed in Chapter 4.

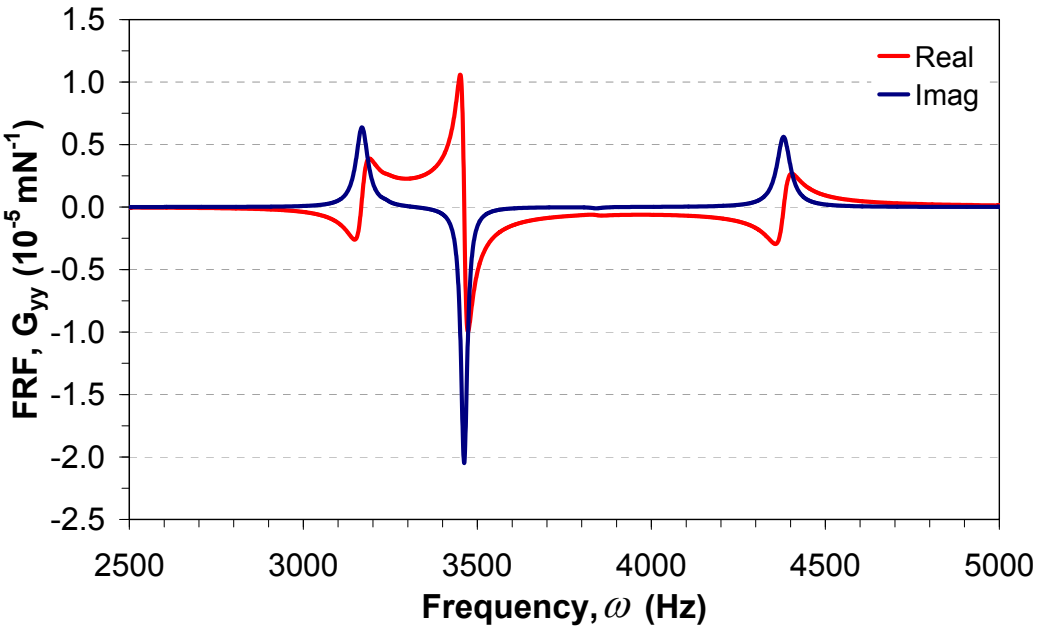

Figure 6.4. FEM identified workpiece varying transfer function at the middle location (130mm along tool path).

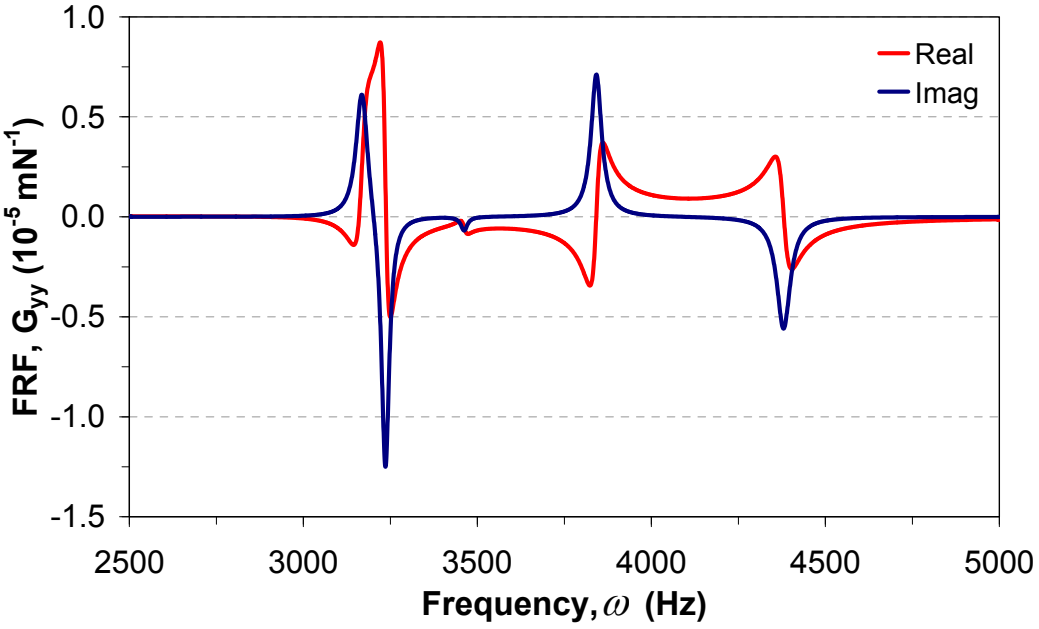

Figure 6.5. FEM identified workpiece varying transfer function at the 3rd quarter location (195mm along tool path).

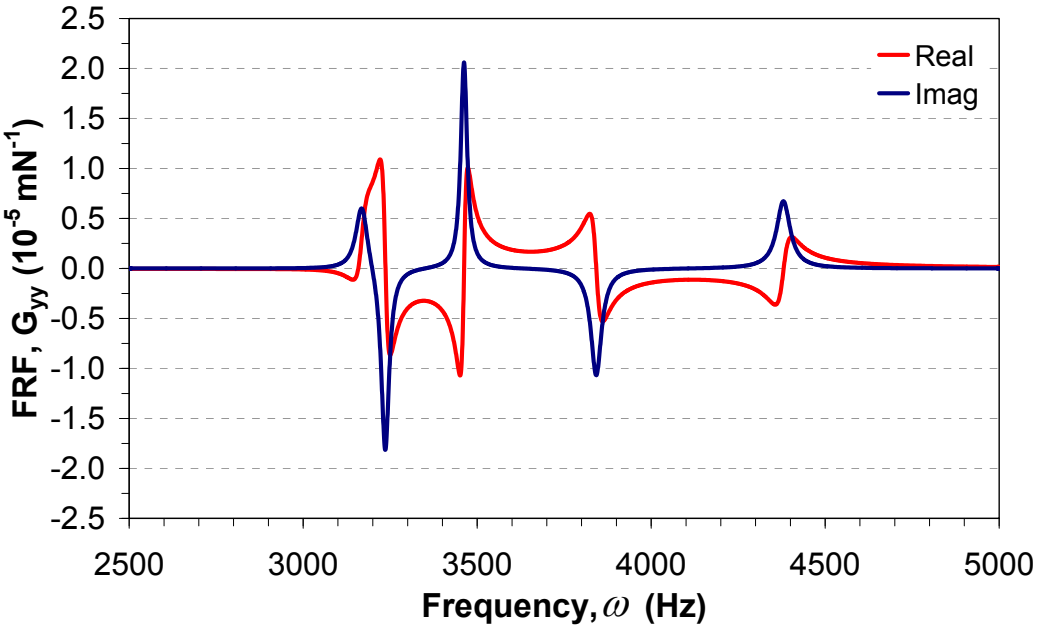

Figure 6.6. FEM identified workpiece varying transfer function at the end location (259mm along tool path).

Table 6.2. Workpiece Dynamic Parameters in Y direction, *W = 3.0mm*

Mode	Experimental Natural Frequency, ω_n (Hz)	Damping Ratio, ζ (10^{-2} %)	Numerical Natural Frequency, ω_n (Hz)
1	3173.9925	6.5375	3168.6005
2	3248.6874	4.1127	3235.6682
3	3453.1690	3.4466	3461.9967
4	3848.8494	4.9615	3842.1306
5	4356.7756	5.3526	4380.0491

6.2.5. Stability Lobes for Non-linear Dynamics

Using the proposed approach, the stability lobe diagram for a 2.0mm radial depth of cut and 20.0mm tool diameter is shown in Figure 6.7, where the unstable region is shown in grey. The transfer function is determined by modal superposition using the identified modal parameters. The different stability lobes predicted for different locations along the workpiece are superimposed in Figure 6.7. The stability lobes predicted are experimentally verified using a radial depth of cut of 2.00mm and a feed of 0.15mm, where the feedrate is simply calculated for each spindle speed.

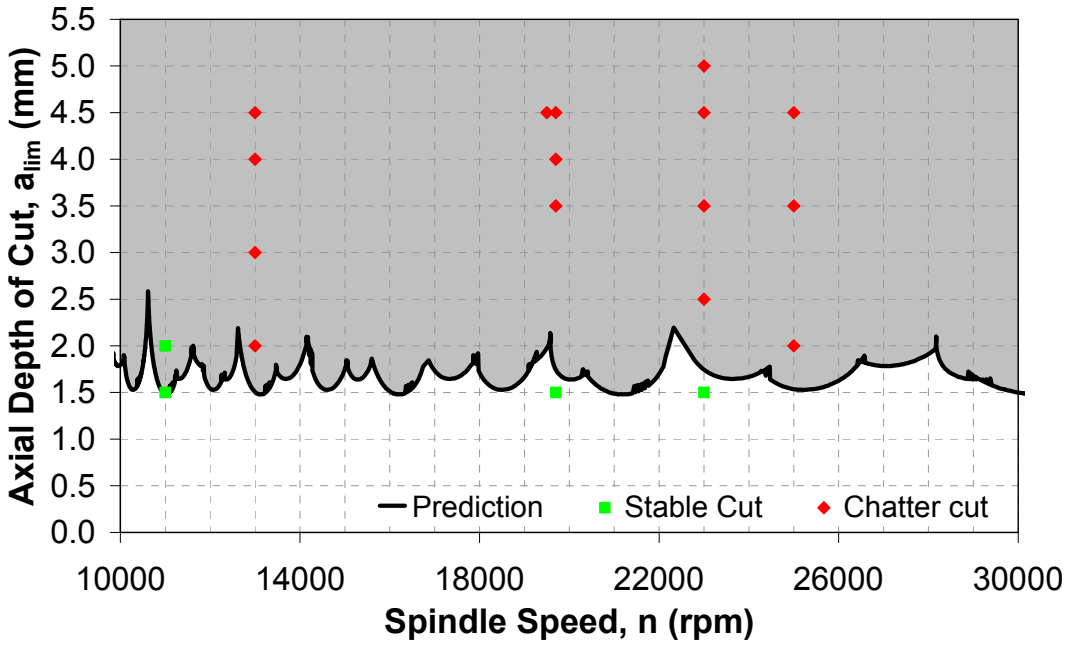

Figure 6.7. Stability Margin Validation.

The presence of chatter is monitored by the spectrum of cutting forces measured and tool vibration measured using an accelerometer built in at the back of the spindle. The different experimental results are analysed and grouped into two categories: stable and chatter cuts. The region predicted to be unstable is in good agreement with the experimental results. This graph shows the collective stability lobes superimposed for different locations, however these are shown in more detail by showing the individual lobes at different locations in Figures 6.8, 6.10, 6.12 and 6.14. These more detailed figures show the location where chatter is predicted ad comparisons are made with experimental surface finish.

For cutting tests between 10000rev/min and 14000rev/min the corresponding lobes and their locations are shown in Figure 6.8. The predictions at 11000rev/min do not match exactly with predicted regions. It is possible that this is due to flip bifurcations, discussed in Chapter 5. The approach in this paper does not predict the flip bifurcations and as was shown by Davies et al. (2000, 2002) in a highly intermittent cutting process, there are extra stable margins that the approach here does not predict. This cutting test can be considered as highly intermittent, hence for completeness the stable margin for flip bifurcations would have to be included using the model developed in Chapter 5. This however might prove to be inefficient considering the computational time required and the fact

that any added lobes might not make a major change to the grey region shown in Figure 6.7. By changing the spindle speed to 13000rev/min at axial depth of cut of 2mm, chatter is seen to develop in the cutting force. Moreover as predicted by the stability lobes, there should be chatter at the start and the end of the wall. It can be seen in the measured experimental cutting forces (Figure 6.10) that the peaks forces at the beginning of the cut and towards the end of the cut are nearly double the peak of the forces at the middle of the cut.

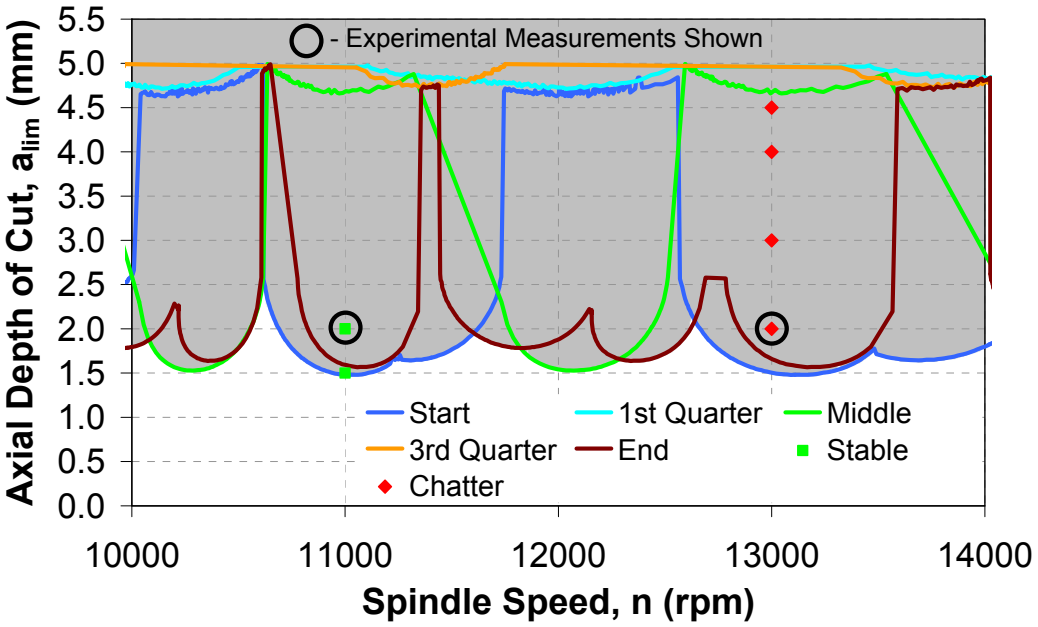

Figure 6.8. Stability lobes experimental validation for 10000rev/min – 14000rev/min.

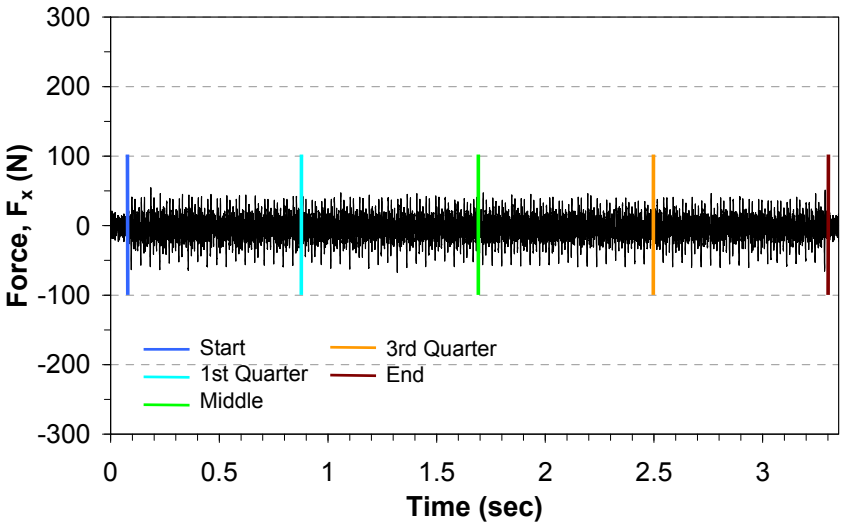

Figure 6.9. Measured cutting forces, Fx for 11000rev/min and 2.0mm axial depth of cut.

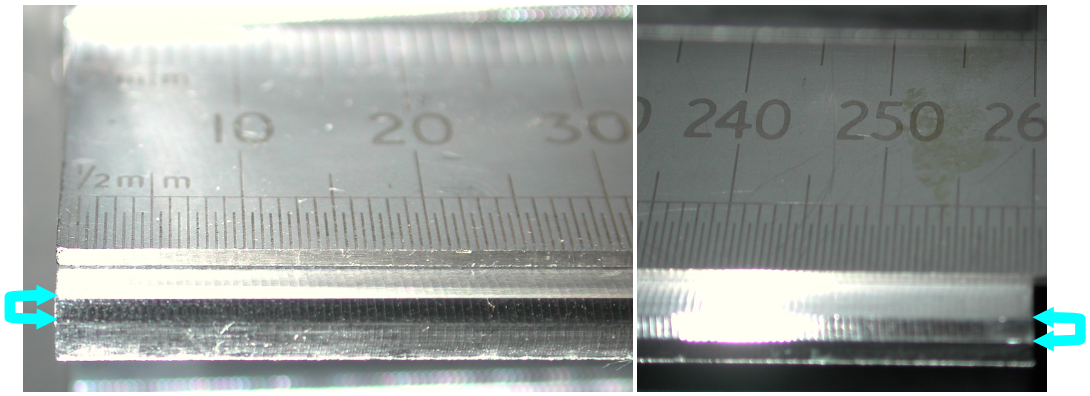

(a) Start location (b) Finish location

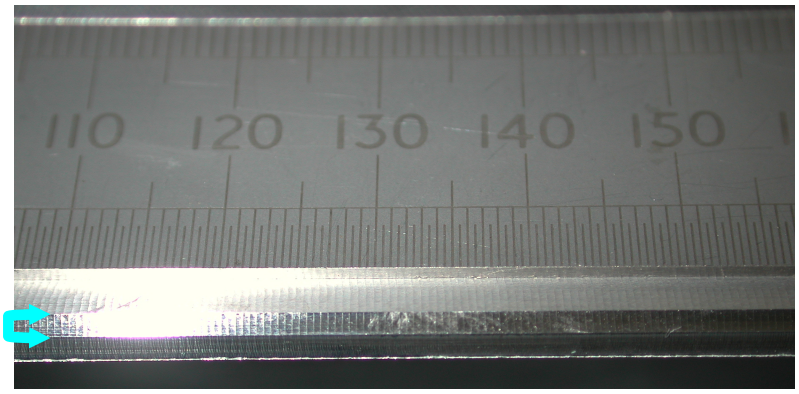

(c) Middle location

Figure 6.10. A good surface finish for 11000rev/min spindle speed and 2.0mm axial depth of cut with no chatter.

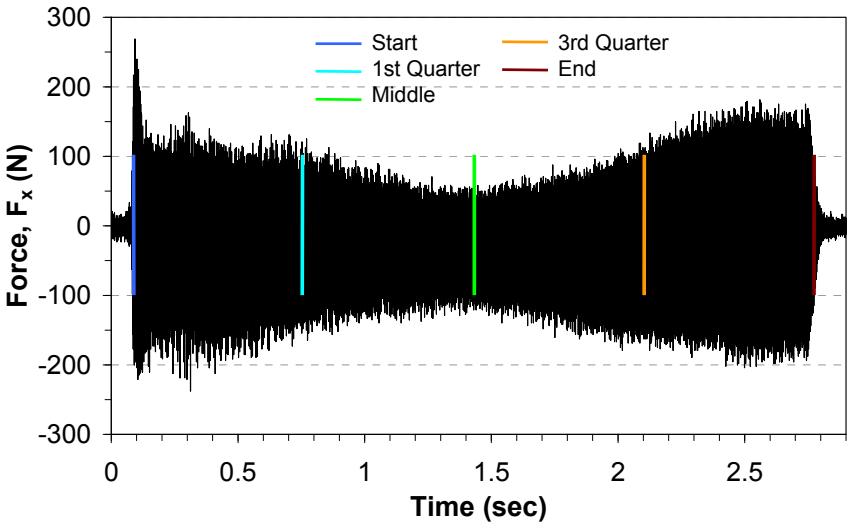

Figure 6.11. Measured cutting forces, Fx for 13000rev/min and 2.0mm axial depth of cut.

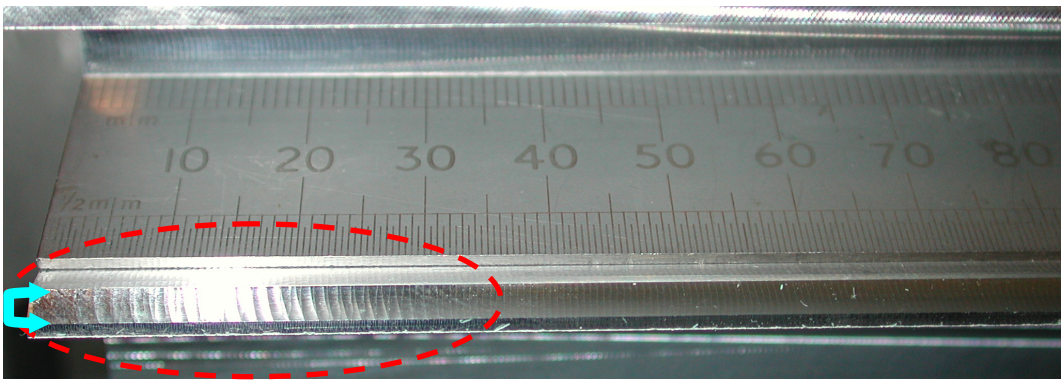

(a) Start location

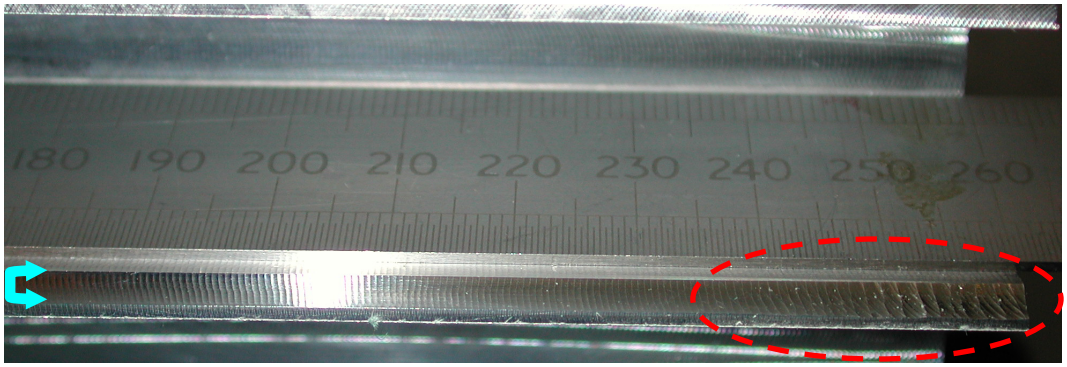

(b) Finish location

Figure 6.12. Surface finish for 13000rev/min spindle speed and 2.0mm axial depth of cut.

This clearly indicates chatter development at the start of the cut, which diminishes towards the middle and develops again as it approaches the end location. The chatter marks are clearly visible on the surface finish for an axial depth of cut of 2.0mm and spindle speed of 13000rev/min (Figure 6.12), while a good surface finish is seen for spindle speed of 11000rpm and axial depth of cut of 2.0mm (Figure 6.11). The machined surface is seen just below the ruler.

For cutting tests between 18000rev/min and 21000rev/min, the predictions are shown to be in agreement with the experiments in Figure 6.13 and the measured cutting force for spindle speed of 19700rev/min and axial depth of cut of 3.5mm is shown in Figure 6.14. Chatter was predicted only at the end of the cut corresponding to an axial depth of cut of 3.5mm and it is seen in the measured experimental cutting forces in Figure 6.14 that the forces increase drastically towards the end of the cut as predicted by the stability lobes.

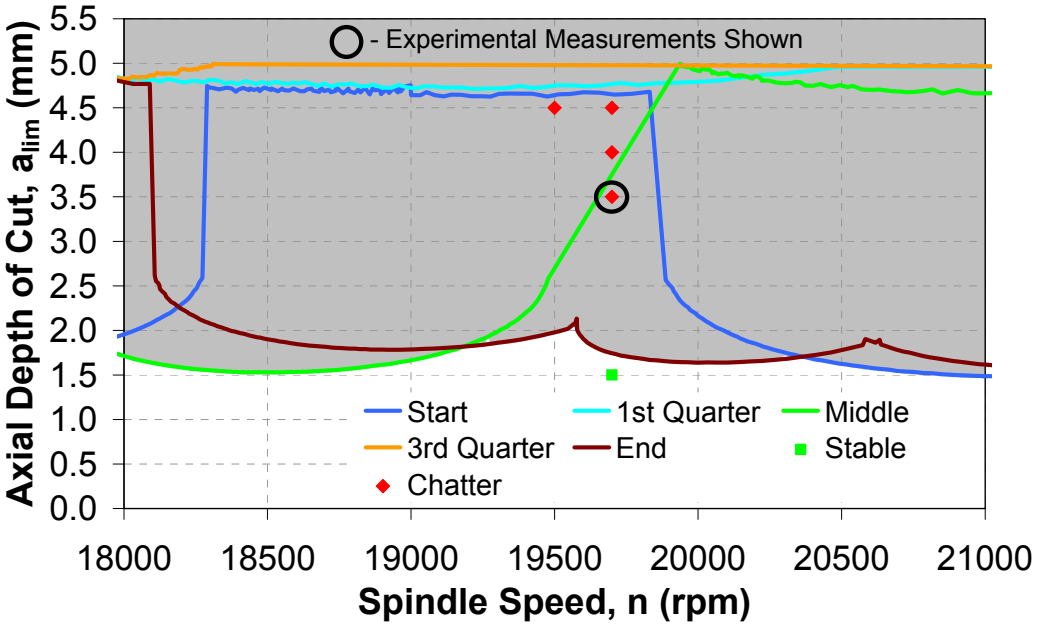

Figure 6.13. Stability lobes experimental validation for 18000rev/min – 21000rev/min.

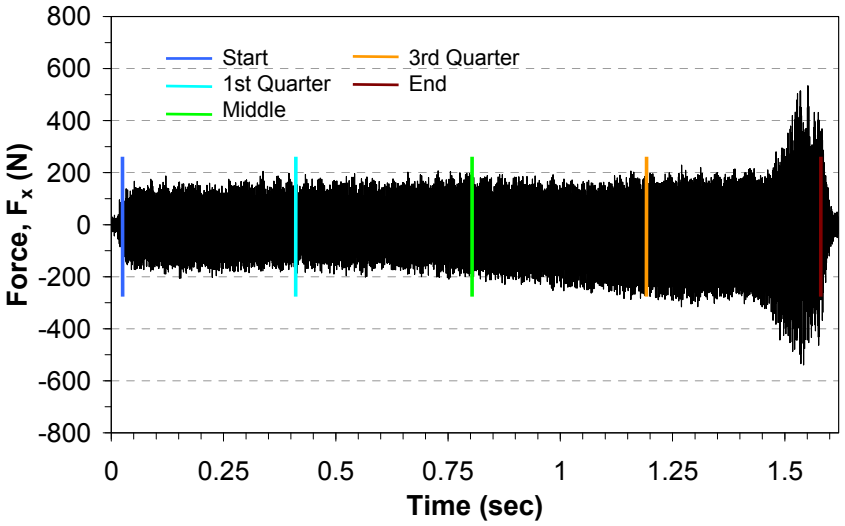

Figure 6.14. Measured cutting forces, Fx for 19700rev/min and 3.5mm axial depth of cut.

To further validate the predictions the surface finish is shown in Figure 6.15 where the slight chatter at the end of the cut can be seen. Contrary to the previous assumptions that the two ends of a thin wall behave similarly and if one end is stable then the other end should be stable and likewise when one end is unstable. It is seen in the surface finish and in the stability lobes that the start is stable and the end is unstable.

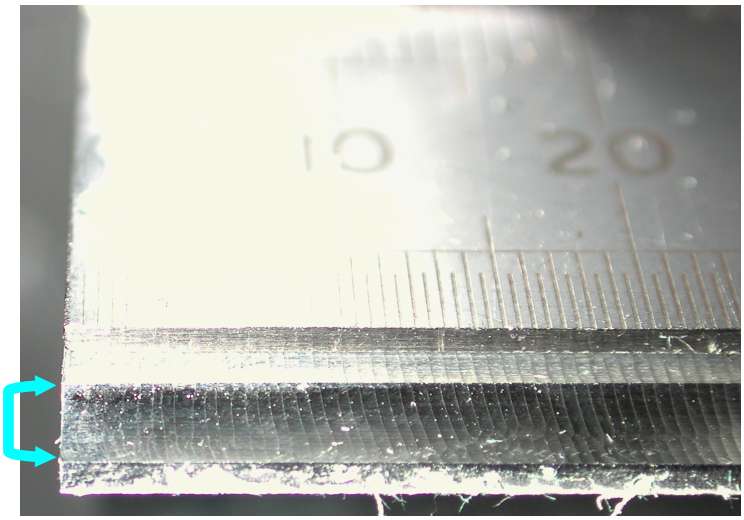

(a) Start location

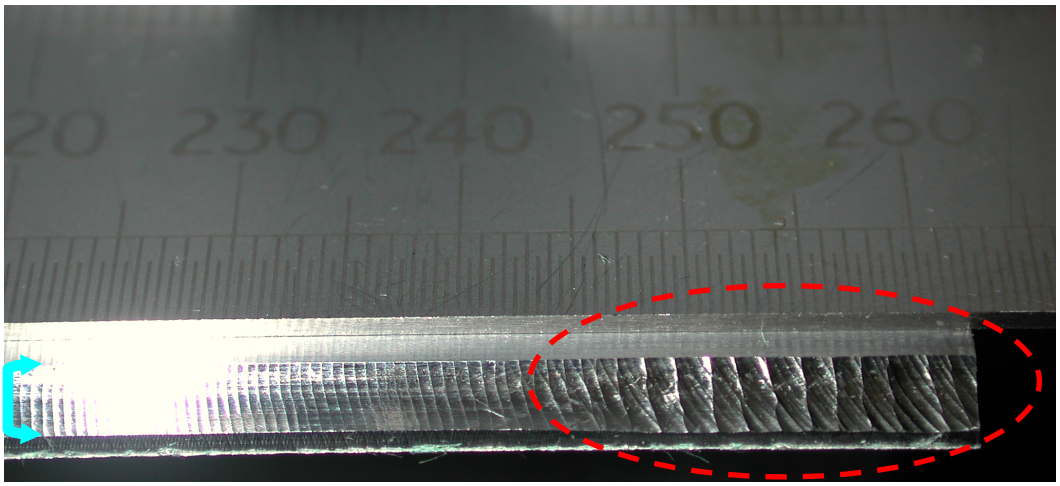

(b) Finish location

Figure 6.15. Surface finish for 19700rev/min spindle speed and 3.5mm axial depth of cut.

For cutting tests between 21500rev/min and 24500rev/min the stability lobes are shown in Figure 6.16. At 23000rev/min spindle speed and 2.5mm axial depth of cut, chatter was predicted at only the beginning of the cut. The surface finish depicts this as shown in Figure 6.17. This again shows that the initial assumption that both ends of a thin wall would behave the same way is wrong, as the surface finish shows contrary to the start region that the end region was stable.

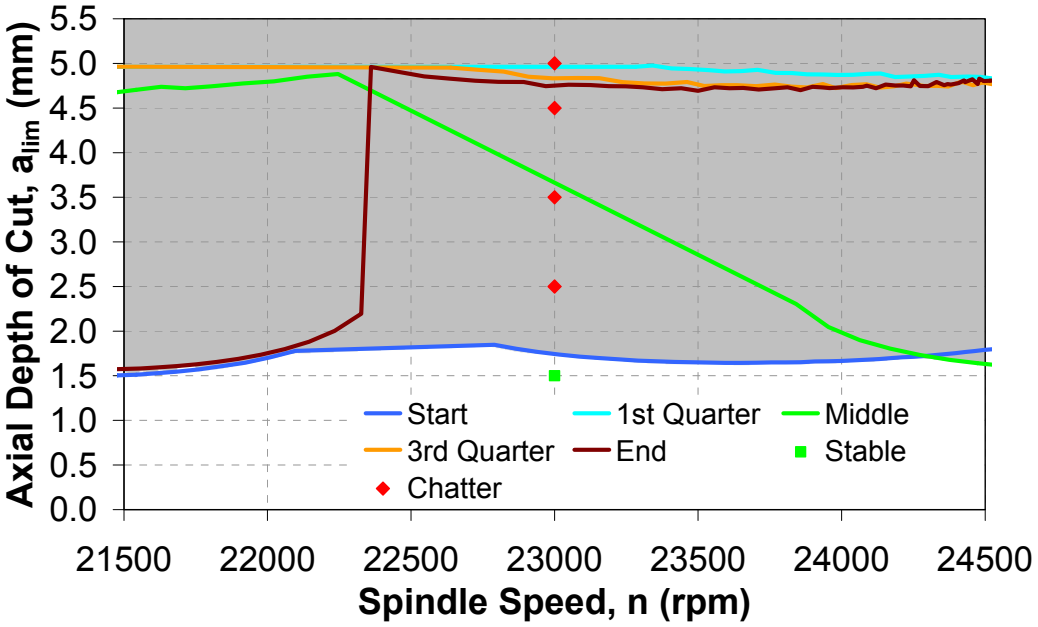

Figure 6.16. Stability lobes experimental validation for 21500rev/min – 24500rev/min.

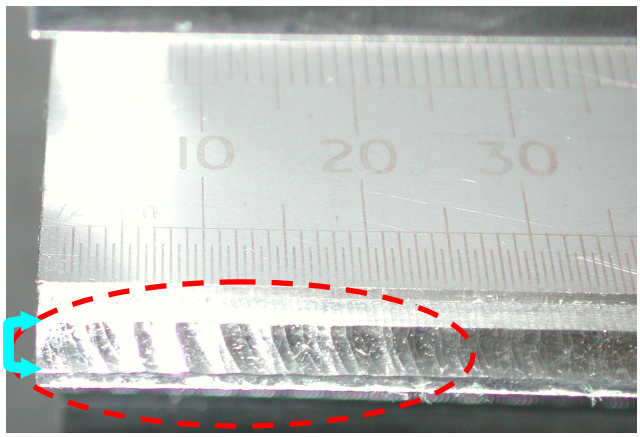

(a) Start Location

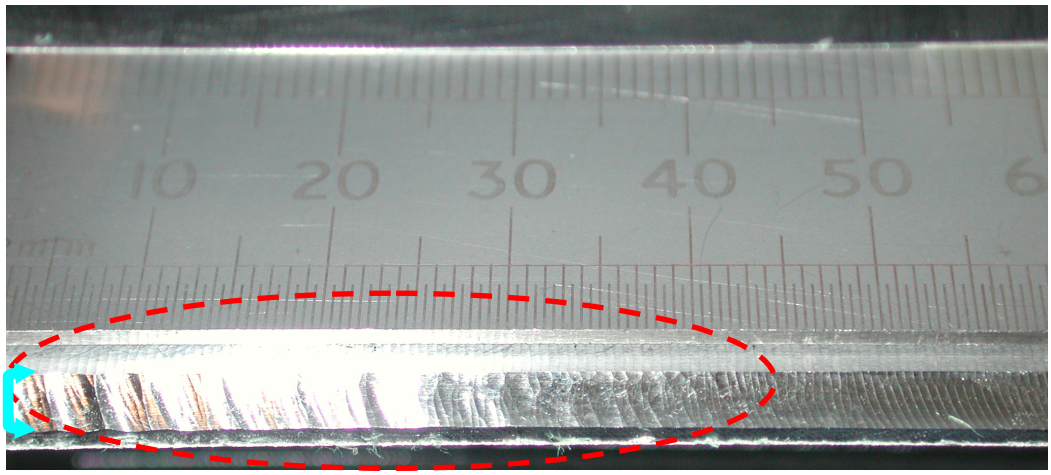

(b) Start Location Continued

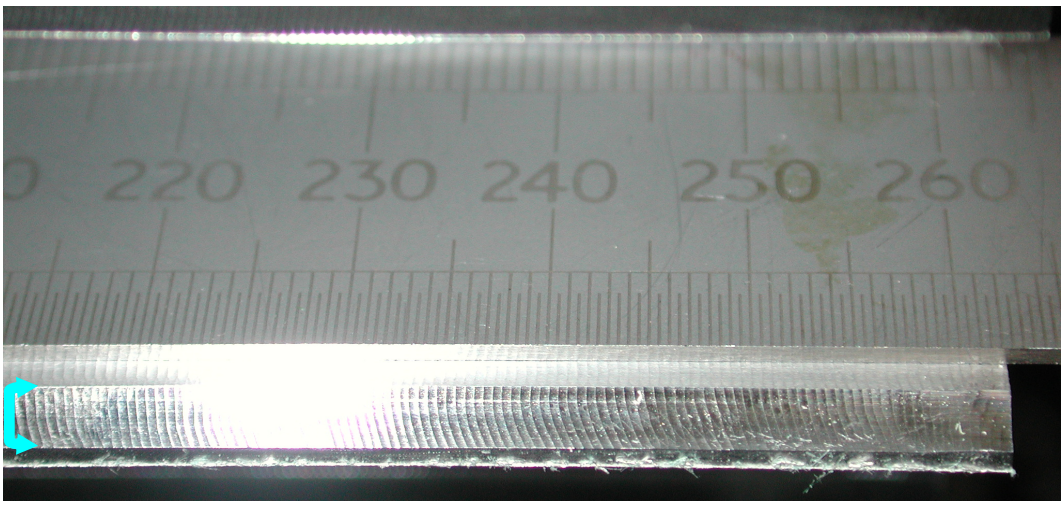

(c) End location

Figure 6.17. Surface finish for 23000rev/min spindle speed and 2.5mm axial depth of cut.

For high spindle speeds between 23500rev/min and 26500rev/min, the stability lobes are shown in Figure 6.18. At a spindle speed of 25000rev/min and an axial depth of cut of 2.00mm chatter was predicted only at the middle of the cut. The cutting forces in Figure 6.19 show that there was chatter towards the middle of the cut as the cutting forces starts off stable and increases quite drastically towards the middle then reduces back again towards the end of the cut.

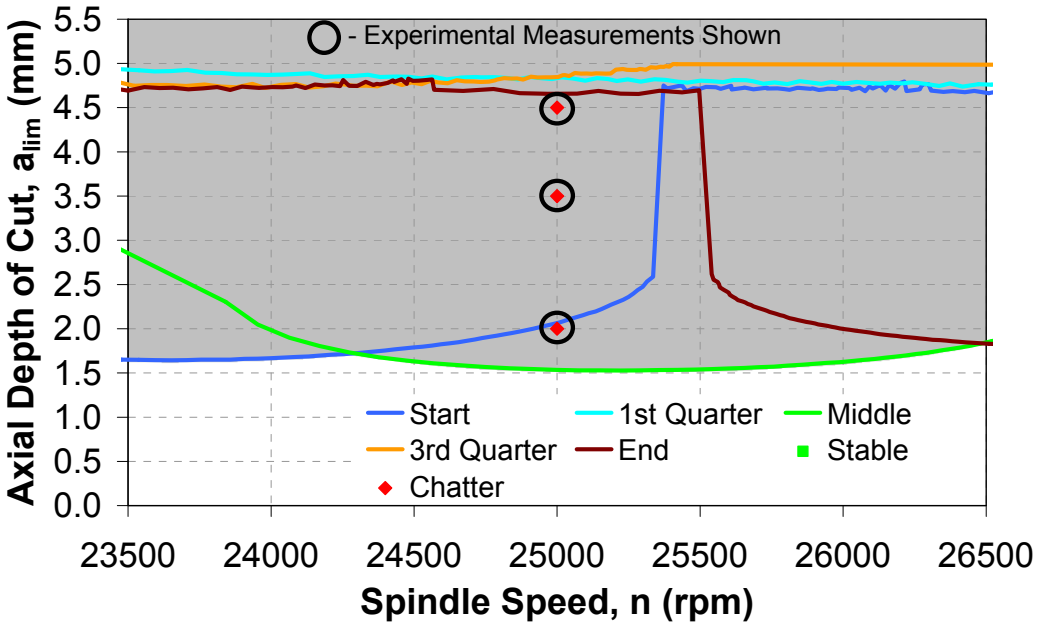

Figure 6.18. Stability lobes experimental validation for 23500rev/min – 26500rev/min.

There was another sharp increase in cutting forces just after the 3rd-quarter location and just before reaching the end. The transfer function would have to be identified at more points in order for this to be included in the stability lobes predictions.

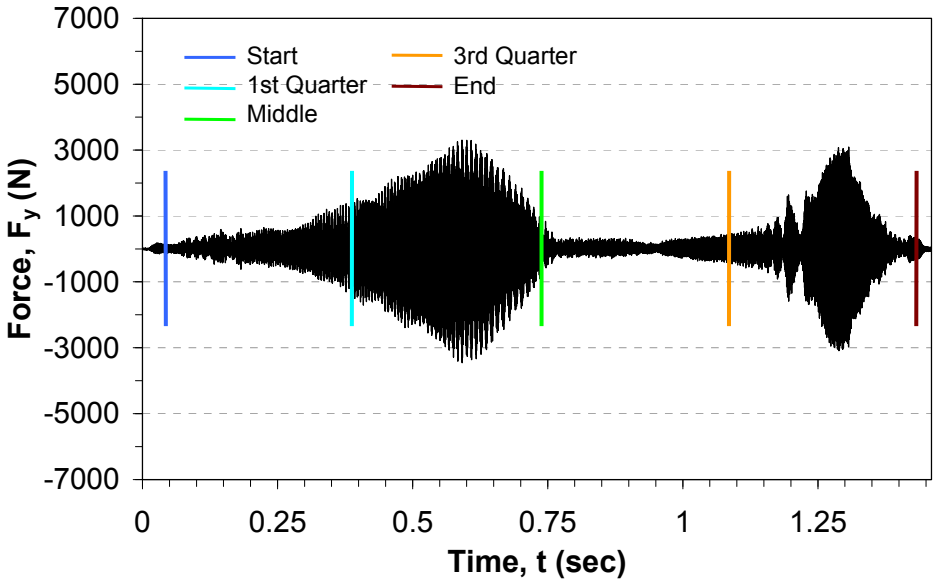

Figure 6.19. Measured cutting forces, Fx for 25000rev/min and 2.0mm axial depth of cut.

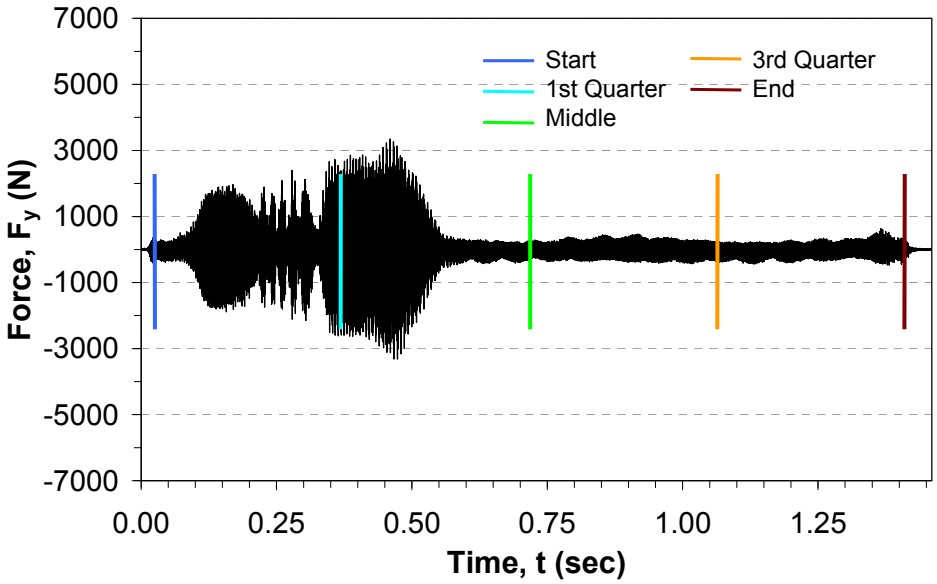

Figure 6.20. Measured cutting forces, Fx for 25000rev/min and 3.5mm axial depth of cut.

At a deeper cut 3.5mm, chatter was predicted at the start and the middle of the cut. The measured cutting forces in Figure 6.20 show that the chatter was located towards the beginning of the cut and the cut stabilized towards the end. Finally at an axial depth of cut of 4.5mm (Figure 6.21), chatter is present at most locations along the cut and this cutting condition is just below the margin in the stability lobes.

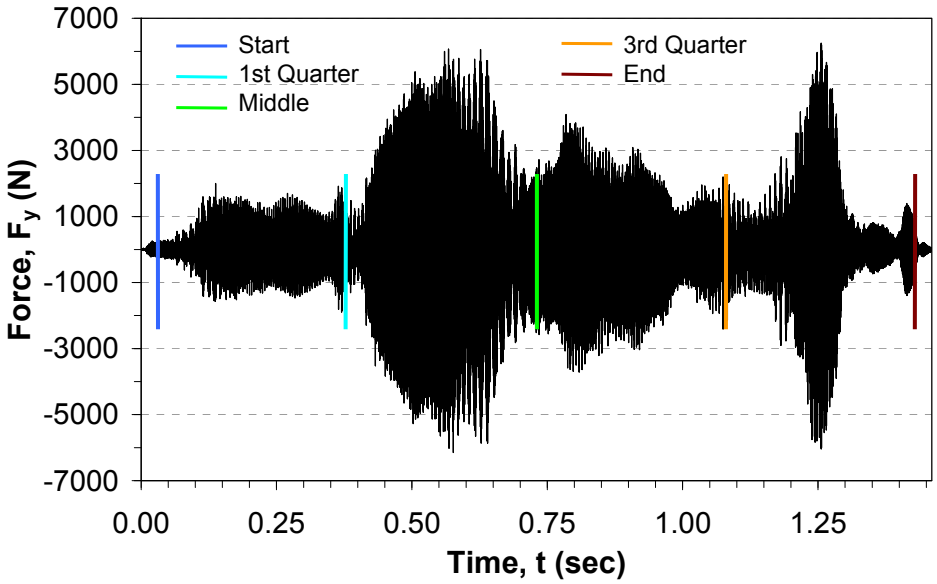

Figure 6.21. Measured cutting forces, Fx for 25000rev/min and 4.5mm axial depth of cut.

From the results obtained both experimentally and through the approach proposed in this chapter, the wall was found to be less prone to chatter at the first and third quadrant of the wall section. This can be seen in the frequency response function identified using the finite element approach (Figures 6.2 – 6.6). The 'FRF' for the weakest points are characterised by higher real and imaginary parts. The stability lobes predicted here are for Hopf bifurcations. In order to predict instabilities due to flip bifurcations, then the higher order approximation model developed in Chapter 5 can be used. This model however requires very high computational resources and even more with the approach proposed in this Chapter, as the stability lobes are predicted at various locations along the wall. From the superimposed stability lobes in Figure 6.7, it can be seen that even if any added lobe is found in any of the individual stability lobes, it would most likely fall in the unstable region of the predictions for another location.

6.3. Summary

In this chapter, a novel approach to predict the stable margin for a thin wall structure, whilst respecting the nonlinearity of the structures dynamics along the tool path was presented. This approach used the FEM approach in Chapter 4 to extract the transfer function and the improvements to the stability lobe model in Chapter 5 were used in all the extracted stable margins. The results are experimentally validated.

Chapter 7

Conclusion

7.1. Concluding Remarks

This thesis has focused mainly on different aspects in the machining of thin wall sections, with various modelling approaches proposed. The well developed mechanistic linear edge force model has been discussed and the mechanistic cutting force coefficients were calibrated for a range of axial depths of cut. They were validated by comparing the predicted cutting forces for varied cutting conditions with experimental results. Improvements to the model were proposed. These improvements consider the nonlinear relationship between the cutting force and the uncut chip thickness. This nonlinearity is caused by the size effect, experienced when using a tool with a blunt cutting edge.

A new and efficient FEM approach to predicting the cutting force coefficients was presented. The approach uses an Arbitrary Lagrangian Eulerian (ALE) mesh formulation. It was shown that the domain can be simplified to a 2-dimensional domain when simulating a non-helical flat end milling tool. However, the proposed approach can still be used to simulate machining with the use of general tools including tools with a corner radius. The results obtained from FEM simulations of the end milling process were used to evaluate the force coefficients. On the one hand, this approach eliminates the need to carry out

cumbersome experiments, otherwise used to calibrate the cutting force coefficients. On the other hand, it perfectly satisfies the assumption that there are no chatter effects in the cutting force data. The coefficients obtained were validated by comparing predicted cutting forces with experimental results reported by Ko et al. (2002). Several comparisons were made with good agreements, using a wide range of cutting conditions. It was also found that an accurate measurement of the edge radius is very crucial when carrying out FEA modelling of end milling processes.

An in-depth study of the cutter and workpiece dynamics was presented and a new trend or relationship between the damping parameters and the structure's geometry was discovered. An approach that makes use of this discovered trend to predict the damping parameters for a different wall thickness from a known wall was proposed. A series expansion was proposed to help model the predicted damping parameters in frequency domain. The accuracy of the discovered trend and the proposed series expansion is seen to match experimental results. A Finite Element (FE) modal analysis approach to predicting the dynamic response of a structure to dynamic excitation was also presented. The accuracy of the discovered relationship is further explored by using the predicted damping ratios in FE time domain vibration simulations. Comparisons were made between the predicted acceleration and the experimentally measured acceleration; showing a satisfactory match. Although the proposed approach to predicting the damping parameters is at its early stages, its application in the machining of thin wall structures was presented. This approach fits naturally with machining of thin walls as the thickness of the wall changes as material is removed. The structure's transfer function was extracted using a proposed FE and Fourier approach.

In the aspect of the prediction of stable margin, the very common three-dimensional stability model of self excited chatter vibrations in milling was improved to fully accommodate the nonlinear cutting force coefficients and the nonlinear axial immersion angle for the first time. In a newly developed model, the effects of higher harmonics on the predicted stability margin were considered. This model still respects the nonlinearities of both the cutting force coefficients and the axial immersion angle. A numerical approach to obtaining a converged solution with very good accuracy was proposed. This improved model was then

adapted to the FE and Fourier approach in an approach to predict the stable margin for a thin wall section, whilst fully considering the nonlinear dynamics, the nonlinear cutting force coefficients and the nonlinear axial immersion angle. The accuracies are seen in the comparisons made between the predicted and experimental results.

The contributions to the knowledge and original thoughts that resulted from this research can be summarized as follows:

- A nonlinear edge force model was developed for the first time. The advantages this model possesses over the linear edge force model would become much more apparent, as more studies on micromilling are performed.
- A finite element approach to extracting the cutting force coefficient was proposed. This makes the whole calibration process more efficient and much easier. There is very little previous work on applying FE methods to the milling process. Therefore this approach also shows the practical application of FE analysis and ALE mesh formulation.
- A previously unknown relationship between damping parameters was presented in this thesis. This relationship was used to predict the structural damping terms, which was previously considered an empirical parameter. This relationship is a fundamental knowledge that when further investigated, could lead to a full understanding of the damping forces, the influence the structure's geometry has on it. Unlike the stiffness and mass parameters, the damping parameters are still not fully understood. This is the reason for the use of experimentally identified damping parameters. A proposed series expansion was used to model the predicted damping terms.
- A new FE and state space approach to extracting the system's Frequency Response Function (FRF) was presented.
- With the damping prediction model and the FE approach the stable margin was fully predicted for the first time without experimental results with satisfactory accuracy. The advantages of this approach extend into both the design and manufacturing stages.
- The widely used stability approach was modified to include the nonlinear characteristics of the cutting force coefficients and the axial immersion

angle. In all previous work using the stability model, the cutting force coefficients and the axial immersion angle have been assumed to be constant. Due to the complex nature of the system's transfer function, attempts to obtain an analytical solution proved very complicated; hence a numerical algorithm was developed to obtain a converged solution.

- For the first time a three dimensional higher-order stability model that considers the effects of higher harmonics from highly intermittent milling process was developed and its formulations systematically presented.
- The FE and Fourier approach was adapted with the improved zeroth-order stability model in a proposed method that predicts the stable margin for a thin wall, taking in account the nonlinear dynamics along the thin wall. Unlike the previous work that made efforts to model varying dynamics, the FE and Fourier approach predicts the structure's FRF with good accuracy. This coupled with the improved stability model helps to predict accurate results. The accuracy is demonstrated in the predicted location of chatter matching precisely with chatter marks in experimental surface finish and also in measured cutting forces. Stability margin predictions that consider the nonlinear dynamics of the workpiece have not been reported before in the literature with this level of accuracy.

7.2. Future Work

One of the main aspects additional studies should focus on is the damping parameters. The ultimate aim is to understand the relationship between the damping parameters and the structural geometry; perhaps first with constant boundary conditions and then taking into account the overall effects of the boundary conditions. With the damping parameters developed, advancements in structural analysis would certainly be accelerated. It will aid in the analysis of dynamic analysis.

The modelling of the system's transfer function using the state space approach should be investigated, as this can be easily used to extract the transfer function at any required point. The advantage of this is being able to obtain the

transfer function for any location (degree of freedom) without having to run the simulation in time domain, before converting into frequency domain.

The approach to predicting the stable margin whilst taking into account nonlinear dynamics should also be further investigated, as this can allow for the adaptive modification of the structures dynamics at locations at which chatter is predicted to occur.

The research algorithms developed in this thesis could also be interfaced with a CAD/CAM system for use in the design and production planning of a variety of components in the aerospace industry.

List of Publications

Adetoro, O. B., Vepa, R., Sim, W. M. and Wen, P. H., 2009(h), **''On the Numerical Prediction of Stability in Thin wall Machining''**, Electronic Engineering and Computing Technology (Book Chapter, citation details to be confirmed)

Abstract: ''In this chapter, the numerical prediction of stability margin in thin wall machining is introduced. The Nyquist criterion is applied to the stability model presented by Adetoro (2009d), while a newly discovered damping prediction approach is presented, which when applied to the FEM and Fourier approach presented by Adetoro (2009d), would allow the prediction of stability margins without the need for experimentally extracted damping parameters.''

Adetoro, O. B., Wen, P. H., Sim, W. M. and Vepa, R., 2009(g), **''Numerical and Experimental Investigation for Stability Lobes Prediction in Thin Wall Machining''**, *Engineering Letters*, Vol. 17(4), pp. 257 – 265 (available at: http://www.engineeringletters.com/issues_v17/issue_4/EL_17_4_07.pdf)

Abstract: ''A Finite Element Analysis (FEA) and Fourier transform approach to obtain frequency response function (FRF) is presented in this paper. The aim in this paper is to eliminate the need for the classical impact experimental approach used in extracting structure's FRF. The numerical and experimental FRFs have been used to obtain stable regions in machining of thin walled structures, which gives a good comparison. Examples are presented and compared with experimental results with a satisfactory agreement.''

Adetoro, O. B., Sim, W. M and Wen, P. H., 2009(f) **‘‘An Improved Prediction of Stability Lobes using Nonlinear Thin Wall Dynamics’’**, *Journal of Materials Processing Technology*, 2010, doi:10.1016/j.jmatprotec (accepted for publication; In Press; dx.doi.org/10.1016/j.jmatprotec.2010.02.009)

Abstract: ‘‘With manufactured sections getting much thinner due to weight requirements, there is the vital need for more accurate prediction of stable cutting conditions in machining. The tools used in machining vary in shapes and design hence a more robust model is required to include these varieties. This paper first presents improvements to the well known stability model, by considering the nonlinearity of the cutting force coefficients, and axial immersion angle and their dependency on the axial depth of cut. Secondly, a Finite Element (FE) and Fourier transform approach to including the nonlinearity of the workpiece dynamics in thin wall machining when predicting stable region is presented. The model and approach are validated extensively using experimental results and a very good agreement has been achieved.’’

Adetoro, O. B., Sim, W. M. and Wen, P. H., 2009(e), **‘‘Stability Lobes Prediction for Corner Radius End Mill using Nonlinear Cutting Force Coefficients’’**, *Machining Science and Technology* (submitted for publication)

Abstract: ‘‘There are a vast number of different types of end mill tools used in the manufacturing industry, each type with a unique and different shape. These tool shapes have a direct influence on the cutting force it generates during machining. This paper presents a more accurate approach to predicting the stability margin in machining by considering the cutting force coefficients and axial immersion angle as a variable along the axial depth of cut. A numerical approach to obtaining a converged solution to the stability model is presented. The results obtained are validated extensively using experimental results and a very good agreement is seen.’’

Adetoro, O. B., Sim, W. M., Vepa, R. and Wen, P. H., 2009(d), **''A New Damping Modelling Approach and its Application in Thin Wall Machining''**, *The International Journal of Advanced Manufacturing Technology* (submitted for publication)

Abstract: ''In this paper, a new approach to modelling the damping parameters and its application in thin wall machining is presented. The approach to predicting the damping parameters proposed in this paper eliminates the need for experiments otherwise used to acquire these parameters. The damping model proposed was compared with available damping models and experimental results. A Finite Element Analysis (FEA) and Fourier transform approach has been used to obtain frequency response function (FRF) needed for stability lobes prediction. Several predicted stable regions using both experimental and numerical FRF's for various examples gave a good comparison.''

Adetoro, O. B., Sim, W. M., Vepa, R. and Wen, P. H., 2009(c), **''Numerical and Experimental Investigation of Damping Parameters for Thin Wall Structures''**, *Journal of Advanced Manufacturing Systems* (submitted for publication)

Abstract: ''In this paper, a novel modelling numerical and experimental investigation has been carried out for thin wall structures in aerospace manufacturing. The aim of this paper is to predict the damping parameters for any given geometry based on identified damping parameters for a known geometry. The damping ratio curve fittings using both Rayleigh and Caughey's series have been studied. The comparison between the proposed damping prediction approach, Caughey's series curve fitting and experimental data is satisfactory. Examples are provided to illustrate the accuracy of proposed method and predicted results are compared with experimental results.''

Adetoro, O. B., Wen, P. H., Sim, W. M. and Vepa, R., 2009(b), **''Stability Lobes Prediction in Thin Wall Machining''**, *Proceedings of the International*

Multi-Conference of Engineers and Computer Scientist, Vol. 1, pp. 520 – 525 (available at: www.iaeng.org/publication/WCE2009_pp20-525.pdf)

Abstract: ‘‘A Finite Element Analysis (FEA) and Fourier transform approach to obtain frequency response function (FRF) is presented in this paper. The aim in this paper is to eliminate the need for the classical impact experimental approach used in extracting structure’s FRF. The numerical and experimental FRFs have been used to obtain stable regions in machining of thin walled structures, which gives a good comparison. Examples are presented and compared with experimental results with a satisfactory agreement.’’

This work was presented in July 2009 at the International Conference of Manufacturing Engineering and Engineering Management (WCE) (London, UK) and was award the best student paper award.

Adetoro, O. B. and Wen, P. H., 2009(a), **‘‘Prediction of mechanistic cutting force coefficients using ALE formulation’’**, *The International Journal of Advanced Manufacturing Technology*, Vol. 46(1-4), pp. 79 – 90 (available at: www.springerlink.com/content/w24636hm42018213)

Abstract: ‘‘This paper demonstrated the use of an efficient and accurate numerical tool (i.e., FEA) in simulating the cutting process and determining both the average and instantaneous cutting force coefficients. The main advantage of this approach compared to other available methods is that it eliminates the need for experimental calibrations. In this approach, an Arbitrary Lagrangian Formulation was employed in the finite element method simulations. This formulation has been gaining more recognition in structural analysis for its combined advantages of both Lagrangian and Eulerian formulations in a single model. Based on the work of Kline et al. (1982), the tool is discretised along the axis into segments and the cutting forces acting on the cutting edge segment are presented in terms of cutting force coefficients. Cutting force coefficients are obtained using the least squares method and cutting force predictions using evaluated coefficients are shown to match experimental results with satisfactory accuracy.

Adetoro, M. B. and Wen, P. H., 2008, **''FEM Evaluation of Mechanistic Cutting Force Coefficients Using ALE Formulation''**, *Proceedings of the 3rd International Conference on High Performance Cutting*, Dublin, Ireland, (HPC-P-023), Vol. 2, pp. 659 – 680

Abstract: ''The investigation to obtain the cutting force coefficients has been carried out over the past two decades by many researchers. However, the outstanding disadvantages of voluminous experimental data acquisition and its analyses still exist. This paper demonstrated the use of an efficient and accurate numerical tool (i.e. FEA), in simulating the cutting process and determining the cutting force coefficients. In this approach, an Arbitrary Lagrangian Formulation (ALE) was employed in the FEM simulations. This formulation has been gaining more recognition in structural analysis for its combined advantages of both Lagrangian and Eulerian formulations in a single model. Cutting force predictions using evaluated coefficients are shown to agree well with experimental results.''

This work was presented in June 2008 at the 3rd CIRP International Conference on High Performance Cutting (Dublin, Ireland).

Wen, P. H., Adetoro, M. and Xu, Y., 2008, **''The fundamental solution of Mindlin plates with damping in the Laplace domain and its applications''**, Engineering Analysis with Boundary Elements Vol. 32(10), pp. 870 – 882

Abstract: ''In this paper, a fundamental solution for the Mindlin plate theory with damping is derived in the Laplace transform domain first time. The applications of this fundamental solution are demonstrated by the method of fundamental solution (MFS). All variables in the time domain can be obtained by the Durbin's Laplace transform inversion method. Numerical examples demonstrate the accuracy of the MFS and comparisons have been made with analytical solutions. To model the cutting machining process, a moving concentrated force on the plate has been investigated. The proposed MFS is shown to be simple to implement and gives satisfactory results for the shear deformable plate under dynamic loads with damping.''

Bibliography

Adetoro, M. B. and Wen, P. H., 2008, ‘‘FEM Evaluation of Mechanistic Cutting Force Coefficients Using ALE Formulation’’, *Proceedings of the 3rd International Conference on High Performance Cutting*, Dublin, Ireland, (HPC–P–023), Vol. 2, pp. 659 – 680

Adetoro, O. B. and Wen, P. H., 2009(a), ‘‘Prediction of Mechanistic Cutting Force Coefficients Using ALE Formulation’’, *The International Journal of Advanced Manufacturing Technology*, Vol. 46(1 – 4), pp. 79 – 90 (available at: www.springerlink.com/content/w24636hm42018213)

Adetoro, O. B., Wen, P. H., Sim, W. M. and Vepa, R., 2009(b), ‘‘Stability Lobes Prediction in Thin Wall Machining’’, *Proceedings of the International Multi–Conference of Engineers and Computer Scientist*, Vol. 1, pp. 520 – 525 (available at www.iaeng.org/publication/WCE2009_pp20-525.pdf)

Adetoro, O. B., Sim, W. M., Vepa, R. and Wen, P. H., 2009(c), ‘‘Numerical and Experimental Investigation of Damping Parameters for Thin Wall Structures’’ *Journal of Advanced Manufacturing Systems* (submitted for publication)

Adetoro, O. B., Sim, W. M., Vepa, R. and Wen, P. H., 2009(d), ‘‘A New Damping Modelling Approach and its Application in Thin Wall Machining’’, *The International Journal of Advanced Manufacturing Technology* (submitted for publication)

Adetoro, O. B., Sim, W. M. and Wen, P. H., 2009(e), ‘‘Stability Lobes Prediction for Corner Radius End Mill Using Nonlinear Cutting Force Coefficients’’, *Machining Science and Technology* (submitted for publication)

Adetoro, O. B., Sim, W. M and Wen, P. H., 2009(f) ‘‘Accurate Prediction of Stability Lobes Using Nonlinear Thin Wall Dynamics’’, *Journal of Material Processing Technology* (submitted for publication)

Adetoro, O. B., Wen, P. H., Sim, W. M. and Vepa, R., 2009(g), ‘‘Numerical and Experimental Investigation for Stability Lobes Prediction in Thin Wall Machining’’, *Engineering Letters*, Vol. 17(4), pp. 257 – 265 (available at: http://www.engineeringletters.com/issues_v17/issue_4/EL_17_4_07.pdf)

Adetoro, O. B., Vepa, R., Sim, W. M. and Wen, P. H., 2009(h), ‘‘On the Numerical Prediction of Stability in Thin wall Machining’’, Electronic Engineering and Computing Technology (Book Chapter, citation details to be confirmed)

Adhikari, S., 2000, *Damping Models for Structural Vibrations*, Ph.D Thesis, Cambridge University, Engineering Department Cambridge, UK

Airey, J. and Oxford, C. J., 1921, ‘‘On the Art of Milling’’, *Transactions of the ASME*, Vol. 43, pp. 549 – 615

Albrecht, P., 1962, ‘‘Self–Induced Vibrations in Metal Cutting’’, *Transactions of the ASME – Journal of Engineering for Industry*, Vol. 84, pp. 405 – 417

Allemang, R. J. and Brown, D. L., 1986, ‘‘Multiple Input Experimental Modal Analysis – A Survey’’, *International Journal of Analytical and Experimental Modal Analysis*, Vol. 1(1), pp. 37 – 44

Altintas, Y. and Spence, A., 1991, ‘‘End Milling Force Algorithms for CAD Systems’’, *CIRP Annals*, Vol. 40(1), pp. 31 – 34

Altintas, Y. and Budak, E., 1995, ‘‘Analytical Prediction of Stability Lobes in Milling’’, *CIRP Annals – Manufacturing Technology*, Vol. 44(1), pp. 357 – 362

Altintas, Y. and Lee, P., 1996, ‘‘General Mechanics and Dynamics Model for Helical End Mills’’, *CIRP Annals – Manufacturing Technology*, Vol. 45(1), pp. 59 – 64

Altintas, Y., Shamoto, E., Lee, P. and Budak, E., 1999, ‘‘Analytical Prediction of Stability Lobes in Ball–End Milling’’, *Transactions of the ASME – Journal of Manufacturing Science and Engineering*, Vol. 121(4), pp. 586 – 592

Altintas, Y., 2000, ‘‘Modeling Approaches and Software for Predicting the Performance of Milling Operations at MAL–UBC’’, *Machining Science and Technology*, Vol. 4(3), pp. 445 – 478

Altintas, Y., 2000, *Manufacturing Automation – Metal Cutting Mechanics, Machine Tool Vibrations, and CNC Design*, Cambridge University Press, 40 West 20th Street, New York, NY, 10011 – 4211, USA

Altintas, Y., 2001, ‘‘Analytical Prediction of Three Dimensional Chatter Stability in Milling’’, *JSME International Journal, Series C: Mechanical Systems, Machine Elements and Manufacturing*, Vol. 44(3), pp. 717 – 723

Altintas, Y. and Engin, S., 2001, ‘‘Generalized Modeling of Mechanics and Dynamics of Milling Cutters’’, *CIRP Annals – Manufacturing Technology*, Vol. 50(1), pp. 25 – 30

Archer, J. S., 1963, ‘‘Consistent Mass Matrix for Distributed Systems’’, *Proceedings of American Society of Civil Engineers, Journal of the Structural Division*, Vol. 89(ST4), pp.161 – 178

Archer, J. S., 1965, ‘‘Consistent Mass Matrix formulations for Structural Analysis Using Finite Element Techniques’’, *Journal of American Institute of Aeronautics and Astronautics*, Vol. 3(10), pp. 1910 – 1918

Armarego, E. J. A. and Whitfield, R. C., 1985, ‘‘Computer Based Modelling of Popular Machining Operations for Force and Power Predictions’’, *CIRP Annals*, Vol. 34, pp. 65 – 69

Armarego, E. J. A. and Deshpande, N. P., 1989, ‘‘Computerized Predictive Cutting Models for Forces in End–Milling Including Eccentricity Effects’’, *CIRP Annals*, Vol. 38(1), pp. 45 – 49

Armarego E. J. A. and Deshpande, N. P., 1991, ‘‘Computerized End–Milling Force Predictions with Cutting Models Allowing Eccentricity and Cutter Deflections’’, *CIRP Annals*, Vol. 40(1), pp. 25 – 29

Arnold, R. N., 1946, ‘‘The Mechanism of Tool Vibration in the Cutting of Steel’’, *Proceedings of the Institution of Mechanical Engineers*, Vol. 154, pp. 261 – 276

Athavale S. M. and Strenkowski, J. S., 1997, ‘‘Material Damage–Based Model for Predicting Chip–Breakability’’, *Journal of Manufacturing Science and Engineering*, Vol. 119 (11), pp. 675 – 680

Baker, M., Rosler, J. and Siemers, C., 2002, ‘‘A Finite Element Model of High Speed Metal Cutting with Adiabatic Shearing’’, *Computers and Structures*, Vol. 80(5 – 6), pp. 495 – 513

Bil, H., Kilic, S. E. and Tekkaya, A. E., 2004, ‘‘A Comparison of Orthogonal Cutting Data from Experiments with Three Different Finite Element Models’’, *International Journal of Machine Tools and Manufacture*, Vol. 44(9), pp. 933 – 944

Boothroyd, G. and Knight, W. A., 1975, *Fundamentals of Machining and Machine Tools*, McGraw–Hill, New York

Bravo, U., Altuzarra, O., Lopez de Lacalle, L. N., et al., 2005, ‘‘Stability Limits of Milling Considering the Flexibility of The Workpiece and The Machine’’, *International Journal of Machine Tools and Manufacture*, Vol. 45(15), pp. 1669 – 1680

Brown, D. L., 1982, ‘‘Modal Analysis – Past, Present and Future’’, *Proceedings of the International Modal Analysis Conference and Exhibit*

Brown, R. H. and Armarego, E. J. A., 1964, ‘‘Oblique Machining with a Single Cutting Edge’’, *International Journal of Machine Tool Design and Research*, Vol. 4, pp. 9 – 25

Budak, E., 1994, *Mechanics and Dynamics of Milling Thin Walled Structures*, Ph.D. Thesis, The University of British Columbia, Vancouver, B.C., Canada

Budak, E. and Altintas, Y., 1995, ‘‘Analytical Prediction of Chatter Stability in Milling Part I: General Formulation’’, *Proceeding of ASME 1995 International Mechanical Engineering Conference and Exposition*, San Francisco, USA

Budak, E., Altintas, Y. and Armarego, E. J. A., 1996, ‘‘Prediction of Milling Force Coefficients From Orthogonal Cutting Data’’, *Transactions of the ASME – Journal of Manufacturing Science and Engineering*, Vol. 118(2), pp. 216 – 224

Budak, E. and Altintas, Y., 1998, ‘‘Analytical Prediction of Chatter Stability in Milling – Part I: General Formulation’’, *Transactions of the ASME – Journal of Dynamic Systems Measurement and Control*, Vol. 120, pp. 22 – 30

Budak, E. and Altintas, Y., 1998, ‘‘Analytical Prediction of Chatter Stability in Milling – Part II: Application of the General Formulation to Common Milling Systems’’, *Transactions of the ASME – Journal of Dynamic Systems Measurement and Control*, Vol. 120, pp. 31 – 36

Budak, E., 2006, ‘‘Analytical Models for High Performance Milling. Part II: Process Dynamics and Stability’’, *International Journal of Machine Tools and Manufacture*, Vol. 46, pp. 1489 – 1499

Cakar, O. and Sanliturk, K. Y., 2005, ‘‘Elimination of Transducer Mass Loading Effects from Frequency Response Functions’’, *Mechanical Systems and Signal Processing*, Vol. 19(1), pp. 87 – 104

Campa, F. J., Lopez de Lacalle, L. N., Lamikiz and A. Sanchez, J. A., 2007, ‘‘Selection of Cutting Conditions For a Stable Milling of Flexible Parts with Bull–Nose End Mills’’, *Journal of Materials Processing Technology*, Vol. 191(1 – 3), pp. 279 – 282

Carrino, L., Giuliano, G. and Napolitano, G., 2003, ‘‘Finite Element Simulation of Orthogonal Metal Cutting’’, *Computational Methods in Contact Mechanics VI*, Vol. 8, pp. 105 – 114

Caughey, T. K. and O’Kelly, M. E. J., 1960, ‘‘Classical Normal Modes in Damped Linear Systems’’, *Transactions of the ASME – Journal of Applied Mechanics*, Vol. 27, pp. 269 – 271

Caughey, T. K. and O’Kelly, M. E. J., 1965, ‘‘Classical Normal Modes in Damped Linear Dynamic Systems’’, *Transactions of the ASME – Journal of Applied Mechanics,* Vol. 32, pp. 583 – 588

Ceretti, E., Fallbohmer, P., Wu, W. T. and Altan, T., 1996, ‘‘Application of 2D FEM to Chip Formation in Orthogonal Cutting’’, *Journal of Materials Processing Technology*, Vol. 59(1 – 2), pp. 169 – 180,

Cooley, J. W. and Tukey, J. W., 1965, ‘‘An Algorithm For The Machine Calculation of Complex Fourier Series’’, *Mathematics of Computations*, Vol. 19(90), pp. 297 – 301

Das, M. K. and Tobias, S. A., 1967, ‘‘The Relation Between Static and Dynamic Cutting of Metals’’, *International Journal of Machine Tool Design and Research*, Vol. 7, pp. 63 – 89

Davies, M. A. and Balachandran, B., 1996, ‘‘Impact Dynamics in The Milling of Thin–Walled Structures’’, *American Society of Mechanical Engineers, Design Engineering Division (Publication) DE*, Vol. 91, pp. 67 – 72

Davies, M. A., Pratt, J. R. and Dutterer, B., 2000, ‘‘Stability of Low Radial Immersion Milling’’, *CIRP Annals – Manufacturing Technology*, Vol. 49(1), pp. 37 – 40

Davies, M. A., Pratt, J. R. and Dutterer, B., 2002, ‘‘Stability Prediction For Low Radial Immersion Milling’’, *Journal of Manufacturing Science and Engineering, Transactions of the American Society of Mechanical Engineers*, Vol. 124(2), pp. 217 – 225

Devor, R. E., Kline, W. A., et al., 1980, ‘‘Mechanistic Model For The Force System in End Milling with Application to Machining Airframe Structures’’, *Manufacturing engineering transactions*, pp. 297 – 304,

Donea J., Fasoli–Stella, D. P. and Giuliani, S., 1977, ‘‘Lagrangian and Eulerian Finite Element Techniques for Transient Fluid Structure Interaction Problems’’, *Transactions of the Fourth SMiRT Conference,* San Francisco (paper B1/2), pp. 15 – 19

Corpus, W. T. and Endres, W. J., 2000, ‘‘A High–Order Solution for the Added Stability Lobes in Intermittent Machining,’’ *American Society of Mechanical Engineers, Manufacturing Engineering Division, MED*, Vol. 11, pp. 871–878

Engin, S. and Altintas, Y., 1999(a), ‘‘Generalized Modeling of Milling Mechanics and Dynamics: Part I – Helical End Mills’’, *American Society of Mechanical Engineers, Manufacturing Engineering Division*, MED, Vol. 10, pp. 345 – 352

Engin, S. and Altintas, Y., 1999(b), ‘‘Generalized Modeling of Milling Mechanics and Dynamics: Part II – Inserted Cutters’’, *American Society of Mechanical Engineers, Manufacturing Engineering Division*, MED, Vol. 10, pp. 353 – 360

Engin, S. and Altintas, Y., 2001(a), ‘‘Mechanics and Dynamics of General Milling Cutters. Part I: Helical End Mills’’ *International Journal of Machine Tools and Manufacture*, Vol. 41, pp. 2195 – 2212

Engin S. and Altintas, Y., 2001(b), ‘‘Mechanics and Dynamics of General Milling Cutters. Part II: Inserted Cutters’’, *International Journal of Machine Tools and Manufacture*, Vol. 41(15), pp. 2213 – 2231

Ewins, D. J., 1984, *Modal Testing: Theory and Practice*, Research Studies Press, Letchworth Hertfordshire, England

Feng, H. Y., and Menq, C. H., 1994, ‘‘The Prediction of Cutting Forces in the Ball–End Milling Process II, Cut Geometry Analysis and Model Verification’’, *International Journal of Machine Tools and Manufacture*, Vol. 34(5), pp. 711 – 719

Fenton, R. G. and Oxley, P. L. B., 1969, ‘‘Mechanics of Orthogonal Machining: Predicting Chip Geometry and Cutting Forces from Work–Material Properties and Cutting Conditions’’, *Proceedings of the Institution of Mechanical Engineers*, Vol. 184, pp. 927 – 942

Frank R. M. and Lazarus, R. B., 1964, ‘‘Mixed Eulerian–Lagrangian Method’’, *Methods in Computational Physics*, Vol. 3, Academic Press, New York

Fujii, Y., Iwabe, H., et al., 1979, ‘‘Effect of Dynamic Behaviour of End Mill in Machining on Work Accuracy (1st Report) – Mechanism of Generating Shape Errors’’, *Bulletin of the Japan Society of Precision Engineering*, Vol. 13(1), pp. 20 – 26

Gadalla, M., 1997, *Improving the Accuracy of Parametric Surfaces Using Cutting Force Synthesis and Surface Offset Techniques*, Ph.D. Thesis, University of Western Ontario, Canada

Goel, B. S., 1967, *Measurement of Dynamic Cutting Force Coefficients*, Ph.D Thesis, McMaster University, Canada

Gonzalo, O., Jauregi, H., et al., 2009, ‘‘Prediction of Specific Force Coefficients From a FEM Cutting Model’’, *International Journal of Advanced Manufacturing Technology*, Vol. 43(3 – 4), pp. 348 – 356

Gradisek, J., Kalveram, M. and Weinert, K., 2004, ‘‘Mechanistic Identification of Specific Force Coefficients For a General End Mill’’, *International Journal of Machine Tools and Manufacture*, Vol. 44(4), pp. 401 – 414

Gradisek, J., Govekar, E., et al., 2005, ‘‘On Stability Prediction for Low Radial Immersion Milling’’, *Machining Science and Technology*, Vol. 9(1), pp. 117 – 130

Grimes, R. G., Lewis, J. G. and Simon, H. D., 1994, ‘‘A Shifted Block Lanczos Algorithm for Solving Sparse Symmetric Generalized Eigenproblems’’, *SIAM Journal on Matrix Analysis and Applications*, Vol. 15, pp. 228 – 272,

Hastings, W. F., Mathew, P. and Oxley, P. L. B., 1980, ‘‘Machining Theory for Predicting Chip Geometry, Cutting Forces etc. from Work Material Properties and Cutting Conditions,’’ *Proceedings of the Royal Society of London, Series A: Mathematical and Physical Sciences*, Vol. 371(1747), pp. 569 – 587

He, J. and Fu, Z., 2001, *Modal Analysis*, Butterworth–Heinemann, Linacre House, Jordan Hill, Oxford OX2 8DP

Henkin, A., 1962, *The Influence of Some Physical Properties on Machinability of Metals*, Ph.D Thesis, University of Michigan Industry, College of Engineering

Herbert, E. G., 1926, ‘‘Measurement of Cutting Temperatures’’, *Proceedings of the Institution of Mechanical Engineers, Vol. 1*, pp. 289 – 329

Hohn, R.E., Shridar, R. and Long, G.W., 1968, ‘‘A Stability Algorithm for a Special Case of the Milling Process’’, *Transactions of the ASME – Journal of Engineering for Industry*, Vol. 90, pp. 325 – 329

Hou, D. and Cheng, K., 2009, *Fundamentals, Applications and Practices, Springer Series in Advanced Manufacturing*, pp. 7 – 20

Insperger, T. and Stepan, G., 2000, ‘‘Stability of the Milling Process’’, *Periodica Polytechnica, Mechanical Engineering*, Vol. 44(1), pp. 47 – 57

Insperger, T., Stepan, G. and Namachchivaya, N., 2001, ‘‘Comparison of the Dynamics of Low Immersion Milling and Cutting with Varying Spindle Speed’’, *Proceedings of the ASME 2001 Design Engineering Technical Conferences, Pittsburgh, Pennsylvania*, paper no. DETC2001/VIB–21616 (CD–ROM and available http://www.mm.bme.hu/~inspi/main.html)

Insperger, T., 2004, ‘‘Vibration Frequencies in High–Speed Milling Processes or A Positive Answer to Davies, Pratt, Duterrer and Burns’’, *Journal of Manufacturing Science and Engineering*, Vol. 126(3), pp. 481 – 487

Insperger, T., Mann, B. P., Surmann T. and Stapan, G., 2008, ‘‘On the Chatter Frequencies of Milling Processes with Runout’’, *International Journal of Machine Tools and Manufacture*, Vol. 48(10), pp. 1081 – 1089

Ismail, F., Elbestawi, M, A., Du, R. and Urbasik, K., 1993, ‘‘Generation of Milled Surfaces Including Tool Dynamics and Wear’’, *Transactions of the ASME – Journal of Engineering for Industry*, Vol. 115, pp. 245 – 252

Itoigawa, F., Childs, T. H. C., Nakamuraa, T. and Belluco, W., 2006, ‘‘Effects and Mechanisms in Minimal Quantity Lubrication Machining of an Aluminum Alloy’’, *Wear*, Vol. 260(3), pp. 339 – 344

Iwata, K., Osakada, K. and Terasaka, Y., 1984, ‘‘Progress Modelling of Orthogonal Cutting by the Rigid–Plastic Finite Element Method’’, *Transactions of the ASME – Journal of Engineering Materials and Technology,* Vol. 106(2), pp. 132 – 138

Kalpakjian, S. and Schmid, S. R., 2003, *Manufacturing Processes for Engineering Materials*, Prentice Hall

Kals, H. J. J., 1971, ‘‘On the Calculation of Stability Charts on the Basis of the Damping and Stiffness of the Cutting Process’’, *CIRP Annals*, Vol. 19, pp. 297 – 303

Kaewunruen, S. and Remennikov, A. M., 2005, ‘‘Applications of Experimental Modal Testing for Estimating Dynamic Properties of Structural Components’’, *Australia Structural Engineering Conference 2005 (ASEC 2005) Newcastle Australia* (CD–ROM and available at http://ro.uow.edu.au/cgi/viewcontent. cgi?article=1285&context=engpapers)

Karlsson and Sorensen, Inc. Hibbitt, 2006, *Abaqus Theory Manual*, 1080 Main Street, Pawtucket Rl., 02860 – 4847 USA

Kegg, R. L., 1965, ‘‘Cutting Dynamics in Machine Tool Chatter’’, *Transactions of the ASME – Journal of Engineering for Industry*, Vol. 87(4), pp. 464 – 470

Kennedy, C. C. and Pancu, C. D. P., 1947, ‘‘Use of Vectors in Vibration Measurement and Analysis’’, *Journal of the Aeronautical Sciences*, Vol. 14(11), pp. 603 – 625

Klamecki, B. E., 1973, *Incipient Chip Formation in Metal Cutting – A Three–Dimension Finite Element Analysis*, Ph.D Thesis, University of Illinois at Urbana–Champaign

Kline, W. A., DeVor, R. E. and Lindberg, R., 1982(a), ‘‘The Prediction of Cutting Forces in End Milling with Application to Cornering Cuts’’, *International Journal of Machine Tool Design and Research*, 22(1), pp. 7 – 22

Kline, W. A., DeVor, R. E. and Shareef, L. A., 1982(b), ‘‘The Prediction of Surface Accuracy in End Milling’’, *Transactions of the ASME – Journal of Engineering for Industry*, Vol. 104, pp. 272 – 278

Kline, W. A. and DeVor, R. E., 1983, ‘‘Effect of Runout on Cutting Geometry and Forces in End Milling’’, *International Journal of Machine Tool Design and Research*, Vol. 23(2 – 3), pp. 123 – 140

Knight, W. A., 1970, ‘‘Some Observations on the Vibratory Metal Cutting Process Employing High Speed Photography’’, *International Journal of Machine Tool Design and Research*, Vol. 10, pp. 221 – 247

Ko, J. H., Yun, W.-S., et al., 2002, ‘‘Development of a Virtual Machining System, Part 1: Approximation of the Size Effect for Cutting Force Prediction’’, *International Journal of Machine Tools and Manufacture*, Vol. 42(15), pp. 1595 – 1605

Ko, J. H. and Cho, D.-W., 2004, ‘‘Feed Rate Scheduling Model Considering Transverse Rupture Strength of a Tool for 3D Ball–End Milling’’, *International Journal of Machine Tools and Manufacture*, Vol. 44(10), pp. 1047 – 1059

Koenigsberger, F. and Sabberwal, A. J. P., 1961, ‘‘An Investigation into the Cutting Force Pulsations During Milling Operations’’, *International Journal of Machine Tool Design and Research*, Vol. 1, pp. 15 – 33

Koenigsberger, F. and Tlusty, J., 1967, *Machine Tool Structures – Vol. 1: Stability Against Chatter*, Pergamon Press, Oxford UK

Koch, K. F., Lilly, B., Kropp, E., and Altan, T., 1990, ‘‘Development of a CAE–Module for Calculating Cutting Forces in 3–Axis Milling of Sculptured Surfaces in Die Manufacturing’’, *National Science Foundation ERC report ERC/NSM–D-90-43*, The Ohio State University

Kwon, Y. W. and Bang, H., 1997, *The Finite Element Method Using Matlab*, CRC Press LLC, 2000 Corporate Blvd, N. W., Boca Raton, Florida 33431

Lajczok, M. R., 1980, *A Study of Some Aspects of Metal Machining Using the Finite Element Method*, Ph.D. Thesis, North Carolina State University

Lacerda, H. B. and Lima, V. T., 2004, ‘‘Evaluation of Cutting Forces and Prediction of Chatter Vibrations in Milling’’, *Journal of the Brazilian Society of Mechanical Sciences and Engineering*, Vol. 26(1), pp. 74 – 81

Lee, E. H. and Schaffer, B. W., 1951, ‘‘Theory of Plasticity Applied to a Problem of Machining’’, *Transactions of the ASME – Journal of Applied Mechanics*, Vol. 18, pp. 405 – 413

Lee, D., and Wilkening, W. W., 1982, ‘‘Material Modelling and High–Speed Machining Process’’, *General Electric Information Series Report No. 82CRD261, General Electric Co., Technical Information Exchange*

Lee, A. C. and Liu, C. S., 1991(a), ‘‘Analysis of Chatter Vibration in the End Milling Process’’, *International Journal of Machine Tool Design and Research*, Vol. 31(4), pp. 471 – 479

Lee, A. C., Liu, C. S. and Chiang, S. T., 1991(b), ‘‘Analysis of Chatter Vibration in a Cutter – Workpiece System’’, *International Journal of Machine Tool Design and Research*, Vol. 31(2), pp. 221 – 234

Lei, S., Shin, Y. C. and Incropera, F. P., 1999, ‘‘Thermo–Mechanical Modeling of Orthogonal Machining Process by Finite Element Analysis,’’ *International Journal of Machine Tools & Manufacture*, Vol. 39(5), pp. 731 – 750

Lim, E. M., Feng, B.Y., and Menq, C. B., 1993, ‘‘The Prediction of Dimensional Errors for Machining Sculptured Surfaces Using Ball–End Milling’’, *American Society of Mechanical Engineers, Production Engineering Division (Publication) PED*, Vol. 64, pp. 149 – 156

Lim, E. M., Feng, H.-Y., et al., 1995, ‘‘Prediction of Dimensional Error for Sculptured Surface Productions Using the Ball–End Milling Process. Part 1: chip geometry analysis and cutting force prediction’’, *International Journal of Machine Tools and Manufacture*, Vol. 35(8), pp. 1149 – 1169

Liu, X. W., Cheng, K., et al., 2002(a), ‘‘Improved Dynamic Cutting Force Model in Peripheral Milling Part I: Theoretical Model and Simulation’’, *International Journal of Advanced Manufacturing Technology*, Vol. 20(9), pp. 631 – 638

Liu, X. W., Cheng, K., et al., 2002(b), ‘‘Prediction of Cutting Force Distribution and its Influence on Dimensional Accuracy in Peripheral Milling’’, *International Journal of Machine Tools and Manufacture*, Vol. 42(7), pp. 791 – 800

Liu, X. W., Cheng, K., et al., 2004, ‘‘Improved Dynamic Cutting Force Model in Peripheral Milling. Part II: Experimental Verification and Prediction’’,

International Journal of Advanced Manufacturing Technology, Vol. 24(11 – 12) pp. 794 – 805,

Liu, X.-W., Cheng, K., Longstaff, A. P., Widiyarto, M. H., and Ford, D., 2005(a), ‘‘Improved Dynamic Cutting Force Models in Ball–End Milling Part I: Theoretical Modelling and Experimental Calibration’’, *International Journal of Advanced Manufacturing Technology*, Vol. 26, pp. 457 – 465,

Liu, X. and Cheng, K., 2005(b), ‘‘Modelling the Machining Dynamics of Peripheral Milling’’, *International Journal of Machine Tools and Manufacture*, Vol. 45(11), pp. 1301 – 1320

Lord Rayleigh, 1878, *Theory of Sound, Vol. 2*, The Macmillan Company, New York (Reprinted 1945 by Dover Publications, New York)

Luo, X. K., Cheng, K., Luo, X. C. and Liu, X. W., 2005, ‘‘A Simulated Investigation on the Machining Instability and Dynamic Surface Generation’’, *International Journal of Advanced Manufacturing Technology*, Vol. 26, pp. 457 – 465

Madhavan, V., Chandrasekar, S. and Farris, T. N., 2000, ‘‘Machining as A Wedge Indentation’’, *Transactions of the ASME – Journal of Applied Mechanics*, Vol. 67(1), pp. 128 – 139

Magnus, W., and Winkler, S., 1966, *Hill’s Equation*, Wiley, NY.

Mallock, A., 1881, ‘‘The Action of Cutting Tools’’, *Proceedings of the Royal Society of London*, Vol. 33, pp. 127 – 139

Mamalis, A. G., Horvath, M., Branis, A. S. and Manolakos, D. E., 2001, ‘‘Finite Element Simulation of Chip Formation in Orthogonal Metal Cutting’’, *Journal of Materials Processing Technology*, Vol. 110(1), pp. 19 – 27

Martellotti, M. E., 1941, ‘‘An Analysis of the Milling Process’’, *Transactions of the American Society of Mechanical Engineers*, Vol. 63, pp. 677 – 700

Merchant, M. E., 1945, ‘‘Mechanics of the Metal Cutting Process. I. Orthogonal Cutting and a Type 2 Chip,’’ *Journal of Applied Physics*. Vol. 16, pp. 267 – 275

Merchant, M. E., 1945, ‘‘Mechanics of the Metal Cutting Process II: Plasticity Conditions in Orthogonal Cutting’’, *Journal of Applied Physics*, Vol. 16, pp. 318 – 324

Merdol, S. D. and Altintas, Y., 2004, ‘‘Multi Frequency Solution of Chatter Stability for Low Immersion Milling’’, *Transactions of the ASME – Journal of Manufacturing Science and Engineering*, Vol. 126(3), pp. 459 – 466

Merritt, H. E., 1965, ‘‘Theory of Self–Excited Machine Tool Chatter’’, *Transactions of the ASME – Journal of Engineering for Industry*, Vol. 87, pp. 447 – 454

Minis, I., Yanushevsky, T., Tembo R. and Hocken, R., 1990, ‘‘Analysis of Linear and Nonlinear Chatter in Milling’’, *CIRP Annals*, Vol. 39, pp. 459 – 462

Minis I. and Yanushevsky, T., 1993, ‘‘A New Theoretical Approach for the Prediction of Machine Tool Chatter in Milling’’, *Transactions of the ASME – Journal of Engineering for Industry*, Vol. 115, pp. 1 – 8

Mitchell, L. D., 1986, ‘‘Signal Processing and Fast – Fourier – Transform (FFT) Analyzer – A Survey’’, *The International Journal of Analytical and Experimental Modal Analysis*, Vol. 1(1), pp. 24 – 36

Montgomery, D. and Altintas, Y., 1991, ‘‘Mechanism of Cutting Force and Surface Generation in Dynamic Milling’’, *Transactions of the ASME – Journal of Engineering for Industry*, Vol. 113, pp. 160 – 168

Moriwaki T., Sugimura, N. and Luan, S., 1993, ‘‘Combined Stress, Material Flow and Heat Analysis of Orthogonal Micromachining of Copper’’, *CIRP Annals*, Vol. 42, pp. 75 – 78

Movahhedy, M., Gadala, M. S. and Altintas, Y., 2000, ‘‘Simulation of the Orthogonal Metal Cutting Process Using an Arbitrary Lagrangian–Eulerian Finite–Element Method’’, *Journal of Materials Processing Technology*, Vol. 103(2), pp. 267 – 275

Natarajan, R. and Jeelani, S., 1983, ‘‘Residual Stresses in Machining Using Finite Element Method’’, *Computers in Engineering, Computer Software and Applications, ASME, New York*, Vol. 3, pp. 19 – 20

Nigm, M. M. and Sadek, M. M., 1977, ‘‘Experimental Investigation of the Characteristics of the Dynamic Cutting Process’’, *Transactions of the ASME – Journal of Engineering for Industry*, pp. 410 – 418

Noh W. F., 1964, ‘‘CEL: A Time–Dependent Two Space–Dimensional Coupled Eulerian–Lagrangian Code’’, *Methods in Computational Physics, Vol. 3*, Academic Press, New York

Opitz, H., 1968, ‘‘Chatter Behavior of Heavy Machine Tools’’, *Quarterly Technical Report No. 2 AF 61 (052) – 916 Research and Technology Division*, Wright – Patterson Air Force Base, Ohio

Opitz, H. and Bernardi, F., 1970, ‘‘Investigation and Calculation of the Chatter Behaviour of Lathes and Milling Machines’’, *CIRP Annals*, Vol. 18, pp. 335 – 343

Oxley, P. L. B. and Welsh, M. J. M., 1963, ‘‘Calculating the Shear Angle in Orthogonal Metal Cutting from Fundamental Stress, strain, Strain–Rate Properties of the Work Material,’’ *Proceedings of the fourth International Machine Tool Design Research Conference*, Pergamon, Oxford, pp. 73–86

Özel, T. and Altan, T., 2000, ‘‘Process Simulation Using Finite Element Method – Prediction of Cutting Forces, Tool Stresses and Temperatures in High–Speed Flat End Milling’’, *International Journal of Machine Tools and Manufacture*, Vol. 40(5), pp. 713 – 738

Özel, T. and Zeren, E., 2005, ‘‘Finite Element Method Simulation of Machining of AISI 1045 Steel With A Round Edge Cutting Tool’’, *Proceedings of 8th CIRP International Workshop on Modeling of Machining Operations, Chemnitz, Germany,* pp. 533 – 541

Özel, T. and Zeren, E., 2007, ‘‘Finite Element Modeling the Influence of Edge Roundness on the Stress and Temperature Fields Induced by High–Speed Machining’’, *The International Journal of Advanced Manufacturing Technology*, Vol. 35(3), pp. 255 – 267

Pantale, O., Bacaria, J. L., Dalverny, O., Rakotomalala, R. and Caperaa, S., 2004, ‘‘2D and 3D Numerical Models of Metal Cutting with Damage Effects’’, *Computer Methods in Applied Mechanics and Engineering*, Vol. 193(39 – 41 SPEC. ISS), pp. 4383 – 4399

Parsons, F., 1923, ‘‘Power Required for Cutting Metal’’, *Transactions of the American Society of Mechanical Engineers*, Vol. 49, pp. 193 – 227

Pednekar, V., Madhavan, V. and Adibi–Sedeh, Amir H., 2004, ‘‘Investigation of the Transition from Plane Strain to Plane Stress in Orthogonal Metal Cutting’’, American Society of Mechanical Engineers, Applied Mechanics Division, AMD, Vol. 255, pp. 513 – 528

Peters, J., Vanherck, P., and Van Brussel, H., 1971, ‘‘The Measurement of the Dynamic Cutting Force Coefficient’’, *CIRP Annals*, Vol. 21(2), pp. 129 – 136

Piispanen, V., 1948, ‘‘Theory of Formation of Metal Chips’’, *Journal of Applied Physics*, Vol. 19, pp. 876 – 881

Press, W. H., Flannery, B. P., Teukolsky, S. A. and Vetterling, W. T., 1992, *Linear Correlation in Numerical Recipes in FORTRAN: The Art of Scientific Computing*, 2nd edition, Cambridge, England, Cambridge University Press, pp. 630 – 633 (available at: http://www.nr.com/oldverswitcher.html)

Ramaraj, T. C. and Eleftheriou, E., 1994, ‘‘Analysis of the Mechanics of Machining with Tapered End Milling Cutters’’, *Transactions of the ASME – Journal of Engineering for Industry*, Vol. 116(3), pp. 398 – 404

Ranganath, S., Campbell, A. B., Gorkiewicz, D. W., 2007, ‘‘A Model to Calibrate and Predict Forces in Machining with Honed Cutting Tools or Inserts’’, *International Journal of Machine Tools and Manufacture*, Vol. 47, pp. 820 – 840

Rosa, P. A. R., Martins, P. A. F., Atkins, A.G., 2007, ‘‘Revisiting the Fundamentals of Metal Cutting by Means of Finite Elements and Ductile Fracture Mechanics’’, *International Journal of Machine Tools and Manufacture*, Vol. 47(3 – 4), pp. 607 – 617

Sabberwal, A. J. P., 1961, ‘‘Chip Section and Cutting Force During the Milling Operation’’, *CIRP Annals*, Vol. 10, pp. 197 – 203

Sanliturk, K. Y. and Cakar, O., 2005, ‘‘Noise Elimination from Measured Frequency Response Functions’’, *Mechanical Systems and Signal Processing*, Vol. 19(3), pp. 615 – 631

J.F. Sarnicola and G. Boothroyd, 1973, ‘‘Machine Tool Chatter: Factors which Influence Cutting Forces During Wave Removing’’, *Proceedings of the Second NAMRC*, pp. 111–128

Sawin, N. N., 1926, ‘‘Theory of Milling Cutters’’, *Mechanical Engineering*, Vol. 48, pp. 1203 – 1209

Seguy, S., Campa, F. J., et al., 2008, ‘‘Toolpath Dependent Stability Lobes for the Milling of Thin–Walled Parts’’, *International Journal of Machining and Machinability of Materials*, Vol. 4(4), pp. 377 – 392

Sekhon G. S. and Chenot, J. L., 1993, ‘‘Numerical Simulation of Continuous Chip Formation during Non–Steady Orthogonal Cutting’’, *Engineering Computations*, Vol. 10, pp. 31 – 48

Shet, C., Deng, X., 2000, ‘‘Finite Element Analysis of the Orthogonal Metal Cutting Process’’, *Journal of Materials Processing Technology*, Vol. 105(1), pp. 95 – 109

Shih, A. J. M., Chandrasekar, S., Yang, H. T. Y., 1990, ‘‘Finite Element Simulation of Metal Cutting Process with Strain–Rate and Temperature Effects’’, *American Society of Mechanical Engineers, Production Engineering Division*, Vol. 43, pp. 11 – 24

Shih, A. J., 1996, ‘‘Finite Element Analysis of the Rake Angle Effects in Orthogonal Metal Cutting’’, *International Journal of Mechanical Sciences*, Vol. 38(1), pp. 1 – 17

Shirakashi, T., Usui, E., 1974, ‘‘Simulation Analysis of Orthogonal Metal Cutting Mechanism’’, *Proceedings of the International Conference on Production Engineering*, Tokyo, Japan, pp. 535 – 540

Shore, H., 1924, *Metal Cutting Temperatures*, Ph.D Thesis, MIT, Cambridge, MA

Sim, C. G., Yang, M. Y., ‘‘Reduction of Machining Errors by Adjustment of Feedrates in the Ball–End Mill Process’’, *International Journal of Production Research*, Vol. 31(3), pp. 665 – 689, 1993

Sisson, T. R. and Kegg, R. L., ‘‘An Explanation of Low Speed Chatter Effects’’, *Transactions of the ASME – Journal of Engineering for Industry*, Vol. 91, pp. 951 – 955, 1969

Slavicek, J., 1965, ‘‘The Effect of Irregular Tooth Pitch on Stability of Milling’’, 6th MTDR Conference Manchester

Smith, S. W., 1997, *The Scientist & Engineer's Guide to Digital Signal Processing*, California Technical Publication, San Diego, 1st edition, (Available: http://www.dspguide.com)

Solis, E., Peres, C. R., Jimenez, J. E., Alique, J. R., Monje, J. C., 2004, ‘‘A New Analytical–Experimental Method for the Identification of Stability Lobes in

High–Speed Milling'', *International Journal of Machine Tools and Manufacture*, Vol. 44(15), pp. 1591 – 1597

Sridhar, R., Hohn, R. E. and Long, G. W., 1968(a), ''General Formulation of the Milling Process Equation'', *Transactions of the ASME – Journal of Engineering for Industry*, Vol. 90, pp. 317 – 324

Sridhar, R., Hohn, R. E. and Long, G. W., 1968(b), ''A Stability Algorithm for the General Milling Process'', *Transactions of the ASME – Journal of Engineering for Industry*, Vol. 90, pp. 330 – 334

Srinivasan, K. and Nachtigal, C. L., 1978(a), ''Investigation of the Cutting Process Dynamics in Turning Operations'', *Transactions of the ASME – Journal of Engineering for Industry*, Vol. 100, pp. 323 – 331

Srinivasan, K. and Nachtigal, C. L., 1978(b), ''Identification of Machining System Dynamics by Equation Error Minimization'', *Transactions of the ASME – Journal of Engineering for Industry*, Vol. 100, pp. 332 – 339,

Stepan, G., Szalai, R., et al., 2005, ''Nonlinear Dynamics of High–Speed Milling – Analyses, Numerics, and Experiments'', *Transactions of the ASME – Journal of Vibration and Acoustic*, Vol. 127(2), pp. 197 – 203

Strenkowski, J. S. and Carroll, J. T., 1985, ''A Finite Element Model of Orthogonal Metal Cutting'', *Transactions of the ASME – Journal of Engineering for Industry*, Vol. 107(4), pp. 349 – 354

Strenkowski J. S. and Moon, K.J., 1990, ''Finite Element Prediction of Chip Geometry and Tool/Workpiece Temperature Distributions in Orthogonal Metal Cutting'', *Transactions of the ASME – Journal of Engineering for Industry*, Vol. 112, pp. 313 – 318

Strenkowski, J. S., Shih, A. J., Lin, J.-C., 2002, ''An Analytical Finite Element Model for Predicting Three–Dimensional Tool Forces and Chip Flow'', *International Journal of Machine Tools and Manufacture*, Vol. 42(6), pp. 723 – 731

Sutherland, J. W. and DeVor, R. E., 1986, ''An Improved Method for Cutting Force and Surface Error Prediction in Flexible End Milling Systems'', *Transactions of the ASME – Journal of Engineering for Industry,* Vol. 108, pp. 269 – 279

Tai, C.-C. and Fuh, K.-H., 1995, ‘‘Prediction of Cutting Forces in the Ball–End Milling Process,’’ *Journal of Materials Processing Technology*, Vol. 54(1 – 4), pp. 286 – 301

Taylor, F. W., 1907, ‘‘On the Art of Cutting Metals’’, *Transactions of the American Society of Mechanical Engineers*, Vol. 28, pp. 31 – 350

Thevenot, V., Arnaud, L., Dessein, G. and Cazenave–Larroche, G., 2006, ‘‘Influence of Material Removal on the Dynamics Behavior of Thin–walled Structures in Peripheral Milling’’, *Machining Science and Technology*, Vol. 10, pp. 275 – 287

Timothy, L. K. and Bona, B. E., 1998, *State Space Analysis: An Introduction*, McGraw–Hill Book Company, New York

Tlusty, J. and Polacek, M., 1963, ‘‘The Stability of Machine Tools Against Self Excited Vibrations in Machining’’, *International Research in Production Engineering*, pp. 465 – 474

Tlusty, J. and Koenigsberger, F., 1970, *Machine Tool Structures*, Pergamon Press Oxford 5th edition, Vol. 1

Tlusty, J. and MacNeil, P., 1975, ‘‘Dynamics of Cutting Forces in End Milling’’, *CIRP Annals*, Vol. 24, pp. 21 – 25

Tlusty, J., 1978, ‘‘Analysis of the State of Research in Cutting Dynamics’’, *CIRP Annals*, Vol. 27(2), pp. 583 – 589

Tlusty, J. and Ismail, P., 1981, ‘‘Basic Nonlinearity in Machining Chatter’’, *CIRP Annals*, Vol. 10(1), pp. 299 – 304

Tlusty, J. and Ismail, P., ‘‘Special Aspects of Chatter in Milling’’, *Journal of Vibration, Acoustics, Stress and Reliability in Design*, Vol. 105, 1983.

Tobias, S.A., Fishwick, W., 1958, ‘‘Theory of Regenerative Machine Tool Chatter’’, *The Engineering London*, Vol. 205

Tobias, S. A., 1965, *Machine Tool Vibration*, Blackie and Sons Ltd, London

Tresca, H., 1978, ‘‘On Further Applications of the Flow of Solids’’, *Proceedings of the Institution of Mechanical Engineers*, pp. 301 – 345

Usui, E., Hirota, A. and Masuko, M., 1978, ‘‘Analytical Prediction of Three Dimensional Cutting Process, Part I: Basic Cutting Model and Energy

Approach'', *Transactions of the ASME – Journal of Engineering for Industry*, Vol. 100, pp. 222 – 228

Usui, E., Hirota, A., 1978, ''Analytical Prediction of Three Dimensional Cutting Process, Part II: Chip Formation and Cutting Force with Conventional Single Point Tool'', *Transactions of the ASME – Journal of Engineering for Industry*, Vol. 100, pp. 229 – 235

Usui, E., Shirakashi, T. and Kitagawa, T., 1978, ''Analytical Prediction of Three Dimensional Cutting Process, Part III: Cutting Temperature and Crater Wear of Carbide Tool'', *Transactions of the ASME – Journal of Engineering for Industry*, Vol. 100, pp. 236 – 243

Van Leer, B., 1977, ''Towards the Ultimate Conservative Difference Scheme IV. A New Approach to Numerical Convection'', *Journal of Computational Physics*, Vol. 23, pp. 276 – 299

Vanherck, P. 1967, ''Increasing Milling Machine Productivity by Use of Cutters with Non–Constant Cutting – Edge Pitch'', *8th MTDR Conference* Manchester

Wallace, P.W. and Andrew, C., 1965, ''Machining Forces: Some Effects of Tool Vibration'', *Journal of Mechanical Engineering Science*, Vol. 7, pp 152 – 162

Wallace, P.W. and Andrew, C., 1966, ''Machining Forces: Some Effects of Removing a Wavy Surface'', *Journal of Mechanical Engineering Science*, Vol. 8(2), pp. 129 – 139

Wan, M., Zhang, W. H., Qin, G. H. and Tan, G., 2007, ''Efficient Calibration of Instantaneous Cutting Force Coefficients and Runout Parameters for General End Mills'', *International Journal of Machine Tools and Manufacture*, Vol. 47 pp. 1767 – 1776

Wen, P. H., Adetoro, M. and Xu, Y., 2008, ''The Fundamental Solution of Mindlin Plates with Damping in the Laplace Domain and Its Applications'', Engineering Analysis with Boundary Elements Vol. 32(10), pp. 870 – 882

Wolfram Research, 2008, *Mathematica Edition: Version 7.0*, Wolfram Research, Inc., Champaign, Illinois

Wu, D. W., 1989, ‘‘A New Approach of Formulating the Transfer Function for Dynamic Cutting Process’’, *Transactions of the ASME – Journal of Engineering for Industry*, Vol. 111, pp. 37 – 47

Yang, M. and Park, H., 1991, ‘‘Prediction of Cutting Force in Ball–End Milling’’, *International Journal of Machine Tools and Manufacture*, Vol. 31(1), pp. 45 – 54

Yucesan, G. and Altintas, Y., 1994, ‘‘Improved Modelling of Cutting Force Coefficients in Peripheral Milling’’, *International Journal of Machine Tools and Manufacture*, Vol. 34(4), pp. 473 – 487

Yucesan, G. and Altintas, Y., 1996, ‘‘Prediction of Ball End Milling Forces’’, *Transactions of the ASME – Journal of Engineering for Industry*, Vol. 118(1), pp. 95 – 103

Yun, W.-S. and Cho, D.-W., 2000, ‘‘An Improved Method for the Determination of 3D Cutting Force Coefficients and Runout Parameters in End Milling’’, *International Journal of Advanced Manufacturing Technology*, Vol. 16, pp. 851 – 858

Yun, W.-S. and Cho, D.-W., 2001, ‘‘Accurate 3–D cutting Force Prediction Using Cutting Condition Independent Coefficients in End Milling’’, *International Journal of Machine Tools and Manufacture*, Vol. 41(4), pp. 463 – 478

Yun, W.-S., Ko, J. H., et al., 2002(a), ‘‘Development of a Virtual Machining System, Part 2: Prediction and analysis of a Machined Surface Error’’, *International Journal of Machine Tools and Manufacture*, 42(15), pp. 1607 – 1615

Yun, W.-S., Ko, J. H., et al., 2002(b), ‘‘Development of a Virtual Machining System, Part 3: Cutting Process Simulation in Transient Cuts’’, *International Journal of Machine Tools and Manufacture*, Vol. 42(15), pp. 1617 – 1626

Zatarain, M., Munoa, J., Peigne, G. and Insperger, T., 2006, ‘‘Analysis of the Influence of Mill Helix Angle on Chatter Stability’’, *CIRP Annals – Manufacturing Technology*, Vol. 55(1), pp. 365 – 368

Zhang, L., 1999, ‘‘On the Separation Criteria in the Simulation of Orthogonal Metal Cutting Using the Finite Element Method’’, *Journal of Materials Processing Technology*, Vol. 89 – 90, pp. 273 – 278

Zienkiewicz O. C., Jain, P. C. and Onate, E., 1978, ‘‘Flow of Solids During Forming and Extrusion: Some Aspects of Numerical Solutions’’, *International Journal of Solids and Structures*, Vol. 14, pp. 15 – 38

Appendix A

A.1. Calibration Experimental and Cutting Conditions

When calibrating the tool's cutting force coefficients, the more feedrates and axial depths of cuts performed the more accurate the results are. During the experiments, a total of 12 axial depths of cuts were performed each at an increment of 0.5mm starting from zero. For each axial depth of cut a total of 20 feedrates were used during which the cutting forces were measured using the scopes. The feed rates used are detailed below in Table A.1. A half radial immersion was used in all the experiments.

Table A.1 Experimental cutting conditions

Cut No	Feed per tooth, s_t (mm)	Feedrate, (mm2/min)
1	0.0500	663.000
2	0.0650	861.900
3	0.0800	1060.800
4	0.0950	1259.700
5	0.1100	1458.600
6	0.1250	1657.500
7	0.1400	1856.400
8	0.1550	2055.300
9	0.1700	2254.200
10	0.1850	2453.100
11	0.2000	2652.000
12	0.2150	2850.900
13	0.2300	3049.800
14	0.2450	3248.700
15	0.2600	3447.600
16	0.2750	3646.500
17	0.2900	3845.400
18	0.3050	4044.300
19	0.3200	4243.200
20	0.3350	4442.100

A.2. Dynamometer Dynamic Properties or Reliability Test

The dynamometer – workpiece setup can be thought of as a system excited by the cutting forces from the tool, being in contact with the workpiece. Therefore according to the equations of motion, it exhibits it own response to the excitations which would in turn induce an error into the readings given. If this excitation should have a frequency that matches the resonance frequency of the dynamometer, then the response of the dynamometer would be at its maximum and so would the errors induced in the readings given. The frequency of the excitation (cutting forces) also known as tooth passing frequency is defined as,

$$\omega_T = \frac{\Omega}{60} \times N \tag{A.1}$$

where, ω_T is the tooth passing frequency, Ω is the spindle speed in revs per min, N is the number of flute.

To determine the dynamics of the dynamometer, the transfer function between the actual input and measured forces is used in similar approach used when extracting the dynamic parameters in Chapter 4. The input force is generated using an instrumented hammer mounted with a small load cell to measure input force. The output is taken directly from the dynamometer with the workpiece mounted on it. The transfer function was obtained using one of the modules in the commercial software package 'CutPro' called 'MalTF', which is a data acquisition and transfer function measurement program. The tests were repeated several times. The magnitudes of the transfer function in the normal (Y) directions are shown below in Figures A.1.

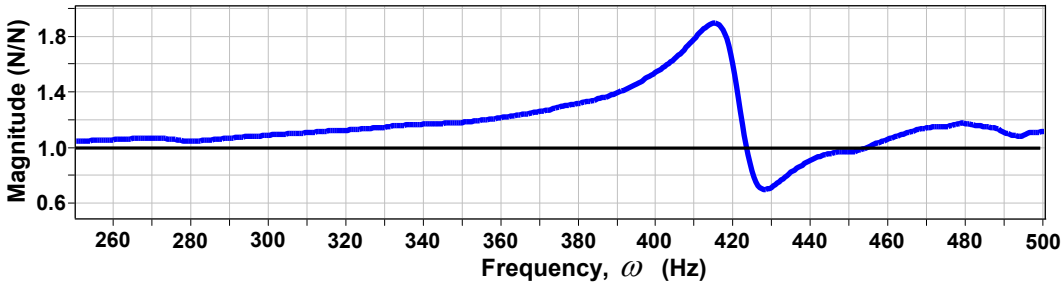

Figure A.1. Transfer function between input force and measured force in normal Y direction.

A magnitude of 1 would imply that the measurements from the dynamometer are not affected in anyway and are the actual cutting forces. It can be seen that up to a frequency of 260Hz, the magnitude of the transfer function is approximately 1. Therefore, a frequency of 221 was during the tool calibration experiments, which corresponds to a spindle speed of 4420 rpm, thereby keeping any induced errors to a minimum.

Appendix B

B.1. Classical Normal Modes Theorem

To show that the system used in this study possess classical modes, the theorem given by Caughey (1965) and Adhikari (2000) (equations 4.4, 4.5, 4.6), are used as follows. The mass normalized modal matrix, $[\Psi]$ was extracted experimentally as,

$$[\Psi] = \begin{bmatrix} 12.2124 & 1.3148 & 2.4899 & 2.8785 & 1.9148 & 0.5610 & -0.0852 & -0.0882 \\ 1.8476 & -2.8091 & -7.0443 & -8.6302 & 3.8660 & 2.1462 & 29.6251 & -2.5560 \\ 0.0738 & 1.9771 & -0.8059 & -1.6753 & 0.3049 & 0.8587 & -0.7356 & 1.3910 \\ 0.0339 & -2.6548 & 3.9066 & -3.2077 & 5.3840 & -12.2339 & 24.0958 & -4.1887 \\ 1.4101 & 0.7898 & 0.5762 & 0.1222 & -0.0390 & 0.0002 & 1.7695 & 7.8925 \\ 0.1547 & -0.0808 & -0.3307 & 0.5472 & -0.0554 & -1.5402 & 1.7370 & -0.3308 \\ 0.0274 & -0.0063 & 0.2667 & -0.6798 & 1.0824 & 0.9663 & 2.4780 & 0.2393 \\ 0.0194 & -0.2480 & -1.9607 & 1.0844 & -2.3948 & -2.4100 & 3.8921 & 1.6301 \end{bmatrix}, \tag{B.1}$$

while the modal stiffness matrix, $[K_p]$ is simply the natural frequency (note the frequency is in radians) squared, giving,

$$K_p = \begin{bmatrix} 6.91E07 & 0 & 0 & 0 & 0 & 0 & 0 & 0 \\ 0 & 1.02E08 & 0 & 0 & 0 & 0 & 0 & 0 \\ 0 & 0 & 1.15E08 & 0 & 0 & 0 & 0 & 0 \\ 0 & 0 & 0 & 1.44E08 & 0 & 0 & 0 & 0 \\ 0 & 0 & 0 & 0 & 1.90E08 & 0 & 0 & 0 \\ 0 & 0 & 0 & 0 & 0 & 2.60E08 & 0 & 0 \\ 0 & 0 & 0 & 0 & 0 & 0 & 3.60E08 & 0 \\ 0 & 0 & 0 & 0 & 0 & 0 & 0 & 5.03E08 \end{bmatrix}, N \cdot m^{-2}, \tag{B.2}$$

and the modal mass matrix is an identity matrix. The modal damping matrix, $[C_p]$ is $[C_p] = [2\zeta_p]$, giving,

$$C_p = \begin{bmatrix} 487.867 & 0 & 0 & 0 & 0 & 0 & 0 & 0 \\ 0 & 53.949 & 0 & 0 & 0 & 0 & 0 & 0 \\ 0 & 0 & 41.685 & 0 & 0 & 0 & 0 & 0 \\ 0 & 0 & 0 & 53.584 & 0 & 0 & 0 & 0 \\ 0 & 0 & 0 & 0 & 40.703 & 0 & 0 & 0 \\ 0 & 0 & 0 & 0 & 0 & 53.207 & 0 & 0 \\ 0 & 0 & 0 & 0 & 0 & 0 & 78.730 & 0 \\ 0 & 0 & 0 & 0 & 0 & 0 & 0 & 361.279 \end{bmatrix}, Kg \cdot s^{-1}, \quad \text{(B.3)}$$

Using the modal matrix extracted experimentally to obtain the system's mass, $[M]$, stiffness, $[K]$ and damping, $[C]$ matrices gives,

$$K = \begin{bmatrix} 1.3E10 & \text{-}3.5E09 & \text{-}4.0E08 & \text{-}9.1eE08 & 1.1E09 & \text{-}3.2E07 & 2.7E08 & -1.5E09 \\ \text{-}3.5E09 & 3.4E11 & -6.8E09 & 2.6E11 & 8.0E09 & 1.8E10 & 2.8E10 & 3.7E10 \\ \text{-}4.0E08 & -6.8E09 & 2.3E09 & -1.2E10 & 5.1E09 & -1.2E09 & -7.3E07 & -7.0E08 \\ \text{-}9.1E08 & 2.6E11 & -1.2E10 & 2.7E11 & -1.E09 & 2.0E10 & 1.9E10 & 3.4E10 \\ 1.1E09 & 8.0E09 & 5.1E09 & -1.3E09 & 3.3E10 & -2.1E08 & 2.5E09 & 8.8E09 \\ \text{-}3.2E07 & 1.8E10 & -1.2E09 & 2.0E10 & -2.1E08 & 1.8E08 & 1.0E09 & 3.3E09 \\ 2.7E08 & 2.8E10 & -7.3E07 & 1.9E10 & 2.5E09 & 1.0E09 & 2.8E09 & 2.4E09 \\ \text{-}1.5E09 & 3.7E10 & -7.0E08 & 3.4E10 & 8.8E09 & 3.3E09 & 2.4E09 & 1.0E10 \end{bmatrix}, N \cdot m^{-2} \quad \text{(B.4)}$$

$$M = \begin{bmatrix} 169.35 & -17.20 & -2.32 & -0.82 & 19.12 & 1.45 & 1.42 & -8.26 \\ -17.20 & 1039.14 & -7.61 & 726.79 & 27.37 & 46.91 & 83.11 & 101.89 \\ -2.32 & 7.61 & 10.68 & -35.44 & 10.66 & -3.88 & 0.58 & -4.12 \\ -0.82 & 726.79 & -35.44 & 809.41 & 9.18 & 58.96 & 55.95 & 93.07 \\ 19.12 & 27.37 & 10.66 & 9.81 & 68.38 & 0.50 & 6.34 & 18.68 \\ 1.45 & 46.91 & -3.88 & 58.96 & 0.50 & 5.94 & 2.22 & 11.33 \\ 1.42 & 83.11 & 0.56 & 55.95 & 6.34 & 2.22 & 8.84 & 3.86 \\ -8.26 & 101.89 & -4.12 & 93.07 & 18.68 & 11.33 & 3.86 & 34.43 \end{bmatrix}, Kg, \quad \text{(B.5)}$$

$$C = \begin{bmatrix} 7.4E04 & 9.0E03 & 2.5E02 & -4.9E01 & 8.3E03 & 9.1E02 & 1.7E02 & -2.7E02 \\ 9.0E03 & 8.0E04 & -2.1E03 & 6.0E04 & -2.2E03 & 4.2E03 & 6.1E03 & 7.0E03 \\ 2.5E02 & -2.1E03 & 1.2E03 & -4.1E03 & 4.0E03 & -3.8E02 & 8.7E01 & 4.0E02 \\ -4.9E01 & 6.0E04 & -4.1E03 & 6.3E04 & -8.6E03 & 4.7E03 & 4.1E03 & 5.5E03 \\ 8.3E03 & -2.2E03 & 4.0E03 & -8.6E03 & 2.4E04 & -6.E02 & 1.0E03 & 5.2E03 \\ 9.1E02 & 4.2E03 & -3.8E02 & 4.7E03 & -6.0E02 & 4.4E02 & 2.1E02 & 6.0E02 \\ 1.7E02 & 6.1E03 & 8.7E01 & 4.1E03 & 1.0E03 & 2.1E02 & 6.3E02 & 6.1E02 \\ -2.7E02 & 7.0E03 & 4.0E02 & 5.5E03 & 5.2E03 & 6.0E02 & 6.1E02 & 2.9E03 \end{bmatrix}, Kg \cdot s^{-1} \quad \text{(B.6)}$$

Therefore using the third condition given in (4.6),

$$[M][K]^{-1}[C] =$$
$$\begin{bmatrix} 1.1E-03 & 1.4E-4 & 5.4E-6 & 1.8E-6 & 1.2E-4 & 1.3E-5 & 2.4E-6 & -5.4E-7 \\ 1.4E-4 & 2.7E-4 & -1.2E-6 & 1.7E-4 & 1.2E-5 & 1.2E-5 & 1.9E-5 & 2.1E-5 \\ 5.4E-6 & -1.2E-6 & 5.1E-6 & -1.2E-5 & 8.9E-6 & -1.1E-6 & 4.4E-7 & 6.6E-8 \\ 1.8E-6 & 1.7E-4 & -1.2E-5 & 1.9E-4 & -1.5E-5 & 1.3E-5 & 1.2E-5 & 1.5E-5 \\ 1.2E-4 & 1.2E-5 & 8.9E-6 & -1.5E-5 & 6.0E-5 & 2.6E-7 & 2.6E-6 & 1.0E-5 \\ 1.3E-5 & 1.2E-5 & -1.1E-6 & 1.3E-5 & 2.6E-7 & 1.5E-6 & 4.3E-7 & 2.4E-6 \\ 2.4eE-6 & 1.9E-5 & 4.4E-7 & 1.2E-5 & 2.6E-6 & 4.3E-7 & 2.0E-6 & 9.0E-7 \\ -5.4E-7 & 2.1E-5 & 6.6E-8 & 1.5E-5 & 1.0E-5 & 2.4E-6 & 9.0E-7 & 9.5E-6 \end{bmatrix}$$
$$= [C][K]^{-1}[M].$$

(B.7)

It can therefore be shown that the other two conditions in (4.4) and (4.5) are both equally satisfied, hence the system is assumed to possess classical normal modes and the damping can be taken as proportional.

B.2. Shape Functions for a 20-node Brick Element

The shape functions N_i, for the 20-node brick element (Figure B.1) used in all the FEM simulations are as (Hibbitt, 2006) follows:

$$N_1 = -\frac{1}{8}(1-\xi)(1-\eta)(1-\zeta)(2+\xi+\eta+\zeta), \quad \text{(B.8a)}$$

$$N_2 = -\frac{1}{8}(1+\xi)(1-\eta)(1-\zeta)(2-\xi+\eta+\zeta), \quad \text{(B.8b)}$$

$$N_3 = -\frac{1}{8}(1+\xi)(1+\eta)(1-\zeta)(2-\xi-\eta+\zeta), \quad \text{(B.8c)}$$

$$N_4 = -\frac{1}{8}(1-\xi)(1+\eta)(1-\zeta)(2+\xi-\eta+\zeta), \quad \text{(B.8d)}$$

$$N_5 = -\frac{1}{8}(1-\xi)(1-\eta)(1+\zeta)(2+\xi+\eta-\zeta), \quad \text{(B.8e)}$$

$$N_6 = \frac{1}{8}(1+\xi)(1-\eta)(1+\zeta)(2-\xi+\eta-\zeta), \quad \text{(B.8f)}$$

$$N_7 = -\frac{1}{8}(1+\xi)(1+\eta)(1+\zeta)(2-\xi-\eta-\zeta), \tag{B.8g}$$

$$N_8 = -\frac{1}{8}(1-\xi)(1+\eta)(1+\zeta)(2+\xi-\eta-\zeta), \tag{B.8h}$$

$$N_9 = \frac{1}{4}(1-\xi)(1+\xi)(1-\eta)(1-\zeta), \qquad N_{10} = \frac{1}{4}(1-\eta)(1+\eta)(1+\xi)(1-\zeta), \tag{B.8i}$$

$$N_{11} = \frac{1}{4}(1-\xi)(1+\xi)(1+\eta)(1-\zeta), \qquad N_{12} = \frac{1}{4}(1-\eta)(1+\eta)(1-\xi)(1-\zeta), \tag{B.8j}$$

$$N_{13} = \frac{1}{4}(1-\xi)(1+\xi)(1-\eta)(1+\zeta), \qquad N_{14} = \frac{1}{4}(1-\eta)(1+\eta)(1+\xi)(1+\zeta), \tag{B.8k}$$

$$N_{15} = \frac{1}{4}(1-\xi)(1+\xi)(1+\eta)(1+\zeta), \qquad N_{16} = \frac{1}{4}(1-\eta)(1+\eta)(1-\xi)(1+\zeta), \tag{B.8l}$$

$$N_{17} = \frac{1}{4}(1-\zeta)(1+\zeta)(1-\xi)(1-\eta), \qquad N_{18} = \frac{1}{4}(1-\zeta)(1+\zeta)(1+\xi)(1-\eta), \tag{B.8m}$$

$$N_{19} = \frac{1}{4}(1-\zeta)(1+\zeta)(1+\xi)(1+\eta), \qquad N_{20} = \frac{1}{4}(1-\zeta)(1+\zeta)(1-\xi)(1+\eta), \tag{B.8n}$$

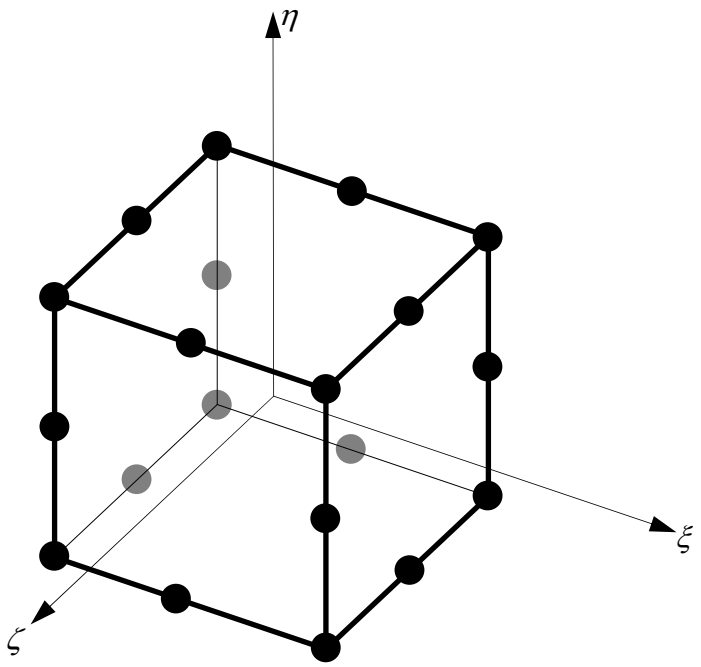

Figure B.1. 20 – Node isoparametric 3-D element.

THIS PAGE IS INTENTIONALLY BLANK